Ultrathin Organic Films Grown by Organic Molecular Beam Deposition and Related Techniques

Stephen R. Forrest

Center for Photonics and Optoelectronic Materials (POEM), Department of Electrical Engineering and the Princeton Materials Institute, Princeton University, Princeton, New Jersey 08544

Received May 2, 1997 (Revised Manuscript Received July 9, 1997)

Contents

1.0. Introduction

During the past decade, enormous progress has been made in growing ultrathin organic films and multilayer structures with a wide range of exciting optoelectronic properties. This progress has been made possible by several important advances in our understanding of organic films and their modes of growth. Perhaps the single most important advance has been the use of ultrahigh vacuum (UHV) as a means to achieve, for the first time, monolayer control over the growth of organic thin films with extremely high chemical purity and structural precision.[1−3] Such monolayer control has been possible for many years using well-known techniques such as Langmuir−Blodgett film deposition,[4] and more recently, self-assembled monolayers from solution have also been achieved.[5] However, ultrahigh-vacuum growth, sometimes referred to as organic molecular beam deposition (OMBD) or organic molecular beam epitaxy (OMBE), has the advantage of providing *both* layer thickness control and an atomically clean environment and substrate. When combined with the ability to perform in situ high-resolution structural diagnostics of the films as they are being deposited, techniques such as OMBD have provided an entirely new prospect for understanding many of the fundamental structural and optoelectronic properties of ultrathin organic film systems. Since such systems are both of intrinsic as well as practical interest, substantial effort worldwide has been invested in attempting to grow and investigate the properties of such thin-film systems.

This paper is a review of recent progress made in organic thin films grown in ultrahigh vacuum or using other vapor-phase deposition methods. We will describe the most important work which has been published in this field since the emergence of OMBD in the mid-1980s. Both the nature of thin-film growth and structural ordering will be discussed, as well as some of the more interesting consequences to the physical properties of such organic thin-film systems will be considered both from a theoretical as well as an experimental viewpoint. Indeed, it will

S0009-2665(94)01014-9 CCC: $28.00

Stephen Forrest graduated from the University of California with a B.A. degree in physics in 1972, and from the University of Michigan with a M.Sc. and Ph.D. degree in physics in1974 and 1979, respectively. From there, he went to Bell Laboratories (Murray Hill) where he did both fundamental and applied research and development of photodetectors for use in long wavelength optical communications systems. In 1982, he became supervisor of the Integrated Optoelectronic Devices and Circuits group at Bell Laboratories. There, he worked on arrays of emitters and detectors, and integrated optical receivers. In 1985, Professor Forrest joined the faculty of the Departments of Electrical Engineering and Materials Science at the University of Southern California where he continued his research on optoelectronic integrated circuits, as well as on a new class of optoelectronic materials: crystalline organic semiconductors. From 1989 to 1992, Professor Forrest served as the Director of the National Center for Integrated Photonic Technology: a consortium of five universities including USC, Columbia, Kent State University, MTT, and UCLA. In 1992, Professor Forrest joined Princeton University as the James S. McDonnell Distinguished University Professor of Electrical Engineering and the Princeton Materials Institute, and as Director of Princeton's Advanced Technology Center for Photonics and Optoelectronic Materials (ATC/POEM). Professor Forrest has served as Associate Editor to the *Journal of Quantum Electronics and Photonics Technology Letters*, has served on the OSA Technical Council, and is on the LEOS Board of Governors. In 1996–97, he was the recipient of the IEEE/LEOS Distinguished Lecturer Award. He is a member of the APS, MRS, and the OSA, and is a Fellow of the IEEE.

be a major objective of this review to place the importance of ultrahigh vacuum deposition in context. As of this writing, there remains considerable discussion as to the necessity for the use of ultrahigh vacuum, and the implication of the need for ultrahigh purity. For example, the attraction of organics for many applications often hinges on the belief that material purity is not important, thus allowing for the realization of devices which are comparatively simple to fabricate and process. These arguments will be considered, and we will attempt to address their importance in various applications.

Beyond the use of UHV to achieve extreme chemical and structural control over organic thin films, it is useful to consider the ultimate motivations for embarking on such a difficult and expensive research endeavor. Perhaps the most compelling reason for studying organic nanostructures stems from the promising scientific and technological results of similar research performed over a span of 25 years in conventional semiconductor heterojunctions grown by the analogous UHV process of molecular beam epitaxy (MBE).[6] By controlling inorganic semiconductor thin film thickness and structure, a wide range of useful and interesting devices based on multiple quantum wells (MQWs) have been demonstrated including low-threshold current laser diodes, low-noise avalanche photodetectors, and high-bandwidth optical modulators.[7−11] The advantageous properties of these MQW structures stems from two factors controlled by the precision of the epitaxial growth process employed: the density of conduction and valence band states (leading to low laser threshold currents[12] and the quantum confined Stark effect[13] employed in optical modulators), and the heterojunction energy band offsets between contacting materials of different composition (leading to the control of current transport). Considerable work in organic thin films has likewise been directed toward achieving these same goals, striving to tailor the materials properties via control of the densities of states and the energy band offsets between differing materials. In addition to these objectives, organic materials in their infinite variety have also been investigated for their application to nonlinear optics[14−18] and other optoelectronic devices.[19−22] Indeed, progress in the growth of organic thin-film nanostructures by UHV techniques such as the demonstration[23,24] of organic MQWs has spawned considerable theoretical work, predicting completely new nonlinear optical phenomena in organic/organic and organic/inorganic MQW structures.[25−29] Hence, we find ourselves at the threshold of realizing an entirely new class of materials, offering nearly unprecedented opportunities for extending our understanding of the fundamental properties of a large class of materials—nanostructured organic molecular crystals. These structures, in turn, promise to have many new and useful properties which will undoubtedly be heavily exploited well into the next century. Even at this relatively early stage of development, vacuum-deposited heterojunction "small molecule"-based organic light-emitting devices are being commercially introduced as the light sources in novel, bright, flat panel displays.[30−32] The applications for such vacuum-deposited organic materials is limited mainly by our ability to control composition and structure of the resulting thin films.

The study of vapor-deposited organic films has been applied to a vast array of molecular systems. However, most of the work which has made the greatest impact to date has concentrated on the study of the growth and optoelectronic characteristics of planar stacking molecules such as the phthalocyanines,[18,21,33,34] and polycyclic aromatic compounds based on naphthalene and perylene. In particular, a molecular system based on perylene—the planar stacking 3,4,9,10-perylenetetracarboxylic dianhydride (PTCDA)—has become the focus of considerable attention in both our own laboratory as well as many laboratories worldwide.[35−43] For this reason, much of the discussion will focus on the growth and properties of the Pc's and aromatic compounds based on naphthalene and perylene which can be treated as archetypes of a larger class of planar stacking molecules which behave in analogous, although not necessarily identical, ways to each other. In addition, some recent results with more unusual materials such as organic salts, and other highly polar compounds will be discussed.

This review is organized as follows: In section 2, the technology of ultrahigh-vacuum growth of organic thin films will be discussed, followed by section 3

where the growth modes of organic thin films will be discussed. We will place the various forms of epitaxy, in particular van der Waals epitaxy and the newly discovered quasi-epitaxy in the context of conventional epitaxy as it applies to inorganic crystalline systems. The relative importance of purity and structural control will also be considered in this section. In section 4, we will review recent results on the optical and electronic properties of ultrathin organic films grown from the vapor phase. In particular, exciton confinement and charge transfer in ultrathin multilayer stacks will be discussed from both theoretical as well as experimental viewpoints. In section 5 we will consider several emerging applications for vapor-deposited organic thin films such as for nonlinear optical and electroluminescent devices. Finally, in section 6 we will summarize the recent findings in the field, and discuss the future prospects of vapor-deposited thin organic films both as they relate to improving our fundamental understanding of these condensed matter systems, as well as to their prospects for use in advanced device applications.

2.0. Techniques for UHV Growth of Organic Thin Films

The most common means for the OMBD growth of organic thin films is to use an ultrahigh-vacuum apparatus such as that shown in Figure 2-1 which is similar, in many respects, to conventional molecular beam epitaxial growth systems. Typically, growth occurs by the evaporation in a background vacuum ranging from 10^{-7} to 10^{-11} Torr of a highly purified powder or, less frequently, a melt of the organic source material from a temperature-controlled oven or Knudsen cell.[6] (It is customary to quote pressures in UHV environments using units of Torr, where 1 Torr = 1 mmHg, or in SI units of Pascal, where 1 Pa = 1 N/m^2. The conversion between these conventions is 1 Pa = 7.5×10^{-3} Torr. For this review, all pressures will be given in units of Torr.) The evaporant is collimated by passing through a series of orifices, after which it is deposited on a substrate held perpendicular to the beam approximately 10−20 cm from the source. The flux of the molecular beam is controlled by a combination of oven temperature (which is maintained somewhat above the sublimation temperature of the source, and well below its chemical decomposition temperature), as well as a mechanical shutter which can switch the beam flux from "on" to "off". By sequentially shuttering the beam flux from more than one Knudsen cell, multilayer structures consisting of alternating layers of different compounds can be grown by this method. Indeed, using sequential shuttering, organic multilayer structures such as multiple quantum wells have been demonstrated.[23,24]

Typical growth rates range from 0.001 to 100 Å/s. Since the monolayer (ML) thickness is from 3 to 5 Å, these rates correspond to from 0.7 ML/h to 30 ML/s. The lower end of this range has a danger of adsorbing contaminants onto the surface at a higher rate than the organic molecules, whereas at the higher rates, growth is extremely difficult to control. For these reasons, most reliable growth data have been obtained at rates of from 0.1 to 5 Å/s. Growth rate is measured using a quartz crystal thickness monitor of the type used in metal thin-film deposition. Between growth runs, the Knudsen cell is often maintained at somewhat below the material sublimation temperature in order to continuously outgas the source. In this manner, very high purity source materials can be achieved and maintained over long periods of time. We speculate that the UHV storage of the source material at elevated temperatures is a key factor in eliminating impurities and moisture which lead to film defects during growth.

Substrate temperature is also an important variable in determining film structure.[1,44−49] A typical range of growth temperatures is from 80 to 400 K. Note that at lower temperatures, impurities tend to quickly adsorb onto the substrate. This is particularly important when growth occurs at only modest background pressures. Under almost all substrate temperatures employed for organic film growth, we assume that the molecules have a sticking coefficient equal to unity—that is, all molecules striking the substrate surface adhere to that surface. This situation results since the molecules are large and the substrate temperature is maintained well below the desorption temperature. However, some researchers have used substrate temperature control to tune the desorption rate, thereby enabling controlled growth of monolayers of some organic molecular materials.[50]

One significant advantage of using UHV is that numerous in situ film diagnostics can be employed both during and immediately after growth.[6,51] Many growth chambers are equipped with reflection high energy electron diffraction (RHEED) to allow for in situ determination of the thin-film crystalline structure.[52,53] In addition, residual gas analysis (RGA) can be employed to determine the molecular species within the chamber during growth, as well as to determine the energy of film−substrate adhesion using thermal desorption spectroscopy (TDS).[54] Other diagnostics include low-energy electron diffraction[55,56] (LEED), which typically is done in a chamber attached to the growth system due to the incompatible geometries of the growth and LEED equipment. Finally, many other vacuum analysis techniques such as UHV scanning tunneling microscopy[57,58] (STM), Auger electron spectroscopy, in situ ellipsometry, etc. have all been employed in conjunction with OMBD simply by installing the appropriate equipment in a chamber which is connected via a vacuum feedthrough to the growth chamber.

Hence, OMBD growth of thin organic films has lead to significant advances in our understanding of growth dynamics as well as fundamental optoelectronic properties of ultrathin organic molecular crystals (OMCs) due to the high control afforded over the grown structure, the assurance of high material purity, and the ability to incorporate many powerful, in situ diagnostics into the growth system. Many of these same advantages have been used with great effectiveness in growing extremely high quality inorganic semiconductors such as GaAs and InP using molecular beam epitaxial techniques. It is not unreasonable to assume that similar advantages can stem from the use of UHV techniques applied to the

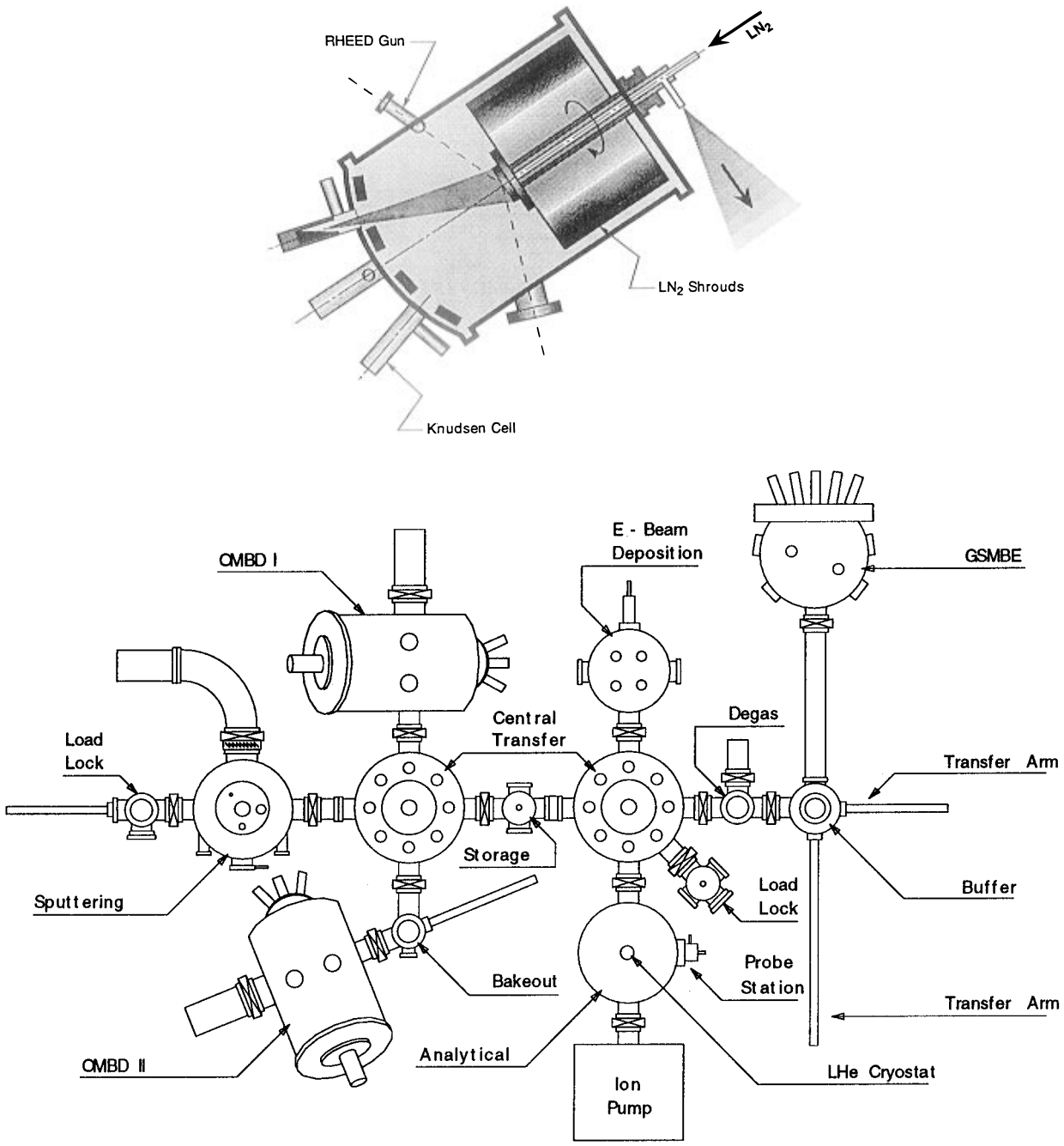

Figure 2-1. (a) Cross-sectional view of the organic molecular beam deposition chamber. The rotating substrate holder can be temperature controlled between 80 and 900 K using a combination of liquid nitrogen cooling and boron nitride heating elements. (b) Layout of the combined OMBD and gas source MBE system in the author's laboratory. There are two chambers for organic growth (OMBD-I and -II), and the MBE chamber is used for the growth of InP-based materials and organic/inorganic heterojunctions. Other chambers include sputtering and electron beam deposition for contact fabrication, and an in situ analysis chamber.

growth of OMC thin films, particularly since, as we will show, many of the constraints of lattice matching which have limited the materials combinations accessible in inorganic semiconductor systems are significantly relaxed in the case of organic thin films. Of course, the nearly infinite variety of molecular compounds available also make OMBD growth of such films a very promising area of investigation.

2.1. Purification of Source Materials

Purification of source materials is essential for assuring that the grown thin film is reasonably free of impurities.[59,60] Furthermore, purification is required to prevent contaminants from entering the high vacuum chamber which might result in a high background pressure, as well as a constant source of contamination of the subsequently grown films due to outgassing from the deposits in the chamber itself. There are several techniques for purification, including gradient sublimation,[59] zone refining from the melt,[61] chromatography,[59,61] etc. Although the highest purity organics have been achieved via zone refining,[61,62] gradient sublimation is the most useful means for purification of the powders employed in OMBD since most of these compounds do not have a liquid phase at atmospheric pressure or below.[1,63]

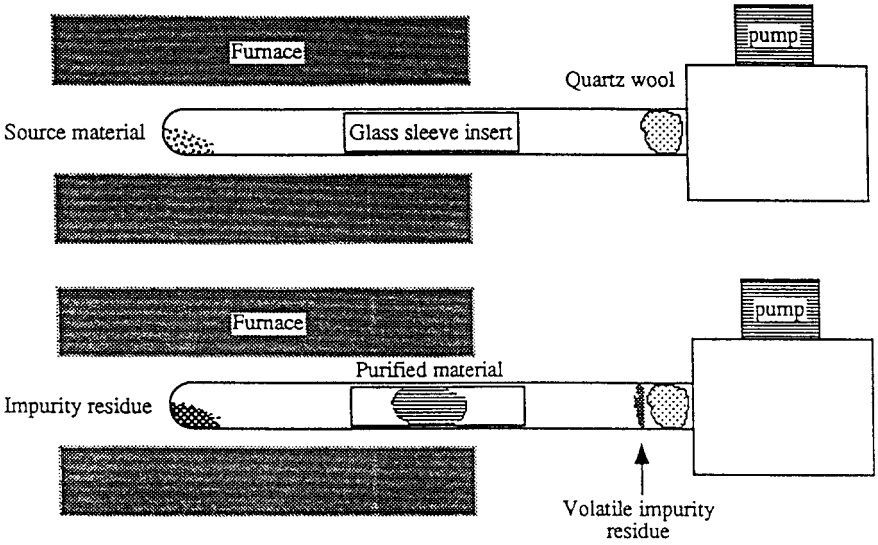

Figure 2-2. Schematic diagram of the apparatus used in thermal gradient sublimation of organic materials as a means to achieve high purity prior to OMBD growth (from ref 450).

Gradient (or train) sublimation purification proceeds as follows: The source materials (such as PTCDA or Copper phthalocyanine, CuPc) as obtained from a commercial source or from laboratory synthesis are successively purified prior to loading the source materials into the ultrahigh vacuum deposition system. Typically, several grams of powdered source material are loaded into the end of a 60 cm long glass tube. A glass sleeve is then placed inside the tube to capture the sublimed material, followed by a wad of glass wool placed at the open end of the tube to prevent the source material from contaminating the pumping chamber (see Figure 2-2). The tube is evacuated to $<1 \times 10^{-6}$ Torr using a turbomolecular or other dry pump, and the end containing the organic source material is inserted into a furnace. The temperature of the furnace is gradually increased until the sublimation point of the material is reached (approximately 400 °C for PTCDA, and 300 °C for CuPc); a process typically taking several days. Purified organic crystals grow on the inside wall of the glass sleeve in the warm zone of the furnace, while more volatile impurities are evacuated. Nonvolatile impurities are left at the hottest end of the glass tube. The glass sleeve insert is then removed, and the crystals are extracted to be used as the source material for the second purification cycle. Before loading the source materials into the OMBD system, organic compounds are often purified in multiple cycles using this method. By the end of the process, ~50% of the original source material has been removed, and the background pressure of the sublimation system is $\sim 10^{-7}$ Torr. The purified materials can then be loaded immediately into the OMBD effusion cells where they are continuously maintained in UHV at elevated temperatures awaiting growth.

2.2. Maintaining Purity during Film Growth

Growth in a UHV environment assures that a minimal density of impurities and defects will be incorporated into the film. To our knowledge, there is no other form of growth of thin films which can assure the low levels of contamination inherent in the OMBD process. However, as noted above, the degree to which impurities are adsorbed onto the substrate surface depend on the quality of the vacuum. Hence, the impurity incorporation rate should be substantially less than the film growth rate. By using simple kinetic theory to estimate the impurity adsorption rate, the time for a monolayer of background gas atoms of mass, m, to be adsorbed onto a substrate surface is[64]:

$$\tau = N_s \zeta (2\pi m k T)^{1/2}/P \qquad (2.1)$$

where N_s is the density of surface atoms required to form a complete monolayer, ζ is the atomic sticking coefficient, P is the background pressure, k is Boltzmann's constant, and T is the temperature. Assuming that the principal residual gas in a vacuum system is nitrogen $\zeta = 1$, and for $N_s = 10^{14}$ molecules/cm^2, then the time required to adsorb a monolayer is $\tau \sim 3$ min at a background pressure of 5×10^{-9} Torr, and 30 min at 5×10^{-10} Torr. Hence, to minimize the incorporation of impurities even at very high vacuums, it is important to employ the fastest growth rate possible which is compatible with achieving the desired film structure and thickness control. Practical growth rates thus lie in the range of 0.1 to 5 ML/s, which is similar to that used in the MBE growth of inorganic semiconductors .

We note that the effects of impurities in organic thin films are not equivalent to their effects in conventional semiconductors such as Si or GaAs. In these latter materials, impurities often take the form of interstitial or substitutional lattice defects which provide excess carriers via the formation of energy levels lying near to either the valence or conduction band edges. Carriers trapped in these "midgap" states are easily thermalized and hence strongly affect the conductivity of the host semiconductor. Most OMCs grown by OMBD, however, are bonded by van der Waals (vdW) forces, and hence impurities do not typically share valences with crystalline energy bands. The defects, therefore, are generally interstitial, with very tight binding of the excess carriers at these localized sites. However, we point

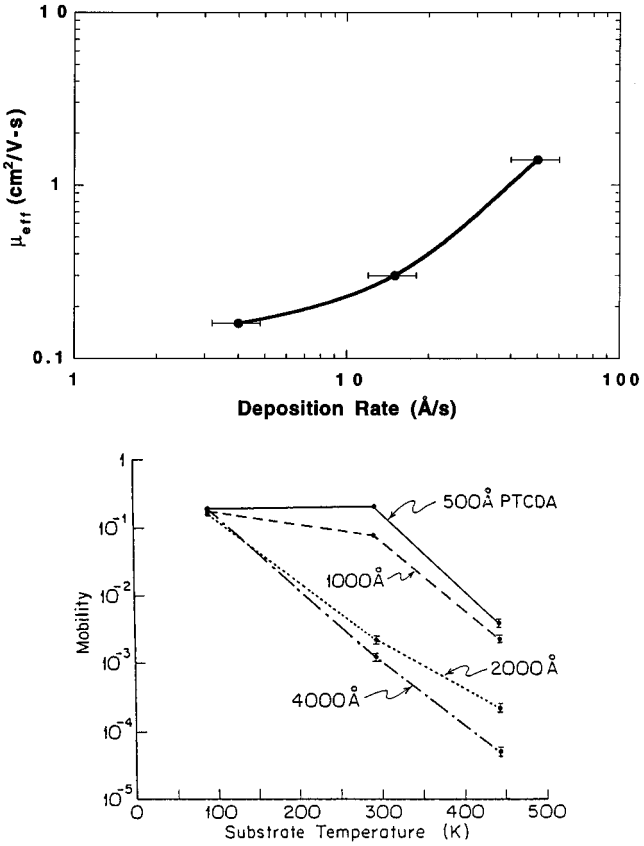

Figure 2-3. (a) Steady-state mobility vs deposition rate of a 1000 Å thick film of PTCDA grown on a 0.5 W cm p-Si substrate at a substrate temperature of 295 K (from ref 65). (b) Hole mobility in the PTCDA layer as a function of PTCDA film deposition temperature. The mobilities are obtained from fits to current−voltage data for films of different thicknesses grown on p-Si substrates (from ref 1).

out that some interstitial defects can be electrically active. A well-known example is O_2^- in CuPc, where the O_2 forms a complex with the Cu thereby providing a high density of holes to the crystal.[19]

More typically, impurities in organic thin films disrupt the regular stacking habits of the molecules. These point defects can thus significantly reduce the charge carrier mobility, as has been observed in vacuum deposited films of PTCDA. This is apparent in Figure 2-3, where charge mobility is plotted as a function of deposition rate[65] (Figure 2-3a) and substrate temperature (Figure 2-3b).[1] It has previously been found that at room temperature, high deposition rates of this particular material can lead to a higher degree of stacking order, as does a lower substrate temperature (see section 3.3.2). Hence, we can infer from these data that stacking faults in closely spaced planar molecular systems such as PTCDA can lead to a reduction in carrier mobility. Impurity incorporation leading to film disorder can also have similar effects on the resulting materials properties.

In contrast, individual atomic impurities may not be sufficiently large to induce stacking faults. Potentially more deleterious crystal defects can result from large molecular impurities present in improperly purified source material, or even from large molecular fractions which result from source molecule decomposition on heating during the sublimation process. The presence of such fractions does not

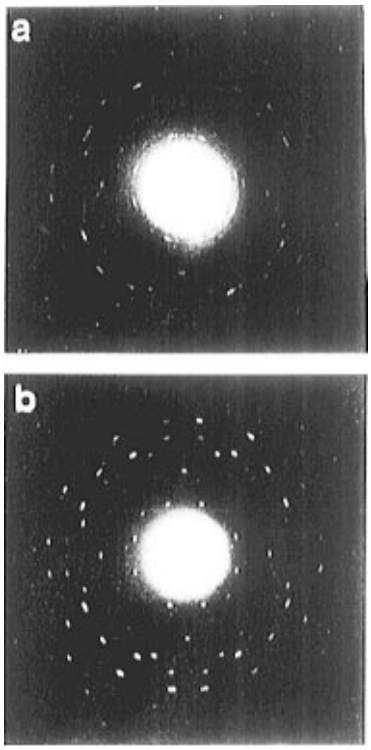

Figure 2-4. Electron diffraction patterns of GaPcCl films grown under (a) 5×10^{-6} Torr and (b) 3×10^{-9} Torr (from ref 66). Note the streaks which are evident in the low vacuum sample a as opposed to the spots indicating a higher degree of orientation in the high vacuum sample b.

depend on the quality of vacuum during deposition, but rather are a function of conditions used during purification and evaporation. Nevertheless, it has been shown that the crystalline quality of the deposited film is directly dependent on the base vacuum of the system. Tanigaki et al.[66] have compared the crystalline structure of films of GaPcCl grown at a rate of 0.5 Å/min on (001)KBr under base vacuums of 5×10^{-6} and 3×10^{-9} Torr. In Figure 2-4 we show the electron diffraction patterns of thin films grown under these two conditions. At the lower base vacuum (Figure 2-4a), the pattern shows streaks which are characteristic of some azimuthal disorder of the film, whereas at higher vacuums (Figure 2-4b), the more sharply defined diffraction spots indicate a correspondingly higher degree of orientational order.

In a series of experiments in our own laboratory, PTCDA was deposited on highly oriented pyrolitic graphite (HOPG) in a conventional, bell jar metal deposition system.[1] This turbo-pumped system had a base pressure of 10^{-7} Torr, and the crystalline powder source materials were loaded into baffled, Mo boats prior to deposition. While it was found that high-resolution STM images of monolayer films could always be obtained from films deposited using the UHV-OMBD system, no clear images could be obtained for similar films deposited in the bell jar system. Instead, thin films deposited in the lower vacuum bell jar system appeared to clump into islands several monolayers in thickness. While we are not certain why this difference in film order is observed, we speculate that it is due to impurities incorporated during growth from the lower vacuum apparatus, along with the presence of moisture in the source material. Given that some of the materials

used are hygroscopic, water molecules may serve as crystal nucleation sites, leading to island growth. Maintaining the source material at elevated temperatures in UHV for long periods, as is done in the OMBD chamber, tends to eliminate moisture, resulting in higher purity source material and hence higher quality monolayer films. This vacuum storage leads to thorough drying and outgassing of the source, possibly achieving material purity over the long term far exceeding that which is at first obtained in the thermal gradient purification process. This purification and maintenance of high material cleanliness cannot be achieved in conventional high-vacuum systems, where a bell jar must be opened between runs, thereby repeatedly exposing the source material to atmosphere.

Finally, we note that there is considerable variation as to the type of pumping used to achieve the UHV environment common to OMBD systems. Due to the volatility of some organic materials, high throughput pumps are generally employed. These include diffusion pumps, turbomolecular pumps, and cryopumps. In our own work, we use a high capacity cryopump during growth, with vacuum between growths maintained with an ion pump. The chamber itself is lined with shrouds which are filled with liquid nitrogen to extract more impurities during growth. This combination leads to a base pressure of 5×10^{-11} Torr, even after numerous depositions have resulted in a heavy accumulation of organic materials on the chamber walls. In our less demanding work in organic thin-film devices, we employ a single turbomolecular pump. In general, oil-containing pumps such as diffusion pumps can backstream (particularly if the liquid nitrogen trap is not kept cold at all times), slowly contaminating the UHV environment. Furthermore, many organic materials (e.g., tris(8-hydroxyquinoline)aluminum, or Alq_3) commonly used in organic electroluminescent devices) can react with diffusion pump oil, drastically reducing the pumping speed after several depositions. Nevertheless, many laboratories worldwide employ diffusion pumps as their primary means for achieving UHV environments due to their low cost and relative ease of maintenance.

3.0. Structure of Organic Thin Films Grown by OMBD

3.1. Definition of Growth Modes

The key difference between the growth of conventional semiconductors and organic thin films is the relaxation of the requirement for lattice matching which, in the former materials systems, significantly limits the combination of materials which can be grown without inducing a high density of lattice defects. For example, due to the strong interatomic bonding characteristic of most semiconductor materials, a close lattice match (typically with strains of $\Delta a/a_S < 10^{-3}$, where a_S is the substrate lattice constant, $\Delta a = |a_F - a_S|$, and a_F is the lattice constant of the thin film) is required when growing films thicker than some critical value (d_c) to avoid the creation of a very high density of misfit dislocations.[67] While such mismatched epitaxy can occasionally be useful for device applications,[68] typically the carrier lifetimes and leakage currents which result from the high defect densities are unacceptable, thereby severely restricting the range of materials accessible to the device engineer. On the other hand, by reducing the cohesive force of the adlayer to the substrate, it has been found that crystalline order can be achieved even though the two contacting materials are highly strained, with $\Delta a/a$ exceeding several percent in some cases. The materials which fall into this class are typically bonded by van der Waals (vdW) forces, and are known as "layered" or vdW solids.[69] Perhaps the largest single class of vdW solids are OMCs such as anthracene, perylene, the phthalocyanines and their derivatives.

While the properties of OMCs have been studied for over 50 years, it has only recently been observed that excellent structural ordering can be achieved by deposition on a wide range of substrates, sometimes without regard for the degree of strain between the film and the substrate.[2,23,37] There has been considerable experimental and theoretical investigation of OMBD growth resulting in ordered thin films, although currently there is no detailed understanding of the range of materials (both film and substrate), and conditions under which long-range structural ordering can be achieved. Indeed, only a loose understanding of the nature of the substrate/adsorbed layer interaction in such vdW-bonded systems has led researchers to term ordered growth of OMCs variously as "epitaxy",[2] "quasiepitaxy",[24] and "van der Waals epitaxy".[69]

Epitaxy, as in the case of inorganic materials, refers to systems where there is a one-to-one commensurate relationship between the molecular positions in the deposited layer and the substrate. For OMCs, there are two types of epitaxy: conventional epitaxy where the molecules are chemisorbed onto the substrate surface[46] and van der Waals epitaxy (vdWE) where physisorption involving only vdW bonding dominates.[70] Slight mismatches between the substrate and film lattices results in "strained vdWE", although for highly strained growth, epitaxial structures tend to relax at a critical thickness (d_c), thereby generating defects. Epitaxy tends to occur as a result of equilibrium growth conditions, and depending on the relative strengths of the adsorbate−adsorbate, and adsorbate−substrate interactions, the layer grows via one of three modes[71] illustrated in Figure 3-1: layer-plus-islands (Stranski−Krastanov), layer-by-layer (Frank−van der Merwe), and island growth (Volmer−Weber). Due to the requirement for commensurability, it is difficult to find OMC/substrate combinations leading to unstrained vdWE, in which case Stranski−Krastanov growth tends to be the most frequently observed mode.

In contrast, quasiepitaxial (QE) structures are those in which the substrate and film are incommensurate over any meaningful lattice length scale. Nevertheless, there can be a well-defined orientational relationship between the film and substrate lattices resulting in azimuthal order, and in some cases residual stress develops in the film as it conforms to the substrate lattice (strained QE). The most interesting feature of strained QE films is that

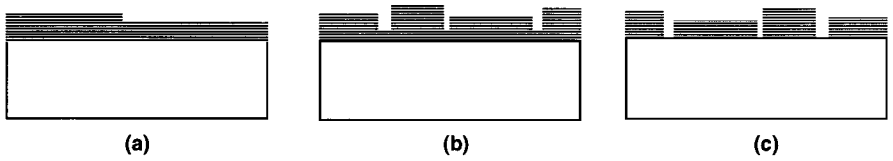

Figure 3-1. Various modes of epitaxial growth: (a) layer-by-layer (Frank−van der Merwe), (b) layer-plus-island (Stranski−Krastonov), and (c) island (Volmer−Weber). The horizontal lines on the epitaxial layers schematically represents individual atomic or molecular layers.

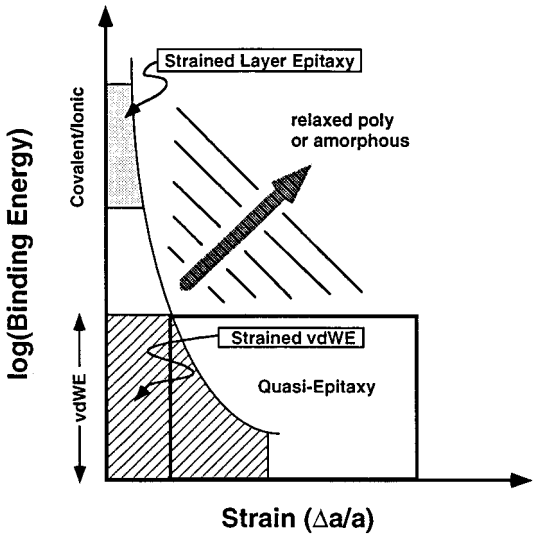

Figure 3-2. Schematic diagram of modes of epitaxy. Epitaxial growth occurs for commensurate lattices while QE growth occurs for vdW bonded incommensurate thin films. The left-hand axis corresponds to unstrained growth. The curved line represents the boundary between ordered and disordered growth assuming a particular value of critical thickness, d_c. The lower the binding energy is, the larger the strain allowed to achieve unrelaxed growth of a given thickness, $d < d_c$ (from ref 78).

they can be distorted from their bulk lattice structure, although there is no significant relaxation of this distortion with film thickness (i.e., $d_c \Rightarrow \infty$). Instead, it has been proposed that strain relaxation in QE films results from periodic variations in the degrees of freedom internal to the adsorbate molecules and their unit cells.[72] This property of vdW-bonded OMCs is a direct result of their very small elastic constants. In contrast to vdWE, QE is primarily achieved under nonequilibrium growth conditions, and since strain relief can occur without inducing disorder, Frank−van der Merwe as well as Stranski−Krastonov growth modes have been observed.[52,73,74]

We note that QE is related to two phenomena previously reported in vdW-bonded solids: "orientational epitaxy" of inert gas atoms physisorbed onto the surface of graphite[75] and the anchoring of liquid crystal molecules onto glass or other prepared substrate surfaces.[76,77] Indeed, the first report of QE ordering also involved OMCs deposited on glass substrates,[65] suggesting a clear link between these phenomena.

Figure 3-2 is a diagram placing these several growth modes in relative context.[78] The vertical axis shows the logarithm of the bond energy to the substrate, where vdW bonds are typically in the range of 1−10 meV/atom[79] (although the binding energy/molecule can exceed 1 eV), whereas for covalent or ionic bonding, the energies range from 100 meV to ~5eV/atom.[80] Unstrained, epitaxial growth corresponds to $\Delta a/a = 0$. The curved line schematically indicates the strain for a constant critical layer thickness:[67] as the bond energy increases, strain must decrease if d_c is to be maintained at a constant value. At higher strains, relaxed polycrystalline or amorphous growth occurs. While different regions of this energy/strain plot are occupied by strained vdWE and QE, there are also areas of significant overlap. That is, for a particular strain energy, strained vdWE or QE structures can be attained, depending on the growth conditions employed.

In this section, we will discuss examples of OMC thin film structures grown into both strained vdWE and QE structures. There are, to our knowledge, no unambiguous examples of completely unstrained, heteroepitaxial vdWE of OMCs, primarily due to a lack of suitable substrates whose lattice constants and space group are matched to that of the adsorbed layer. To distinguish between these growth modes, very high resolution materials characterization is needed. Unfortunately, given the inherent fragility of many of the materials used, and the unusual structural nature of the resulting films, very few high-resolution tools have been developed, and few films have been completely characterized. To date, the most thoroughly studied system is that based on the the planar organic molecule, PTCDA, which has been the focus of considerable study due to its regular, planar stacking properties on a variety of substrates.[1,37,46] This is a particularly interesting system on which to focus our attention since both epitaxial and QE films of PTCDA have been grown under a range of growth conditions. Several phthalocyanine and porphyrin-based systems have also received much attention.[33,81] These and other example materials will be used to illustrate the unprecedented range of growth modes and structures which are accessible via the combination of OMBD and organic molecular solid-state systems.

3.2. Epitaxy and van der Waals Epitaxy

The most extensive studies of epitaxial growth of OMC films have concentrated on the phthalocyanines (Pc) layered on ionic substrates such as the alkali halides,[82−89] metals,[90] and on passivated surfaces[53,81,91] of Si(111) and GaAs(111). Other systems consisting of C_{60} deposited on various substrates such as mica[92,93] and semiconductor substrates[94] have also been studied in some detail. Typical conditions leading to epitaxial growth of planar molecules include low growth rates (<0.001 to 0.01 ML/s) and high substrate temperatures (~100−200 °C, depending on the sublimation temperature of the organic molecule). These conditions result in the growth of *equilibrium*

Table 1. Surface Unit Mesh Lattice Constants for Pc's on Different Substrates[a] (From Refs 83 and 97)

molecule	bulk (nm)	KBr (nm)	KCl (nm)	KI (nm)	NaCl (nm)	MoS_2 (nm)	Se-GaAs(111)B (nm)	H-Si(111) (nm)
VOPc		1.40	1.41		1.26	1.37	1.37	1.38
AlPcCl		1.48	1.41	1.50	1.43		1.44	1.38
PbPc	1.27	1.40	1.41		1.26			

[a] All distances in nanometers.

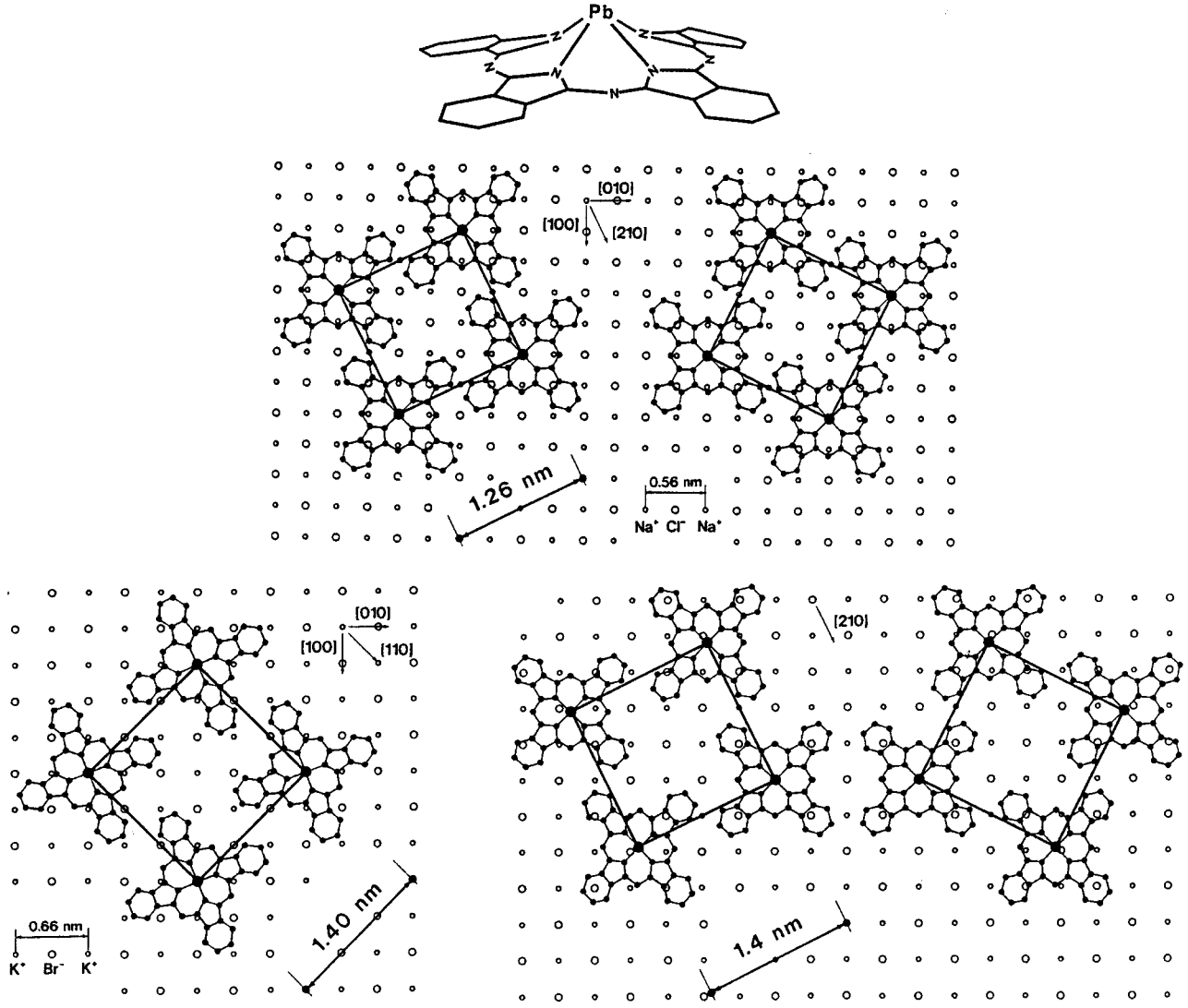

Figure 3-3. (a) Molecular structural diagram of PbPc. Proposed epitaxial orientations of PbPc on (b) NaCl and (c) KBr. For PbPc on KBr, two different arrangements are proposed: commensurate type A (left), and incommensurate type B′ (right) (from ref 83).

thin film structures, where the incident molecules have sufficient thermal energy after deposition to arrange themselves into their minimum energy configuration.

Epitaxial molecular thin films are typically grown into structures which are determined by the substrate lattice rather than by the bulk structure of the organic molecular solid itself. Since the substrates used are typically inorganic crystals whose structure is considerably different than the OMC, neither the lattice constant nor the lattice symmetry of these two contacting layers are matched. This has two consequences: due to the flexible nature of the vdW force responsible for the cohesion of the organic layers, the structure of the thin film can be substantially distorted from bulk. This severe lattice distortion, however, results in a large stress within the film, thereby creating disorder after the growth of only a few monolayers.[46,83] In effect, the mismatched film relaxes to its bulk structure within 1−5 ML, resulting in a rough columnar surface morphology (corresponding to Stranski−Krastanov growth[71]). The film relaxation prevents the growth of molecularly flat films with thicknesses beyond only a few monolayers.

An example of organic thin-film epitaxy is the OMBD growth of PbPc on KBr(001) and NaCl(001) as studied using in situ reflection high-energy electron diffraction[83] (RHEED). For these experiments (summarized in Table 1), the growth rate was from 0.003 to 0.008 ML/s with the substrate maintained at room temperature. Figure 3-3a shows the molecular structure of PbPc, where the Pb atom forms an out-of-plane pyramid with the surrounding ligands.

The PbPc bulk monoclinic lattice forms a commensurate square lattice when deposited onto several alkali halide crystal surfaces. For example, Figure 3-3, parts b and c, shows the first ML structure of PbPc on NaCl and KBr, respectively, as inferred from the RHEED patterns obtained immediately after growth. To the accuracy achieved using RHEED (±5%), the lattice constants are considerably different in these two cases. For example, for PbPc on NaCl, the lattice constant is $a_F = 1.26$ nm (comparable to the bulk lattice parameter of 1.27 nm), whereas for KBr, this distance is $a_F = 1.40$ nm, or a difference of 11%. In the case of growth on KCl(001), commensurability is achieved by the PbPc forming two equivalent $\sqrt{10}\times\sqrt{10}$-R±18.4° (type B) surface meshes with a considerably expanded unit cell of $a_F = 1.41$ nm. Here, we use the conventional notation to define molecular surface reconstructions. Thus, $(m\times n)$ denotes a surface unit mesh which is $m\times n$ times larger than the underlying lattice. If rotated from the underlying lattice by θ°, then the notation is $(m\times n)$Rθ°. If the surface mesh is centered on (rather than commensurate with) the bulk lattice, the notation is c$(m\times n)$.

On KBr, two different lattices are observed: the 3×3 (type A) commensurate lattice mesh with $a_F = 1.40$ nm coexists with a much smaller proportion of an *incommensurate* (i.e., quasi-epitaxial) type B′ lattice where the PbPc unit cell is parallel to the [210] substrate axis. Many organic materials, such as the Pc's, have more than a single structure. Hence, while investigations of PbPc do not identify more than a single commensurate, but highly strained isomorph, we cannot entirely rule out the possibility that a less strained (i.e., more commensurate) form of PbPc has actually been achieved. Nevertheless, lacking the ability for growth of smooth films more than a few monolayers thick provides evidence for highly strained structures. To accommodate the significantly expanded PbPc structure when deposited onto KBr, it was suggested[83] that the molecules rotate such that the phenyl group of one molecule fits into the "hollow" of an adjacent molecule to minimize the intralayer vdW potential. In all cases discussed, steric congestion between neighboring molecules causes them to minimize their vdW binding energy by rotating about an axis normal to the molecular plane, with the degree of rotation determined by the size of the surface mesh required to achieve commensurability. Utilizing the additional degrees of freedom within the unit cell, the molecules remain parallel to the substrate.

The molecule−substrate bonding is primarily due to electrostatic interactions between the metal atom with the anion in the substrate lattice. The importance of electrostatic interactions in determining structure is inferred from extended Huckel model calculations, which suggest that a charge of from 0.4 to 0.6 e is localized on the Pb atom. Hence, the resulting epitaxial structure of Pc thin films is determined by two factors: strong electrostatic attraction between the adlayer and the substrate, and vdW forces within the layer itself which are minimized by the molecular rotational adjustments noted above. The importance of electrostatic attraction to the ionic substrate is apparent when we observe that the lattice constants of the surface unit mesh of different organics on the same substrate (e.g., KCl) are the same (Table 1), independent of the equilibrium (bulk) constant of the thin film. The total strain energy increases with film thickness until the epitaxial layer relaxes, resulting in a highly disordered structure after only a few monolayers (typically < 5 ML, depending on the degree of strain).

Note that the electrostatically bonded thin films are not consistent with the definition of vdWE. In some cases, it might be possible to grow one or two strained "wetting" layers which are bonded electrostatically, followed by the vdWE or QE growth of subsequent layers to form an ordered thin film, resulting in Stranski−Krastonov layer-plus-island morphology. In one approach to reducing substrate−thin film interactions, several Pc molecular systems have also been grown on H-terminated Si(111) and Se-terminated GaAs(111) surfaces using conditions similar to those employed for the growth of Pc's on the alkali halides.[53,91] Atomically flat, regularly terminated monohydride (−SiH) Si(111) surfaces can be prepared by immersing the clean Si substrate in HF solution immediately prior to growth. Growth of VOPc on such a surface resulted in a nearly equilibrium (unstrained) square lattice with $a_F = 1.38$ nm. Long range structural order could then be maintained for thicknesses as large as 20 ML, indicating low stress in the first few anchoring layers. In contrast, a lattice constant of $a_F = 1.38$ nm is too small to easily fit the larger AlPcCl molecule. The resulting stress in these latter films generates poorly ordered layers of even a few ML thickness.

The perylene-based molecule, PTCDA, has also been found to grow epitaxially on alkali halides, with growth extending to very thick films.[46] To accommodate the strain, however, highly textured columnar structures result. This Stranski−Krastanov growth is stable even for thick films since the domain size is small. Once the growth is nucleated at the substrate−film interface, the lattice structure almost immediately relaxes into its bulk crystal habit, resulting in numerous small domains which grow without significant strain since the contact surface area of the domain with the substrate is also small.

Epitaxy of PTCDA on NaCl(001) and KCl(001) substrates has been studied extensively by Mobus et al.[46] where equilibrium growth was achieved by maintaining the substrate at 200 °C at a growth rate of 0.08 Å/s (corresponding to ~1.5 ML/min). Under these conditions, the slowly arriving molecules have sufficient thermal energy to diffuse along the substrate surface until they find a minimum (equilibrium) energy site. This results in highly columnar growth, with voids arising between neighboring islands. Within the islands, the molecules form regular stacks, with the PTCDA (102) plane lying parallel to the substrate surface.

Using transmission electron microscope diffraction, it was found that PTCDA grows into two, coexisting α and β polymorphs. The appearance of these two modifications of the PTCDA unit cell (whose lattice constants are provided in Table 2), shown in Figure 3-4, suggest that the strong substrate−organic film

Table 2. Unit Cell Parameters of PTCDA and NTCDA

parameter	α-PTCDA[a]	β-PTCDA[b]	NTCDA[a]
space group	$P2_1/c(C_{2h}^5)$	$P2_1/c(C_{2h}^5)$	$P2_1/c(C_{2h}^5)$
a (Å)	3.72	3.78	7.89
b (Å)	11.96	19.30	5.33
c (Å)	17.34	10.77	12.74
β	98.8°	83.6°	109.04°
Z	2	2	2

[a] From ref 99. [b] From ref 46.

interaction (when compared to the intralayer interaction within the OMC itself) in epitaxially grown organic films plays a determining role in the resulting PTCDA structure, similar to that observed for the Pc's. This interaction also determines the azimuthal orientation of the crystalline domains, as the adlayer minimizes energy by finding a commensurate orientation with the substrate. Several orientations of the molecules within the islands relative to the substrate lattice have been observed, and these are shown in Figure 3-4 for α- and β-PTCDA on NaCl and KCl. For example, on NaCl, the [0,1] unit mesh axis of α-PTCDA is rotated by $\theta = 4°$ with respect to the [110] NaCl axis, whereas for β-PTCDA, $\theta = 7°$ or 31°. For all of these arrangements, the four carbonyl oxygen atoms align to a Na^+ ion in a commensurate superstructure which can repeat over distances of several PTCDA unit cells. Due to the high lattice symmetry, there are eight symmetry-equivalent orientations for each of the two forms of PTCDA on NaCl, and all eight are observed after a single growth run. The situation for PTCDA on KCl is similar to NaCl, except that the preferred orientations for both α and β forms is $\theta = 24°$, which provides a nearly perfect epitaxial alignment of two opposite O atoms with the K^+ ions on the substrate. This preferred alignment to the substrate cations suggests that electrostatic interactions play a role for PTCDA growth on alkali halides similar to that found for the Pc's.

Epitaxy of PTCDA on metals has also been investigated by Seidel and co-workers.[95] In that work, monolayers of PTCDA were deposited onto precleaned (by sputtering with 500eV Ar^+ ions and

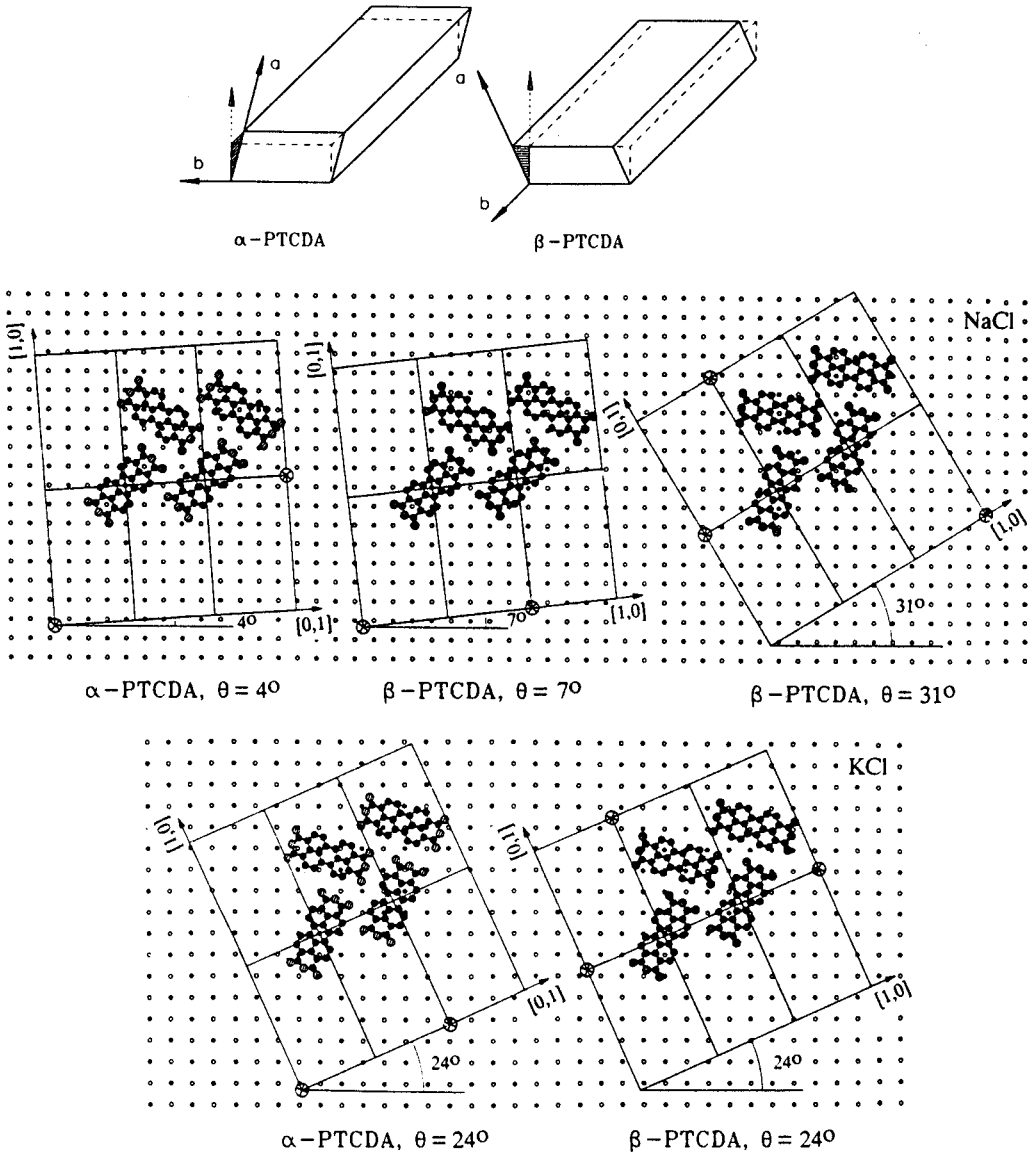

Figure 3-4. α and β isomorphs of PTCDA and their proposed orientations when grown on NaCl and KCl. In all cases, the PTCDA (102) lies parallel to the substrate surface. These orientations are regarded as tentative, since no precise microscopic registry has been determined in all cases (from ref 46).

heating to 1000 K) Ag(110) surfaces. Under the conditions used, epitaxy (rather than coincident or quasi-epitaxial growth) was inferred, although as will be shown in section 3.3.2.3, the growth mode of PTCDA achieved on metal substrates depends sensitively on the conditions used in the process.

For the case of PTCDA/Ag(110), growth occurred at a background pressure of $<4 \times 10^{-10}$ Torr and at a growth rate of $\sim 7 \times 10^{-3}$ ML/s. The same structure was obtained for substrate temperatures ranging between 200 and 380 K during growth. The resulting ML films were examined by both LEED and STM to determine the unit cell structure and size. LEED data were taken at near normal incidence using a beam energy of 16 eV assuring no damage was incurred by the film during measurement. To within the accuracies of the measurement techniques used (which typically are ~5−10%), it was found that a commensurate superstructure was aligned along the Ag (100) lattice direction, with the following relationships between the PTCDA unit vectors (**a***, **b***) and those of Ag ($\mathbf{g_1}$, $\mathbf{g_2}$):

$$\mathbf{a}^* = 3\mathbf{g_1} + 2\mathbf{g_2}$$

$$\mathbf{b}^* = 3\mathbf{g_1} - 2\mathbf{g_2}$$

Lack of Moiré patterns in the STM images provides additional confirmation that the PTCDA lattice is commensurate with the underlying Ag(110) lattice.[96]

Interestingly, the structure of the first ML of PTCDA is strongly distorted from its bulk structure, similar to the case observed for several Pc's grown epitaxially on alkali halide substrates discussed above. This is apparent in the STM images[95] of PTCDA ML's grown on Ag(110) terraces shown in Figure 3-5a. For example, as opposed to the normal herringbone structure of bulk PTCDA with two molecules per surface cell (with dimensions **a** = 11.96 Å and **b** = 17.34 Å and $\beta = 98.8°$, given by the α form in Table 2), epitaxy on Ag(110) results in a surface unit cell where the molecules are in a nearly square lattice with $Z = 1$, **a*** = 11.8 ± 0.5 Å, **b*** = 12.5 ± 0.5 Å and $\beta = 83.2°$. These results were consistent whether obtained via LEED or STM. Occasionally a defect in the lattice was observed, as indicated by the arrow in Figure 3-5a, where one monolayer appears to have "reverted" into its bulk, herringbone structure. This is indicative of a competition between minimizing energy within a layer as opposed to minimizing energy between the layer and the substrate. The critical balance between these factors governs the ultimate growth mode of organic thin films as it does in the case of inorganic materials, and will be discussed in greater detail in the following sections.

This extreme distortion of the unit cell, which was also observed in β-PTCDA discussed previously, is due to the strong covalent interactions between the carbon and silver atoms in the monolayer and substrate, respectively. The strength of this interaction was confirmed by thermal desorption of multiple PTCDA layers previously deposited on Ag. It was found that while the upper layers could be desorbed without decomposition, desorption of the final layer resulted in molecular fragmentation due to strong substrate−molecule adhesion.

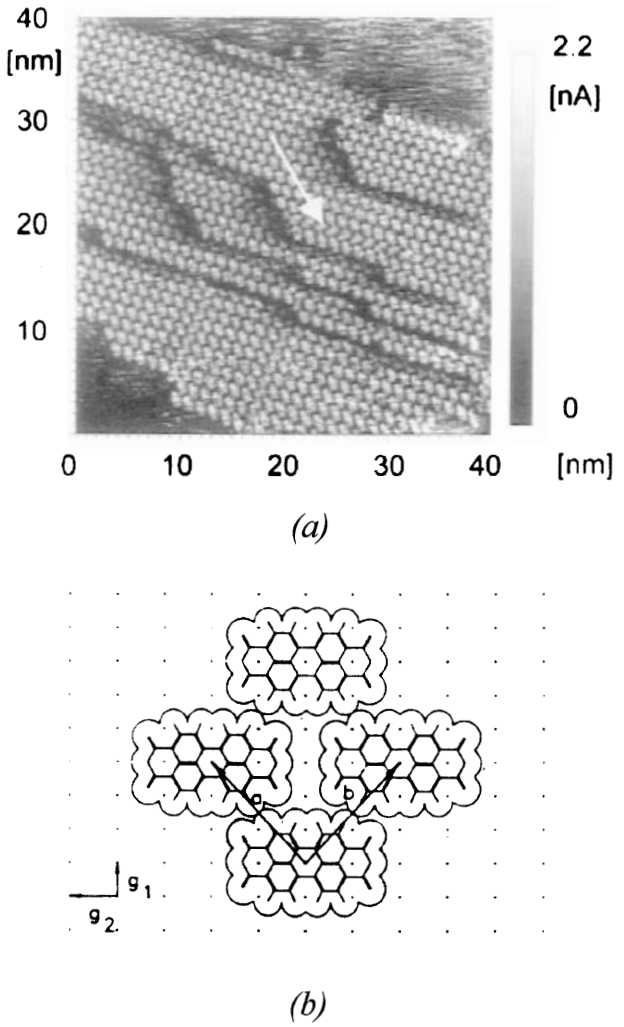

Figure 3-5. (a) Scanning tunneling microscope image of several terraces of PTCDA on a Ag(110) surface. Arrow indicates row where the molecular orientation is reversed from other rows on that same substrate terrace. (b) Proposed comensurate superstructure of a ML of PTCDA on Ag(110), where the Ag(110) surface mesh is indicated by the dots, with lattice paramters $g_1 = 2.089$ Å and $g_2 = 4.08$ Å (from ref 95).

Minimum energy calculations were also used to provide a quantitative understanding of the observed structures.[95] For these calculations, the vdW energy, nonbinding electrostatic energy between atoms in the molecule and substrate, bond stretch and angular distortion energies, and dihedral angular torsion were summed to obtain the total adlayer energy and then minimized using standard methods. These calculations confirmed the distorted structure shown in Figure 3-5b, with a lattice of **a*** = **b*** = 11.92 Å and $\beta = 86.67°$, which is reasonably close to the measured values.

To summarize the results given in the examples of the Pc's and PTCDA, epitaxy is achieved under growth conditions which allow for an equilibrium, lowest energy structure to nucleate. Typically, this occurs for elevated substrate temperatures, low growth rates, and strong substrate−adlayer interactions (e.g., ionic bonding for PTCDA on alkali halide substrates). In the case of Pc or PTCDA growth on alkali halides, or of PTCDA on Ag(110), it can be shown that the unit cell of the adlayer can be significantly distorted from its bulk dimensions in

order to achieve a commensurate epitaxial structure. While this allows for the growth of a highly strained initial ML, thicker films tend to relax, thereby inducing a high density of defects along with a rough surface. In the case of PTCDA with its very strong intramolecular binding, the molecules azimuthally orient with respect to the substrate to achieve a commensurate, or nearly commensurate structure. The experimental resolution of these experiments[46,66,82,83,95,97] is not sufficient, however, to determine the degree of strain resulting from this overgrowth. Nevertheless, the epitaxial PTCDA layers exhibit highly textured, island growth resulting from different domains of different polymorphs of the PTCDA structure nucleating in spatially distributed regions of the substrate. This mode of strain relaxation appears to be a universally observed characteristic of strained-vdWE organic thin film growth.

Finally, some recent attempts have also been made to find substrates whose lattice parameters closely match those of the overlayer in order to achieve nearly unstrained vdWE. To our knowledge, the best example of such growth[98] is that of the nonlinear chromophore, 4′-nitrobenzylidene-3-acetamino-4-methoxyanaline (MNBA) on the (010) plane of nearly lattice-matched single crystals of the organic salt: ethylenediammonium terephthalate (EDT). The lattice constants of the two bulk crystals in the (010) plane are **a** = 8.3814(9) Å and **c** = 7.4871(5) Å with β = 115.336(5)° for MNBA, compared with **a** = 8.381(8) Å and **c** = 7.471(4) Å with β = 115.32(5)° for EDT. Thus, at room temperature, the maximum strain is $\Delta a/a < 0.3\%$.

Single crystals of EDT were prepared by slow evaporation or by controlled supercooling out of solution. This yields (010) surfaces (determined by X-ray diffraction) in the millimeter range. Prior to growth, the surfaces were cleaned using thermal desorption in vacuum by ramping the temperature up to 120 °C with a dwell time of 30 min, at which time the heteroepitaxial layer of MNBA was grown. Optimum growth of MNBA was obtained at a background pressure of 10^{-9} Torr, a substrate temperature of T_{sub} = 80 °C, and a rate of 0.1−0.2 Å/s. These conditions resulted in island growth morphology, with asymmetric islands typically 1×10 μm^2 oriented normal to the [001] direction of the EDT substrate. The islands appear to fill less than 50% of the substrate surface area. It was also noted[98] that the range of temperatures over which this degree of order could be obtained was quite narrow: below T_{sub} = 75°, the island orientation became random, whereas at T_{sub} > 85 °C, the desorption rate became so high such that MNBA no longer was deposited.

The island orientation is clearly apparent in optical micrographs, and was confirmed by the strong dependence of the second harmonic intensity generated by MNBA on the fundamental optical pump beam (at a wavelength of λ = 1.064 μm) polarization angle. It was found that the maximum second harmonic signal was obtained for polarizations parallel to the substrate [100] direction, while the signal was reduced by a factor of 90 for perpendicular polarizations. From this result, it was concluded that the [100] directions of EDT and MNBA were coincident.

3.3. Quasi-Epitaxy

The most thoroughly studied quasi-epitaxial system is PTCDA grown on a variety of substrates,[1,37,99] including highly oriented pyrolytic graphite (HOPG),[43,58,70,100] Au(111),[73] Se-terminated GaAs (100),[55,101] glass,[37] and polymers.[102] Additional examples of this growth mode include several additional examples of neutral organic molecules on amorphous quartz,[103] and HOPG,[96,104] C_{60} and C_{70} on GaSe and MoS_2,[105] and possibly C_{60} on Au(111).[106] In contrast to epitaxy, QE growth is a *kinetically* controlled, nonequilibrium process, resulting in structures which can be significantly distorted from the bulk. The conditions leading to kinetically controlled growth are high deposition rates and low substrate temperatures. An ordered film structure is obtained due to dominant intralayer molecule-molecule interactions (as compared to epitaxy, where interlayer forces dominate).

3.3.1. Theory of QE

In this section, a theoretical framework and experimental basis for QE growth of archetype vdW-bonded molecular thin films is presented. The model which has been developed by Zhang and Forrest[72] is calculationally simple in that it replaces the large number of pairwise atom−atom potentials which must be summed between adjacent molecules by a single, approximate, ellipsoidally symmetric molecule−molecule potential. We note, however, that the approach is inherently limited since it only predicts equilibrium structural configurations without providing information as to the growth conditions required to achieve a given structure. To date, these conditions have been experimentally discovered via a process of trial and error. The model has thus far been applied to structures consisting of the planar molecules PTCDA and 3,4,7,8-naphthalenetetracarboxylic dianhydride (NTCDA), with results in good agreement with observation.

While models have also been previously developed to understand epitaxial growth using approximations similar to those employed here (e.g., using the rigid lattice approximation[107,108]), epitaxial systems are *inherently* different from QE systems. The primary difference lies in the incommensurability of QE layers with the substrate. Whereas one can model epitaxial growth by a harmonic potential with a period equal to the atomic spacing of the substrate,[107] incommensurate lattices cannot be treated as such since the potential between overlayer and substrate is anharmonic. Hence, the analytical solutions which are attained for epitaxial systems must be replaced by computationally intensive methods.

Extending models of purely van der Waals-bonded molecules to systems where long-range (but weak) intra- and interlayer Coulomb binding plays a role can significantly complicate the problem, and has not been treated in detail. However, the calculational methods employed for vdW systems can, in principle, be extended to include these and other bonding forces (e.g., hydrogen bonding, high order multipoles, ionic and covalent bonds, etc.).

Interestingly, inclusion of Coulomb forces between the molecule and the substrate only complicates the

calculation when these forces do not dominate. When such interactions are strongly dominant, as in the case of VOPc on alkali halide (and hence ionic) substrates, conventional epitaxy results (section 3.2). In this case, *intralayer* interactions between molecules, which are largely responsible for determining the bulk structure of OMCs, are not significant, and the equilibrium configuration of the first monolayer is accurately determined by the single molecule/substrate binding energy.[109] In effect, this is the defining difference between epitaxy and QE. As noted above, this strong substrate−molecule binding characteristic of epitaxial growth results in the generation of a high density of defects, leading to amorphous or highly polycrystalline films thicker than few monolayers.

The primary requirement for QE is that there exists a range over which a surface molecule can be translated relative to the substrate without a significant change in energy. If the potential between molecules within a layer is ϕ_{intra}, and between molecules in different layers is ϕ_{inter}, then this condition is related to the relative magnitudes of the inter- and intralayer compressibilities (or elasticities) via

$$\phi_{intra}'' \gg \phi_{inter}'' \tag{3.1}$$

where ϕ'' is the second derivative of ϕ relative to the several thin-film spatial degrees of freedom. In this "static" approximation, the condition for QE is relatively independent of the absolute magnitudes of the crystal binding energies, ϕ_{intra} or ϕ_{inter}. As in many cases involving large planar molecules, $\phi_{inter} > \phi_{intra}$ while $\phi_{inter}'' << \phi_{intra}''$. This differs from atomic vdW systems where there is no strict adherence to these conditions.[110] This point is noteworthy since it illustrates an inherent difference between the previously studied "orientational epitaxy" of inert gas atoms vdW-bonded to metal and graphite surfaces,[75] and QE of spatially extended molecules bound by similar forces on a substrate with considerably higher spatial frequency (due to its smaller lattice constant) than the adsorbed molecular layer.

3.3.1.1. Based on Energy Minimization. The condition in eq 3.1 has been examined by calculating the vdW bond energy between 2D interfaces of PTCDA and HOPG using the atom−atom potential method.[79] Here, the total bond potential is given by $\Phi = \sum\phi_{ij}$, where ϕ_{ij} is the potential between the ith and jth *atoms* in two molecules, or in a molecule and the substrate. Now, ϕ_{ij} can be approximated for vdW solids using the Buckingham potential:

$$\phi_{ij} = -\alpha_{ij}/r_{ij}^{6} + \beta_{ij}\exp(-\gamma_{ij}r_{ij}) \tag{3.2}$$

The radial distance between atoms i and j is r_{ij}, and α, β, and γ are vdW constants for each pair of atoms. The minimum energy corresponding to the equilibrium crystal configuration is obtained when $\Phi' = 0$ and $\Phi'' > 0$.

There are several assumptions made when applying the atom−atom potential procedure:[79] (i) The model is static. That is, the calculation applies to equilibrium at $T = 0$ K, and hence it cannot predict dynamic growth processes, nor does it consider vibrational contributions at $T > 0$. Typically, these latter effects are small compared with Φ. (ii) The vdW forces are isotropic, and are not significantly perturbed by the molecular structure. (iii) The molecules are rigid (i.e., there are no internal molecular degrees of freedom. (iv) There is no significant contribution to the intermolecular energy arising from Coulombic forces, higher order multipoles, etc. Previous calculations for planar, nonpolar molecules[79] such as anthracene and coronene have shown that these assumptions are generally valid.

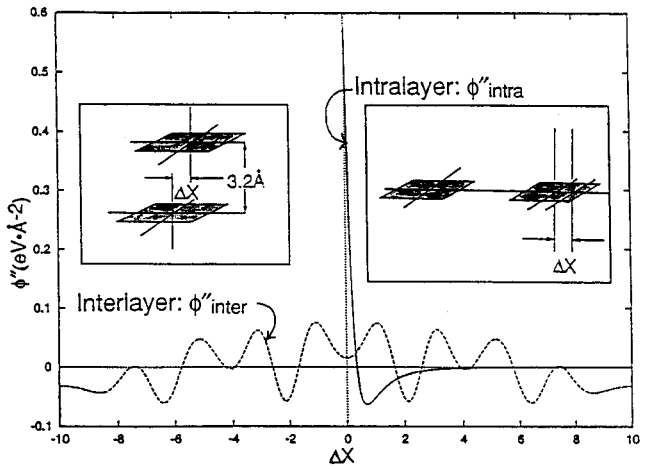

Figure 3-6. Calculated interlayer (ϕ_{inter}'') and intralayer (ϕ_{intra}'') compressibilities as a function of displacement from equilibrium (Δx) of a PTCDA crystal. The condition for QE: $\phi_{intra}'' \gg \phi_{inter}''$ at $\Delta x = 0$ is clearly achieved for this material system (from ref 78).

The condition for QE (i.e., $\phi_{intra}'' >> \phi_{inter}''$) can be understood from the plot of elastic constants between individual PTCDA molecules shown in Figure 3-6, where the compressibility within a layer (proportional to ϕ_{intra}'') is clearly larger than the elastic shear (proportional to ϕ_{inter}'') near the equilibrium molecular separation of $\Delta x = 0$. In this case, the overlayer is only slightly distorted when deposited onto a substrate, allowing for some adjustment of the position of the relative layer orientation without inducing a large strain energy. In effect, the potential surface of the molecule−substrate interaction (shown in the inset of Figure 3-6) has a relatively broad minimum (leading to a small ϕ_{inter}''), allowing for the required orientational adjustment between lattices without a large expense of strain energy. This broad energy minimum is a direct result of the short range vdW binding energy, and the spatial extent of planar molecules such as PTCDA and the Pc's. That is, the more extended molecules result in a higher interfacial compressibility (i.e., lower elasticity, ϕ_{inter}''). Such molecules have a broader range of energy-equivalent positions, and therefore can result in the growth (under appropriate conditions) of an incommensurate overlayer with only a small interfacial strain energy, as required for ordered QE growth.

These assumptions lead to a picture of a QE thin film as a rigid overlayer, *relatively* undistorted when placed in contact with the incommensurate substrate. This rigid overlayer approximation greatly simplifies calculations of the full QE structure, as will be shown below. Since the overlayer has a very low spatial periodicity as compared with the substrate, strain may be relieved through modifications of the *internal*

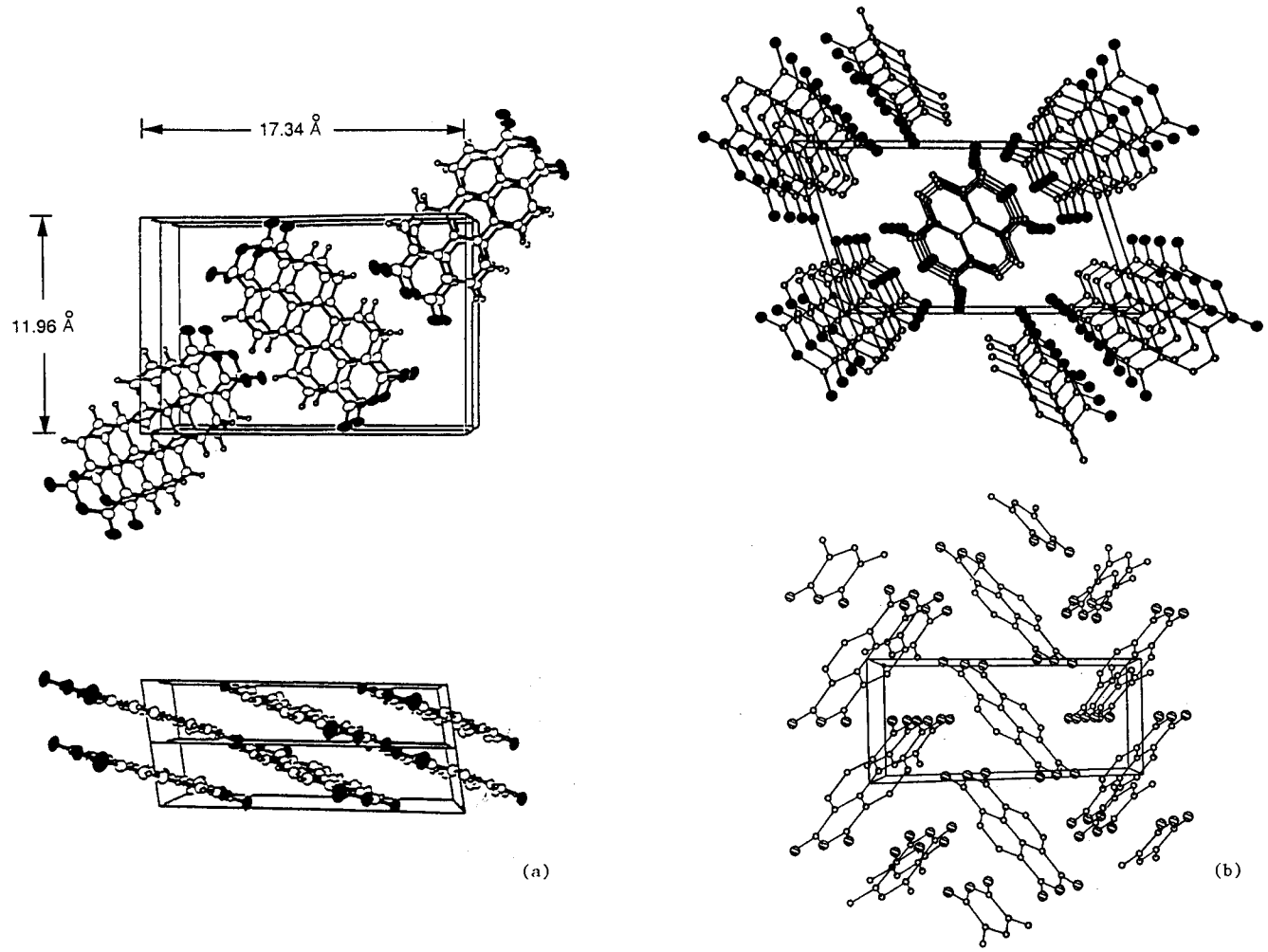

Figure 3-7. Perspective views of the unit cells of (a) PTCDA and (b) NTCDA.

degrees of freedom within the larger, adsorbed molecular lattice. However, as will also be shown in the following section, precision structural measurements suggest that QE films can have significant strain when grown on substrates where $\phi_{inter}'' \approx \phi_{intra}''$. The resulting elastic distortion of the film as compared to the bulk lattice structure does not appear to relax even in the thickest films studied.[111] This suggests that the details of QE structures are considerably more complex than predicted by the model discussed here, although the general features of QE structures are indeed predicted by the somewhat simplified assumptions used to make the calculations both intuitively useful and calculationally tractable.

The accuracy of the method has been tested by calculating the bulk crystal structure of PTCDA, and then comparing these results with existing crystallographic data. Note that calculation of the full bulk structure is a complex 3D problem involving numerous degrees of freedom between the several molecules in the cells. Hence, only limited aspects of the 3D structure are calculated to test the model. Perspective views of the bulk PTCDA and NTCDA unit cells are provided in Figure 3-7, parts a and b, respectively,[63] with details of the structures compiled in Table 2.

The energy of two organic molecules stacked one above the other was calculated as a function of intermolecular distance along the stacking axis, using

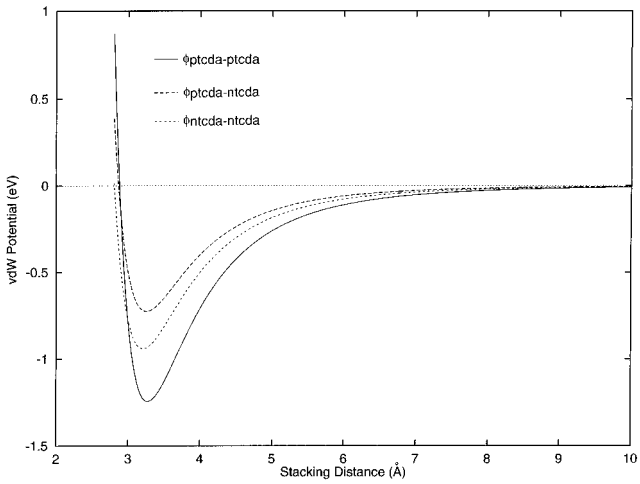

Figure 3-8. The van der Waals potential as a function of interplanar stacking distance of a PTCDA dimer, a NTCDA dimer, and a PTCDA/NTCDA stack. For each curve, the two molecules are centered with respect to each other, with their molecular planes parallel (from ref 99).

previously published values for the atomic vdW coefficients,[112,113] with the results plotted in Figure 3-8. Bonding energies for PTCDA-PTCDA, NTCDA-NTCDA, and PTCDA-NTCDA dimers are all plotted in the figure. It is apparent that the equilibrium distance (or "vdW radius") in the stacking direction (assuming that the molecular planes of adjacent

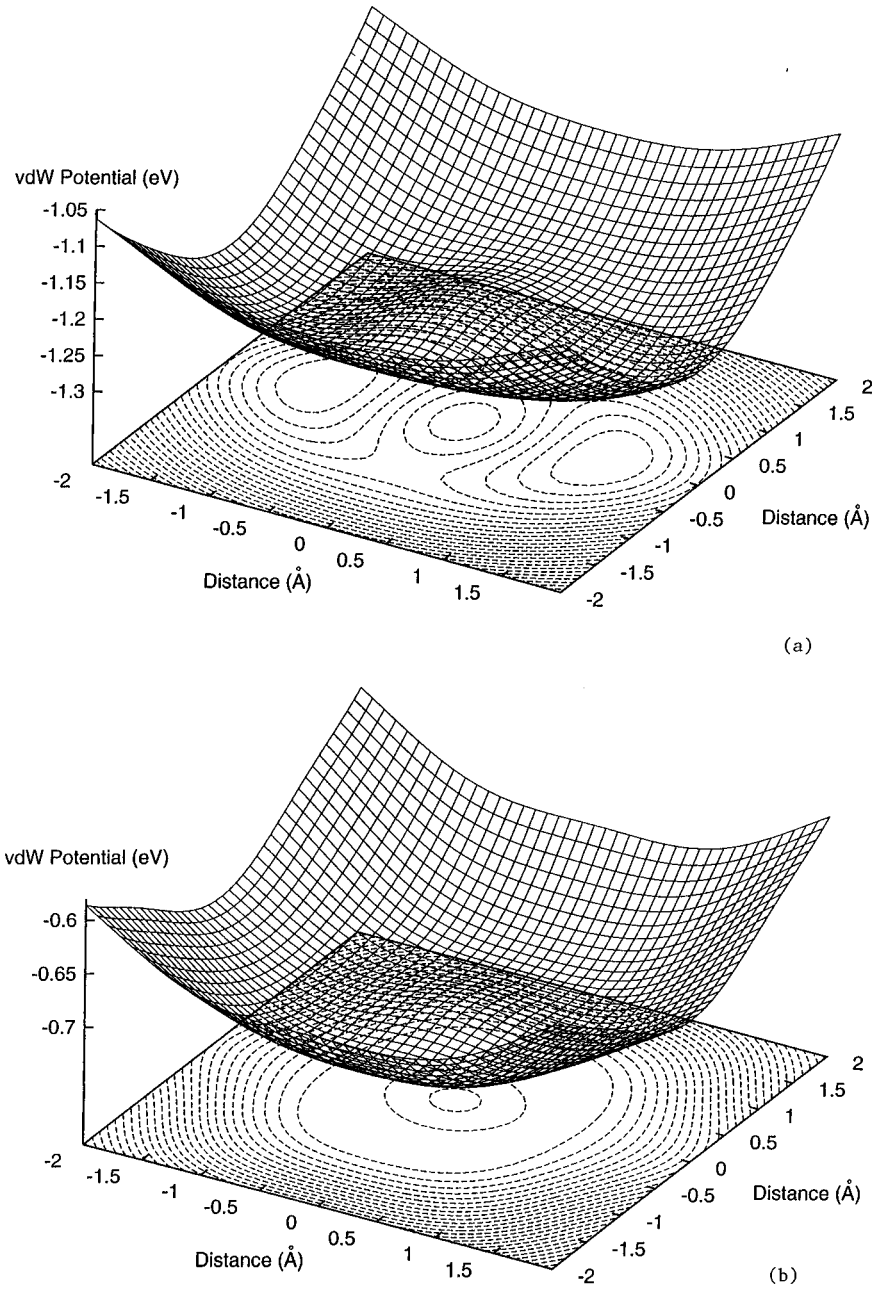

Figure 3-9. The 2D dimer energy surface for (a) PTCDA and (b) NTCDA for the molecules oriented with their planes parallel (from ref 99).

molecules are parallel, which is not the case for the NTCDA-NTCDA bulk crystal) are generally in the range from 3.20 to 3.26 Å, corresponding to the experimentally determined value of 3.21 Å for PTCDA. Furthermore, the binding energy of the PTCDA dimer is approximately −1.3 eV, corresponding to 24 kcal/mol. This value is consistent with the sublimation energies[114] of many aromatic molecules similar to PTCDA and NTCDA.

Once the stacking distance along the *c* axis is fixed, the two molecules are translated in the *xy* (base) plane with respect to each other to generate the energy surfaces for PTCDA and NTCDA dimers shown in Figure 3-9, parts a and b, respectively. There are degenerate energy minima at ±1.1 Å from the center of the PTCDA molecules, and ±1.0 Å for the NTCDA molecules. The energy minima are displaced from the molecular center of mass and are located along the long molecular axis. The equilibrium molecular offset is experimentally observed in the PTCDA bulk structure, resulting in the molecular lamella stacking along the (102) axis. That is, there is an 11° tilt of the molecular plane within the unit cell, which has been widely observed for PTCDA deposited on such insulating substrates as glass[65] and polymers.[22,115] Interestingly, this 11° tilt is not observed for PTCDA on conducting substrates such as Au or GaAs, suggesting that more complex charge exchange interactions not included in these calculations may exist for these situations.

The energy of a 2D surface mesh consisting of five PTCDA molecules placed in their characteristic base-centered rectangular structure, shown in Figure 3-10, was also calculated. For this calculation, all angles and dimensions were varied (including the relative angle of the central molecule with respect to the plane defined by the four corner molecules) to achieve the minimum energy configuration, with the result

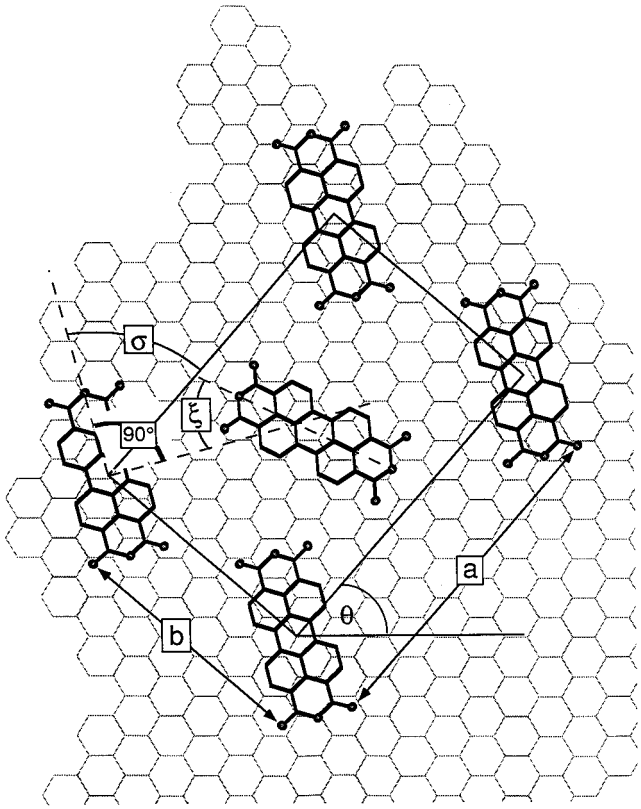

Figure 3-10. Surface unit mesh of PTCDA on a graphite substrate defining angles and dimensions referred to in the text.

shown in the figure. The angles and dimensions of the calculated surface unit cell agree well with the actual surface unit as determined from RHEED and STM (see Table 3). We note that the surface unit cell is enlarged by 25% over that obtained for a bulk cell, with the calculated minimum energy corresponding to $x_{min} = 20.0 \pm 0.5$ Å and $y_{min} = 15.7 \pm 0.5$ Å. This accounts for (although it somewhat overestimates) the reconstructed surface dimensions of PTCDA observed by both STM and RHEED. The surface cell minimum energy is obtained for all molecules in a coplanar configuration. By placing a second layer at 3.21 Å above the surface, the cell minimum energy is achieved only when x_{min} and y_{min} are decreased to values approaching their experimentally obtained bulk distances of $x_{min} = 17.34$ Å and $y_{min} = 11.96$ Å. Also, the central molecule of the surface cell is rotated to an angle of $\xi = 0.48 \pm 0.02$ rad, also consistent with observation.

The orientation of the adsorbed layer with respect to the substrate lattice is defined by angle, θ, between the primitive vectors in the two lattices (see Figure 3-10). From this figure, θ is a well-defined quantity for all epitaxial systems; whether they are commensurate, incommensurate, or coincident.[104] The value of θ leading to $\Phi'(\theta) = 0$ and $\Phi''(\theta) > 0$

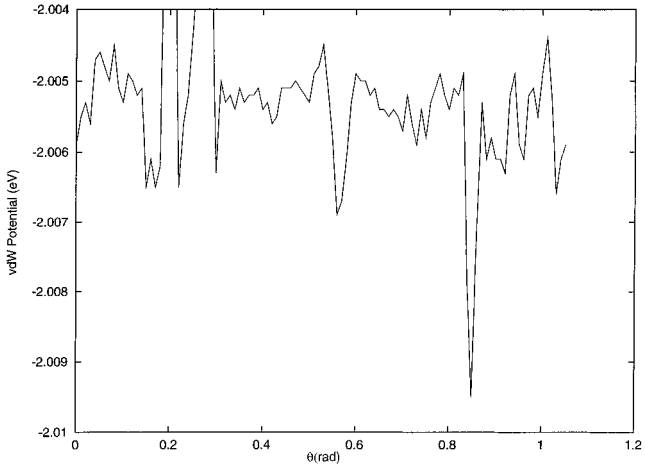

Figure 3-11. Binding energy of a monolayer of PTCDA on a graphite substrate as a function of relative lattice angle, θ, as defined in Figure 3-10. The vertical axis is the energy normalized to the binding energy per PTCDA molecule (from ref 99).

corresponds to the equilibrium lattice configuration. On the basis of these arguments, and using the "rigid lattice" approximation where the layers are translated with respect to each other without distortion, θ has been calculated for a monolayer of PTCDA deposited on graphite,[99] with the results shown in Figure 3-11. Here, a sufficiently large lattice (10×10 PTCDA unit cells, or ~50 000 atoms) was considered to ensure insensitivity of the result to layer boundaries and variations due to center of mass translation of the overlayer. An energy minimum of −4 meV was noted at $\theta_{min} = 0.85$ rad, where the energy axis in Figure 3-11 is normalized to a single adsorbed molecule of PTCDA (−2.0 eV). This relatively small energy perturbation/molecule (<0.3%) justifies the assumption that the overlayer structure is not strongly influenced by the substrate, in contrast to atomic vdW systems (e.g., Ar on graphite) where the rotational energy is ~5% of the bond energy.[116] Note that θ_{min} is in relatively good agreement with the experimental value[43,58,70] of $\theta = 0.84 \pm 0.07$ rad (see Table 3) obtained by STM.

Both RHEED and X-ray data[52,73] indicate unit cell dimensions that are somewhat smaller than predicted by this simple theory. This discrepancy is in part due to formation of an expanded first ML, and then subsequent relaxation into a structure closer (but not identical) to the bulk crystal habit of PTCDA. A transition interfacial layer of dimensions different from subsequent layers appears to be one mechanism for the relief of strain in these incommensurate QE systems; a feature noted in studies of the transition from equilibrium growth (i.e., at high substrate temperature, T_{sub}) to nonequilibrium, or QE, growth (at low T_{sub}) of PTCDA on Au(111) (see section 3.3.2.3).

Table 3. Surface Unit Cell Parameters[a] for PTCDA on Graphite

	a (Å)	b (Å)	σ (rad)	ξ (rad)	θ (rad)	ref(s)
theory	20.0 ± 0.5	15.7 ± 0.5	0.86 ± 0.02	0.48 ± 0.02	0.86 ± 0.02	72,99
STM	20.5 ± 1.2	14.2 ± 1.5	0.96 ± 0.03	0.61 ± 0.17	0.90 ± 0.06	43,58,70
RHEED	22.4 ± 1.0	16.0 ± 1.0				52,70,73

[a] Dimensional parameters defined in Figure 3-10.

This calculation was also used to study molecular interfaces consisting of NTCDA on a crystalline PTCDA substrate.[99] Experimental evidence obtained for alternating multilayer stacks of these materials[23,70] imply that the layers form ordered crystalline organic multiple quantum well structures. Due to the extended size of the molecules in both layers and to the large number of pairwise atomic interactions between each molecule, the method outlined in eq 3.2 is calculationally impractical. For example, to determine the intermolecular potential between just two PTCDA molecules requires 1444 pairwise interaction potential calculations. The calculations have been substantially simplified by Zhang[72] by replacing the $\sim 10^3$ atomic interactions between each NTCDA and PTCDA molecule with an approximate, *single*, elliptically symmetric molecular potential assuming a fixed intermolecular stacking distance. One such potential which has been shown to provide a good fit to molecules within a given layer is similar to the Buckingham potential, viz.:

$$\phi_{ij}(\theta)_{\mathrm{EP}} = -\alpha(\theta)/(r_{ij} - \delta(\theta))^6 + \beta(\theta)\exp[-\gamma(\theta)(r_{ij} - \delta(\theta))]r_{ij} - \delta(\theta) \geq 0 \quad (3.3)$$

where r_{ij} is now the center−center distance between *molecules*, $\delta(\theta)$ is the distance of "closest approach" of two adjacent molecules as calculated from their core repulsion, and the vdW constants are functions of the angle (θ) between unit cells in the overlayer and substrate. An alternative potential form which also provides a good fit to the atom−atom calculation, especially for molecules between planes, was approximated using

$$\phi_{ij}(\theta)_{\mathrm{EP}} = -\phi_{\mathrm{o}} \exp[-|x/\eta(\theta)|^{\varphi(\theta)} - |y/\kappa(\theta)|^{\lambda(\theta)}] \quad z = \mathrm{d} \quad (3.4)$$

where the distance in the z direction is held fixed at the interplanar spacing of d. The angular dependencies of the parameters such as α, β, δ, etc. were determined by translating one molecule over the substrate at a fixed z (equilibrium) distance in both the a and b crystalline directions while calculating the full atom−atom potential using eq 3.2. This provides values for α_a, α_b, etc., or similarly for the parameters in eq 3.4. To determine these parameters at other off-axis angles, an ellipsoidal dependence was assumed:

$$(\alpha(\theta)\cos\theta)^2/\alpha_a{}^2 + (\alpha(\theta)\sin\theta)^2/\alpha_b{}^2 = 1 \quad (3.5)$$

This calculational technique has been shown to be reasonably accurate (to within ±5% of the measured crystal dimensions), allowing for the semiquantitative determination of equilibrium film−substrate structures consisting of relatively complex molecules.[1] In any case, we note that the accuracy of using a full atomistic potential is limited as well. Commonly, the values of the various vdW coefficients used in such pairwise calculational methods are adjusted to match the predicted to the observed crystal structure to reduce inherent inaccuracies. Similar "iterative" procedures can also be applied to finding the optimal values of the effective coefficients

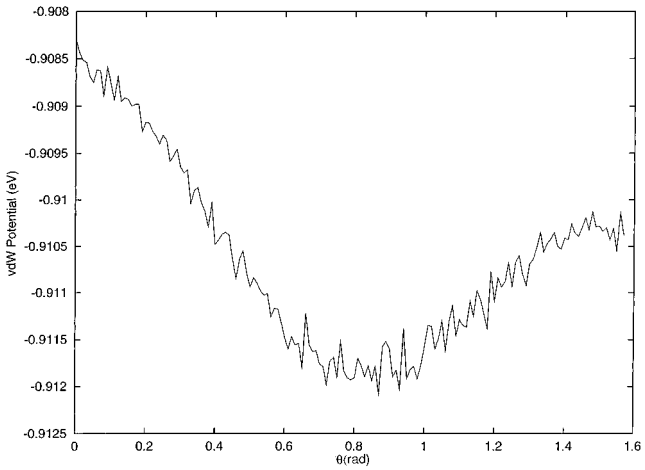

Figure 3-12. Binding energy of a monolayer of NTCDA on a PTCDA substrate as a function of relative lattice angle, θ, between the a axes of the two surface unit cells. The vertical axis is the energy normalized to the binding energy per NTCDA molecule (from ref 99).

derived from eq 3.5, although the overall accuracy of this procedure is found to be adequate for predicting the observed QE systems to which it has been applied.

Recently, it has been suggested[117] that while the ellipsoidal approximation is well adapted to the calculation of structures involving simple, small planar molecules such as PTCDA, it may not be appropriate for larger molecules, or molecules which exhibit some out-of-plane (3D) structure, such as the phthalocyanines. To generalize these approximations to account for complex molecular shapes, Liu et al.[117] represent the molecule (CuPc in the case of their work) by a limited set of "interaction sites" representing a cluster of atoms in the molecule, and spatially arranged to approximate the shape of the actual molecule. The Lennard−Jones potential is then used, along with effective vdW coefficients derived for each interaction site, to calculate the lowest energy crystal structures. For CuPc, the 54 atoms were replaced by 13 spherically symmetric sites, thereby eliminating 95% of the pairwise calculations required to determine the interaction between two like molecules. The number and distribution of sites chosen is determined by a compromise between the requirement to simply represent molecular geometry and symmetry, and the need to include as much of the interaction physics as possible without introducing an excessive number of sites. Using this method, a structure resembling that of the planar stacking α form of CuPc was calculated,[118] although the more common herringbone β-CuPc was not found.[117] Hence, while this interaction site model considerably simplifies calculations for complex molecular structures, as in all such methods, one must be aware that the approximations can significantly impact the accuracy of the technique.

The ellipsoidal approximation of Zhang and Forrest[72](eqs 3.3 to 3.5) has been applied to determined the equilibrium structure of a NTCDA monolayer (1000Å radius) deposited on a PTCDA "substrate" of equal size. The preferred orientation of the NTCDA lattice on PTCDA shown in Figure 3-12 is $\theta_{\mathrm{min}} = 0.75 \pm 0.05$ rad, defined as the angle between

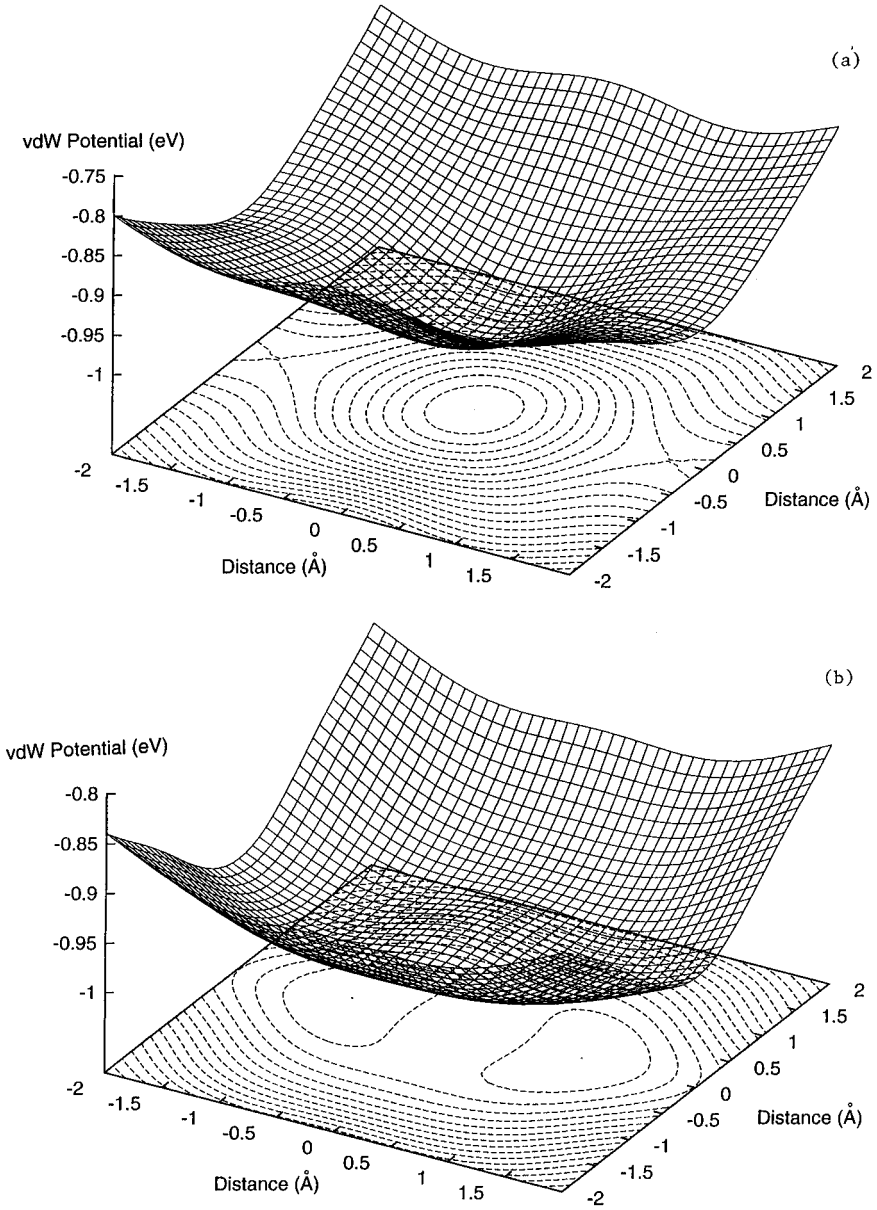

Figure 3-13. 2D potential surface of (a) benzene and (b) coronene on a PTCDA substrate. Here, the molecular planes of the substrate and admolecules are parallel (from ref 99).

the *a* axes of the two unit cells. The "noise" in the plot results from rounding errors and the limited size of the lattices considered. The minimum energy for PTCDA/NTCDA structures is broad (as compared to PTCDA-on-graphite) due to the low spatial frequencies of the lattices and the large spatial extent of the molecules in the two layers. Nevertheless, the existence of such an energetically favored configuration (with −3.5 meV/molecule normalized to the PTCDA/NTCDA dimer binding energy of −0.90 eV) suggests that this materials combination can grow as an orientationally ordered, crystalline multilayer stack under the appropriate thermodynamic conditions, as has been previously observed.[23,52]

From the foregoing results, we infer that the dependence of the orientation on molecular structure is implicit in the requirement that $\phi_{inter}'' << \phi_{intra}''$. The generality of this condition was tested by calculating ϕ_{inter}'' and ϕ_{intra}'' as functions of molecular "shape" for several polyacenes in the series of benzene, naphthalene, pyrene, perylene and coronene "deposited" on a PTCDA substrate. The calculated energy surfaces (normalized to their minimum values, ϕ_o) for single benzene and coronene molecules on a PTCDA substrate lattice are shown in Figure 3-13. It is apparent that the energy minimum of the larger molecule is extremely broad and flat as compared to that of benzene. Hence, the shear stress (ϕ_{inter}'') for the coronene/PTCDA interface is much smaller than that of benzene, which should enhance the probability for successful QE growth of incommensurate overlayers of the larger molecule.

The normalized shear stress $(\Delta^2\phi_{inter}/\Delta a^2)/\phi_o$ for a molecule on a PTCDA lattice is plotted in Figure 3-14 as a function of molecular moment of inertia, I_{mol} (normalized to benzene, I_{benz}). Here, $\Delta^2\phi/\Delta a^2$ is the energy difference divided by the surface area enclosing the energy 15% larger than its value at ϕ_o. Hence, $\Delta^2\phi_{inter}/\Delta a^2$ is the normalized incremental shear stress which is numerically evaluated from the calculated values of $\phi(x,y)$. Furthermore, the normalized moment of inertia of a particular molecule,

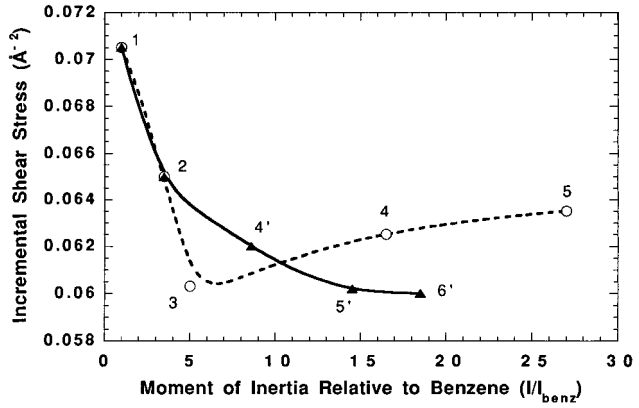

Figure 3-14. Incremental shear stress ($1/\phi_o\{\Delta^2\phi/\Delta a^2\}$)for several molecules deposited on a PTCDA substrate lattice calculated as a function of molecular moment of inertia relative to benzene. The shear stress is normalized in each case to the minimum dimer potential energy, ϕ_o. The moment of inertia is calculated about the axis perpendicular to and centered in the molecular plane. The solid line is for the molecules: 1 = benzene, 2 = naphthalene, 4′ = pyrene, 5′ = perylene, and 6′ = coronene (with 1, 2, 4, 5, and 6 carbon rings, respectively), and the dashed line is for the molecules: 3 = anthracene, 4 = tetracene, and 5 = pentacene (with 1, 2, 3, 4, and 5 carbon rings, respectively) (from ref 99).

I_{mol}/I_{benz}, is calculated about an axis perpendicular to, and centered in, the molecular plane of the adsorbed molecule, providing a measure of the molecular mass distribution relevant in facially stacked, discotic systems.

The normalized shear stress decreases monotonically with increasing molecular size, or number of carbon rings (solid line, Figure 3-14). Hence, we expect that the ability to grow ordered, QE layers on PTCDA (or similar planar molecule) substrates increases as we progress from smaller (benzene) to larger, "rounder" molecules (coronene).

Molecular shape also plays a significant role in determining structure. Hence, I_{mol} was also determined for a series of *linear* polyacenes deposited on PTCDA (dashed line). Here, the calculation is made for benzene, naphthalene, anthracene, tetracene, and pentacene (with 1, 2, 3, 4, and 5 rings, respectively). The shear stress decreases monotonically for the three smallest molecules, at which point it begins to increase for the larger molecules. This increase results since PTCDA has a perylene "core" which extends to only three rings. Hence, longer molecules (e.g., tetracene and pentacene) extend beyond the central molecule in the PTCDA surface cell, and overlap the spaces between adjacent substrate molecules. For the longest molecules, the rings can extend to the carboxyl end groups of adjacent substrate molecules. These effects will tend either to leave the shear stress unchanged (as in the case of tetracene-PTCDA), or result in a small increase due to core repulsion from adjacent molecules (pentacene-PTCDA).

These results suggest that QE is favored when both the molecular shape and size of the substrate and overlayer molecules are approximately matched. This suggests that ordered QE growth is a general property of a large range of planar molecules which are bonded primarily by vdW forces to the substrate.

We emphasize that while these calculations predict the favored, or minimum energy configuration of the grown layers, the degree and extent of layer ordering which is actually achieved depends critically on the nonequilibrium thermodynamic conditions under which growth occurs. These conditions are not predicted by this inherently static model, although we find that certain low energy "thresholds" between structural isomorphs predicted in the theory suggest that growth at low temperatures is favorable for achieving uniform crystalline order, as has been experimentally observed in many cases. However, a nonstatic model is required to unambiguously determine the growth conditions which lead to maximum structural ordering.

The molecular film alignment to the substrate also must depend on the symmetry of the substrate. For example, PTCDA, NTCDA, and CuPc lattices are monoclinic, and hence they have 2-fold symmetry. To ensure alignment of neighboring islands nucleated separately during the onset of growth, the substrate must have a comparable symmetry. As shown in the case of graphite[58,70] (see section 3.3.2.1), adjacent molecular islands nucleate with their principal axes rotated at angles of $m(\pi/3)$, where $m = 0, \pm1, \pm2, \pm3$. This higher order substrate symmetry results in the formation of grain boundaries between islands. Other substrates with natural 2-fold symmetry (such as an organic thin film or other monoclinic lattice), or with a preferred 2-fold directionality (e.g., glass with a strain axis parallel to the surface,[65] exposed step edges on semiconductor substrates oriented 1−2° from a principal lattice plane, narrow polymer stripes as used as waveguide buffer layers,[22,115] etc.) therefore can serve to avoid the occurrence of such grain boundaries. Indeed, step-edge growth has been shown[119] to result in appropriate 2-fold symmetry leading to extended order in both strained vdWE systems such as VOPc on H-terminated Si(111), and for PTCDA on polymer ribs.[22]

These results suggest that large, vdW-bonded planar molecules readily order on a variety of substrates without necessitating that the overlayer and substrate be lattice-matched or commensurate. We note, however, that simply depositing large planar molecules on the substrates will not necessarily reduce the interfacial shear stress. An additional condition favoring QE growth is that the *shape* of the molecule (or the atomic mass distribution) must be similar to the substrate molecular shape. That is, QE growth is favored for approximately round, planar molecules deposited on similarly shaped molecules in the substrate. It is somewhat less favored (although not ruled out) in the case of long, linear molecules deposited on this same substrate structure.

3.3.1.2. Coincidence Models. Although energy minimization calculations used to determine equilibrium layer structures are physically justified, there remain several problems with their practical application and overall predictive ability. Among the most obvious of shortcomings of these methods are given in the following:

(1) The calculations are cumbersome. Given n atoms in the epitaxial layer and m atoms in the substrate, the total number of atomic pair interac-

tions which must be considered is $n \times m$. For the calculations to be realistic, both n and m must be sufficiently large using a suitable choice of lattice boundary conditions. As noted in the previous section, for PTCDA on HOPG, ~100 unit cells were considered before adequate accuracy was achieved. There are means to make these calculations more efficient by, for example, recognizing that vdW interactions fall off as $1/r^6$. Hence, only nearest- and next-nearest-neighbor interactions need to be considered. Alternatively, approximations such as the ellipsoidal potential or interaction site methods can be employed. Nevertheless, the method is calculationally intensive with results which often do not provide an intuitive understanding of the systems under study.

(2) The number of degrees of freedom is very large. Compounding the problem of large computational scale is the high multiplicity of degrees of freedom inherent in the complex molecular structures and positions within the unit cell basis. That is, by rotating, twisting, or stretching a bond within a molecule, or by changing the relative positions of two molecules within a unit cell, the total energy of the overlayer with respect to the substrate can be significantly altered. An accurate, predictive calculation must therefore include minimization of *total energy with respect to all of these degrees of freedom*. As noted in the previous section, the calculations were considerably simplified (and indeed made tractable) by significantly limiting the degrees of freedom available to the adsorbed layer. For example, molecules were restricted to lie in a single plane, and even their internal bond lengths were, in effect, fixed by assuming an "ellipsoidal" potential approximation.

(3) The calculations must include sufficient physics to be accurate. For PTCDA on HOPG or NTCDA, only vdW bonds were included in the treatment. While this is adequate for many molecular/substrate systems, in some cases (e.g., VOPc on Si(111)), Coulombic attraction, hydrogen bonding, higher order multipoles, etc. must also be included.[109] If Coulomb forces are small, they can complicate the problem significantly due to their long-range nature.

Hence, other methods have been suggested to attain a more "intuitive" picture for determining the preferred azimuthal orientation, θ, of the adsorbed layer and the substrate lattices in incommensurate, QE systems. The most common methods can broadly be termed "coincidence models".[43,96,104,120] These models are based on two hypotheses: (i) Overlayer energy is minimized by maximizing commensurability with the substrate. That is, the minimum energy is achieved when the largest number of lattice sites are commensurate with substrate lattice sites. (ii) "Commensurability" on some arbitrarily defined lattice scale can often be achieved by azimuthally rotating one lattice with another. This commensurability, when characterized by the alignment of two high symmetry axes of the lattices is called "point-on-line coincidence". An example of such coincidence is shown schematically in Figure 3-15, where commensurate, incommensurate and point-on-line coincident lattice alignments are schematically illustrated. Note that these "models" still rely on the primary condition for QE: i.e., $\phi_{intra}'' >> \phi_{inter}''$, where coincidence is achieved only by assuming a rigid overlayer largely undistorted by its deposition on the substrate.

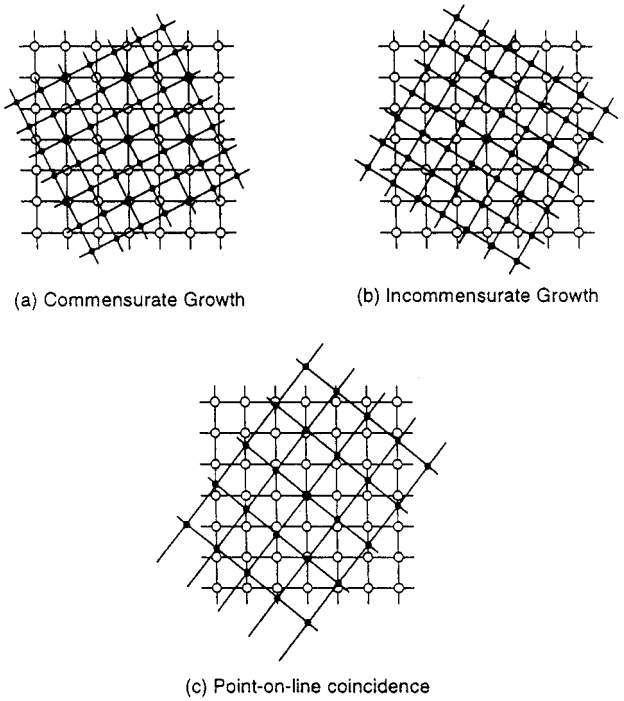

Figure 3-15. Schematic diagrams of three types of epitaxial orientations: (a) commensurate, (b) incommensurate, and (c) point-on-line coincident growth (from ref 123).

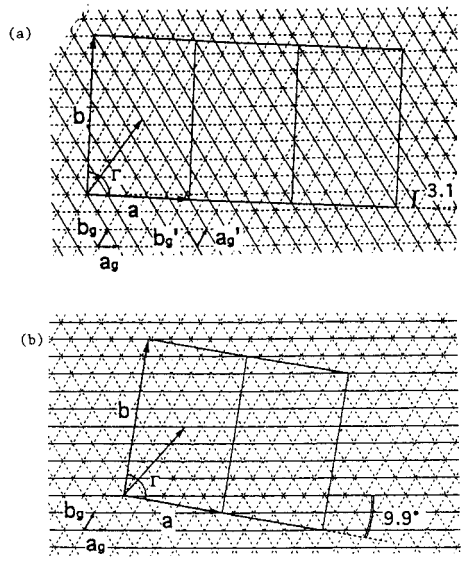

Figure 3-16. Schematic diagrams of two different point-on-line coincidence orientations of PTCDA on graphite (0001) proposed by Hoshino et al. (ref 43). For the type I orientation (upper panel), PTCDA molecules at (3**a**,**b**) on the equilibrium (bulk) surface unit mesh nearly coincide with points on the graphite lattice. For type II orientations (lower panel), PTCDA molecules at (2**a**,**b**) are in close coincidence with points on the graphite lattice.

Point-on-line (POL) coincidence has been proposed[43,96] to govern the orientation of such materials as PTCDA on HOPG, where two coincident lattices are found relative to the (0001) graphite surface. In Figure 3-16, we show these two orientations corresponding to angles of 3.1° and 9.9° of the PTCDA (010) with the graphite symmetry axis. Both of these

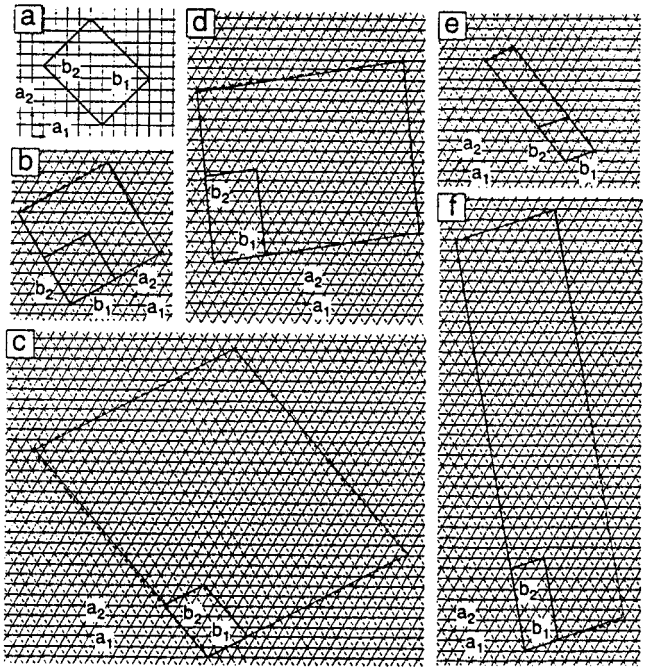

Figure 3-17. Schematic representations of overlayer orientations on substrates for several incommensurate systems. The perimeter of the primitive unit mesh is shown by the lines in the corners of the larger, coincident, nonprimitive supercells exhibiting POL coincidence. The various systems correspond to (a) PTCDA/Cu(100), (b) CuPc/MoS_2, (c) $(Pe)_2ClO_4$/HOPG, (d) TTF-TCNQ/Au(111), (e) β-$(ET)_2I_3$ (type I)/HOPG, and (f) β-$(ET)_2I_3$ (type II)/HOPG. Here Pe = perylene, ET = bis(ethylenedithiolotetrathiafulvalene), TTF = tetrathiafulvalene, TCNQ = tetracyanoquinodimethane (from ref 120).

orientations have been experimentally inferred from analysis of the Moiré patterns observed in the STM images (see section 3.3.2.1, Figure 3-21), and the orientation at 9.9° has also been determined from minimum energy calculations discussed in the previous section.

While this approach can provide some physical insight into the alignments observed, coincidence models lack a compelling physical foundation.[121] Since they are not based on energy arguments, they are incapable of predicting the preferred orientation out of many potential POL coincidence possibilities. Furthermore, the results are completely independent of the details of physical structure of the molecules within a unit cell, or the degrees of freedom accessible to the atoms within the cell. For example, if molecule A in a lattice with a basis of M molecules is replaced by a completely different molecule, B, in a unit cell of equivalent dimension but with a basis M′, the POL technique will predict *exactly the same overlayer orientation* as in the first case. This is a natural consequence of the coincidence models dependence on geometrical rather than energetic considerations. Finally, although the POL model requires only that lattice vectors coincide in the substrate and adsorbate lattices, the molecular and atomic sites need only be commensurate at the corners of the larger "supercell" such as those outlined in Figure 3-16. More extreme examples of such commensurate supercells[120] are provided in Figure 3-17. In such examples, there is no obvious energetic justification for requiring coincidence along the chosen axes, where we emphasize that virtually all molecules and atoms in the supercells are incommensurate with the substrate lattice.

While these geometrical, POL coincidence methods have "little direct theoretical significance",[120] Hiller and Ward have made some useful approximations which provide an energy-based justification for the observation that several QE systems appear to favor alignment at, or close to substrate axes of high symmetrical order. We first recognize that simple (i.e., monoatomic) lattice potentials can be approximated by a periodic potential of the form (in one dimension):

$$V = V_o \cos(2\pi x/a) \tag{3.6}$$

where V_o is the strength of the interatomic potential, x is the displacement, and a is the substrate (1D) lattice constant. Defining the transformation matrix, **C**, which depends on the relative azimuthal relationship between the adsorbed layer and the substrate lattice, we have

$$\frac{V}{V_o} = \frac{1}{2}\frac{\sum_i\sum_j\left\{2 - \cos\left[2\pi(ij)[\mathbf{C}]\begin{pmatrix}1\\0\end{pmatrix}\right] - \cos\left[2\pi(ij)[\mathbf{C}]\begin{pmatrix}0\\1\end{pmatrix}\right]\right\}}{\sum_i\sum_j} \tag{3.7}$$

where i,j are the lattice sites of the adsorbed layers. The matrix, **C**, is defined by

$$C = \begin{pmatrix} b_1\sin(\alpha-\theta)/a_1\sin(\alpha) & b_1\sin(\theta)/a_2\sin(\alpha) \\ b_2\sin(\alpha-\theta-\beta)/a_1\sin(\alpha) & b_2\sin(\theta+\beta)/a_2\sin(\alpha)\end{pmatrix} \tag{3.8}$$

where $a_{1,2}$, α and $b_{1,2}$, β are the primitive vectors and angles of the substrate and adlayer unit meshes, respectively (see Figure 3-16). The results[120] of calculating the relative potential, V/V_o, as a function of azimuthal angle, θ, for the several supercells of Figure 3-17 are shown in Figure 3-18. Here, $V/V_o = 0$ corresponds to the case of perfect commensurability (i.e., true epitaxy), whereas complete incommensurability corresponds to $V/V_o = 1$. In general, therefore, QE is described by systems whose energy lies between these extremes. In each of the cases studied by Hiller and Ward, there is a well-defined angle at which the supercell achieves a minimum energy, consistent with full energy calculations discussed in section 3.3.1.1.

Whether or not this method predicts the true azimuthal orientation of the two lattices depends critically on the choice of potential for the substrate, the shape, and composition of the overlayer molecules, and the symmetry and composition of the basis lattices. While simple vdW systems such as PTCDA on HOPG may be adapted to this treatment, the relative orientation of even such simple lattices

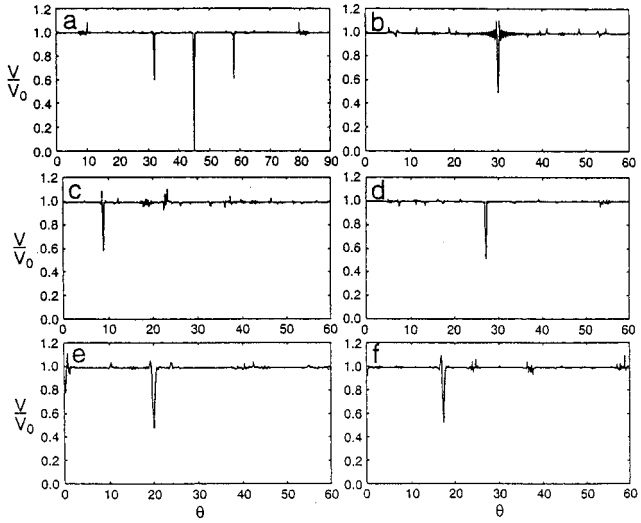

Figure 3-18. Normalized energy (V/V_0) on azimuthal angle (θ) for the overlayer−substrate combinations in Figure 3-16, assuming an overlayer dimension of 20 × 20 unit cells: (a) PTCDA/Cu(100), (b) CuPc/MoS_2, (c) $(Pe)_2ClO_4$/HOPG, (d) TTF-TCNQ/Au(111), (e) β-$(ET)_2I_3$ (type I)/HOPG, and (f) β-$(ET)_2I_3$ (type II)/HOPG (from ref 120).

cannot be accurately predicted due to the lack of correspondence between the choice of $V(x)$ and the true interatomic potentials which fully incorporates the inherent "flexibility" of the adsorbate lattice. This flexibility manifests itself via the stretching, twisting, or rotation of any number of inter- and intramolecular bonds which are not considered in the POL coincidence technique. Indeed, in the POL treatment, each molecule in the adsorbate layer was approximated by a single "point" potential. While this is a reasonable approximation of the case of an inert gas molecule (e.g., Ar) adsorbed on graphite, the approximation must break down for spatially extended molecules whose spatial period is large compared to that of the substrate, such as an OMC on an inorganic or organic substrate. Nevertheless, such coincidence models appear to explain observations of some simple vdW-bonded systems, and provide an intuitive rationale which is useful in guiding more computationally intensive methods such as those discussed in section 3.3.1.1.

3.3.1.3. Mass Density Waves. It is useful to compare the process of QE with the previously observed phenomenon of "orientational epitaxy" which describes the structure of layers of physisorbed inert gas atoms bonded by vdW forces onto lattice-mismatched graphite substrates. The most obvious difference is that, in the case of orientational systems, the spatial frequency of oscillation of the substrate atomic potential is nearly equal to that of the adsorbed inert gas layer. The interatomic distance is simply determined by the packing of the atomic hard spheres. This is in contrast to QE systems where the adsorbed molecular spacing is substantially larger than the interatomic distances in the substrate lattice. It was proposed that mismatch between adsorbate inert gas atoms and the substrate in orientational systems results in small, periodic, static density variations (mass density waves, or MDWs) in the overlayer.[75,116] Competition between longitudinal and transverse modes in these MDWs

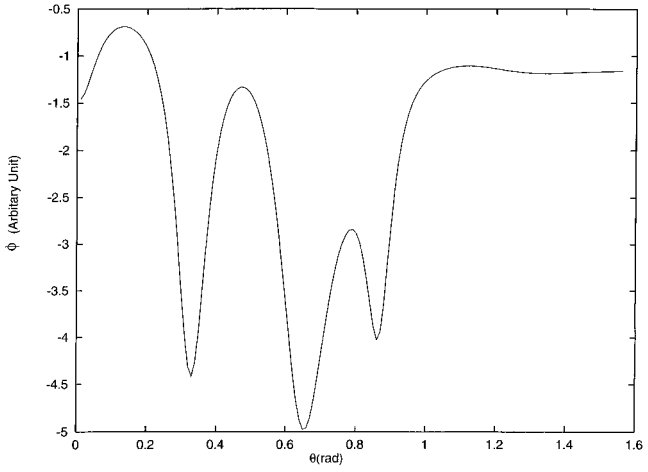

Figure 3-19. Relative lattice energy for a NTCDA surface unit cell on NTCDA as a function of orientation, θ, as a result of strain induced in the adlayer. This energy is in addition to the rigid lattice energy calculated in Figure 3-12 and is expected to be small by comparison (from ref 99).

results in an energetically preferred angle (θ_{min}) between reciprocal lattice vectors **G** and τ of the substrate and adsorbed layers, respectively. It was shown that, for the special case of long MDW wavelength, θ_{min} is determined by minimizing:

$$\phi = -\sum_{l} \frac{\bar{u}_{\mathbf{G}}^2[\mathbf{G}\cdot\epsilon_l(\mathbf{G})]^2}{M\omega_l^2(\mathbf{G})} \qquad (3.9)$$

where $\bar{u}_{\mathbf{G}}^2$ is the average displacement of a molecule in the overlayer, M is the molecular mass, and ϵ_l and ω_l are the eigenvectors and eigenvalues of the dynamical equation defined by $D(\omega_l)\lambda(\omega_l) = \omega_l\lambda(\omega_l)$. Here, $D(\omega_l)$, is the dynamical matrix operator,[80] and $\lambda(\omega_l)$ are the Bloch functions for the PTCDA surface lattice. This approach requires that the phonon dispersion curves ($\omega_l(\mathbf{G})$) for the adsorbed 2D lattices be calculated along the various crystal axes assuming vdW bonding described by eq 3.2. When applied to PTCDA and NTCDA, these calculations yield two transverse and one longitudinal acoustic phonon mode.[99] Optical modes were ignored since ω_l for these terms is large, resulting in a small contribution to eq 3.9.

Summing the contributions from each mode gives the MDW energy for NTCDA shown in Figure 3-19. The several peaks correspond to the summation of phonon modes, ω_l, along the various crystal directions, with an energy minimum at $\theta_{min} = 0.65$ rad. Note that the contribution to the total layer energy due to this lattice distortion should be small in incompressible molecular lattices (where $M\omega_l^2$ is very large due to the large molecular mass and high vibrational energy), and thus should not significantly alter the position of the NTCDA/PTCDA energy minimum from that shown in Figure 3-12.

Note that the lattice distortion energy accounted for in eq 3.9 is a second-order effect in molecular systems, whereas in relatively compressible atomic vdW lattices (where M and ω_l are small) this effect should dominate.[75,116] However, the presence of MDWs in QE systems may nevertheless provide a mechanism for reduction in total strain energy, and

indeed may already have been observed for PTCDA on HOPG (using STM) and on Au(111) (using X-ray diffraction).[58,73] That is, MDWs may manifest themselves as periodic variations in a degree of freedom with a unit cell (e.g., a small angular rotation of the molecules with respect to each other, with the angle periodically varying over several unit cells). These periodic variations may provide a means to reduce the total crystal energy induced by lattice strain, thereby eliminating the formation of dislocations or other macroscopic lattice defects. Furthermore, the addition of the MDW energy to that of the otherwise unperturbed adlayer via eqs 3−9 may induce some deviation from point-on-line reconstruction.

3.3.2. Observation of QE Growth

To test the above assumptions regarding the conditions which are required to achieve QE thin films, PTCDA has been grown on several different substrates with varying magnitudes of substrate/adlayer interactions. The case of PTCDA on HOPG has been the most thoroughly studied, and from the foregoing discussion, it is apparent that the QE layer should be azimuthally oriented with respect to the graphite lattice without inducing significant strain in the thicker QE layer. In addition, PTCDA has been grown on Au(111) and GaAs which have somewhat stronger substrate−molecular interactions than in the case of HOPG, resulting in a strained-layer QE PTCDA thin film. Below, we consider each of these cases in detail to provide a comprehensive picture of the nature of QE thin-film growth for different bond energies between the substrate and epitaxial layer.

3.3.2.1. STM Imaging of PTCDA and NTCDA Monolayers on HOPG. The onset of QE growth has been thoroughly investigated by examining monolayers of PTCDA[43,57,58,70] and NTCDA[122] grown on HOPG under UHV and atmospheric ambient conditions. Experiments described here were primarily conducted in UHV, using electrochemically etched tungsten tips and mechanically sheared Pt-Ir tips.[58] The PTCDA was deposited at a rate of 3−10 Å/min on substrates held from 80 K to slightly above room temperature,[43,58,70,122] whereas the NTCDA growths were performed for substrate temperatures in the range of from −30 to 100 °C.[122] The film thickness studied in these experiments ranged from submonolayer coverage up to 2−3 ML. While it is difficult to obtain STM images with molecular resolution for thicker layers due to the low conductivity typical of OMCs, nevertheless, PTCDA layers up to 60 Å thick deposited on Se-passivated (100)GaAs have been successfully imaged using UHV STM.[123]

Figure 3-20 is a high-resolution image of a 1 ML thick film of PTCDA. The shapes of the two molecules within the unit cell are distinct; one appears as a figure-eight while the other less well resolved molecule appears as two parallel lines. The dimensions of the PTCDA rectangular unit cell (Figure 3-20) were found to be $a = 13.2 \pm 0.45$ Å and $b = 19.5 \pm 0.6$ Å, which agree with measurements of PTCDA on HOPG[43,57,70] done under ambient conditions suggesting the as-grown layers are stable. These results are also consistent with the enlargement of the bulk unit cell[36] in the (102) plane ($a = 11.96$ Å, $b = 19.91$ Å). A similar cell enlargement has been observed the first few ML of PTCDA on Au(111)[73] and for PTCDA on alkali halide substrates.[46,124] As noted in section 3.3.1.1, this enlargement is anticipated for monolayer QE films of PTCDA due to the reduced vdW bond energy in 2D as compared with 3D.

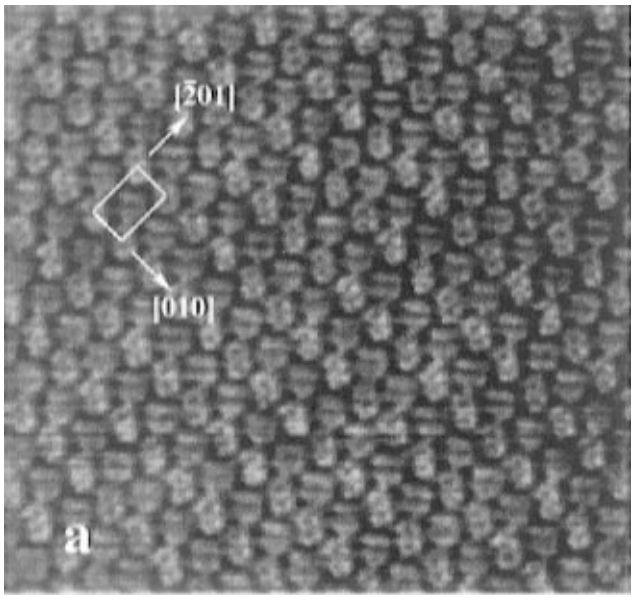

Figure 3-20. A 200 Å × 200 Å STM image of PTCDA on HOPG showing a unit cell consisting of two molecules indicating the crystallographic directions. Image taken in the constant current mode under UHV conditions, with a tip current of 200 nA and voltage of −800 mV (from ref 58).

The orientation of the molecular layer with respect to the HOPG can be obtained by maneuvering the tip into holes in the overlayer[58] or by removing the layer with the tip.[122] Alternatively, by increasing the current, the tip penetrates the thin film, providing a direct image of the underlying graphite lattice.[70] By these means, the angular relationship between the substrate and the overlayer can be directly determined. For PTCDA, two domain orientations are observed with respect to the HOPG: The first (type I) is at an angle of 3° ± 3° between the *a* axis ([010] direction) of the PTCDA and the [11$\bar{2}$0] direction of graphite,[43,57,58] and the second[1,43,58,70,123] (type II) is at an angle of 10 ± 1°. Although these measurements are only accurate within 1° or 2°, the type II orientation is clearly consistent with the calculated structure, which predicts $\theta = 10.7 \pm 1°$. Both arrangements are consistent with the POL coincidence fits of 3.1° and 9.9° (see Figure 3-16). All of these experimental and theoretical results obtained for PTCDA on HOPG are summarized in Table 4.

Moiré patterns shown in Figure 3-21 indicate a periodic superstructure at an angle of 10.5° with respect to the *b* axis ([$\bar{2}$01] direction) of the PTCDA unit cell. This result differs from Ludwig et al.[42] in which Moiré fringes were observed parallel to the *b* axis resulting from a proposed commensurate 1×3 superstructure. Due to the weak vdW bond and the

Table 4. Summary of Growth Parameters Measured for PTCDA on HOPG[a]

analytical technique	unit cell dimensions (Å)	orientation to $[11\bar{2}0]$ (deg)	molecular axes orientation
Bulk PTCDA (102) plane (from XRD) (ref 36)	$a = 11.96$		48.9° to $[\bar{2}01]$
	$b = 19.91$		41.1° to [010]
STM (refs 1 and 70)	$a = 15.2 \pm 1.6$	$\theta = 13.0 \pm 4$	$55 \pm 1.7°$ to $[\bar{2}01]$
	$b = 21.6 \pm 2.2$		$35 \pm 1.7°$ to [010]
total energy calculation (refs 72 and 99)	$a = 15.6 \pm 0.5$		$49.3 \pm 1°$ to $[\bar{2}01]$
	$b = 19.8 \pm 0.5$	$\theta = 10.7 \pm 1$	$40.7 \pm 1°$ to [010]
LEED (ref 42)	$a = 12.5 \pm 0.75$	$\theta = -3 \pm 0.15$	
	$b = 19.2 \pm 0.7$		
STM (ref 42)	$a = 12.7$	$\theta = \pm 3.2$	~49.5 to $[\bar{2}01]$
	$b = 19.2$		~40.5 to [010]
STM (ref 43)			
polytype I	$a = 12.69$	$\theta = \pm 3.1$	
	$b = 19.22$		
polytype II	$a = 12.37$	$\theta = \pm 9.9$	
	$b = 19.43$		
STM (ref 123)	$a = 13.2 \pm 0.45$	$\theta_1 = \pm 3$	$48.6 \pm 1.9°$ to $[\bar{2}01]$
	$b = 19.5 \pm 0.6$	$\theta_2 = \pm 10.5 \pm 3$	$41.4 \pm 1.9°$ to [010]

[a] Table from ref 123.

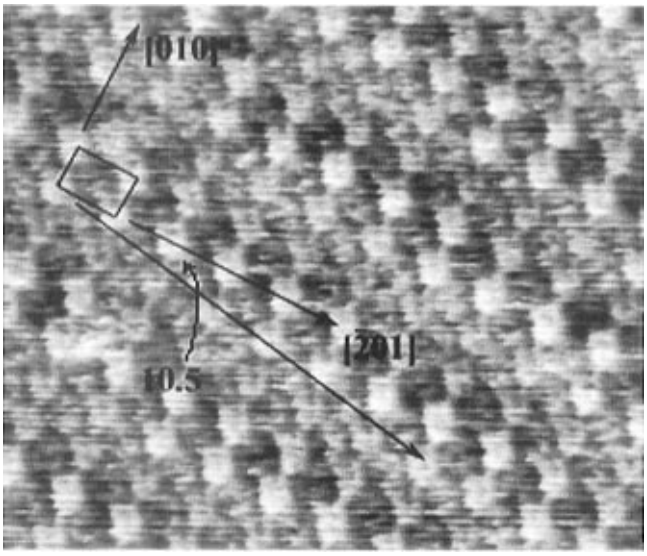

Figure 3-21. A 200 Å × 200 Å STM image of a monolayer of PTCDA on graphite showing Moiré fringes oriented parallel to the long arrow. The fringes are at a 10.5° angle to the *b* axis (at [010]) of the PTCDA unit cell (from ref 58).

numerous degrees of freedom available to the layer as a means for reducing total energy (c.f., section 3.3.1.1), it is unlikely that the molecules form a rigid, commensurate reconstruction on a scale equivalent to the repeat distance in the Moiré pattern (~119 Å along the [010] direction and ~215 Å along the ($[\bar{2}01]$ direction). Indeed, such a commensurate superstructure (extending over >32 substrate unit cells) has also been proposed[122] for NTCDA on HOPG, and NTCDA on MoS_2, which is equally unlikely, particularly in view of the fact that small inaccuracies in calculating the size of the overlayer cell from the STM image can lead to large variations in this superstructure periodicity. Instead, these results imply that the overlayer is incommensurate with the substrate, consistent with the QE growth model.

To further understand the contrast apparent in STM images of organic monolayers, images have been obtained for a wide range of tip biases. For example, a voltage-dependent contrast of the PTCDA layer has been observed.[58] Recall that the two molecules in the bulk (102) plane are tilted out of the plane,[36] a situation which might also obtain for monolayer films on HOPG. The slight difference in height between the two molecules would be observable when the tip is closest to the film (i.e., low bias voltages).

However, the surface unit cell is expanded from that of the bulk, suggesting that molecules in the first ML probably lie parallel to the substrate plane. Thus, the molecules aligned with their long axis close to a symmetry axis of the substrate are expected to have low contrast due to increased interaction with the substrate. In this case, the molecules imaged with higher intensity at low biases would actually be less strongly bound due to a reduced substrate/adlayer orbital overlap. At higher biases, these subtle effects would not be observed,[58] giving rise to an equal intensity for both molecules in the STM images as observed. It is likely that a combination of both topographic and electronic effects contribute to the voltage dependent contrast. Indeed, this interpretation has been confirmed by electron-density calculations for the PTCDA/graphite interface.[125]

Figures 3-22a and 3-23a are STM images of filled and empty states, respectively. The images are taken at the lowest bias voltages below which the contrast of the organic monolayer is unobservable. Under these conditions, it is found that the PTCDA molecules can be imaged with submolecular resolution.[58] Molecular electron density calculations based on independent optimization of molecular orbitals (or ZINDO)[43,58,126−128] are shown in Figures 3-22b and 3-23b for PTCDA. There is a clear correspondence between the calculated HOMO and LUMO bands and the filled and empty electronic state images, respectively. The highly electronegative oxygen atoms in the carbonyl groups are calculated to have an excess charge of ~0.4 e compared with that on the nearest carbon neighbor. Nevertheless, the energy of these states lie *lower* than the HOMO, with no significant contribution to the STM images. Instead, the π bonds in the perylene core contribute most to determining the HOMO energy, and hence are most clearly apparent in the STM images.

The interpretation of these molecular images has been tested by Strohmaier et al.[122] who also examined

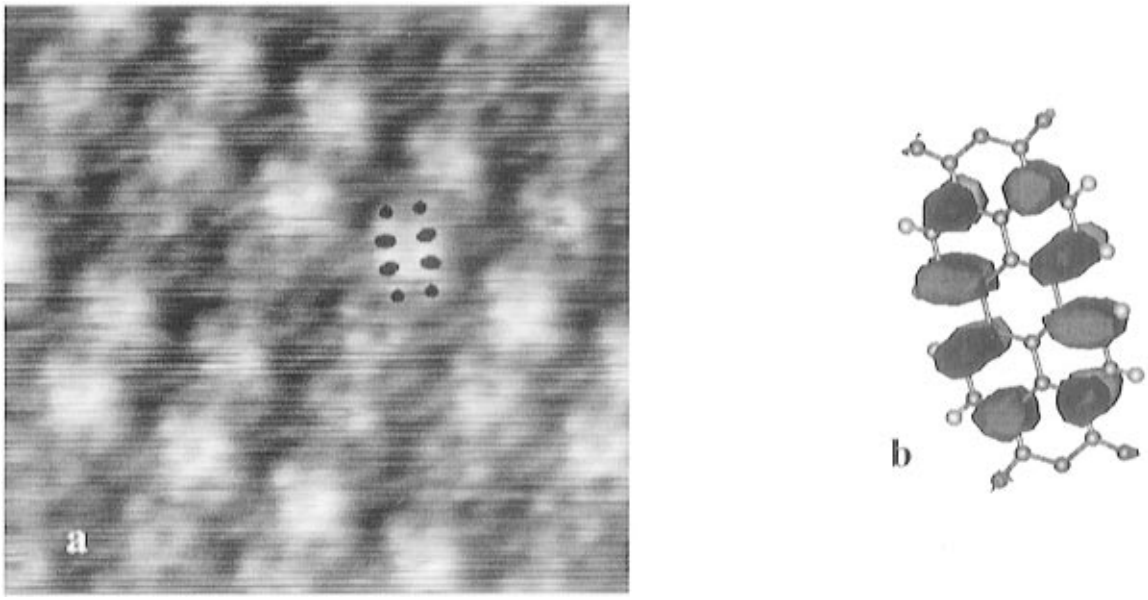

Figure 3-22. (a) Low bias, 100 Å × 100 Å filled state STM image of PTCDA on graphite. Measurement conditions are a tip current of 0.1 nA and a voltage of −250 mV. (b) Molecular orbit calculation indicating the HOMO of a PTCDA molecule (from ref 58).

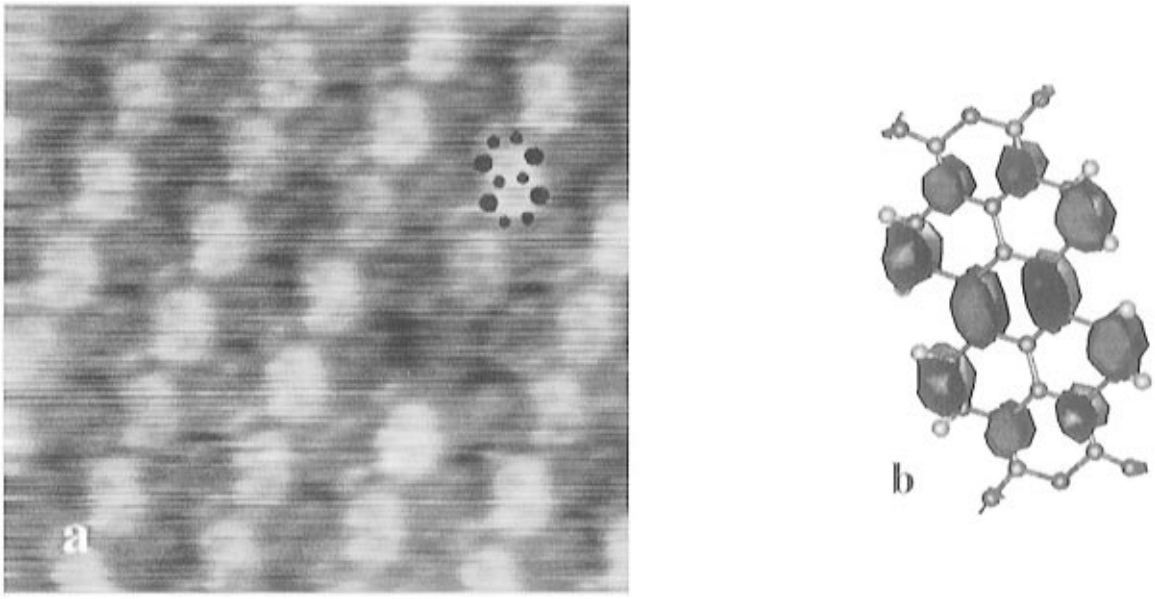

Figure 3-23. (a) Low bias, 100 Å × 100 Å empty state STM image of PTCDA on graphite. Measurement conditions are a tip current of 0.1 nA and a voltage of +250 mV. (b) Molecular orbit calculation indicating the LUMO of a PTCDA molecule (from ref 58).

the smaller molecule, NTCDA. If the contrast mechanism is the same for both PTCDA and NTCDA, the number of contrast maxima should be equal to the number of C−C bonds in the molecular core, corresponding to the ten observed for PTCDA and six for NTCDA. This has been confirmed as illustrated in the STM image of Figure 3-24a where the "figure eight" characteristic of the larger PTCDA molecule has been replaced by a simple "ringlike" image for NTCDA. In Figure 3-24b, molecular orbital calculations of the NTCDA LUMO are shown which correspond well to the observed image of the C−C bond arrangement.

Since the contrast in the STM images have been confirmed to result from the overlap of molecular orbitals in the thin film and substrate, the image striations, or Moiré patterns, can thus be analyzed to accurately determine the relative orientation of the two lattices.[96] This can be understood by considering the geometrical relationship between the two contacting lattices in Figure 3-25. Here, we write the unit vectors of the molecular layer, **a** and **b** in terms of the substrate vectors, $\mathbf{a}_g$ and $\mathbf{b}_g$ using

$$\mathbf{a} = k\mathbf{a}_g + l\mathbf{b}_g + \Delta\mathbf{a} \qquad (3.10a)$$

$$\mathbf{b} = i\mathbf{a}_g + j\mathbf{b}_g + \Delta\mathbf{b} \qquad (3.10b)$$

where i, j, k, and l are integers, and $\Delta\mathbf{a}$ and $\Delta\mathbf{b}$ are vectors which arise due to the mismatch between the incommensurate lattices. It can be shown that depending on the values of $\Delta\mathbf{a}$ and $\Delta\mathbf{b}$, either a two dimensional or one dimensional Moiré pattern will result. These two types of patterns are illustrated

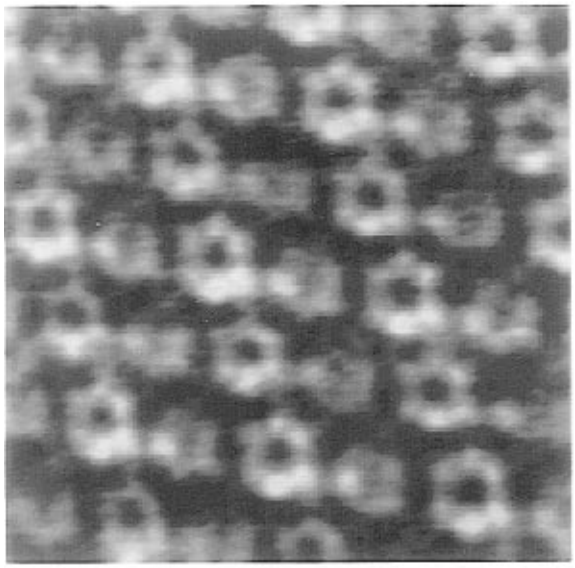

(a)

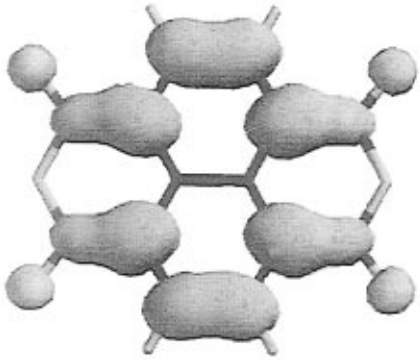

(b)

Figure 3-24. (a) STM image of NTCDA molecules on graphite showing six tunneling current maxima in a hexagonal arrangement corresponding well to the LUMO calculated for this molecule shown in **b**. Imaging conditions were a sample voltage of −900 meV and a tip current of 45 pA (from ref 122).

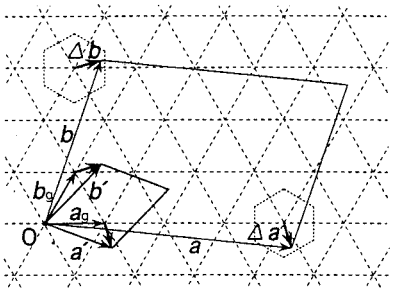

Figure 3-25. Schematic of the surface unit mesh of an organic epitaxial layer (solid lines) with dimensions **a**, **b**, lying on a substrate (dashed lines) with unit mesh parameters, $\mathbf{a}_g$, $\mathbf{b}_g$. Also shown are the "discrepancy vectors", Δa and Δb and reduced lattice vectors, $\mathbf{a}'$ and $\mathbf{b}'$ (from ref 96).

in Figure 3-26, parts a and b, respectively, and have both been observed experimentally (see Figure 3-21 for a 1D pattern[58] resulting from PTCDA on HOPG, and Figure 3-27 for a 1D image[96] due to 1,4-dithioketo-3,6-diphenylpyrrolo[3,4-*c*]pyrrole, or DTPP, on HOPG). With a coordinate transformation, vectors $\Delta\mathbf{a}$ and $\Delta\mathbf{b}$ can be rewritten in terms of the substrate lattice coordinates using

$$\mathbf{a}' = \mathbf{a}_g + \Delta\mathbf{a} = \mathbf{a}_g + p\mathbf{b}_g + q\mathbf{b}_g \quad (3.11a)$$

$$\mathbf{b}' = \mathbf{b}_g + \Delta\mathbf{b} = \mathbf{b}_g + r\mathbf{a}_g + s\mathbf{b}_g \quad (3.11b)$$

where p, q, r, and s are numbers. Clearly, for the special case of $\Delta\mathbf{a}||\Delta\mathbf{b}$, these values are related by $ps - qr = 0$. Referring once again to Figure 3-26, the Moiré fringe unit vectors can be expressed in terms of the transformation coordinates, $\mathbf{a}'$ and $\mathbf{b}'$, by introducing an additional set of numbers, λ_a, and λ_b, which provide the periods of the contrast modulation along these two directions. Hence, the Moiré patterns become periodic (with well-defined "basis" vectors, $\mathbf{a}_M$, $\mathbf{b}_M$) for

$$\Delta\mathbf{a} = (m\mathbf{a}_g + n\mathbf{b}_g)/\lambda_a \quad (3.12a)$$

$$\Delta\mathbf{b} = (m\mathbf{a}_g + n\mathbf{b}_g)/\lambda_b \quad (3.12b)$$

where integers m and n satisfy the relationship $pn - qm = 0$. For a 1D pattern, the equation of the Moiré line intersecting the origin is $\lambda_a y + \lambda_b x = 0$. Furthermore, the existence of these patterns imply that $\Delta\mathbf{a}$ and $\Delta\mathbf{b}$ are parallel to the substrate directions defined by the lines $(n,-m)$, and the end points of the vectors $\mathbf{a}'$ and $\mathbf{b}'$ lie on that same line.

From this treatment, an accurate relationship between the ML film and the substrate lattices can be determined from the existence of the Moiré patterns in the STM image. This has been done by Hoshino and co-workers[43,96,104] for the cases of PTCDA, DPP, and other molecules deposited on HOPG. For PTCDA on HOPG, the results obtained from the Moiré analysis are consistent with earlier, direct measurements where the substrate and film were independently imaged (see Table 4). We note, however, that the Moiré analysis is considerably more accurate, providing angular relationships to perhaps within ±0.5°, whereas direct imaging accuracies typically do not exceed ±2°.

The Moiré fringe patterns therefore provide a striking example of several predicted features of QE growth. For example, the patterns may indicate the presence of MDWs acting to reduce stress due to lattice mismatch (see section 3.3.1.3), although this explanation is difficult to verify given the limited spatial resolution of the STM image. Alternatively, the Moiré pattern may be due to electronic orbital interactions between the film and the substrate, as have been observed by STM for the vdWE growth of transition metal dichalcogenides[69,129] such as $MoSe_2$ on MoS_2. A small angular misalignment of the film produces a large change in the angle of the Moiré pattern. Nevertheless, whether the observed contrast modulation is due to MDWs or due to orbital overlap (i.e., electronic) effects, both explanations are consistent with an incommensurate overlayer having a structure which, to first order, does not depend on the lattice constant of the substrate, but which tends

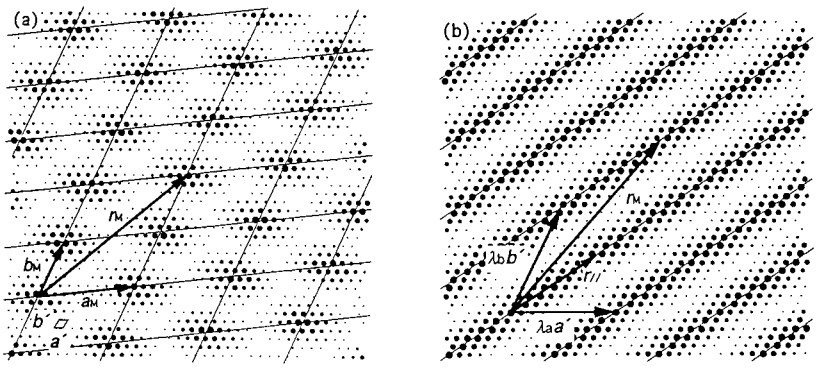

Figure 3-26. Calculated Moiré patterns for two representative cases of an organic layer on a substrate following a point-on-line coincidence behavior. The larger points indicate where the center of a molecule lies closest to a substrate lattice point. The diagrams correspond to (a) $\mathbf{a}' = 1.1\mathbf{a}_g - 0.02\mathbf{b}_g$, $\mathbf{b}' = 0.01\mathbf{a}_g + 1.15\mathbf{b}_g$. The small parallelogram indicates the unit cell of the adsorbed layer, and *aM* and *bM* are the unit cells of the Moiré pattern. (b) $\mathbf{a}' = 1.1\mathbf{a}_g$, $\mathbf{b}' = -0.08\mathbf{a}_g + \mathbf{b}_g$. Here $\mathbf{r}_{||}$ indicates the direction of the one dimensional Moiré line, and λ_a, λ_b are the periods of the 1D contrast modulation along $\mathbf{a}'$ and $\mathbf{b}'$ in the adsorbed layer, respectively (from ref 96).

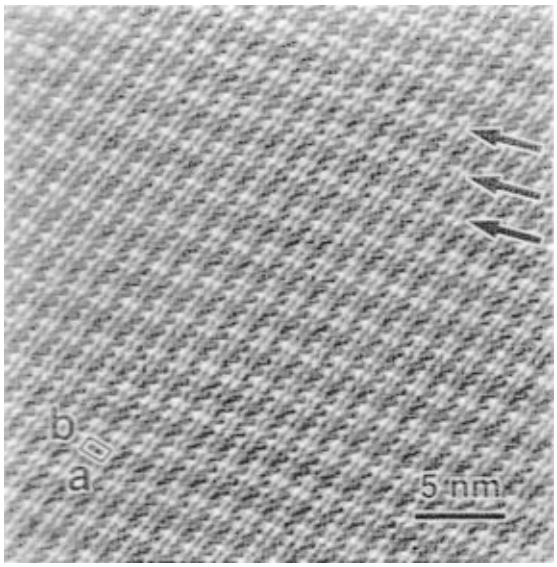

Figure 3-27. A 250 Å × 250 Å filtered STM image of DTPP film deposited on graphite. The parallelogram in the image indicates the surface unit mesh of DTPP. 1D periodic contrast modulation of the Moiré pattern is indicated by the arrows (from ref 96).

to slightly misalign from a symmetry axis in order to reduce strain.[72]

Scanning tunneling microscope images taken over larger fields of view show boundaries between adjacent OMC film domains. For example, an STM image over an area of $(750Å)^2$ near such a domain boundary of PTCDA on HOPG is shown in Figure 3-28a, with a similar image for NTCDA on HOPG shown in Figure 3-28b. In both cases, the angle between the epitaxial molecular axes measured in different grains is always observed to be an integer multiple of $\pi/3$ rad.[1,43,58,122] Although HOPG possesses only 3-fold rotational symmetry, nucleating islands of PTCDA on the surface of graphite are energetically identical at rotations of $\pi/3$ rad.[99] The absence of any other angles in the observed STM images provide additional strong evidence for a preferred angle of orientation between the organic layer and the substrate, which is striking evidence for QE growth. That is, even though the two lattices are incommensurate, they align in a consistent fashion with respect to each other. This observation also points to a fundamental and obvious limitation of quasiepitaxy: If the symmetries of the two lattices are not identical, the deposited layer must contain high-angle grain boundaries between islands which have separately nucleated at different lattice sites. Given that the monoclinic cells characteristic of many crystalline organic semiconductors have only 2-fold symmetry, achieving perfect or near-perfect film order is restricted to growth on substrates with similarly low symmetries.[65,102,119]

Finally, STM has also been used to determine the relative orientation between layers in PTCDA films of from 2 to 3 ML in thickness in order to study the evolution of film growth immediately following nucleation.[58] Figure 3-29 shows detailed images of two sides of a PTCDA step from 1 to 2 ML coverage. The domain orientation is clearly the same in each of the two layers, with the step-edge aligned along the PTCDA *a* axis. The observation of preferential alignment of step-edges along the *a* axis implies an anisotropy of the *intra*layer binding forces which are greater perpendicular to the *b* axis than to the *a* axis, leading to low-energy steps along the [010] direction. That is, the lack of small islands suggests that there is high surface molecular mobility even at room temperature and that molecules have a significantly lower energy when attached to a large domain.

Furthermore, these STM images are consistent with QE ordering. Specifically, growth begins as an ordered overlayer which is not lattice matched to the substrate and continues in a quasi-epitaxial, slightly strained, layer-by-layer manner.[70,73,74,99] In addition, the small angle observed between the PTCDA and the $[11\bar{2}0]$HOPG axis is consistent with calculations which suggest that the overlayer orientation is determined by energy minimization with respect to the substrate. Due to the low energy of the vdW bond, however, the strain induced by the lattice mismatch is not sufficient to strongly distort the overlayer on a scale observable by STM.

3.3.2.2. In Situ Observation of the Evolution of QE Growth. RHEED has proven to be a useful tool for providing a direct observation of the *evolution* of PTCDA film nucleation and subsequent growth from monolayer (ML) to multilayer stacks.[52,100] Use of RHEED as a means for in situ growth has led to a more complete understanding of how highly ordered

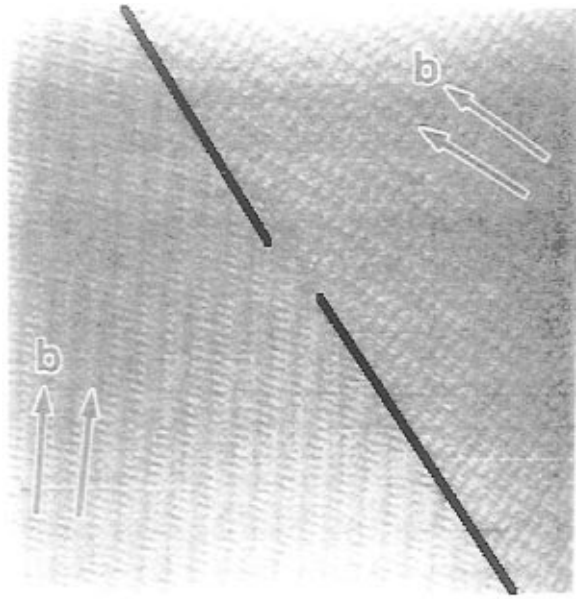

(a)

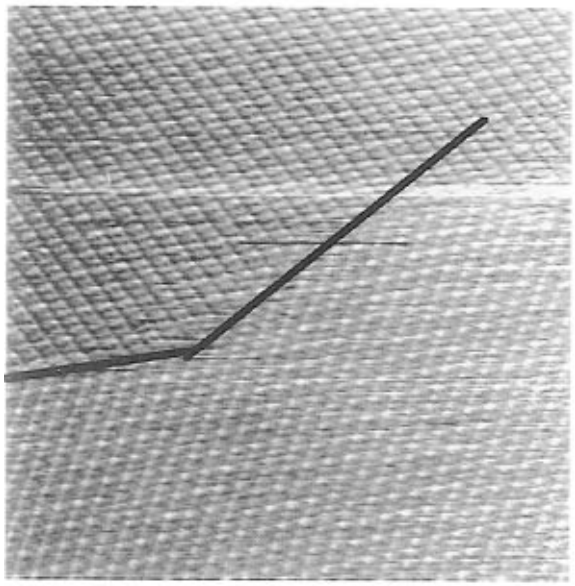

(b)

Figure 3-28. (a) STM image of a domain boundary of PTCDA grown on a graphite lattice. The arrows in each domain indicate the *b* axis of the PTCDA lattice and the direction of the 1D contrast modulation. Experimental conditions are a tip current of 20 pA and a sample voltage of 400 mV (from ref 43). (b) A 500 Å × 500 Å STM image of a domain boundary of NTCDA grown on graphite. The angle between domains is 120° due to the hexagonal symmetry of the substrate. Experimental conditions are a tip current of 18 pA and a sample voltage of −500 mV (from ref 122).

QE and vdWE films can be achieved.[2,3,81,82,91,97,105,130−135] Typically, RHEED patterns are obtained using an ∼8 keV electron beam directed onto the film surface at an angle of from 1° to 2°. Care must be taken to minimize exposure of the thin film to the e beam since extended bombardment by high energy electrons can cause damage to fragile organic molecules such as NTCDA.[100]

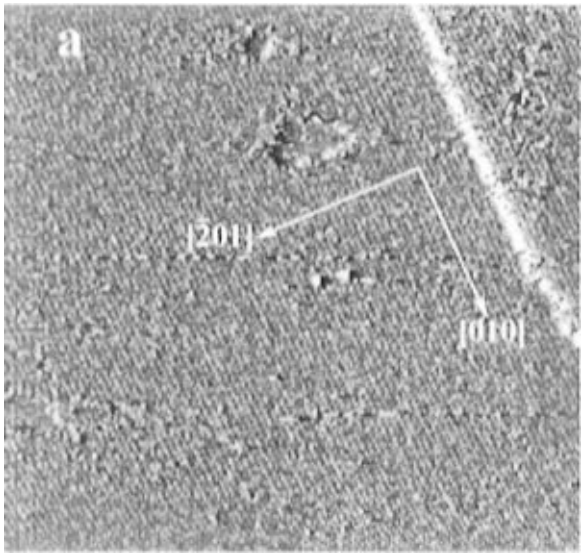

Figure 3-29. STM image of a step up from a monolayer to a second layer of PTCDA deposited on graphite. The striations in the image are due to heightened contrast along the *a* axis of the PTCDA unit cell to which the step is aligned (from ref 58).

A typical series of RHEED patterns[1,52] obtained during a growth sequence of PTCDA on HOPG is shown in Figure 3-30. The RHEED pattern for the bare graphite substrate is shown at the top left. From the measured spacing of the streaks and the beam parameters, a surface unit cell (or surface net) spacing of 2.17 ± 0.04 Å was measured, corresponding to the (220) reflection of graphite. After ∼1 Å of PTCDA is indicated on a crystal microbalance thickness monitor, the graphite streaks fade, and completely vanish after a full ML (∼3 Å) is grown. At a film thickness of 10 Å (∼3 ML), the graphite features are replaced by a set of long, continuous streaks shown in Figure 3-30, indicating that the first few layers of PTCDA are both crystalline and smooth. The dimensions of the surface unit mesh inferred from these patterns are compiled in Table 3 and indicate a somewhat expanded surface reconstruction from the bulk, consistent with both calculations and STM data also provided in the table.

Continuous streaks indicate film flatness (to within a monolayer) over a coherence length of the electron beam.[136,137] While the contact between the beam and the film surface is typically a few millimeters in length, the coherence length is only on the order of a few hundred Ångstroms. Hence, continuous streaks indicate a molecularly smooth surface over at least this distance. STM studies discussed in the previous section have indicated a layer-by-layer growth mode on HOPG covering areas ≥(1000 Å).[2] As will be shown in the following section, this distance in fact exceeds several micrometers for PTCDA growth on Au(111) which has a substantially higher interaction energy (and correspondingly larger ϕ_{inter}'') than for HOPG. Hence, we anticipate that continuous RHEED streaks in the case of PTCDA and NTCDA on graphite are indicative of molecularly flat layers over extremely large distances.

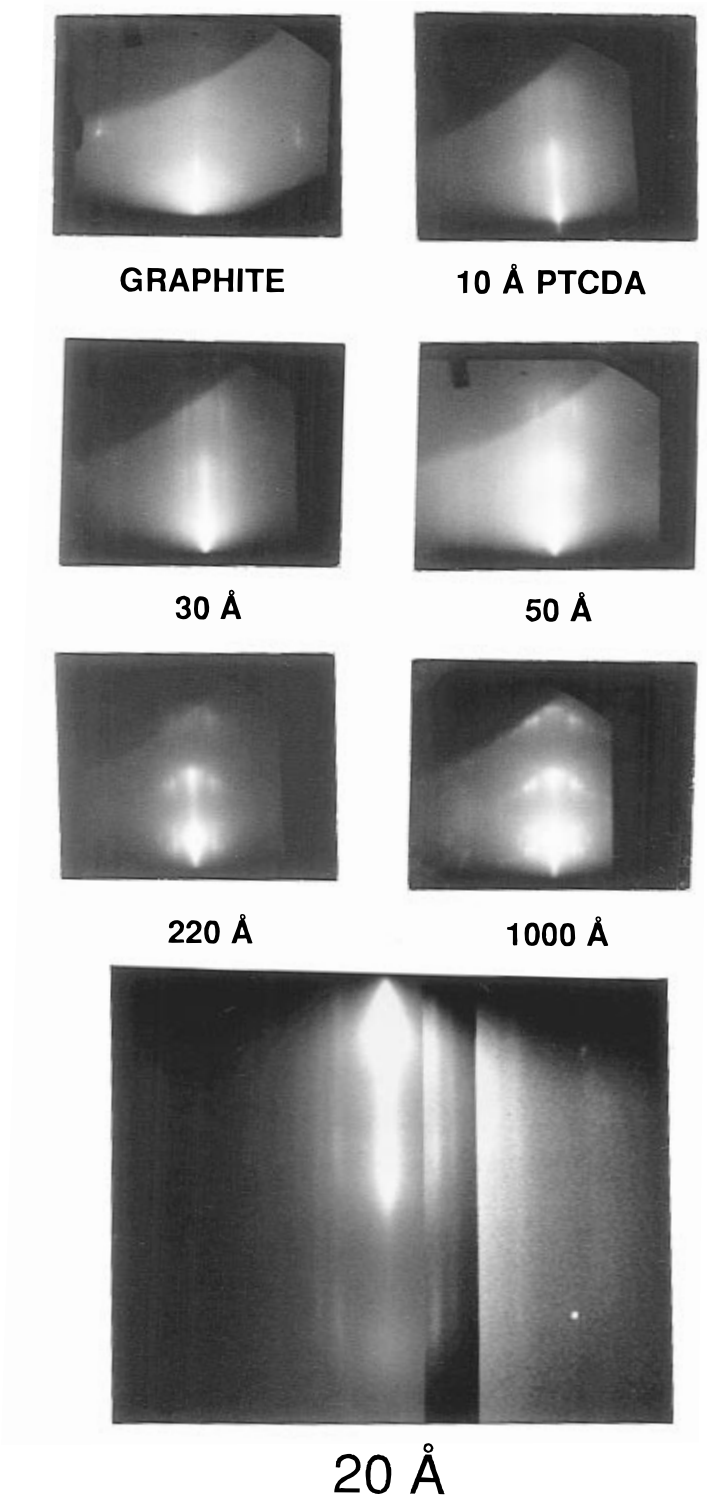

Figure 3-30. A series of RHEED patterns obtained for different thicknesses of PTCDA grown on HOPG (whose pattern is shown in the upper left). The 20 Å film RHEED pattern shown at the bottom has been contrast enhanced to exhibit the detail in the brightest and faintest part of the pattern (from ref 1).

As growth proceeds to 20 and 50 Å, the positions of the intense streaks remain unchanged, although variations in intensity begin to appear at 50 Å (~15 ML) along the length of the streaks, even though the growth rate has remained at 0.5 Å/s. These RHEED patterns show that the crystalline organic layer retains a high degree of surface planarity and order. As the film thickness is increased to 220 Å, and then finally to 1000 Å (Figure 3-30, bottom), the RHEED pattern periodicity remains unchanged from its value for thinner layers, although the continuous streaks have broken into several segments separated by very faint streak remnants. As noted above, this streak segmentation indicates that the film surface has become uneven on a molecular scale, although the crystalline structure remains unchanged.

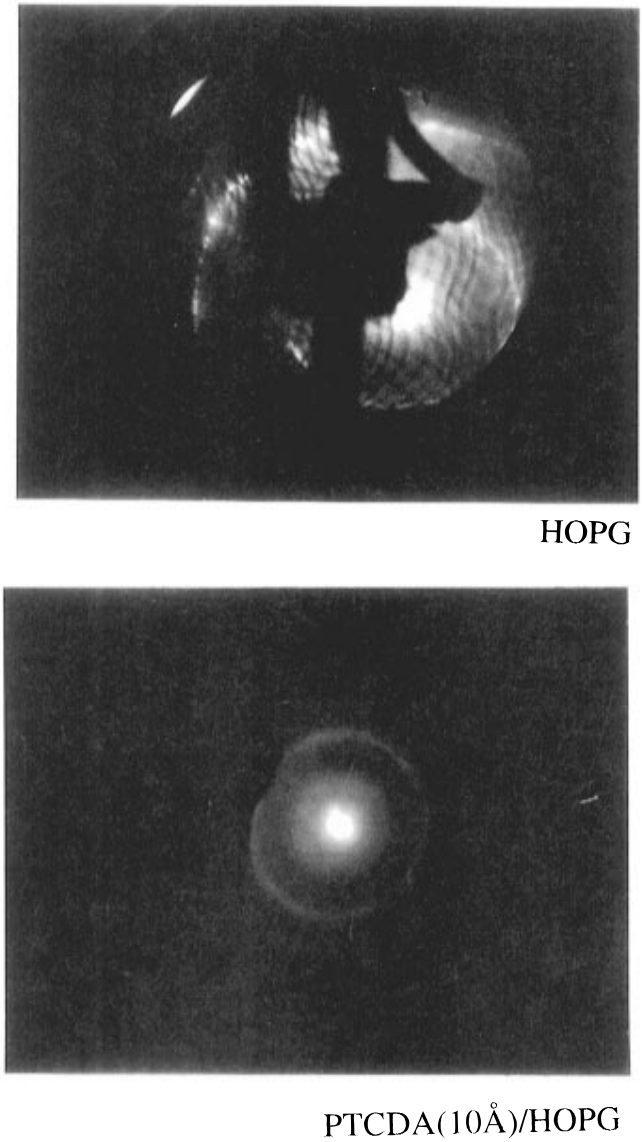

Figure 3-31. Low-energy electron diffraction pattern from (a) a bare HOPG surface and (b) a 50 Å thick PTCDA film grown on HOPG. The electron beam energies were 100 eV for image a and 13 eV for image b (from ref 101).

The *azimuthal* orientation of PTCDA on HOPG has been further examined using low energy (~15 eV) electron diffraction which is performed at near normal electron beam incidence.[101] Figure 3-31, parts a and b, are LEED patterns obtained from bare HOPG and from a 50 Å PTCDA layer grown on a room temperature HOPG surface, respectively. Both exhibit a ring-like structure characteristic of multiply rotated, single-crystal domains distributed on a flat surface. In Figure 3-31a, the radius of the inner-ring corresponds to reflections from lattice planes spaced at 2.46 Å, characteristic of HOPG. The pattern, therefore, results from a superposition of multiple hexagonal grains slightly rotated with respect to each other.

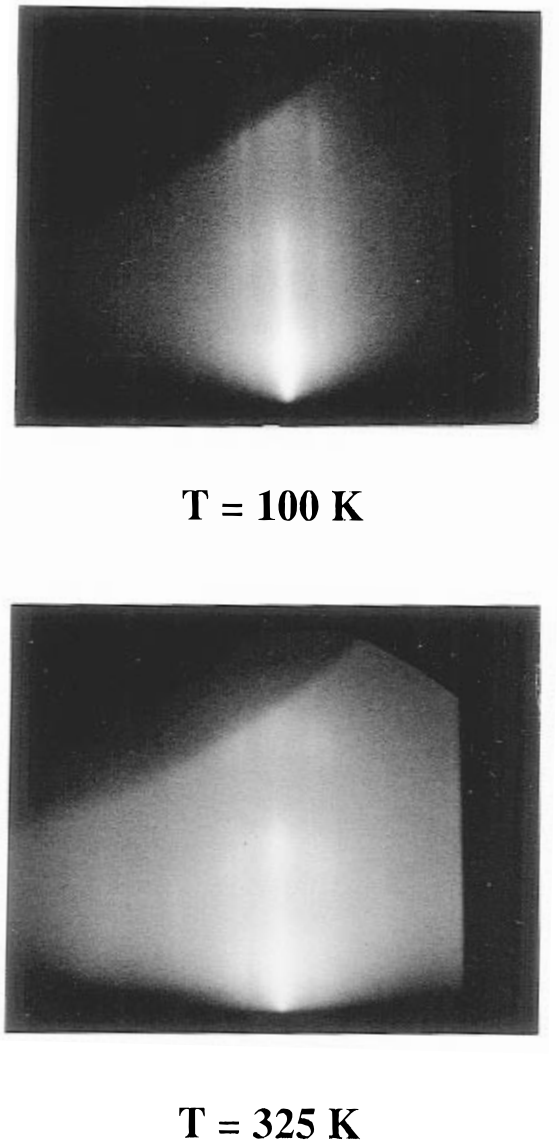

Figure 3-32. RHEED patterns obtained for 30 Å thick PTCDA films grown on a HOPG substrate held at T_{sub} = 100 K (top) and T_{sub} = 325 K (bottom) during growth (from ref 1).

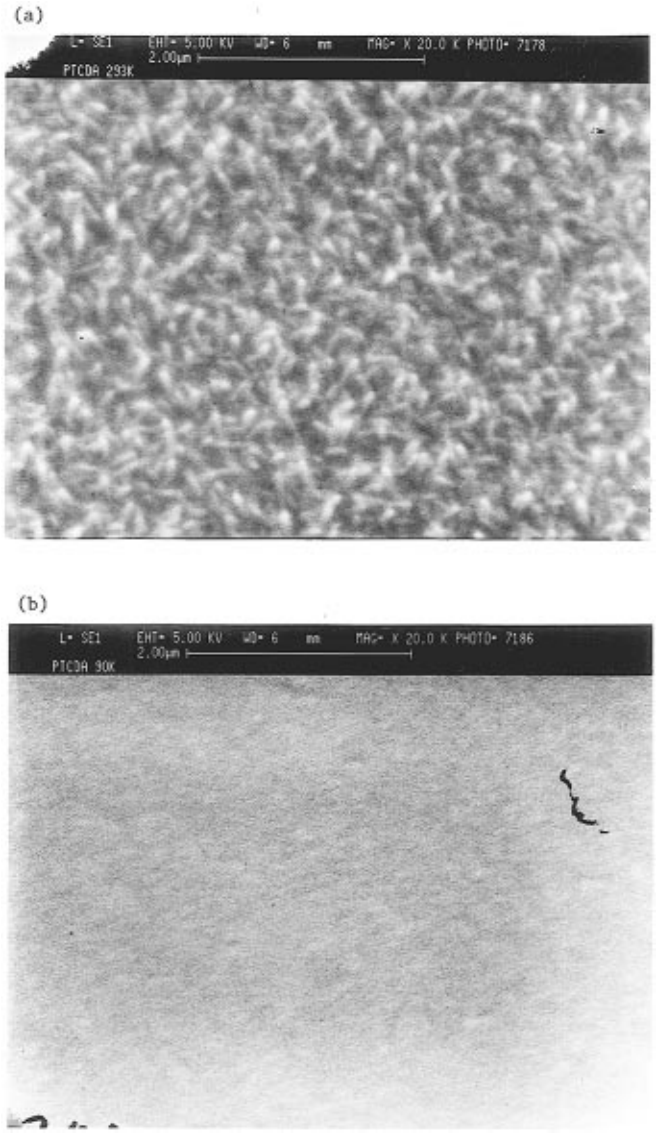

Figure 3-33. Scanning electron microscope images of the surface of a PTCDA film grown on glass at a substrate temperature of (a) T_{sub} = 293 K and (b) T_{sub} = 90 K (from ref 1).

The PTCDA diffraction rings in Figure 3-31b are continuous, indicating the existence of multiple PTCDA domains distributed inside the HOPG domains. As in the case of the RHEED experiments, the dimensions of the PTCDA single-crystal domains (approximately several micrometers) are larger than the LEED coherence length (100−200 Å), as evidenced by the thinness of the diffraction rings.

As discussed in section 3.3.1, QE is a kinetically controlled growth mode, with the resulting structure depending on a balance between thermal energy, bond energy, and rate of deposition. Hence, we anticipate that structure depends critically on the substrate temperature.[45,47,48,138−140] While substrate temperature effects have been examined in detail for PTCDA on Au(111) (see section 3.3.2.3), they have also been studied for PTCDA on HOPG using in situ RHEED.[52] In Figure 3-32, the RHEED patterns for two, 30 Å thick (~9 ML) PTCDA films grown on HOPG substrates temperatures of T_{sub} = 100 K (top image), and at T_{sub} = 325 K (bottom image) are compared. The discontinuous RHEED streaks for growth at elevated temperatures suggests a somewhat less planar PTCDA surface than for the case of the low temperature growth. This difference in surface morphology is also apparent from scanning electron microscope images taken for samples grown under similar conditions to those in Figure 3-32. For example, 0.4 μm thick PTCDA films deposited at room temperature at a rate of 3−5 Å/s consist of a mesh of crystalline filaments approximately 0.2 μm long, as shown in Figure 3-33a. These crystalline filaments are oriented randomly on the surface. For the same films deposited at 90 K (Figure 3-33b), the surface is smooth, and a uniform, more ordered, film is achieved.

Studies of QE growth of single organic layers has also been extended to organic multilayer structures.[1,100,138,139,141−145] As will be shown in section 4, such organic multilayers have recently become the focus of considerable interest due to their numerous device applications,[24−27,146−149] as well as their usefulness in revealing many aspects of fundamental excitations in OMCs which have been inaccessible via

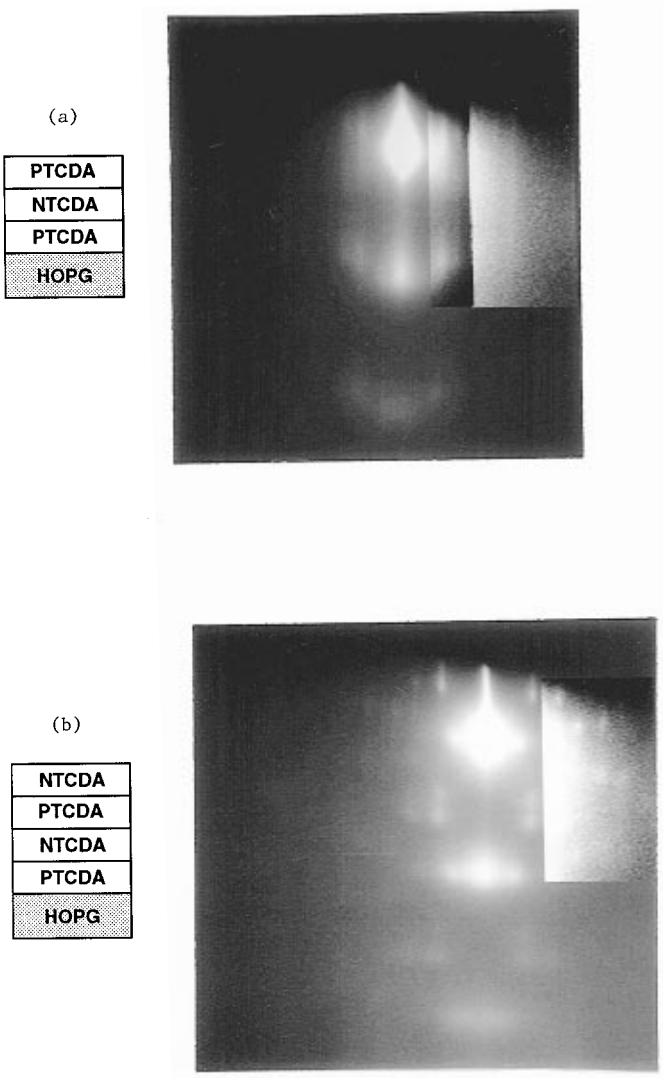

Figure 3-34. RHEED pattern of multilayers of PTCDA and NTCDA grown on a HOPG substrate. (a) PTCDA on NTCDA on PTCDA and (b) NTCDA on PTCDA on NTCDA on PTCDA. All layers are 20 Å thick(from ref 1).

studies of the bulk material properties.[23,24,29,34,150−152] Hence, understanding of structure is integral to revealing the physical properties of these interesting structures. Using RHEED diffraction patterns from alternating thin films of PTCDA on NTCDA, it was found that each layer is crystalline with its own well-defined surface unit cell, regardless of significant lattice mismatch with the underlying layer on which it was deposited.[100]

A typical series of RHEED patterns[1,100] obtained during the growth of a PTCDA/NTCDA alternating layer structure is shown in Figure 3-34. Figure 3-34a shows the pattern resulting from the subsequent deposition of 20 Å (~3 ML) of NTCDA on 20 Å of PTCDA (c.f., Figure 3-30) on HOPG, followed by a second 20 Å thick layer of PTCDA; i.e., a total of 60 Å of organic material. The electron beam was observed to damage the fragile NTCDA layer very rapidly; the streaks fading in only a few seconds. To ensure a good surface for the growth of the second layer of PTCDA, therefore, the first layer of NTCDA was not exposed to the beam. Streaks for the top PTCDA layer are apparent as in the case for a single layer PTCDA film, and are measured within experimental error to be at identical lattice spacings to those measured from the first PTCDA layer deposited on HOPG. Clearly, the second layer of PTCDA remains crystalline and two-dimensional. Furthermore, the surface unit cell of PTCDA grown on NTCDA is observed to be identical to PTCDA grown on HOPG, despite the different lattices of the underlying layers in those two cases. The RHEED pattern from the second layer of PTCDA also indicates that the underlying NTCDA layer is planar, thus resulting in a sharp PTCDA/NTCDA interface.

Figure 3-34b shows the RHEED pattern resulting from the subsequent deposition of a second 20 Å thick layer of NTCDA; a total of 80 Å of organic film material. As in the case of the other layers, the fourth layer of the organic heterostructure exhibits crystalline order, with a different RHEED pattern, and hence surface unit cell, to that of PTCDA. Following the example of PTCDA, some surface reconstruction from the bulk lattice spacings is expected. Assignment of the streaks suggested a reconstructed NTCDA surface unit cell of dimensions 13.0 ± 0.6 Å $\times$ 5.1 ± 0.2 Å.

It is also apparent that the herringbone crystal structure of NTCDA[63,122,153] will result in some diffraction out of the substrate plane even if the layer is completely flat, i.e., the electron beam will provide limited 3D structural information along the NTCDA *a* axis which will manifest itself as diffuse spots in the diffraction image. This represents a RHEED pattern in which spots from the "3D" diffraction and streaks from the "2D" diffraction are expected to appear in the same image. The planarity of the NTCDA layer is inferred by the ability to grow a highly planar layer of PTCDA on its surface.

As an additional example of QE deposition, Figure 3-35a shows the image from a 20 Å thick layer of CuPc grown on top of a 20 Å thick PTCDA film on HOPG.[1] The many orders of diffraction visible in the pattern indicate a crystalline layer of CuPc of unit mesh dimensions of 13.3 ± 1 Å $\times$ 17.5 ± 1 Å. This is reasonably consistent with the "rowlike" phase previously observed in STM images[154,155] of a monolayer of CuPc with a 2D surface unit cell with $b = 17.5 \pm 1$ Å, $c = 15.5 \pm 1$ Å, and angle between the *b* and *c* axes of $\alpha = 98 \pm 1°$.

Figure 3-35b shows the RHEED pattern resulting from the deposition of a further 20 Å of PTCDA on top of the CuPc. The diffuse arcs indicate a layered structure, but no crystalline order within the layers. The CuPc surface is clearly unsuitable for growth of PTCDA due to 3D growth in the CuPc layer, as indicated by the lack of extended streaks in the CuPc RHEED pattern. From these observations, we conclude that although lattice matching is not strictly required, a molecularly flat surface is a necessary condition to achieve QE growth.

This apparent "asymmetry" in growth order has also been observed for VOPc/PTCDA multilayer structures. It was found that,[152] starting with growth

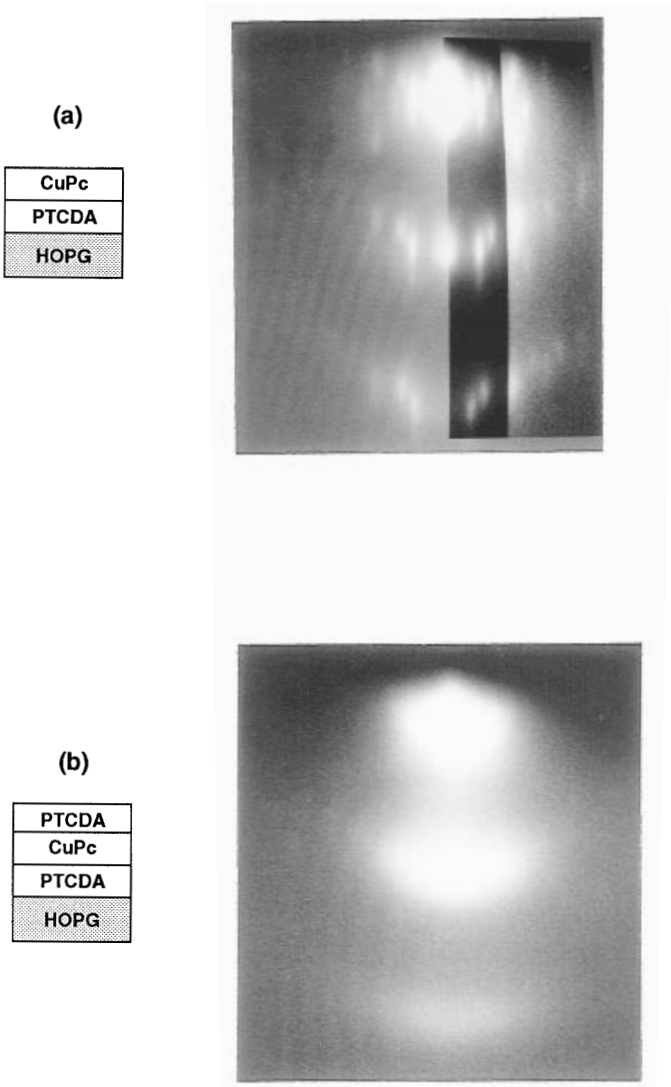

Figure 3-35. RHEED pattern of multilayers of PTCDA and CuPc grown on a HOPG substrate: (a) CuPc on PTCDA and (b) PTCDA on CuPc on PTCDA. All layers are 20 Å thick. Note that b indicates amorphous growth of the top layer (from ref 1).

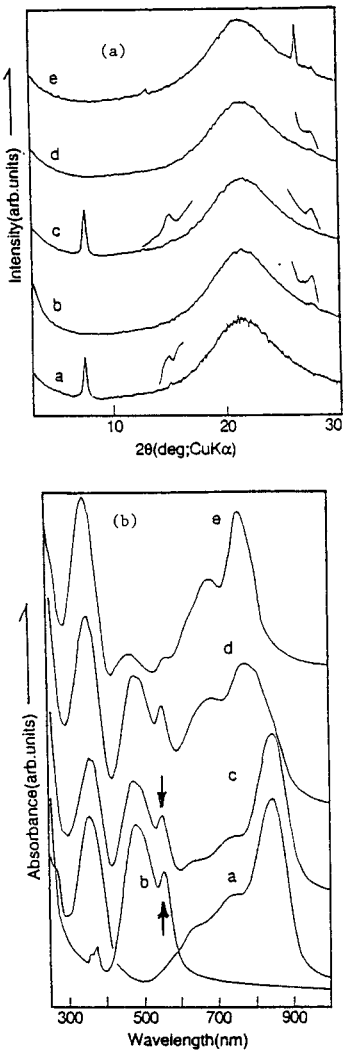

Figure 3-36. (a) X-ray diffraction data for films deposited at room temperature: (curve a) 15 nm VOPc, (curve b) 15 nm PTCDA, (curve c) 15 nm PTCDA/15 nm VOPc, (curve d) 15 nm VOPc/15 nm PTCDA bilayer, (curve e) 105 nm VOPc/15 nm PTCDA bilayer. (b) Optical absorption spectra for the same films shown in part a (from ref 152).

on a quartz substrate maintained at room temperature, layers of PTCDA grown on VOPc exhibited considerable stacking order, whereas the opposite combination (VOPc on PTCDA) tended to result in the amorphous growth of VOPc on an otherwise ordered PTCDA layer. This is apparent from the X-ray diffraction patterns shown in Figure 3-36a. Curve a is for a 15 nm VOPc film, whereas b is for a PTCDA film of similar thickness. The broad peak at $2\theta = 21°$ is the background from the substrate. For samples consisting of 15 nm of PTCDA grown on 15 nm of VOPc (curve c), peaks are due to stacking of phase II VOPc molecules along the (010) direction (at $\theta = 7.54°$). However, when the deposition order is reversed, the (010) peak disappears indicating significant film disorder, similar to the case of PTCDA grown on CuPc.[1]

The structural differences between the films also influences their exciton spectrum, as shown in Figure 3-36b. Small blue shifts of the PTCDA peak (marked by an arrow in curves b and c) are observed when this material is deposited on the surface of VOPc. Otherwise, the spectra of both PTCDA and VOPc remain unchanged from their bulk absorption. As will be shown in section 4, this small blue shift is probably a result of quantum size effects observed in ultrathin PTCDA layers. In contrast to these relatively minor effects, there are considerable differences in the absorption spectra of VOPc depending on whether PTCDA is deposited as the first or the second layer. These shifts, particularly in curves d and e, where the VOPc lies on the surface of the PTCDA layer, are strongly indicative of considerable film disorder, consistent with the X-ray data. From these crystallographic and absorption data, we conclude that the structure of the VOPc depends critically on the order of growth. This "interface asymmetry" has been widely observed in the growth of III−V heterojunctions,[156,157] and is attributed to the different rates of atomic diffusion (i.e., P−As exchange is considerably more active at InP/InGaAs interfaces than at InGaAs/InP heterojunctions[158]). This observation for Pc/PTCDA interfaces also indicates that intermolecular diffusion can play a role in determining film structure. It is a direct result of the bonding energy at the VOPc/PTCDA interface

Table 5. GIXD Diffraction Peak Positions and Widths (From Ref 73)

(h,k,l)	$Q_{\|\|}$ (Å^{-1})	$\Delta Q_{\|\|}$ (Å^{-1})	Q_z (Å^{-1})	ϕ (deg)
(0,1,2)	0.8230 ± 0.0005	0.015 ± 0.0006	0.367 ± 0.003	0.05 ± 0.06
(0,1,2)[a]	0.8213 ± 0.0004	0.0115 ± 0.0006	0.372 ± 0.004	17.19 ± 0.05
(0,2,4)	1.641 ± 0.001	0.0186 ± 0.0017	0.74[b]	0.3 ± 0.4
(0,1,1)[a]	0.6064 ± 0.0005	0.012 ± 0.001	0.2087 ± 0.005	23.39 ± 0.07
(0,1,1)	0.6065 ± 0.0005	0.0139 ± 0.001	0.209[b]	19.64 ± 0.06
(1,0,2)	0 ± 0.003		1.949 ± 0.0006	

[a] These diffraction peaks come from different sublattices, whose orientation differs only by multiple of 60° with respect to the substrate. [b] The exact Q_z position of these peaks was not measured.

and the substrate temperature during growth which promotes molecular diffusion along the surface. Such diffusion processes play even a greater role in disrupting the flatness of organic/inorganic semiconductor and organic/metal superlattices.[144,145,159,160] That is, the large heat of condensation associated with inorganic materials may induce significant interface diffusion prohibiting the realization of molecular abruptness in these cases.

3.3.2.3. Strain Evolution in QE Systems: PTCDA on Au(111). An interesting feature of QE is that the strained layer does not necessarily relax into its equilibrium (bulk) crystal habit even after several hundreds, or even thousands of Ångstroms have been grown. To develop a complete picture of the nature of these thin films, nucleation, growth, and strain of PTCDA on Au(111) have been studied[73,74,140] using glancing incidence X-ray diffraction (GIXD). Here, Au(111) serves as an ideal substrate on which to study strained QE films since the PTCDA/Au(111) bond energy is higher than for the relatively unstrained case of PTCDA on HOPG. However, the binding energy is not so high that lattice-matched epitaxy occurs. As we have shown in section 3.2, epitaxy results in the buildup of strain energy, leading to amorphous or polycrystalline growth after only a few monolayers are deposited. Even though the substrate-molecule interactions in PTCDA/Au(111) are sufficiently strong to introduce strain into the thin film, they are not strong enough to lift the characteristic $23 \times \sqrt{3}$ reconstruction of the substrate surface. This indicates that PTCDA molecules are physisorbed onto Au(111) via vdW interactions and that there is relatively little charge exchange across the interface.

Studies of PTCDA on Au(111) have provided the most comprehensive and precise picture of organic thin film growth by either epitaxial or quasi-epitaxial modes. For these studies,[73,111] PTCDA films were grown on Au(111) substrates by OMBD at a rate of 0.1−0.2 Å/s. The growth was performed in the same chamber which housed the X-ray diffractometer (with an X-ray wavelength of $\lambda = 1.285$ Å) attached to the National Synchrotron Light Source at Brookhaven National Laboratories.

The 2D structure of PTCDA/Au(111) grown at room temperature can be determined from the Bragg peak positions as a function of momentum transfer parallel to the surface, $Q_{||}$, and the azimuthal orientation, ϕ, of the diffraction peaks with respect to the Au surface Bragg rods. The spacing and stacking of the 2D PTCDA lamella were determined by the magnitude of the momentum transfer perpendicular to the surface plane, Q_z. Table 5 summarizes the GIXD data taken from the diffraction spectra in Figure 3-37. The lattice spacings are consistent with those obtained from RHEED[52,73] provided in Table 3.

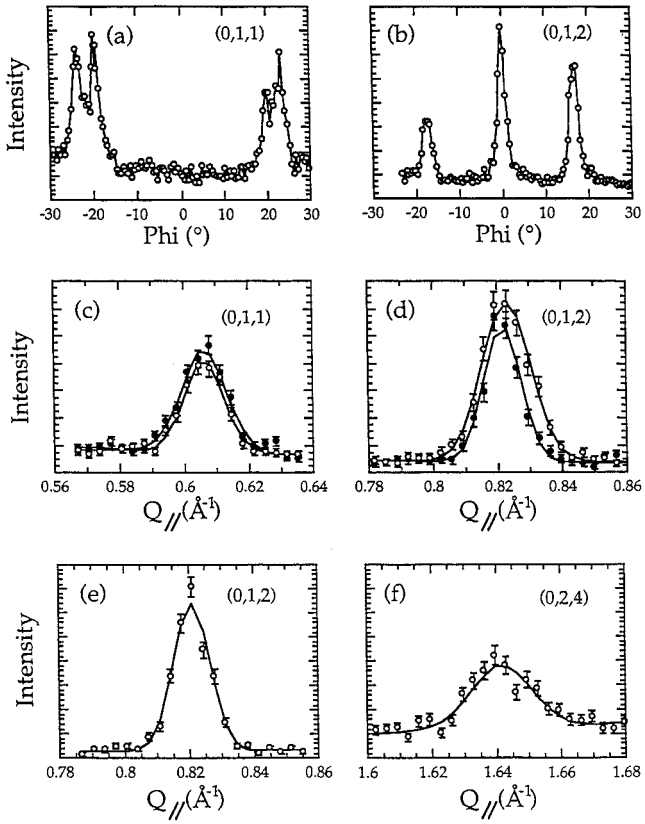

Figure 3-37. GIXD data vs momentum transfer parallel to the substrate, $Q_{||}$, and the azimuthal orientation, ϕ. Azimuthal scan of the (a) (011) diffraction peak and (b) (012) peak. (c) Radial scan of the (011) diffraction peak for $\phi = 23.4°$ (closed circles) and $\phi = 19.6°$ (open circles). (d) Radial scan of the (012) diffraction peak for $\phi = 0°$ (closed circles) and $\phi = 17.2°$ (open circles). (e and f) : High-resolution radial scans through the (012) and (024) peaks, respectively ($\phi = 17.2°$). The solid lines in c−f are fits to the data (using a Gaussian and a linear background), while the lines in a and b simply connect the data points. The resolution was $\Delta Q_{||} = 0.009$ Å^{-1} and $\Delta Q_z = 0.18$ Å^{-1}. In a, c, and f, the intensities are multiplied by a factor of 2 (from ref 73).

In Figure 3-37, parts a and b, we show the *azimuthal* dependence of the (011) and (012) diffraction peak intensities. The film/substrate azimuthal orientation is defined by the alignment of the (012) diffraction peak along the azimuth containing the Au surface diffraction at $\phi = 0$ (see Figure 3-37b). The Bragg spacing of the (012) plane is incommensurate by 2% with respect to the nearest multiple of the substrate lattice spacing.

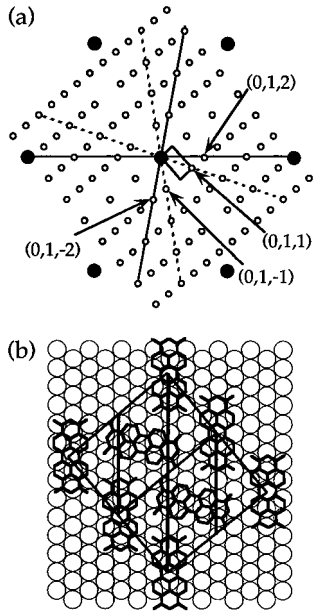

Figure 3-38. Schematic of the (a) reciprocal, and (b) real space, incommensurate structure of the PTCDA film on Au(111), with the unit cell noted in each. In a, the open (closed) spots indicate the positions of the PTCDA (Au surface) diffraction conditions as a function of $Q_{||}$. The dashed and solid lines in a denote the azimuths in which the (0 1 ±1) and (0 1 ±2) peaks are found, respectively. Note that the azimuth containing the (012) diffraction peak is aligned with the Au surface diffraction peak (solid spot). The vertical solid lines in b denote the (012) Bragg planes (from ref 73).

A PTCDA film having a particular orientation (with its symmetry equivalent orientations separated by 60°) exhibits both (012) and (01$\bar{2}$) Bragg peaks, which have an azimuthal separation ($\Delta\phi$) determined by the lattice spacings (a,b), of the PTCDA unit cell given by[111]

$$\Delta\phi = \phi_{0\bar{1}2} - \phi_{01\bar{2}} = 2\tan^{-1}(2b^*/a^*) = 2\tan^{-1}(2a/b) \quad (3.13)$$

where a^* and b^* are the reciprocal lattice vectors corresponding to the (010) and (001) Bragg peaks, respectively. For an unstrained PTCDA lattice, a/b = 0.6007 (see Table 2) corresponding to a peak separation of $\Delta\phi$ = 100.5°. Given the 6-fold symmetry of the top Au layer, this results in an azimuthal separation of 19.5°. Therefore, an unstrained PTCDA film aligned along ϕ = 0° would exhibit (012) Bragg peaks at ϕ = 0°, and (01$\bar{2}$) Bragg peaks at ϕ = 19.5° and 40.5° (as well as at symmetry equivalent orientations separated by 60°), as observed in Figure 3-37. Consequently, while the (012) and (01$\bar{2}$) Bragg peaks are equivalent with respect to the film, they have inequivalent orientations with respect to the Au substrate (see Figure 3-38).

Note that some samples show a larger number of peaks than in Figure 3-37. For example, in some cases,[111] $\Delta\phi$ = 15.2 ± 0.3°, which is significantly smaller than $\Delta\phi$ = 19.5° observed in Figure 3-37. The number of inequivalent film orientations apparently depends upon the detailed characteristics of the Au substrate and growth conditions.[73,111] Some of the variability between Au substrates may be due to variations in their surfaces, such as the magnitude and direction of the surface miscut.

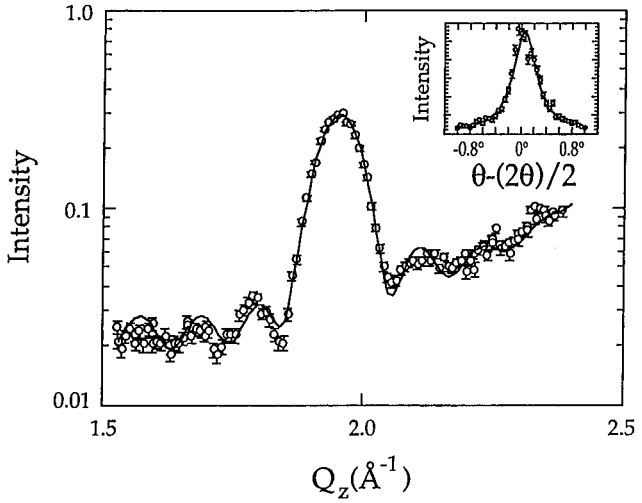

Figure 3-39. Radial scan data as a function of Q_z of the (102) Bragg peak corresponding to the lamella spacing. The slowly increasing "background" is due to the Au surface truncation rod. The inset shows the rocking curve of the (102) peak, showing alignment with the surface normal of the Au substrate. Resolution was $\Delta Q_{||}$ = 0.09 Å^{-1}, and ΔQ_z = 0.009 Å^{-1} (from ref 73).

From eq 3.13, the aspect ratio (a/b) of the PTCDA unit cell can be determined. For example, $\Delta\phi$ = 15.2 ± 0.3° corresponds to an aspect ratio of a/b = 0.649 ± 0.003. Defining strain as $\delta = ([a/b]_{film} - [a/b]_{bulk})/([a/b]_{bulk})$, then δ = 8%. In the context of inorganic growth, this is an extreme degree of strain. Similarly, the aspect ratio for the ϕ = 30° domain is found to be a/b = 0.615 ± 0.003, corresponding to a strain of δ = 2.4%. The dependence of the lattice strain upon the azimuthal orientation of incommensurate domains with respect to the *same* substrate is a demonstration of the QE nature of this film system.

The X-ray diffraction intensity near the (102) PTCDA Bragg peak as a function of the momentum transfer perpendicular to the surface, Q_z, is shown in Figure 3-39. The interplanar stacking distance inferred from the diffraction peak position is d_{102} = 3.22 ± 0.01 Å, consistent with bulk values for this molecule. A rocking scan through this peak (inset, Figure 3-39) indicates that the (102) direction is aligned with the Au(111) surface normal to within <0.1°, implying that the PTCDA molecules lie flat on the Au(111) surface. The existence of fringes on either side of the PTCDA Bragg peak implies that the film has a well-defined crystalline thickness over the ~1 mm^2 area of the X-ray beam spot, while the rapid attenuation of these fringes suggests some degree of film roughness. In contrast, films grown at higher substrate temperatures do not show these oscillations, due to complete 3D islanding. Both of these features will be discussed further below.

While the (102) peak width, ΔQ, determines the average thickness, L, of the films ($\Delta Q = 2\pi/L$), the shape of this diffraction peak (in particular, near the shoulders) provides a measure of the disorder in the film thickness. These data are described by an incoherent superposition of the scattering from a uniform, 17 ML PTCDA film and the Au surface, although the lack of complete destructive interference

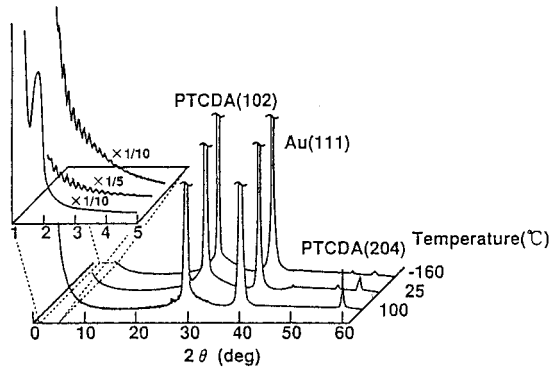

Figure 3-40. X-ray diffraction patterns of PTCDA films on Au(111)-coated $LaSF_6$ substrates deposited at different substrate temperatures. The oscillations at small θ indicate considerable film flatness (from ref 140).

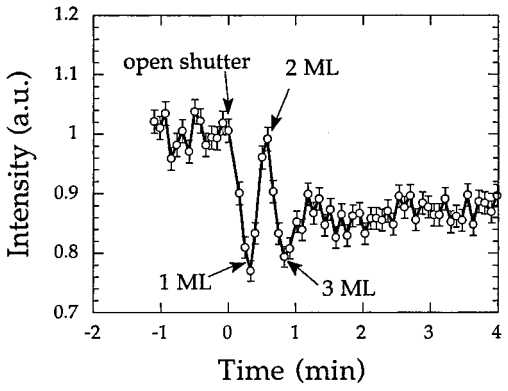

Figure 3-41. Time dependence of the X-ray specular reflectivity at the PTCDA anti-Bragg point. Oscillations in the intensity are clearly observed after the shutter is opened at $t = 0$, and the coverages corresponding to each successive monolayer are indicated. Film growth conditions are 4.7 ML/min at $T_{sub} = 75$ °C (from ref 74).

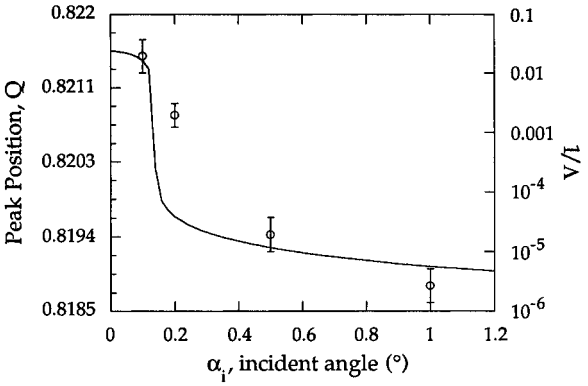

Figure 3-42. Plot of the peak radial position, Q, of the (012) Bragg peak for PTCDA on Au(111) as a function of the incident angle, α. Also shown is the inverse penetration depth, 1/Λ (1/Å), as a function of α. The shift in the Bragg peak position appears when the incident angle is decreased below the critical angle, α_c (i.e.,, when the penetration depth becomes smaller than the film thickness) (from ref 73).

suggests a limited roughness of the layers. The film surface has been examined[111] using atomic force microscopy (AFM). An average domain size of ~500 nm is observed, with layer-by-layer growth within the domains resulting in nearly monolayer flat PTCDA surfaces. This domain size is consistent with the dimensions of the Au substrate domains, suggesting that nucleation at substrate domain step edges may determine surface morphology in strained QE systems.[119] The PTCDA domains are separated by narrow valleys, indicating that strain relief is occurring via a Stranski−Krastonov growth mechanism.

Similar results, indicating even smoother PTCDA surfaces were found by Fuchigami et al.[140] In Figure 3-40 are shown the X-ray diffraction patterns obtained as a function of growth temperature. As in the work of Fenter,[111] the PTCDA (102) planes are found to lie parallel to the Au(111) substrate surface, and hence only the (102) and (204) reflections are visible in these spectra. This conclusion was verified by measuring the relative intensities of the out-of-plane and in-plane molecular vibrations using Raman scattering. There are very pronounced oscillations in the GIXD diffraction patterns as the X-ray glancing angle, θ, approaches 0°. These oscillations, only apparent for samples grown at $T_{sub} < 100$ °C, indicate the existence of very flat organic film surfaces when grown under nonequilibrium (i.e., QE) conditions. This improved order and surface flatness is consistent with electron micrographs obtained for these same samples.[140] This study showed that the total average molecular orientation improved considerably as substrate temperature was reduced.

The evolution of growth was quantified using the intensity dependence of the specular X-ray reflection as a function of film thickness.[74] Figure 3-41 shows the specular beam intensity obtained during PTCDA growth at a rate of 4.2 ML/min, and a substrate temperature of 75 °C. These intensity oscillations result from interference between the PTCDA and Au Bragg truncation rods,[161] and coincide with the onset of film growth on the Au(111) surface. The oscillations are present for 3−4 ML, after which they cease, giving way to an average intensity due to a constant level of coherence between X-rays reflected from the substrate and film surfaces. This suggests the presence of a ~3 ML thick "wetting layer" occurs under this elevated substrate temperature, followed by further growth of islands which eventually occupy most of the substrate surface area. As the film thickness increases, however, the regions between the layers fill in, resulting in relatively flat film surfaces.

In contrast to PTCDA on Au(111), studies of thick (0.4 μm) PTCDA films grown under nonequilibrium conditions (i.e., high growth rates or low substrate temperatures) exhibit extremely flat surfaces without any evidence for islanding when grown on amorphous substrates.[1] Furthermore, studies of ~300 Å thick PTCDA films on oxidized silicon substrates[162] or on HOPG[52] as well as some reports[140] of PTCDA on Au(111) did not find any evidence for island nucleation. This suggests that the appearance of islands depends critically on details of the substrate surface and the strength of the organic film/substrate interaction.[72]

To determine the mechanism for strain relaxation on Au(111) substrates, the PTCDA lattice dimensions as a function of depth in thicker films have also been examined.[73] In Figure 3-42, the (012) peak position of an 1100 Å thick film on Au(111) is plotted as a function of the X-ray beam incident angle. Since X-rays exhibit total external reflection, the penetra-

tion depth, $\lambda \approx 40$ Å, of X-rays is greatly reduced at incident angles below the critical angle of $\alpha_c = 0.16°$ (for PTCDA at $\lambda = 1.285$ Å), and hence varying this angle provides the depth dependence of the film lattice parameters. These data show a small monotonic shift in radial peak position, Q, as a function of incident angle, indicating some minor strain relaxation in the top ~40 Å of the film. However, this relaxation is only $\Delta \sim 0.2\%$, whereas in this case the film itself is strained by at least 3.8% from its bulk (equilibrium) structure. Hence, QE films have the unique property of growing into nonequilibrium structures determined, to some degree, by the mismatch of the adlayer lattice to that of the substrate. These nonequilibrium structures do not relax, but rather the strain is *frozen in* to a structure established by the first or second ML. In effect, the substrate acts as a template, generating a "new" crystal structure depending on the details of the substrate and the strength of the substrate/organic thin film interaction.

Strain, as observed for PTCDA/Au(111), cannot build up indefinitely without generating a high misfit dislocation density. One mechanism suggested in section 3.3.1.3 for strain relief is via generation of MDWs, which result in periodic variations in one of the several unit cell degrees of freedom. In incommensurate systems, adjacent unit cells within the first ML are in slightly different (but spatially correlated) positions with respect to the substrate lattice. Hence, the degree of perturbation within a particular unit cell to minimize energy will also be spatially correlated to neighboring cells. This spatial correlation should then give rise to a periodic (but small) variation in the positions of atoms within the surface net. These periodic variations are a manifestation of MDWs in large molecular systems as compared to monatomic inert gas atom systems where the lattice positions themselves are periodically displaced.[116]

While there is as yet no conclusive evidence for such MDWs in QE films, Fenter and co-workers[73] observed that the (012) PTCDA diffraction peak position was 0.12% larger than the $(01\bar{2})$ peak, and the width of (012) peak was also 30% larger than that of the $(01\bar{2})$ peak (see Figure 3-37c−f). The broadening mechanism is not fully understood, however, the (0 1 ±2) Bragg planes differ only in their orientation with respect to the Au(111) substrate (Figure 3-37d), so these structural asymmetries may reflect the perturbation of the PTCDA lattice due to its interaction with the Au substrate. This broadening is consistent with a MDW since it is strongest near the (012) direction which lies along the Au symmetry axis, and is weakest at large angles with respect to this alignment direction, where the $(01\bar{2})$ and $(01\bar{1})$ peaks are found at ~77° and ~83° relative to the (012) peak orientation, respectively.

From the foregoing discussion, it is apparent that QE is a kinetically controlled growth mode resulting in strained, nonequilibrium structures. To explore the conditions leading to a transition between QE and equilibrium epitaxial structures, both the substrate temperature and deposition rate were varied, and correlated with the resulting PTCDA on Au(111)

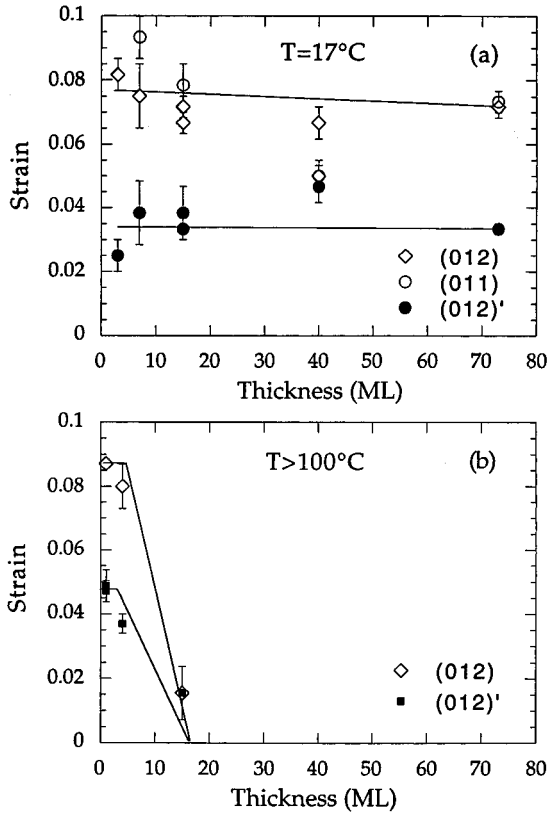

Figure 3-43. Lattice strain, defined as the fractional deviation of a/b from bulk, as a function of PTCDA film thickness plotted for (a) the NEQ regime (with a deposition rate of ~4 ML/min), and (b) the EQ regime (with the 4.4 and 17.3 ML films grown at $T_{sub} = 170$ °C, while the 1 ML film was grown at 100 °C at a growth rate of 0.8 ML/min). In a, the strain for the (012) domain is derived independently through the separation of both the (0 1 ±2) and (0 1 ±1) Bragg peaks (from ref 111).

structure.[111] It was found that there are two well-defined growth regimes: QE is achieved under nonequilibrium conditions (NEQ) of high growth rate and/or low substrate temperature, whereas unstrained epitaxy is achieved at equilibrium (EQ) with low growth rates and/or high substrate temperature. In Figure 3-43a, lattice strain is a plotted vs film thickness for films grown under NEQ conditions. Although the magnitude of δ is large, there is no apparent decrease of the strain even for film thicknesses of up to ~70 ML (>200 Å). This implies either that the critical thickness of the PTCDA film is very large or that the kinetic barrier to relieve the strain is sufficiently high that the strain is frozen-in at room temperature. The lack of strain relief is consistent with studies of PTCDA/NTCDA multilayers grown under similar conditions. There it was found[163] that the exciton−phonon coupling, a property expected to be extremely sensitive to strain, did not change as the PTCDA layer thickness was increased from 10 to 500 Å (see Figure 4-15).

The evolution of the film surface roughness is shown in Figure 3-44 for films grown at both high ($T_{sub} \geq 100$ °C, or EQ) and low ($T_{sub} = 17$ °C, or NEQ) substrate temperatures, with a significant difference in morphology for growth under these two conditions. While NEQ films indicate a slow, monotonic evolution of the surface width, films grown at high temperature exhibit a much stronger dependence of the surface

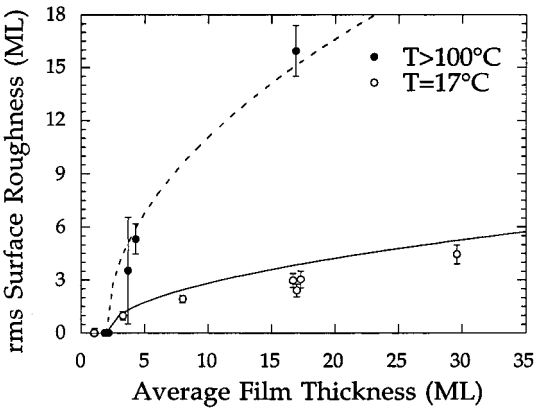

Figure 3-44. Root mean square surface roughness of PTCDA films on Au(111), for NEQ films (open circles, grown at $T_{sub} = 17$ °C) and EQ films (closed circles, grown at $T_{sub} \geq 100$ °C). The solid line follows evolution of film roughness for random deposition offset by 2 ML to take into account the wetting layer. The dashed line is a guide for the eye (from ref 111).

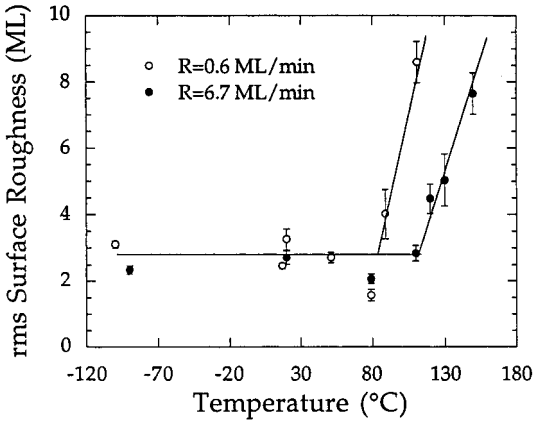

Figure 3-45. Root mean square surface roughness of PTCDA films on Au(111) as a function of substrate temperature for two different growth rates (R). Note that the cross-over temperature between the NEQ and EQ regimes, as indicated by the sharp increase in surface roughness with T_{sub}, increases substantially with growth rate (from ref 111).

width for thicknesses >2 ML. The dramatic increase of the surface roughness (particularly under equilibrium conditions), indicates that incomplete wetting occurs at high temperatures. In Figure 3-43b, the strain for this epitaxial film is also shown vs thickness. These data indicate that strain in films of a few monolayer thickness is similar to that found for all of the nonequilibrium (NEQ) films, although the strain is completely relieved for EQ films thicker than 10 ML. Hence, the changes in film morphology and lattice strain are both due to strain relief in the thick, epitaxial (EQ) films. The solid curve in Figure 3-44 is a calculation assuming growth occurs by the random arrival of molecules with no surface diffusion. This model somewhat overestimates the surface roughness in the EQ regime, where a small roughness of ~4 ML (rms) is observed for 30 ML thick films, indicating the existence of a residual surface diffusion at 17 °C.

To understand the transition between the NEQ and EQ regimes, in Figure 3-45, the evolution of the surface roughness is plotted as a function of the substrate temperature at two different growth rates.[111] This plot shows that the transition is associated with an abrupt increase in the film surface width due to formation of large 3D islands as the film evolves towards the equilibrium, incomplete wetting morphology. Also, at low growth rates, the roughness in the QE regime is indistinguishable from that found at higher rates, although the transition temperature boundary between EQ and NEQ regimes decreases by ~40 °C when the growth rate is decreased by an order of magnitude. The transition between regimes (and hence surface morphologies) results from a critical balance between adsorption and diffusion processes, while the film morphology is independent of the growth rate and substrate temperature within the NEQ (quasi-epitaxial, or kinetic) regime.

The increased order of NEQ films is also apparent from the X-ray pole figure plots for the more weakly bonded system of PTCDA on glass shown in Figure 3-46 for two different growth rates,[65] with the substrate held at room temperature in both cases. The pole figure measures the crystalline texture of the sample by plotting the intensity of the intermolecular, (102) Bragg reflection as a function of polar angle with respect to the film normal. Note that AFM measurements of glass substrates similar to those used for the experiment in Figure 3-46 indicate a very smooth surface[138] with an rms roughness of <0.3 nm. From Figure 3-46, rapid, nonequilibrium growth results in a very high degree of order, with the (102) direction tilted at 11° from the substrate normal. In contrast, at lower deposition rates, the film is randomly oriented. These data are consistent with the PTCDA/Au(111) results discussed above.

Returning to Figure 3-45, we note that films grown at NEQ do not undergo a transition to the EQ morphology when annealed for several hours at $T_{sub} \approx 100$ °C. Therefore, the transition to 3D morphology appears to be due to details of the growth dynamics, suggesting that the NEQ and EQ regimes are not simply different film phases separated by a thermal activation barrier. This is an extremely significant finding since it explains the apparently contradictory observation that high order and flat surfaces are routinely observed at substrates cooled to very low (−100 °C) temperatures, a value well below that which is expected to supply sufficient thermal energy for molecular diffusion to occur. In the absence of diffusion, only amorphous growth would normally be anticipated. However, these results suggest that a residual transient surface mobility of the PTCDA molecules is achieved upon adsorption when the latent heat of molecular surface condensation is converted to kinetic energy upon adsorption. That is, a 3D morphology results when the molecular diffusion length (at elevated temperatures) is larger than the average mesa size. In contrast, when the diffusion length is smaller than the size of a typical mesa (at NEQ), the mesa maintains the molecularly flat terraces observed by AFM.

These observations lead to a clear picture of the thermodynamic conditions leading to NEQ, or quasi-epitaxial growth: on one hand QE films may exhibit

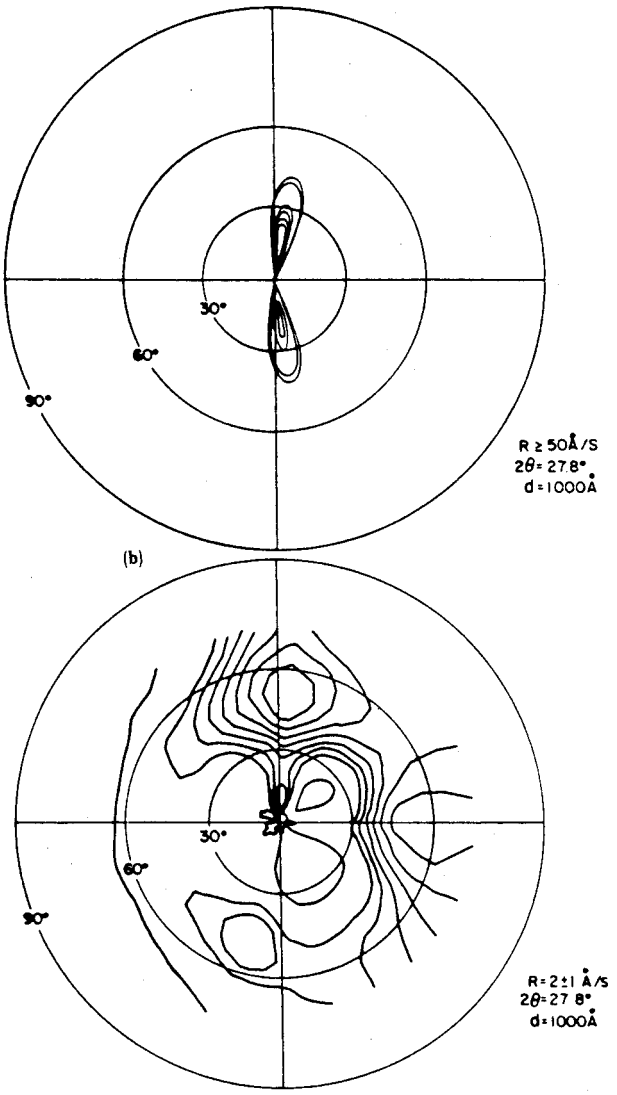

Figure 3-46. X-ray pole figure for the (102) PTCDA Bragg reflection for (a) deposition on glass at a rate of ≥50 Å/s and (b) deposition on glass at a rate of 2 ± 1 Å/s. For a, each contour represents at 10% change in X-ray peak intensity, whereas in b, each contour represents at 1% change (from ref 65).

a significant lattice strain. On the other hand, there is only a weak film/substrate interaction as evidenced by the 2D azimuthal disorder. These two observations can be, at least qualitatively, reconciled by noting that organic materials are generally much "softer" than inorganic materials. For a given distortion, the strain energy per layer is comparatively smaller for organic films as compared to mismatched inorganic films. Furthermore, this strain can be reduced by taking advantage of the many degrees of freedom with the molecular unit cell. Both observations are consistent with a relatively weak film−substrate interaction.

3.3.2.4. Quasi-Epitaxial Growth of PTCDA on Semiconductor Surfaces. As discussed in the previous section, very strong bonding between the substrate and the thin film can result in epitaxial growth, and ultimately in considerable disorder when the film thickness is increased to greater than its critical value, d_c. This transition between epitaxy and QE has recently been clearly illustrated by growth of PTCDA on Se-passivated, and on as-grown GaAs(100) surfaces as studied by low-energy electron diffraction (LEED).[101] In the case of the (2×4)-c(2×8) and c(4×4) reconstructed as-grown surfaces, the dangling Ga bonds generate a high density of states within the bandgap at the surface of GaAs. These free orbitals form bonds to the PTCDA molecules which, therefore, are not free to nucleate into an ordered layer. Since in this case, $\phi_{intra}'' \ll \phi_{inter}''$, amorphous or extremely fine-grained polycrystalline films are grown. On the other hand, a (2×1) reconstructed Se-passivated GaAs does not have any midgap states since all surface orbitals are filled. Hence, the PTCDA surface bonding is considerably weaker (leading to $\phi_{intra}'' \gg \phi_{inter}''$), resulting in the growth of an ordered, incommensurate QE layer with 4-fold azimuthal symmetry with respect to the substrate Se dimer layer.

The experiments in which this "transition" from amorphous to QE growth on a GaAs surface was studied were carried out in a dual-chamber UHV system consisting of a MBE chamber for the growth of GaAs, interconnected with a surface analysis chamber equipped with LEED, and a PTCDA effusion cell. For the Se experiments, 2000 Å thick layers of undoped GaAs were first grown on (100) GaAs substrates at $T_{sub} \approx 550$ °C. The c(4×4) and (2×4)-c(2×8) reconstructions were obtained by annealing at 250 and 450 °C, respectively. Se passivation was achieved by in situ deposition on the as-grown GaAs surface. The PTCDA film thickness ranged between 3 and 150 Å for these studies, with T_{sub} kept at room temperature during deposition. These relatively rapid deposition rates on room temperature or cooled substrates result in oriented, although strained, incommensurate PTCDA QE films.[73]

The LEED patterns in Figure 3-47, parts a and b, were obtained from the (2×4)-c(2×8) GaAs(100) surface and from a 50-Å PTCDA overlayer grown on that substrate, respectively. The (2×4)-c(2×8) pattern exhibits streaks in the [011] direction, due to a combination of point defects, steps, and displacements leading to kinks in the As dimer row structure. The poorly defined LEED pattern from the PTCDA layer grown on this surface (Figure 3-47b) indicates that the 2D order is very poor in the plane parallel to the (100) GaAs surface. However, the presence of the sharp specular spot suggests regular stacking of the molecules in the direction perpendicular to the GaAs surface, characteristic of PTCDA films grown under almost all conditions.[54]

There are significant differences between growth on reconstructed GaAs surfaces and those passivated using a Se layer as clearly shown for a 50 Å PTCDA layer grown on Se-GaAs in Figure 3-48. The LEED pattern in Figure 3-48a displays the (2×1) symmetry of the passivated surface. Previous studies of Se-passivated GaAs surfaces[164−166] indicate that the substrate surface is characterized by 1ML of Se dimers bound to second-layer Ga atoms, a layer of Se atoms replacing As atoms in the third layer, and 0.5 ML of Ga vacancies in the fourth layer. The Se dangling bonds (DB) are filled, eliminating states within the GaAs bandgap, thus reducing the substrate/molecular bond energy.

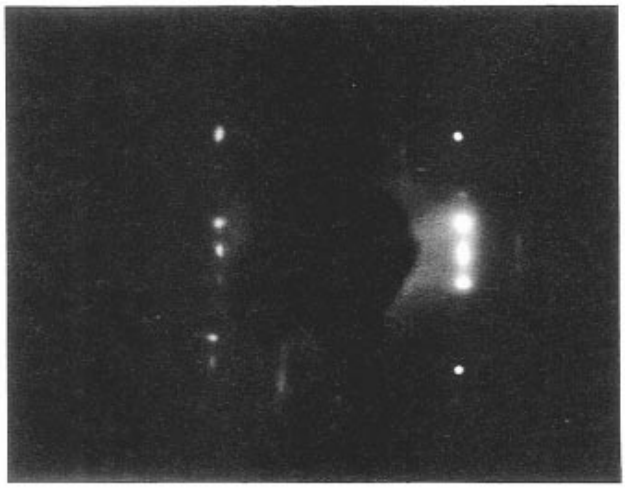

GaAs (2x4)-c(2x8)

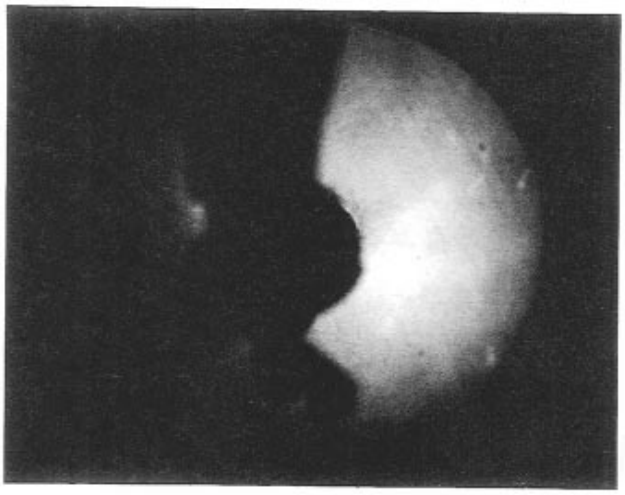

PTCDA(50Å)/GaAs (2x4)-c(2x8)

Figure 3-47. Low-energy electron diffraction (LEED) pattern from a (a) (2×4)-c(2×8) reconstructed GaAs surface; and (b) 50 Å PTCDA film grown on top of that surface. Beam energies are 65 eV for a and 13 eV for b (from ref 101).

The Se passivation of the GaAs surface leads to a remarkable improvement of the 2D order in the PTCDA thin film as compared to unpassivated surfaces. The LEED pattern of Figure 3-48b exhibits sharp spots indicative of long-range order at the PTCDA surface, and a 2-fold symmetry with respect to the substrate. The symmetry of the PTCDA pattern is identical for monolayer films (3−10 Å), thin films (30−200 Å), and thick films (∼500 Å), suggesting that the PTCDA film grows from the onset in a stable structure, consistent with results for PTCDA on Au(111). Considering the large lattice mismatch between PTCDA and GaAs, this indicates that the interface interaction is sufficiently weak to allow the film to relax to near its bulk unit cell structure, a necessary condition for QE.[99] Indeed, quantitative analysis of the PTCDA/Se-GaAs diffraction pattern suggests a unit mesh dimension which closely corresponds to the (102) plane of the bulk crystal. The *c* axis of the cell is rotated by ∼40° with respect to (but incommensurate with) the direction of the Se

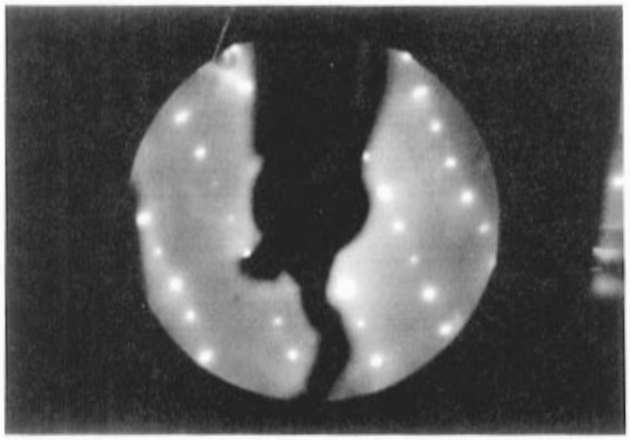

Se/GaAs-(2x1)

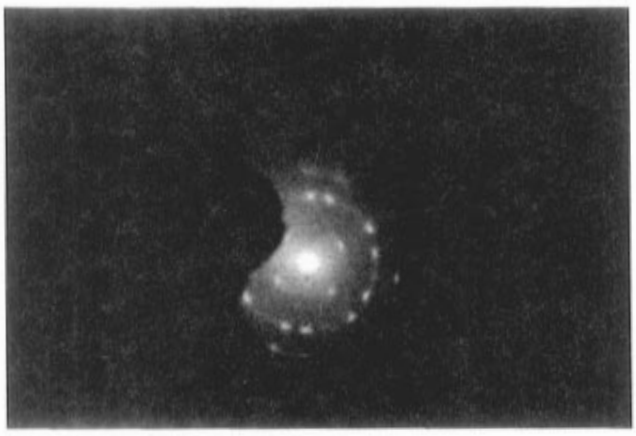

PTCDA(50Å)/Se/GaAs

Figure 3-48. Low-energy electron diffraction (LEED) pattern from a (a) (2×1) Se-passivated GaAs(100) surface; and (b) 50 Å PTCDA film grown on top of that surface. Beam energies are 83 eV for a and 13 eV for b (from ref 101).

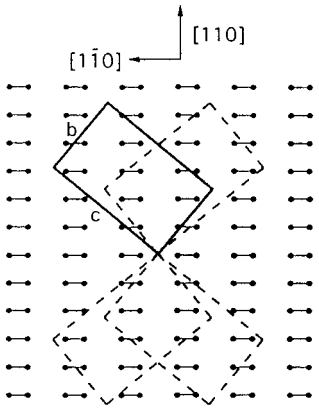

Figure 3-49. Proposed orientation of the PTCDA lattice with respect to the Se dimers on the GaAs surface. There are two orientations possible, as indicated by the solid and dashed lines (from ref 101).

dimers, as shown in Figure 3-49. Since the Se-passivated substrate reconstruction remains observable by LEED following the initial deposition of PTCDA,[101] as was also found for PTCDA on Au(111),

the interface interaction is weaker than the interatomic binding energies within the GaAs crystal and its surface.

The 2D order of a PTCDA layer deposited on the c(4×4) reconstructed GaAs surface is found to be considerably improved from that of the layer grown on the (2×4)-c(2×8) surface.[101] The symmetry of the diffraction pattern is similar to that of the layer grown on the Se-passivated surface, indicating that the structures of the unit cells in the two cases are also similar. In contrast to growth on the Se-GaAs surface, the diffraction spots are elongated and somewhat diffuse, suggesting a reduced single-crystal domain size. Nevertheless, the observation that large single-crystal PTCDA domains can be grown on such "nonpassivated" surfaces is somewhat unexpected.

To understand the driving forces leading to ordered growth on these different GaAs surface reconstructions, Hirose et al.[101] noted that the film−substrate interaction is determined by coupling between molecular energy levels and the substrate surfaces states,[167] as shown in Figure 3-50. The ionization energy of the condensed phase of PTCDA is 6.4 ± 0.15 eV vs 5.5 ± 0.1 eV for GaAs. Assuming that charge transfer at the PTCDA/GaAs interface is small, consistent with the lack of perturbation of the as-grown GaAs LEED pattern after PTCDA deposition, these energies suggest that the PTCDA HOMO lies below the GaAs valance-band maximum.[101]

The interactions suggested for PTCDA/Se-passivation GaAs are shown in Figure 3-50a. The passivated substrate surface has no significant density of states in the band gap.[166] Thus the molecule−substrate coupling must occur via states that overlap with the valence or conduction bands. However, coupling between the PTCDA HOMO and the filled DB (interaction 2, Figure 3-50a) should be small since both levels are doubly occupied. Furthermore, coupling between the HOMO and empty states in the conduction band should also be weak (interaction 1) given the large energy difference between these levels. As on H-terminated Si(111)[53,91] and Se-terminated GaAs(111),[81] the high degree of structural perfection of the substrate surface added to a weak interaction of the molecules with the inert surface produces the necessary conditions for QE. The passivation of the substrate eliminates the chemically active sites derived from unsaturated dangling bonds. The elimination of these sites weakens the molecule−surface interaction, leading to the required QE condition, viz.: $\phi_{inter}'' \ll \phi_{intra}''$. A well-defined orientation of the unit cells with respect to the substrate is observed, and corresponds to a minimum in the interface interaction energy.

The situation for (2×4)-c(2×8) and c(4×4) reconstructed GaAs surfaces is considerably different. While no intrinsic surface states exist deep in the gap,[168,169] the density of extrinsic surface defects for the (2×4)-c(2×8) surface is large (Figure 3−50, parts b and c). The strong interaction between PTCDA molecules and this surface was attributed in part to coupling between the HOMO and empty and partially filled gap states (interaction 1, Figure 3-50b). Thus, the lack of 2D order in the PTCDA layer is due

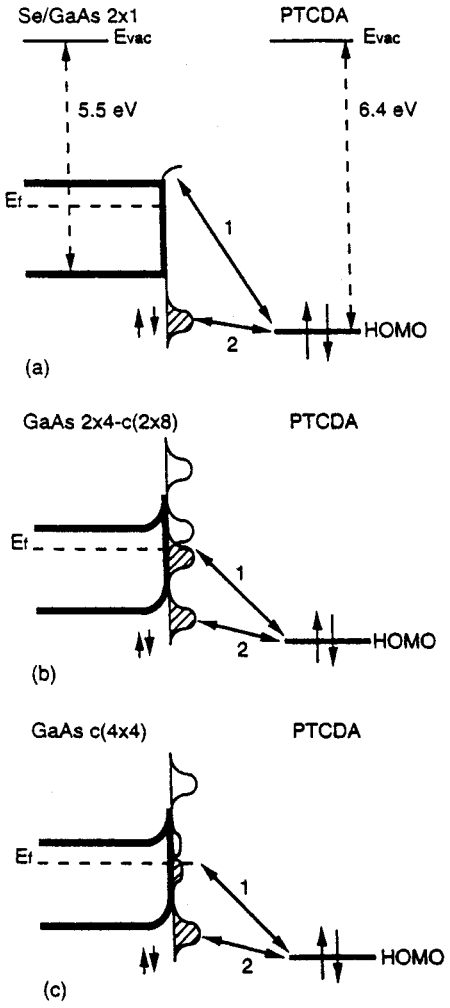

Figure 3-50. Schematic band diagrams showing the proposed interactions (indicated by the solid, numbered arrows) between PTCDA molecules and (a) the (2×1) Se-passivated, (b) the (2×4)-c(2×8), and (c) the c(4×4) GaAs(100) surfaces. The PTCDA highest occupied molecular orbital (HOMO) is fully occupied, and the filled (cross-hatched curved regions) and empty (unfilled curved regions) state distributions at the GaAs surface are also schematically indicated to lie within the GaAs band gap (indicated by the bold lines). Ionization energies for PTCDA and GaAs are shown in a by the dashed lines. The n-type GaAs Fermi energy, E_f, is also shown (from ref 101).

to interactions of the molecule energy levels with these extrinsic and intrinsic states associated with large ϕ_{inter}''.

The weaker c(4×4) GaAs/PTCDA interaction is due, to some extent, to the higher structural quality of the c(4×4) surface,[101] leading to a reduction in defect-induced gap states. This weaker interaction leads to the observed improvement in film order, as compared with the more highly defected (2×4)-c(2×8) GaAs surface.

A second organic/semiconductor system studied[1] was PTCDA on (100)Si substrates with a very thin surface layer of native SiO_2. The presence of the oxide results in a reduction in the substrate/film bond energy, thereby allowing for ordered film growth to occur. Figure 3-51a shows the X-ray diffraction patterns for 4000 Å thick PTCDA films deposited on (100)Si wafers at T_{sub} = 90 and 293 K, and Figure 3-51b shows the diffraction patterns for PTCDA films

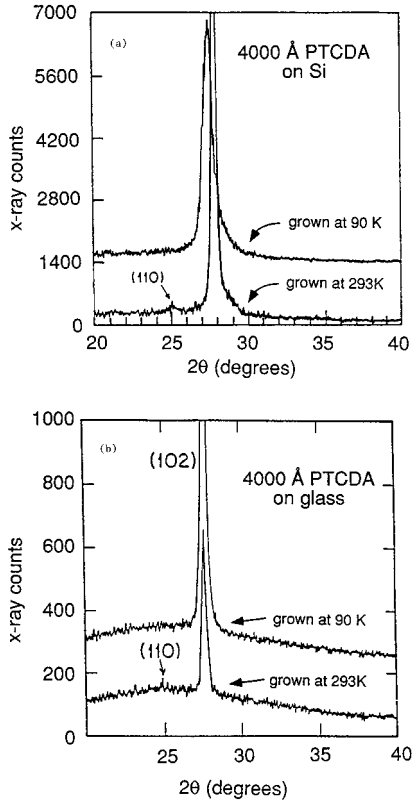

Figure 3-51. X-ray diffraction patterns for PTCDA deposited (a) on Si and (b) on glass. The substrate temperature used during growth is indicated in the figure. Spectra in each figure displaced along the vertical axis for clarity. The strong central peak corresponds to the (102) reflection in PTCDA (from ref 1).

deposited under the same conditions on glass substrates. The background intensity observed in Figure 3-51b is due to X-ray scattering from the glass substrates. For the samples deposited at 293 K, in addition to the prominent (102) diffraction peak, a small (110) peak is also present, indicating the polycrystalline nature of the films. The (110) peak is observed in all samples deposited at room temperature or above, regardless of the substrate materials used. On the other hand, only one diffraction peak is observed for films deposited on substrates held at 90 K, indicative of significantly improved stacking order of the PTCDA films. Using either Si or glass substrates, the (102) peak intensity of the samples deposited at low temperature is about three times that of the samples deposited at room temperature. The strong diffraction intensity provides evidence for improved structural ordering in the samples deposited at low temperature.

As in the case of PTCDA on Au(111), residual strain is developed in organic films deposited at low temperatures, as observed by diffraction peak broadening. The full width at half maximum of the (102) diffraction peak for the samples deposited at low temperature is about twice that of the samples deposited at room temperature. Also, there is a slight peak shift in the sample deposited on the Si substrate corresponding to strain-induced increase in the intermolecular planar spacing of 0.026 Å. Such a shift is not present in the sample deposited on glass substrates.

When films are deposited at low substrate temperature (T_{sub} < 120 K) or high deposition rate (>50 Å/s), it is apparent that molecules form stacks characterized by long-range order, with disorder resulting from deposition at elevated temperatures or low deposition rates. This ordering can also be inferred from the electrical and dielectric properties of organic−inorganic heterojunctions[1,37,38,65] (OI-HJ). For example, it has been shown that the current (I) vs voltage (V) characteristics of OI-HJ devices at low current density (J) can be modeled using:[37,65,170,171]

$$J = J_{so}\{\exp(-qV_d/nkT) - 1\} \qquad (3.14)$$

which describes thermionic emission current over the barrier at the OI interface. Here, V_d is the voltage drop across the heterointerface and is given by $V_d = V_a - V_o$ where V_a is the applied voltage and V_o is the voltage drop across the organic thin film. At low forward bias where J is small, then $V_d \approx V_a$. Also, q is the electronic charge, and $n \approx 2$ is the ideality factor. As has been shown previously (also, see section 5.1), J_{so} is the saturation current which is a function of the OI-HJ energy barrier height.[171]

At high forward currents, carrier transport is dominated by space-charge effects in the organic film, in which case $V_o = V_a - V_d$, and

$$J = (9/8)\epsilon\mu V_o^2/d^3 \qquad (3.15)$$

where μ is the majority carrier mobility in the organic thin film, ϵ is the permittivity, and d is the film thickness. Hence, by measuring $J(V)$ at high current densities where $J(V) \approx V^2$, the steady state carrier mobility can be determined. By correlating mobility with film growth conditions, the degree of stacking order can be inferred since μ is ultimately determined by the π-bond overlap between molecules in the stack.

A typical PTCDA/Si OI diode structure is shown in the inset of Figure 3-52. Fabrication of such test structures has been described previously.[37,63] Figure 3-52 shows the forward biased $I-V$ characteristics for OI-HJ devices with 2000 Å thick PTCDA films deposited at different T_{sub}. For the sample with T_{sub} = 90 K, the forward current has an exponential dependence on voltage due to charge diffusion across the OI heterointerface in the low bias voltage regime and then exhibits a roll off in current due to space-charge-limited current.[171] For the sample with PTCDA deposited at T_{sub} = 443 K, the forward current has no exponential dependence for the entire voltage range studied, indicating a low carrier mobility. Fits to the $I-V$ data using analyses of the dark current discussed above are also shown by the solid lines in Figure 3-52. From these fits, the carrier mobility in the organic films decreases from 0.16 cm^2/(V s) for the sample deposited at 90 K to 2 × 10^{-4} cm^2/(V s) for the sample deposited at 443 K, indicating a corresponding reduction in stacking order. Note that the highest film mobilities obtained for PTCDA are ~1 cm^2/(V s) measured[65] for PTCDA deposited on Si(100) substrates held at room temperature at a rate of >10 Å/s (see Figure 2-3a)—corresponding to non-equilibrium conditions expected to result in QE ordering.[111]

The mobility measurements have been explained in terms of the thin-film structural properties. For

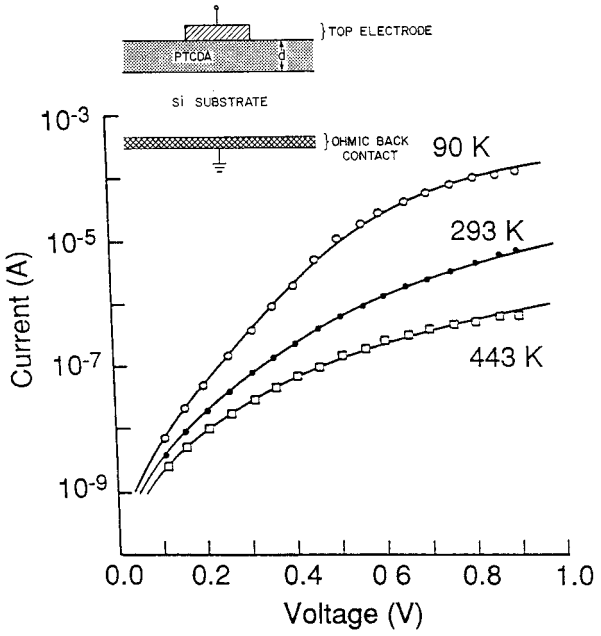

Figure 3-52. Forward-biased current−voltage characteristics for In/2000 Å PTCDA/p-Si devices (with a top contact area of 5.5×10^{-4} cm^2) where the organic layer was deposited at different temperatures indicated. Solid lines are fits to the data using theory described in text. Inset: Structure of a typical OI-HJ device (from ref 63).

PTCDA films deposited on glass or SiO_2 at low temperatures or high deposition rates,[65] molecules form stacks tilted at an angle of 11° from the substrate normal. Due to the large π-orbital overlap along the stacking axis, charge (primarily holes[37,171−174] for PTCDA) injected into the organic films are transported along the stacking direction, giving rise to the high mobilities observed. In contrast, films deposited at elevated temperatures exhibit randomly oriented molecular stacks. This disorder results in a reduction in orbital overlap between molecules stacked normal to the substrate plane, thereby reducing the carrier mobility in this direction by almost 4 orders of magnitude in some cases. While inferences about the stacking order can be made from these mobility measurements, they provide no information about the order within the plane of the film where the mobility is extremely small due to negligible in-plane π-system overlap between molecules.

In addition to the substrate temperature dependence on the carrier mobility in organic films, the mobility also has a thickness dependence for films deposited at elevated temperatures (293 and 443 K).[1] Except for the films deposited at 90 K, as the thickness of the film increases, the mobility decreases. Such a thickness dependence is also apparent in the surface morphologies of PTCDA films deposited at room temperature.[1] For example, for a 500 Å thick sample deposited at room temperature, no surface texture is observed, indicating structural ordering which accounts for the high carrier mobility. On the other hand, for a 2000 Å thick film deposited at room temperature, considerable surface texture is observed, indicating the polycrystalline nature of the films which give rise to a reduction in carrier mobility.

One consequence of the anisotropic crystal structure in QE PTCDA films is that the films exhibit enormous anisotropies in both their conductive and dielectric properties. For example, the in-plane conductivity of PTCDA films is found to be at least 6 orders of magnitude lower than the conductivity perpendicular to the film plane. It is has also been found that the dielectric properties of highly ordered films have a considerable degree of anisotropy along different crystalline directions.[140,175] Provided that there is crystalline alignment throughout the QE film, the anisotropy in the dielectric constant (ϵ) between directions perpendicular and parallel to the thin film plane (and hence approximately perpendicular and parallel to the molecular stacking axis) follows: $(\epsilon_\perp - 1)/(\epsilon_{||} - 1) \approx d^2/L^2 \approx 0.22$ due to anistropies in the dipole oscillator strength. Here, $d = 3.21$ Å is the intermolecular planar stacking distance, and L is the length of the π system along the perylene molecular core. This approximation assumes that m* is isotropic (which has been found to be reasonable[176,177]) and that the dipole moment is due to a completely delocallized charge distribution in the extended π system. Experimentally, it has been found[175] that $(\epsilon_\perp - 1)/(\epsilon_{||} - 1) = 0.26$ for PTCDA, which is close to the value predicted by the above model.

Furthermore, the index of refraction measured[175] at a wavelength of $\lambda = 1.064$ μm in the direction perpendicular to the substrate plane is $n_\perp = 1.36 \pm 0.01$, whereas parallel to the plane, $n_{||} = 2.017 \pm 0.005$, resulting in an index difference (or birefringence) of $\Delta n = 0.66$. This structural order is maintained along waveguides approaching 1 cm in length, as determined by a lack of rotation of the optical polarization vector propagating in such guides grown on amorphous Teflon[22] or polyimide buffer layers.[102] Such remarkable long-range alignment is possibly initiated by ordered nucleation of PTCDA molecules at the edges of the buffer layer strips, followed by growth from this initial crystalline "template". To our knowledge, these are the largest index anisotropies ever measured for thin films, giving further evidence for the *nearly* perfect crystalline order achieved in QE growth.

Further evidence for crystalline order of OMBD-grown PTCDA films has been obtained through measuring optical propagation loss in PTCDA waveguides. In recent experiments, waveguides deposited on polyimide buffer layers[102] (with $n_{\text{buffer}} = 1.6 > n_\perp$) have losses <1 dB/cm for transverse electric (TE) mode-polarized light, although extremely high losses were measured for transverse magnetic (TM) mode propagation. This indicates that there is a low density of grain boundaries which would result in high scattering losses. Scattering from grain boundaries, which is commonly observed in polycrystalline waveguides has two effects: (i) outcoupling from waveguide surfaces, and (ii) scattering of TE into TM modes which are extremely lossy in waveguides where $n_{\text{TM}} \cong n_\perp < n_{\text{buffer}}$. While low loss provides only inferential evidence for the high degree of crystalline order of the films, it nevertheless suggests that the number of grain boundaries in long (~1 cm) waveguides is very small, and that the optic axis is oriented such that its projection is along the waveguiding direction (since other orientations would lead to rotation of the TE

Table 6. Structure of Fullerenes on MoS_2(0001) and GaSe(0001) (From Ref 105)

	MoS_2				GaSe			
	experiment		closest match		experiment		closest match	
molecule	axis	$\Delta a/a$ (%)	axis	$\Delta a/a$ (%)	axis	$\Delta a/a$ (%)	axis	$\Delta a/a$ (%)
C_{60}	$[11\bar{2}0]$	5.2	$[11\bar{2}0]$	5.2	$[11\bar{2}0]$	12.7	$[14\bar{5}0]$	0.7
C_{70}	$[10\bar{1}0]$	1.3	$[10\bar{1}0]$	1.3	$[11\bar{2}0]$	4.4	$[11\bar{2}0]$	4.4

mode, and hence large optical loss). Since the optic axis has a fixed orientation with respect to the unit cell, the molecules with the thin-film waveguide must all be approximately oriented in the same direction relative to each other and the buffer layer, suggesting a uniform, QE growth of the organic thin film.

3.3.2.5. Other QE Systems. Several other systems beyond the well-studied PTCDA have been reported which exhibit the characteristic, incommensurate but ordered growth of an organic vdW solid on an inorganic substrate typical of QE. An interesting example system demonstrating QE growth is that of C_{60} and C_{70} on various substrates including MoS_2(0001), GaSe(0001) and H-passivated Si(111).[105,130,178] For these experiments, the films were studied by RHEED after growth at a rate of ~0.02 ML/s with the substrate temperature at 80 to 150 °C. It was found that the layers preferentially align along either the $[11\bar{2}0]$ or $[10\bar{1}0]$ substrate axes, even though the lattice mismatch ranged from 1.3% to 12.7%. Here, the hcp lattice constant of C_{60} is $a_F = 1.00 \pm 0.02$ nm, and for C_{70}, $a_F = 1.06 \pm 0.04$ nm. These results[105] are summarized in Table 6. In one case (C_{60} on GaSe), the mismatch for film alignment along the $[11\bar{2}0]$ direction was 12.7%, although C_{60} is nearly commensurate with the $[14\bar{5}0]$ direction where the lattice mismatch is only 0.7%. This azimuthal orientation is preferred due to the lower surface energy of the incommensurate structure. Sakurai et al.[105] propose that the alignment is ultimately determined by a competition between commensurability and the alignment along step edges which tends to follow a principal crystalline axis. However, it has been found[72,99] that commensurability does not *necessarily* lead to the lowest energy configuration in vdW-bonded thin films (see section 3.3.1), since more energy is expended in distorting the film lattice than is gained by forming a commensurate lattice. This is the underlying principle governing QE growth, and is a direct result of the competition between the relatively weak, attractive vdW bond between substrate and adlayer, and the short range but strong core−core repulsion within the adlayer itself.

Nucleation along step edges or other substrate inhomogeneities has been observed in several experiments to initiate ordered QE growth independent of commensurability of the film with the substrate.[119] For example, PTCDA has been shown to align with its (100) axis parallel to the edges of polymer strips,[22,102] and perhaps even to glass.[37] Nucleation from edges and vicinal planes on semiconductor surfaces provides evidence that the internal energy of the thin film can, in some cases, play a greater role than anchoring to the substrate surface in ultimately determining molecular alignment of QE films. This phenomenon has also been observed for perfluorotetracosane [n-$CF_3(CF_2)_{22}CF_3$] and poly(tetrafluoroethylene) [$(CF_2)_n$, or PTFE] on PTFE substrates which were first prepared by mechanically rubbing along one direction.[179] These phenomena are not unlike that giving rise to anchoring and long-range ordering of liquid crystal molecules on substrates such as polymers and glass.[76]

It has also been found[105] that unstrained C_{60} films as thick as 100 ML grow layer-by-layer on MoS_2, as determined from uniform, continuous RHEED patterns.[130] While it has been suggested that C_{70} on MoS_2 films are epitaxial due to the relatively small lattice mismatch (1.3%), we note that such mismatches are extremely large for more strongly bonded epitaxial layers such as group III−V semiconductors. In the absence of any evidence for strong bonding between C_{70} and MoS_2 and given the inaccuracies inherent in RHEED measurements, this apparently commensurate growth is not yet firmly established, and more probably is similar to the QE growth of C_{60} on this same substrate material.

As noted above, the weak interaction of PTCDA on Au(111) leaves the surface reconstruction of Au(111) unchanged after growth.[73] In contrast, deposition of C_{60} on Au(111) can result in significant substrate surface reconstruction,[106,180,181] suggesting that the C_{60} is chemisorbed, rather than vdW-bonded to this substrate. For example, Fartash[106] has shown that under nonequilibrium growth conditions (i.e., at substrate temperatures ranging from 130 to 290 °C, and at deposition rates of ~3 Å/s, or approximately 0.5 ML/s) several different, nearly equal energy phases of C_{60} can coexist on the Au(111) surface. Using GIXD it was found that a commensurate phase rotated 30° relative to the Au(111) symmetry axis (R30.0) coexists with an incommensurate, in-phase (R0.0) form of C_{60}. A third phase is also observed with R13.0 shifting to R14.2 as the temperature is increased above ~150 °C. The strong substrate−film interaction results in a lifting of the Au(111) $23\times\sqrt{3}$ reconstruction. This case does not, therefore, correspond to either QE or vdWE, since vdW forces have been replaced with stronger molecule/substrate bonding. Since the resulting film structure can be substantially different than its equilibrium crystal habit, subsequent layers tend to be highly disordered, similar to the case of vdWE of Pc's on alkali halide substrates.

In some instances of QE growth (e.g., PTCDA on GaAs), surface bonding can be very strong as determined by thermal desorption measurements where the last ML of PTCDA is extremely difficult to remove except at very high substrate temperatures.[54] In this case, disordered growth of subsequent layers beyond the first ML is observed. However, the first chemisorbed ML can also serve as a "wetting" layer to the substrate, followed by subsequent, vdW-bonded

QE growth of the thin film. While no strong evidence has yet been presented for the existence of transition regions leading to ordered QE growth, their presence can be inferred in cases where unusually strong binding of the adlayers to the substrate has been determined by such methods as thermal desorption spectroscopy.

Finally, we note that strained QE growth has also recently been observed in Pb-stearate and Mn arachidate thin films on mica prepared by Langmuir−Blodgett (LB) techniques.[182] These films form incommensurate, strained lattices on mica substrates, with the lattice gradually relaxing to its bulk dimensions as the film thickness is increased to several monolayers. As in the case of OMBD-grown QE films, the LB films are azimuthally ordered with respect to the substrate lattice even in the absence of lattice matching. Furthermore, these films achieve their long-range order since the interlayer interactions are stronger than the substrate/film interactions—a condition which is identical to that leading to QE via vacuum deposition techniques. This observation of QE achieved by LB deposition suggests that QE, and its analogous growth mode of vdWE, are general properties common to all vdW-bonded systems.

3.4. Growth of Other Multilayer Structures by OMBD

In section 3.3.2, several examples were provided where alternating, ultrathin layers of two different organic molecular crystals were grown to form multilayer stacks or structures. Since these structures exhibit unique optical and electronic properties which differ from those of bulk thin films (see section 4), we discuss here the growth of multilayer structures based on materials other than PTCDA and related compounds considered above. There are two separate classes of such multilayers which have been the subject of considerable recent work: organic/organic (or heterogeneous) multilayers consisting of the combination of layers consisting of two or more organic compounds, and organic/inorganic (or hybrid) multilayers which consist of an OMC and an inorganic molecular layer placed in an alternating geometry.

3.4.1. Organic/Organic Multilayer Structures

Several phthalocyanine-based multilayer structures have been studied recently.[143] In that work, alternating multilayers of CuPc and MgPc were grown by OMBD on very flat Si(100) and Si(111) substrates cooled to $T_{sub} < 173$ K, and at a rate of 5 Å/min to ensure layer-by-layer growth and uniform interface properties. The thickness of each layer ranged from 30 to 100 Å. Compositional characterization of the layers was accomplished using secondary ion mass spectroscopy (SIMS) which could easily track the Cu and Mg concentrations as a function of film depth. Clear oscillations in the SIMS profile indicated good compositional uniformity of even the thinnest layers, suggesting a lack of intermixing of compounds across the interfaces. High-resolution cross-sectional TEM also indicated flat and uniform

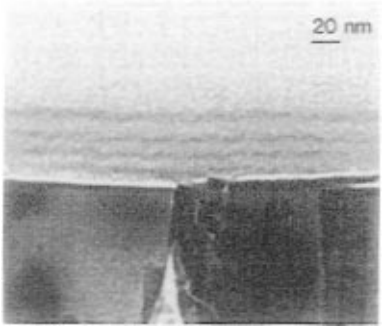

Figure 3-53. Cross-sectional transmission electron micrograph of a multilayer structure consisting of 50 Å CuPc alternating with 50 Å MgPc layers deposited on a Si(100) substrate. The contrast between the MgPc and CuPc layers is apparent (from ref 143).

interfaces, as is clearly shown for the 50 Å/layer of the CuPc/MgPc multilayer in the micrograph in Figure 3-53. Further structural analysis of these multilayers was performed using Fourier transform infrared (FTIR) spectroscopy to determine the molecular tilt angle with respect to the substrate plane. Here, FTIR probes molecular bonds which lie parallel to the incident light polarization vector. By tuning the wavelength to the phthalocyanine out-of-plane C−H bond bending modes at 730 cm^{-1}, it was found that the molecules are tilted at 22° with respect to the substrate surface. That is, the Pc molecules are found to lie at a steep inclination with respect to the substrate, which has also been found for PTCDA molecules which tilt at approximately 11° with respect to glass[37] or polymer surfaces.[22,102]

This same group[138,139] has investigated another system of planar molecules based on alternating layers of 5,10,15,20-tetraphenylporphyrin (H_2TPP; $C_{44}H_{30}N_4$) and (5,10,15,20-tetraphenylporphyrinato)zinc (ZnTPP, $C_{44}H_{30}N_4Zn$) grown at a rate of 1 Å/min on Si(100) substrates held at different temperatures ranging from 233 K to 363 K. As in the case of perylene-based thin films, the best surface morphologies and order of the H_2TPP films were found at the lowest temperatures (T_{sub} = 233 K), where an rms roughness of 2.2 Å, equal to that of the substrate, was obtained. At the highest growth temperatures (T_{sub} = 363 K), the surface morphology was discontinuous, becoming continuous but quite rough at intermediate (T_{sub} = 323 K) temperatures. Multilayer periods of 23.7 and 121 Å were grown, with the thinnest layers corresponding to the diameter of a single H_2TPP molecule. As in the case of Pc-based multilayers,[143] FTIR spectroscopy was employed to check the angle of the deposited H_2TPP molecules. It was confirmed that the C−H bond tilt could be used to infer a tilt of 75° of the molecular plane to the substrate.

These authors provide excellent examples of layer-by-layer QE growth on both Si(100) and glass (with an rms roughness measured by AFM of 2.4 Å), both of which have previously been found[65] to be suitable substrates on which to achieve ordered QE growth. Figure 3-54 shows small-angle X-ray diffraction (SAXD) patterns of several H_2TPP/ZnTPP on Si(100) multilayer samples with different layer thicknesses and numbers of periods (ranging from 20 to 40). The

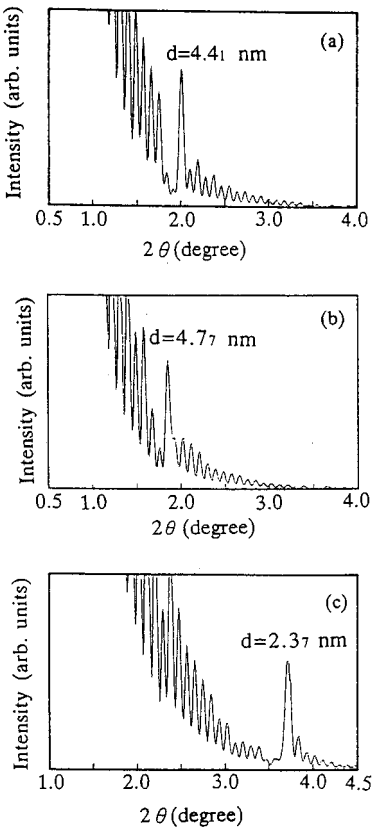

Figure 3-54. Small-angle X-ray diffraction spectra of several different superlattice films grown on Si(100) substrates at T_{sub} < 233 K: (a) 20 periods of H_2TPP(11 Å)/ZnTPP(33 Å); (b) 20 periods of H_2TPP(33 Å)/ZnTPP(11 Å); (c) 40 periods of H_2TPP(11 Å)/ZnTPP(11 Å) (from ref 138).

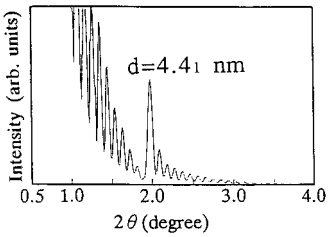

Figure 3-55. Small-angle X-ray diffraction spectrum of a H_2TPP(22 Å)/ZnTPP(22 Å) superlattice grown on a Corning 7059 glass substrate (from ref 138).

substrate was dipped in 1% HF in H_2O solution immediately prior to growth to remove the native oxide. Similarly, Figure 3-55 shows a SAXD pattern for a H_2TPP(11 Å)/ZnTPP(110 Å) multilayer grown on glass. For both substrates, the clearly resolved oscillations at small X-ray incident angles indicates extremely good coherence between the X-rays scattered from the various layers due to very flat and uniform interfaces over the entire X-ray beam cross-sectional area. These oscillations, in conjunction with SIMS data[138] indicating abrupt compositional discontinuities between each layer (i.e., no evidence for molecular intermixing between layers), suggest that this system does not require lattice matching to achieve molecularly flat interfaces with long-range order, as expected for QE growth.

Akimichi et al.[183] investigated the growth of another molecular system consisting of pentacene/tetracene multilayers on glass substrates. Here, the growth rate was 1.6 Å/s for the tetracene layers, and 0.2 Å/s for pentacene on glass held at room temperature. Multilayers consisted of layer thicknesses ranging from 14 ML to <1 ML, and the number of periods ranged from 10 to 200. Both X-ray diffraction and photoluminescence spectroscopy were used to investigate the resulting thin-film structures. The X-ray spectra were obtained in the Bragg−Brentano geometry (i.e., $\theta - 2\theta$ scans), and it was found that the diffraction peak due to intermolecular stacking was surrounded by satellite peaks when more than three molecular layers were grown in a given stack. These satellite peaks were attributed to the existence of a well-defined superlattice period. Modeling of the X-ray diffraction spectra for ideal superlattices was consistent with this conclusion, providing evidence that the interfaces between layers of differing molecular composition were flat due to a layer-by-layer growth mode. However, for superlattices consisting of layers less than three molecules deep, the satellite peaks vanished due to compositional intermixing. All of these findings were confirmed by photoluminescence spectra of the samples, which suggest material intermixing in the thinnest layer structures. This finding sets a lower limit on the thickness of the superlattices that can be achieved with this materials system.

Growth of organic multilayer structures with monolayer control has recently been demonstrated by taking advantage of a combination of substrate temperature control and the differential sublimation temperatures of various molecular species employed in the superlattice.[50,184] The method of growth, called molecular layer deposition, or MLD, is analogous to atomic layer epitaxy (ALE) employed for inorganic semiconductor MQW structures,[185−188] where the growth of each atomic layer is self-terminating due to the thermodynamic conditions or the bonding nature of the various molecules employed. In effect, MLD is "self-assembly" in the vapor phase. Yoshimura, Tatsuura, and Sotoyama[50] demonstrated the monolayer control of growth by employing pyromellitic dianhydride (PMDA, or $C_{10}O_6H_2$) alternated with either 2,4-diaminonitrobenzene (DNB) or 4,4′-diaminodiphenyl ether (DDE). These molecules were chosen due to their considerably different sublimation temperatures (T_s), and hence their deposition is controlled by adjusting the substrate temperature. That is, when $T_{sub} > T_s$, the molecular sticking coefficient is small, resulting in no deposition. On the other hand, by predepositing a molecule (molecule A) whose bond energy with molecule B ($E_{A-B} = kT_{A-B}$), is higher than the bond energy of the molecule to itself ($E_{B-B} = kT_{B-B}$), and then adjusting the substrate temperature such that $T_{B-B} < T_{sub} < T_{A-B}$, a condition is created where only a single (but complete) monolayer of molecule B can be deposited on a layer of molecule A. That is, once a saturated ML of molecule B is deposited, no further deposition can occur since the substrate temperature is $T_{sub} > T_{B-B}$. To deposit a second monolayer of molecule A, the substrate temperature is adjusted to $T_{A-A} < T_{sub} < T_{B-A}$, and the process is repeated. All steps result, therefore, in the saturated growth of single monolayer film stacks in an alternating, layer-by-layer process.

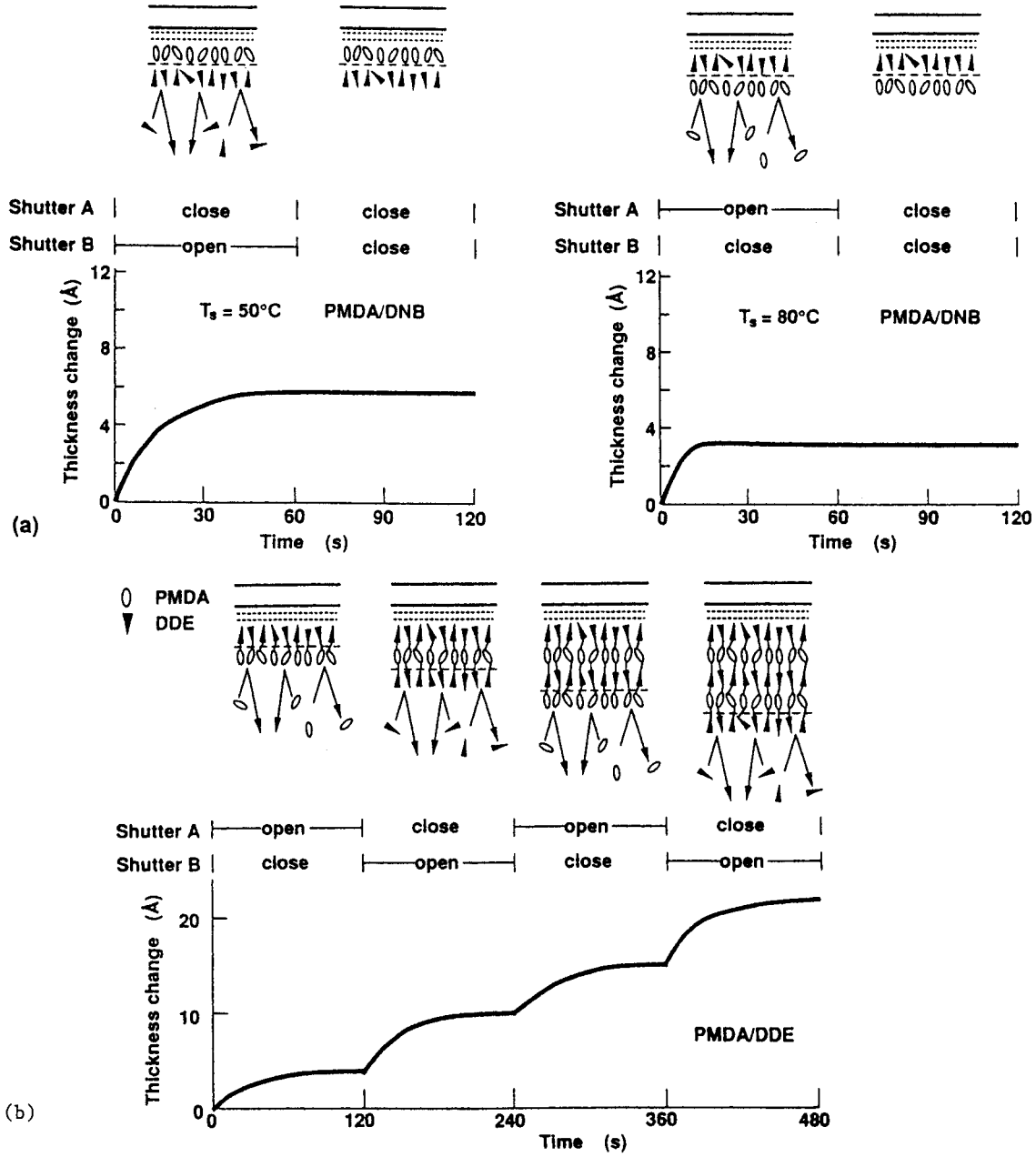

Figure 3-56. Molecular layer deposition sequences for two different polymer structures: (a) Film thickness vs shutter operation for DNB growth on a PMDA layer (left) and PMDA growth on a DNB layer (right) and (b) polymer film growth by MLD using PMDA and DDE as the precursors (from ref 50).

The process of MLD of PMDA and DNB is shown schematically in Figure 3-56. Here, the carbonyl−oxy−carbonyl groups of PMDA combine with the amino group in DNB (or DDE) to form alternately connected polymer chains. In contrast, the carbonyl−oxy−carbonyl and amino group self-bond energies are relatively weak, fulfilling the major requirement of this growth process. To accomplish the saturated alternating monolayer growth for this materials system, the substrate temperature was set at T_{sub} = 50 °C which results in the thermal energy exceeding that of the internal bond energy of DNB, thereby allowing for only a single ML of DNB to form on the predeposited PMDA layer (Figure 3-56a). Completion of a monolayer was clearly indicated by a crystal microbalance thickness monitor which served as the substrate for the organic films. Next, the substrate temperature is adjusted to T_{sub} = 65 °C which results in the desorption of the DNB. This process of adsorption followed by desorption was evidence that a single, saturated ML growth was achieved. The alternate growth of PMDA on DNB could be accomplished at T_{sub} = 80 °C, as shown in Figure 3-56b. Successive growth of PMDA/DDE multilayers were grown by this method, as shown in Figure 3-56c, resulting in a 100 Å thick continuously alternating (PMDA-DDE)$_n$ polymer (with n = 15) oriented in the surface-normal direction. While this process can be slow and difficult to control, especially for molecular combinations whose sublimation energies are close to the intermolecular bond energies, it nevertheless is an exciting proof-of-principle demonstration of saturated layer-by-layer control of growth in the vapor phase. This process has the potential for adaptation to laser-assisted growth, where the temperature can be locally and rapidly varied to initiate growth which is heterogeneous in both the surface normal and in-plane directions.

3.4.2. Organic/Inorganic Hybrid Multilayer Structures

Many interesting physical properties of hybrid organic/inorganic multilayer structures have been predicted, including unique nonlinear optical properties resulting from a new excitation—the hybrid Frenkel−Wannier exciton existing at the organic/inorganic interface.[160,189] Furthermore, such hybrid combinations may provide means for combining the optimal properties of very heterogeneous materials systems in ways which, to date, have not been anticipated. Hence, controlled growth of hybrid organic/inorganic superlattices represents an entirely new approach to tailoring materials properties, while providing unprecedented challenges to the materials scientist in achieving flat, uniform interfaces between materials with vastly different structural and chemical properties.

There are several issues which must be considered in the growth of these structures. The primary concern is the large difference in evaporation temperatures of organic and inorganic materials. For example, Ti and Si used in CuPc/oxide multilayers[190] are typically evaporated at Knudsen cell temperatures of 2270 and 1700 K, respectively. This is considerably higher than the temperature (650 K) used for CuPc sublimation. The highly energetic atomic species can therefore melt, sublime, or decompose the underlying organic layer during the deposition process, resulting in disordered structures or rough interfaces, thereby seriously degrading the control over the properties of the structure. Furthermore, many crystalline ceramics or other inorganic materials must be deposited on substrates maintained at high temperatures. Once again, this high temperature may be incompatible with the physical characteristics of the organic materials used, resulting in sublimation from the substrate, or even decomposition. Finally, incompatibilities in materials chemistry can result in unacceptable or unanticipated changes in the properties of the materials composing the hybrid structure. For example, CuPc is known to be doped by oxygen.[21] In the fabrication of oxide/CuPc multilayers, therefore, we anticipate the electrical properties of the CuPc will be strongly determined by the details of the deposition process.

In spite of these difficulties, successful growth of hybrid organic/inorganic superlattices has already been achieved. Perhaps the most interesting demonstration has been the growth of CuPc/TiO_x and CuPc/SiO_2 multilayer structures.[144,190,191] Here, the deposition of the metals was done in an O_2 ambient maintained at 2×10^{-4} Torr, with the deposition rate of all constituents at 1 Å/s. To ensure that only the α form of CuPc was grown, the Si substrate temperature was $T_{sub} = 200$ °C. This low substrate temperature resulted in amorphous oxide growth. In the case of TiO_x (with $x \approx 1.5$ for these conditions), crystalline growth occurs at $T_{sub} > 400$ °C, resulting in an electron mobility of 1−2 $cm^2/(V\ s)$. In contrast, the mobilities of the amorphous materials grown by Takada and co-workers were too low to be determined. Twenty period multilayer stacks consisting of alternating layers of 50 Å CuPc followed by an equal thickness of either the Ti or Si oxide were grown.

The structures were studied by SIMS, X-ray diffraction, AFM, and TEM. The AFM images of the multilayer stacks indicated very flat interfaces with a roughness of <7 Å.[144] However, asymmetries between the interfaces were found using this imaging technique. The TiO_x/CuPc interface was not as easily scratched by the AFM tip as was the CuPc/TiO_x interface, suggesting some interpenetration (and subsequent "hardening") of the CuPc surface by the deposited Ti atoms. While some interface disruption was inferred from this observation, the depth to which the interface was affected was beyond the resolution of the X-ray and SIMS measurements made, suggesting very limited extent to the damage. Indeed, the quality of these interfaces is readily apparent from the remarkable cross-sectional transmission electron micrographs of several different CuPc/oxide samples shown in Figure 3-57. A cross-sectional view of a CuPc/SiO_2 superlattice is shown in Figure 3-57a, providing direct observation of the superlattice structure. The layers appear to be relatively uniform, although the interface roughness is readily observed for the individual, 50 Å thick layers. A more detailed micrograph of a CuPc/TiO_x interface is shown in Figure 3-57b. Here, an interface roughness of approximately 1ML (as determined over the ∼500 Å range of the micrograph) is observed. In addition, the four *individual* CuPc molecular layers are clearly observed in the lower half of the image. By depositing submonolayer thicknesses of CuPc on TiO_x, island growth can be observed, as shown in the micrograph in Figure 3-57c. These islands are in fact small, highly ordered structures with dimensions of 20 nm × 60 nm completely buried in a TiO_x matrix which is deposited over the CuPc. Since the organic material is surrounded on all sides by the oxide, this appears to be a means to grow organic "nanoboxes" and other low-dimensional structures once only thought possible using inorganic semiconductor nanostructures.

In a second series of investigations, heterogeneous multilayer structures consisting of 3,4,9,10-perylenetetracarboxylic diimide (PTCDI) or CuPc combined with the low dielectric constant metal fluoride, MgF_2, were investigated.[145] The substrate used was Corning 7059 glass. Deposition of organic films ranging in thickness from 5 to 50 Å was done at a rate of 20 Å/min on substrates maintained at room temperature. The alternating MgF_2 film was deposited at the same rate to a thickness of 30 Å in all samples. The structures consisted of 20 superlattice periods. Analysis of the grown structures was accomplished using SAXD and FTIR. Good layer thin uniformity was observed even for the thinnest PTCDI and CuPc layers as determined by small-angle Bragg reflections from the repeating superlattice structure. Further, analysis of the FTIR spectrum of PTCDI indicated that the molecules stack nearly parallel to the surface plane. In contrast, no such uniform stacking of CuPc was observed. This was attributed the coexistence of both the α and β forms of the CuPc crystal,[21,118] resulting in considerable structural disorder. The optical properties of these structures was also dependent on film thickness, as will be discussed in section 4.3.

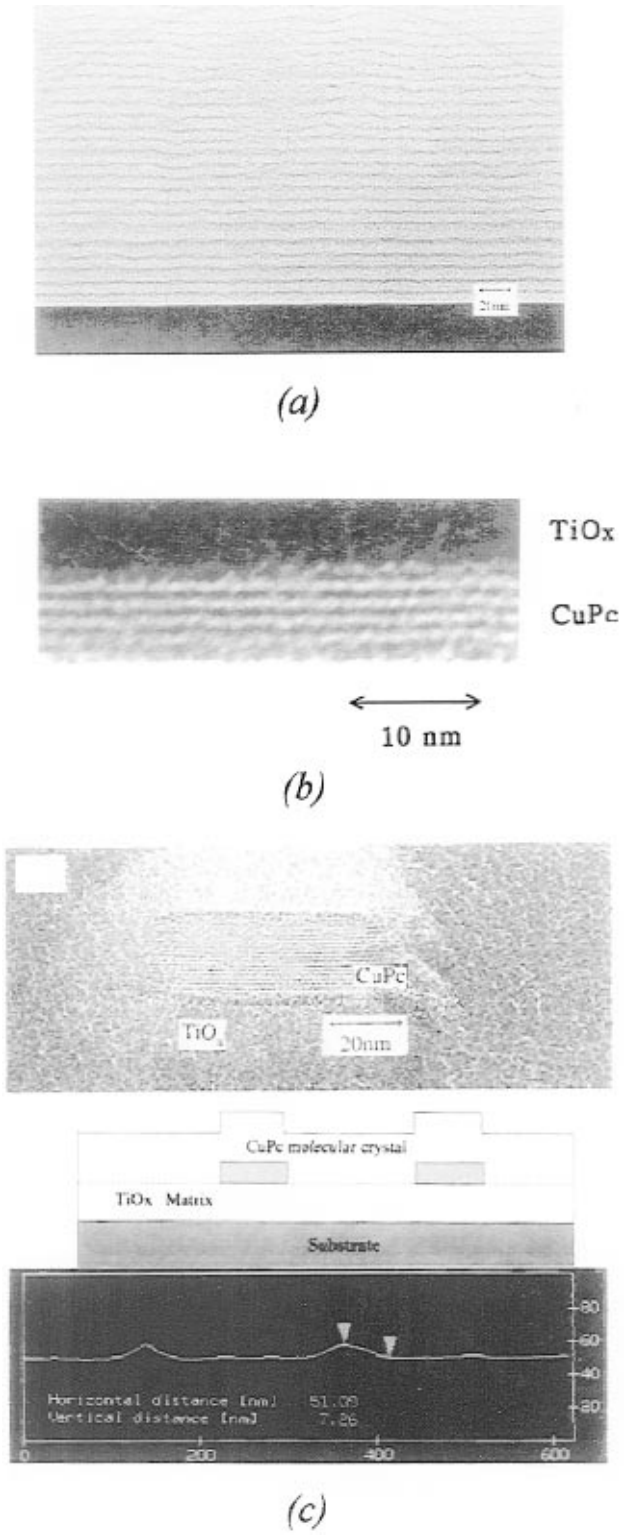

Figure 3-57. Cross-sectional TEM images of several different multilayer structures: (a) CuPc/SiO_2 superlattice pealed off of a Si substrate. Bright and dark regions correspond to the CuPc and SiO_2 layers, respectively. (b) High-resolution image of a single TiO_x layer on CuPc. Four monolayers of CuPc can clearly be resolved beneath the TiO_x. (c) CuPc "nanobox" in a TiO_x matrix. In the lower view is a schematic representation of the structure and an AFM scan showing the surface profile of the buried structure (from ref 190).

This group[159] also investigated the growth and optical properties of 30 period, tris(8-hydroxyquinoline)aluminum (Alq_3)/30 Å (MgF_2) superlattices, where the amorphous Alq_3 layer thickness was varied from

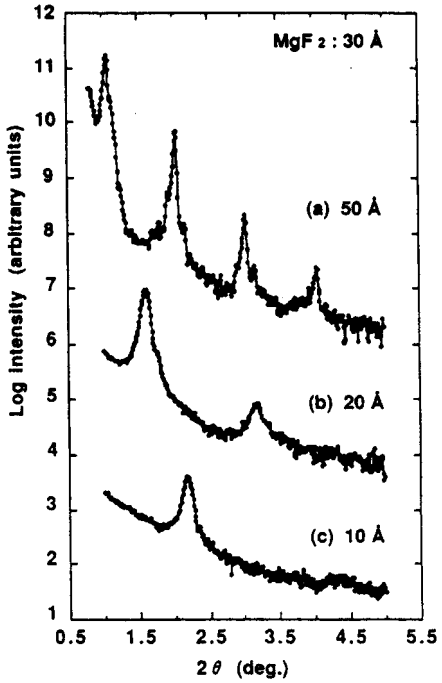

Figure 3-58. Small-angle X-ray diffraction patterns for multilayer structures consisting of 30 Å thick MgF_2 layers alternated with Alq_3 layers whose thicknesses are indicated (from ref 159).

10 to 50 Å, and deposition was on either glass or Si(100) substrates at a rate of 20 Å/min. As in the case of the PTCDI and CuPc multilayers, these structures were investigated by small-angle X-ray diffraction, with spectra shown in Figure 3-58. Very good agreement was found between the designed layer thickness and that inferred from the positions of the small angle Bragg peaks observed. Strong Bragg reflections are observed even for the thinnest (10 Å) Alq_3 layers, indicative of flat and uniform interfaces. Here, layer nonuniformity would result in a broadening and attenuation of the peaks which is not seen in these diffraction patterns.

3.5. Summary of Growth Results

Ultrahigh vacuum, organic molecular beam deposition has been shown to be a highly versatile technique for the growth of a wide range of organic and hybrid organic/inorganic thin film structures which comprise a promising new class of engineered materials for optical and electronic device applications. In this section, we have compared the growths of several different archetype organic compounds on a variety of substrates. We find that, depending on relative strengths of the bond interactions within a film, or between the film and substrate, the resulting film lattices are commensurate (i.e., epitaxial or vdWE), or are incommensurate (i.e., quasi-epitaxial) with the substrate. Epitaxial films are bonded to the surface by a combination of vdW and electrostatic forces, whereas vdWE film binding is primarily via only the vdW force. Finally, in spite of the incommensurability of QE films, they can nevertheless exhibit long-range order and have a unique orientational relationship with the substrate lattice.

With regard to QE, we have focused to a considerable degree on several aspects of film growth, from

the monolayer to the bulk thin film stage for the model planar molecules: PTCDA and NTCDA. Structural data obtained from monolayer and multilayer thin-film stacks indicate ordering into structures which are consistent with predictions made using simple energy-based models describing QE growth. The agreement between theory and measurement indicates that the fundamental assumptions regarding quasi-epitaxial growth (i.e., that the interlayer compressibility be much larger than the compressibility within a layer) are supported by observation for large, planar, van der Waals-bonded molecular solids such as PTCDA and NTCDA. These theoretical predictions have also been extended to the growth of two dissimilar organic molecules. The experiments presented here on multilayer stacks of PTCDA-on-NTCDA also provide evidence to support the theoretical results. The high degree of ordering strongly influences such macroscopic film properties as optical birefringence, a pronounced anisotropy in the dielectric and conductive properties of the films, film morphology, and carrier mobility.

Taken in the context of a growing body of evidence for QE growth of a large number of molecular species on a wide variety of substrates, it is apparent that QE growth of van der Waals-bonded planar organic molecules is a general property of these materials systems. Since this property has been shown to strongly influence the macroscopic optoelectronic film properties (see section 4), quasi-epitaxially grown organic thin films may open the way to an unprecedented range of applications in photonics and electronics. Strain energy in QE films is relieved by subtle variations in the internal lattice degrees of freedom. While QE films are nonequilibrium structures which differ from the bulk structure of the OMC, they are nevertheless found to be stable over a wide range of conditions such as temperature, pressure, etc. Hence, QE may result in an entirely new class of materials whose structural, and hence optical and electronic properties may be tuned simply by the choice of substrate or growth conditions employed.

In some respects, QE growth is similar to "orientational epitaxy" observed for inert gas atoms physisorbed onto graphite surfaces, and also is similar to the ordering of liquid crystal molecules to glass and polymer surfaces. By studying the common features of these seemingly disparate growth phenomena, we can gain a deeper understanding of the underlying physics, and hence improve our control over vdW film growth.

4.0. Optoelectronic Properties of OMBD-Grown Organic Films

Having demonstrated that OMBD is a useful tool to grow well-defined structures with interfaces between layers which are flat on the molecular scale, the next step is to determine how the optoelectronic properties of such organic nanostructures differ from those of bulk films. In particular, as the film thickness approaches that of an electron de Broglie wavelength, we anticipate that the films will exhibit quantum phenomena which are not observed in thicker (or "bulk") films. However, we note that such quantum phenomena will be much more difficult to observe in organic thin films than in conventional semiconductors or metals due to the localized nature of excitations in vdW-bonded materials such as OMCs. For this reason, the structures need to be correspondingly smaller in OMCs before quantum size effects can be observed and possibly exploited for device applications.

In the previous section, we have demonstrated that organic thin films can be controllably grown to dimensions of only a few monolayers. Hence, choosing archetype, extremely closely packed organic systems such as PTCDA or bis[1,2,5]thiadiazolo-*p*-quinobis(1,3-dithiole) (BTQBT)[192−194] which might exhibit a developed and extended band structure, provides opportunities to study, for the first time, the nature of fundamental quantum excitations in OMCs using precision nanostructures. In this section we will provide a detailed review of such studies of PTCDA-based multilayers, along with conclusive experimental and theoretical evidence that fundamental optical excitations (called "excitons") can indeed be modified in certain nanostructured OMC systems characterized by a high degree of π-orbital overlap between adjacent molecules. Furthermore, we will review data relating to "quantum confinement" in organic nanostructures and discuss the class of molecules where such phenomena are expected to be clearly observed. We note that virtually all such data accumulated thus far relate to the quantum confinement of excitons in ultrathin organic layers. However, quantum confinement of charge carriers (i.e., electrons and holes) is also possible, and should lead to the observation of a broad new range of electronic properties unique to organic nanostructures.[25−27,29]

4.1. Excitons in Ultrathin Organic Films Grown by OMBD

The nature of excitons in OMCs has been the subject of intense debate for over thirty years.[195] In Figure 4-1, we illustrate the three types of excitons

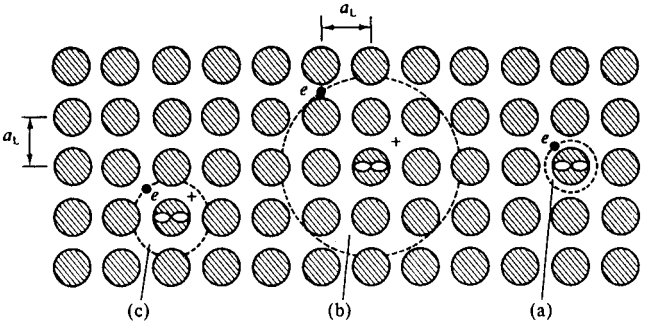

Figure 4-1. Schematic representation of the various types of excitons in semiconductors and insulators. The cross-hatched circles represent molecular lattice positions, with lattice constant a_L. (a) Small radius, or Frenkel exciton with radius $a \approx a_L$. This exciton corresponds to a molecular excited state. (b) Large radius ($a \gg a_L$), hydrogen-like, Wannier−Mott exciton commonly found in inorganic semiconductor materials. (c) Intermediate radius ($a > a_L$) charge transfer (CT) exciton proposed to lead to photoconductivity in many organic molecular crystals. The "figure-eight" within each excited state represents the molecular p bond (from ref 196, p. 71).

found in crystalline solids. Excitons in OMCs have been described as either Frenkel or charge-transfer (CT) states.[196] A Frenkel exciton is a correlated electron−hole pair localized on a single molecule, whereas the electron in a CT state is correlated with a hole located at a neighboring molecular site. In this sense, CT excitons resemble Wannier excitons common in uncorrelated inorganic systems, where the interaction energy between atomic cores is large and the radius of the exciton is often more than an order of magnitude greater than the interatomic separation. Independent of the scale, these fundamental excitations are called excitons since they share the property of having a nonnegligible mobility within the crystal. Due to its spatial extent, it is possible for the CT exciton binding energy to be modified from its bulk value when the electron−hole pair separation (or exciton radius) is on the order of the film thickness. On the other hand, we do not expect such effects to be observed for Frenkel states due to their strong localization at a single molecule. Given that OMBD can create nanostructures on the scale of the exciton radius, we now have the opportunity to study many of the details of these fundamental excitations which have previously been inaccessible using bulk structures, thereby providing a deeper understanding of the physics of carrier transport and the optical properties of a large class of organic molecular solids.

With this perspective in mind, considerable work on quantifying the optical properties in OMBD-grown nanostructures has been carried out over the last several years. These studies have focused primarily on highly controlled, relatively defect free, and well-characterized "model" compounds based on OMBD-grown PTCDA thin films and its analogs. In this section, we will discuss some of these results in detail since they lead to an entirely new perspective and understanding of fundamental excitations in OMCs which have only been possible due to the precise control of structure and material purity through OMBD growth. At the end of this section, we will discuss phenomena in other, less thoroughly characterized organic-based multilayer structures.

4.1.1. Spectroscopic Identification of Excited States in PTCDA

The first step in understanding quantum size effects in ultrathin, OMBD-grown organic films is to unambiguously identify the various features in the molecular exciton spectrum. For this purpose, the absorption and fluorescence spectra of both films and dilute solutions of the model compound, PTCDA, have been thoroughly studied.[197] Thin films were grown on cooled (~85 K) glass substrates following procedures discussed in section 2. Solution samples were prepared by dissolving prepurified PTCDA crystalline powder in dimethyl sulfoxide, $(CH_3)_2S{:}O$ (DMSO) and other solvents via sonication. PTCDA is found to be weakly soluble in DMSO, ensuring a small solvent/molecule interaction, while limiting the most concentrated solution to only 2 ± 1 μM.

The absorption spectrum of the 2 μM stock solution in DMSO, shown in Figure 4-2a, has four clearly resolved peaks with a shoulder on the high energy side of the 2.7 eV peak. In addition, the low-energy tail (defined as the energy at which the absorption

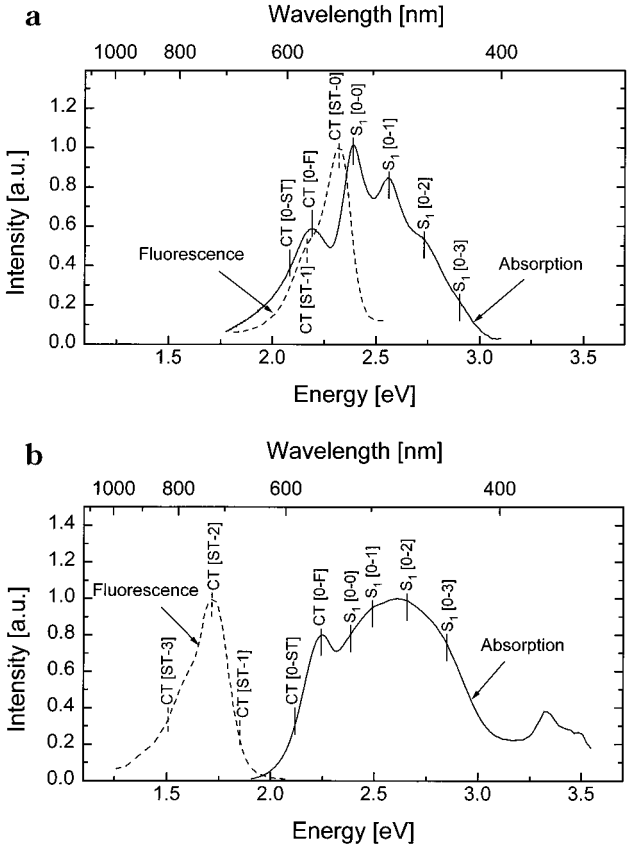

Figure 4-2. Absorption (solid line) and fluorescence (dashed line) spectra of (a) 2 μM solution of PTCDA in DMSO, and (b) 1000 Å thick PTCDA film. The energy position for each absorption and fluorescence transition is identified (from ref 197).

is >5% of its peak value) extends to $E < 1.90$ eV. This is compared to the thin-film absorption spectrum (Figure 4-2b) with a broad feature at $E > 2.3$ eV and a distinct, narrow peak centered at $E = 2.23$ eV. Furthermore, the low-energy tail is comparatively short, extending to only $E \approx 2.0$ eV.

There are significant differences between the fluorescence spectra of PTCDA solutions and thin films. The solution fluorescence spectrum (Figure 4-2a) has a maximum at $E = 2.32$ eV, with a shoulder at $E = 2.18$ eV. In contrast, the thin-film short wavelength fluorescence is completely quenched, with the peak fluorescence centered at $E = 1.70$ eV, and with an additional feature at $E = 1.55$ eV. No significant changes in the shape of the thin-film or solution fluorescence spectra were observed as the pump energy was changed from $E = 2.72$ to 2.05 eV.

The absorption was also studied as a function of concentration of PTCDA in solution (Figure 4-3a). To quantitatively study the spectral features, each solution absorption spectrum was fit to six Gaussian peaks with the parameters provided in Table 7. The four high-energy Gaussian curves correspond to the distinct absorption peaks, whereas the fitting parameters for the two lowest curves at $E = 2.23$ eV and 2.12 eV were chosen to agree with electroabsorption[177] and photoconduction[172,173] data in PTCDA thin films. Table 7 also shows the results of a similar fit to the thin-film absorption spectrum, where the two lowest energy peaks are obtained from these same studies.

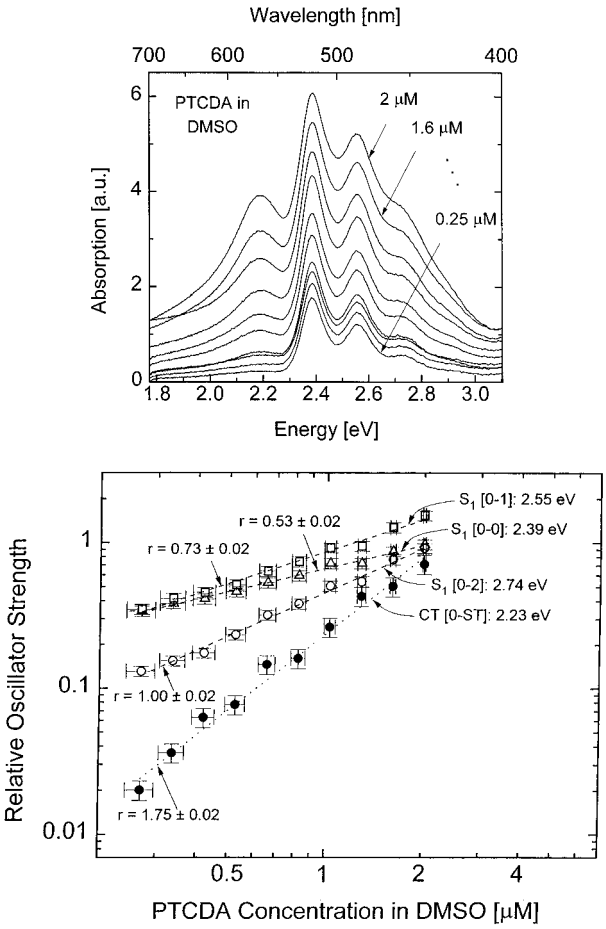

Figure 4-3. (a) Absorption spectrum of PTCDA in DMSO solution as a function of PTCDA concentration. Each dilution step reduces PTCDA concentration to 80% of the starting solution. (b) Relative oscillator transition strength (proportional to the integrated area) of $E = 2.20$ eV, $E = 2.39$ eV, $E = 2.55$ eV, and $E = 2.74$ eV solution absorption peaks as a function of PTCDA in DMSO concentration. The slopes refer to the linear fits (straight lines) to the data. The plot was normalized to the oscillator strength of the S_1 [0-0] transition at a concentration of 2 μM (from ref 197).

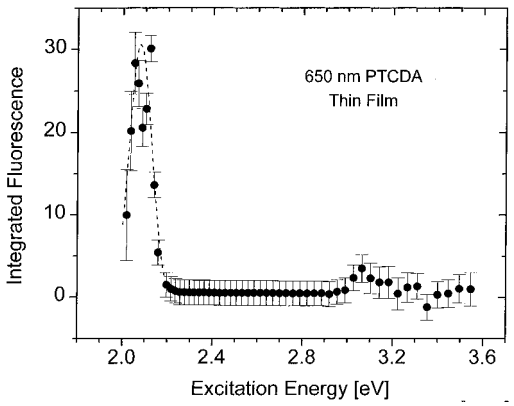

Figure 4-4. Excitation fluorescence spectrum of a 650 nm thick PTCDA film sample (from ref 197).

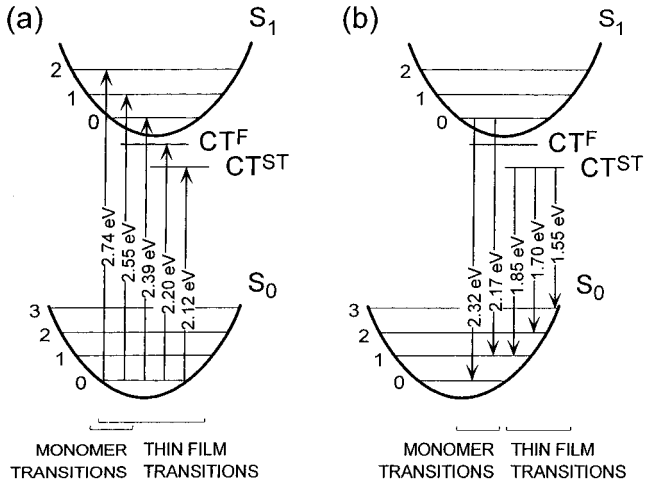

Figure 4-5. (a) Absorption and (b) fluorescence configuration space diagrams along with direct transitions proposed for PTCDA (from ref 197).

The dependence of the $E = 2.23$, 2.39, 2.55, and, 2.74 eV integrated peak areas (which are proportional to the transition oscillator strength) as a function of PTCDA concentration [k] in DMSO are shown in Figure 4-3b. Both the $E = 2.74$ and 2.23 eV peaks rapidly decrease with respect to the $E = 2.39$ eV peak, however only the 2.23 eV peak completely attenuates at concentrations of $[k] \leq 0.25\ \mu$M. For the three higher energy peaks, the rate of decrease in absorption with decreasing PTCDA concentration is a function of energy, where the 2.39 eV peak shows the smallest rate of decrease.

The excitation spectrum of the luminescence peak centered at $E = 1.70$ eV of a 650 nm thick film is shown in Figure 4-4. Low fluorescence efficiency (<1%) is observed at $E < 2.2$ eV, with a peak at ~20 times its short wavelength efficiency at 2.10 eV, which has been attributed to a bulk rather than a surface phenomenon.[197]

The configuration space representations of the molecular levels in PTCDA shown in Figure 4-5 are used to interpret these solution and thin-film spectra. Here, Figure 4-5a corresponds to the absorption

Table 7. Numerical Fit to the Absorption Spectra of PTCDA Thin Films, and 2 and 0.25 μM Solutions of PTCDA in DMSO[a]

	thin film				2 μM solution				0.25 μM solution			
transition	E_0 (eV)	ΔE (eV)	FWHM (eV)	f	E_0 (eV)	ΔE (eV)	FWHM (eV)	f	E_0 (eV)	ΔE (eV)	FWHM (eV)	f
CT [0-ST]	2.11		0.17	0.46	2.12		0.36	1.10	2.16		0.50	0.63
CT [0-F]	2.23		0.14	2.03	2.20		0.16	0.73	2.20		0.16	0.06
S_1 [0-0]	2.38	>0.11	0.14	1.00	2.39	>0.16	0.10	1.00	2.39	>0.17	0.09	1.00
S_1 [0-1]	2.49	>0.17	0.21	2.86	2.55	>0.19	0.16	1.58	2.56	>0.17	0.13	1.03
S_1 [0-2]	2.66	>0.19	0.23	3.20	2.74	>0.16	0.16	0.94	2.73	>0.17	0.12	0.39
S_1 [0-3]	2.85		0.26	3.31	2.90		0.13	0.22	2.90		0.23	0.41

[a] Each spectrum was fit to six gaussian shapes corresponding to six transitions identified in the text and noted in the left-most column. For each gaussian curve, the peak energy (E_0), energy difference of the neighboring energy peaks (ΔE), the full width at half maximum (FWHM), and the integrated area below the curve (f) normalized to the area of S_1 [0-0], are indicated. (From Ref 197).

transitions, whereas Figure 4-5b provides the fluorescence transitions occurring after nuclear relaxation. The electronic ground state of PTCDA is spin-singlet (labeled S_0 in Figure 4-5). The high oscillator strength of the absorption features in Figure 4-2 is therefore a signature of spin-allowed singlet-to-singlet transitions. The distinctly different behavior of the high-energy solution absorption spectra at $E = 2.39$, 2.55, 2.74, and 2.90 eV, as compared to the broad peak at 2.23 eV as a function of solution concentration suggests that these two groups of transitions are associated with separate manifolds. The equal spacing between the four high-energy solution absorption peaks (c.f., Table 7) arises since they originate from transitions between different vibronic states (ν_n) in the singlet, S_1 band, labeled $S_1[0-\nu_n]$ (with $\nu_n = 0$, 1, 2, 3). In solution, the absorption spectral shape of these S_1 transitions is not significantly influenced by the PTCDA concentration in DMSO (Figure 4-3a), indicating that S_1 is Frenkel-like, i.e., the excitation is largely confined to the individual monomers.

In contrast, the absorption centered at $E = 2.23$ eV is strongly affected by concentration, becoming vanishingly small for $[k] < 0.1$ μM solutions. This is expected for an *aggregate state* arising from the $\pi-\pi$ orbital overlap of closely stacked PTCDA molecules, and is similar to previous observations of absorption by aggregate states in other organic crystals[198−200] such as α-perylene, tetracene, and C_{60}. Since PTCDA is only weakly soluble in DMSO, small particles with three-dimensional crystalline properties (e.g., extended CT states) form a suspension in solution. As the colloidal solution is diluted, the concentration of aggregate particles is reduced to the extent that, at the lowest concentrations, their contribution to the absorption spectrum is negligible. Thus, the 2.23 eV absorption feature has been assigned[197] to a charge-transfer (CT) exciton of the extended PTCDA crystal structure. The lower energy of the 2.23 eV peak as compared to the S_1 state is also consistent with CT state properties.[195]

Since monomers are the dominant species in the most dilute solutions, and since the fluorescence spectrum does not significantly change with concentration, the solution fluorescence in Figure 4-2a has been attributed to direct monomer transitions from S_1 to S_0 (see Figure 4-5b). In contrast, the thin-film fluorescence spectrum peaks at 0.60 eV lower energy than does the monomer fluorescence (Figure 4-2b). The fluorescence quantum efficiency of the thin films has been found to be significantly lower than that of solutions due to phonon-enhanced fluorescence quenching (internal conversion). Therefore, despite a small aggregate concentration in PTCDA solutions, only a very low fluorescence yield has been observed for the aggregate peak in solution.[197] The S_1 absorption lines of aggregates and thin films are broader than for monomers due to the increased coupling of phonon modes with electronic transitions in solids. Further, since the fluorescence quantum efficiency in the excitation spectrum peaks at 2.10 eV corresponding to the low-energy tail of CT (c.f., Figure 4-4), the CT state is likely the initial level in the fluorescence process, and there are nonradiative losses in the $S_1 \rightarrow$ CT transitions.

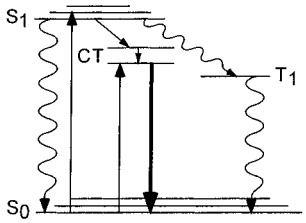

Figure 4-6. Proposed transitions between the lowest lying thin-film PTCDA energy levels. The straight and wavy lines indicate single-step and multi-step nonradiative transitions, respectively (from ref 197).

These observations suggest that most S_1 excitons undergo either $S_1 \rightarrow S_0$ internal conversion that is sufficiently fast to effectively compete with fluorescence, or intersystem-crossing into a nonradiative triplet state, T_1, which is typically lower in energy than S_1. Figure 4-6 summarizes the various possible transitions between the lowest energy states found for PTCDA thin films. Both internal conversion for $S_1 \rightarrow S_0$ and the spin-forbidden $T_1 \rightarrow S_0$ nonradiative transitions lead to the low quantum yield of solid PTCDA.

In molecular crystals such as pyrene and perylene, strong exciton-phonon coupling results in the formation of self-trapped excitons. These states are lower in energy than the corresponding free excitons and can be solely responsible for the observed fluorescence. Self-trapping in PTCDA has also been identified[197] by analyzing the low-energy thin-film absorption (or Urbach) tail of the CT state.[201] Due to strong exciton−phonon coupling, self-trapping is very likely. In that analysis, a small self-trapping energy of $\Delta E_{ST} = 0.04 \pm 0.02$ eV was measured, placing the self-trapped CT exciton (denoted CT^{ST}) at 2.19 ± 0.05 eV, which is in reasonable agreement with 2.11 ± 0.04 eV obtained through numerical fits to the absorption spectrum.[197] In contrast, the small radius S_1 exciton is not subject to long-range lattice interactions, and hence does not self-trap. From the small Stokes shift (<0.1 eV) between the solution peak absorption and fluorescence spectra (Figure 4-2a), it is likely that relaxation occurs directly from the free S_1 state into S_0, which can also be inferred from the short solution fluorescence lifetime of 4.0 ± 0.5 ns characteristic of such transitions.[202] In contrast, the self-trapped CT state of PTCDA thin films have a fluorescence lifetime[24] for excitation into S_1 approximately three times longer, at 10.8 ± 0.5 ns. The relatively short lifetime of solution luminescence implies a lack of significant self-trapping for S_1.

4.1.2. Fluorescence and Absorption Spectra of PTCDA/NTCDA MQWs

Having unambiguously identified the CT exciton in PTCDA as an extended, or aggregate state, we expect its energy to be changed when it is confined in nanostructures whose dimensions are comparable to the effective exciton radius, a^*. That is, by growing ultrathin films of dimension $\sim a^*$, we anticipate that the energy barriers at the film surfaces will "confine" the exciton within that film, and hence increase its binding energy accordingly. These con-

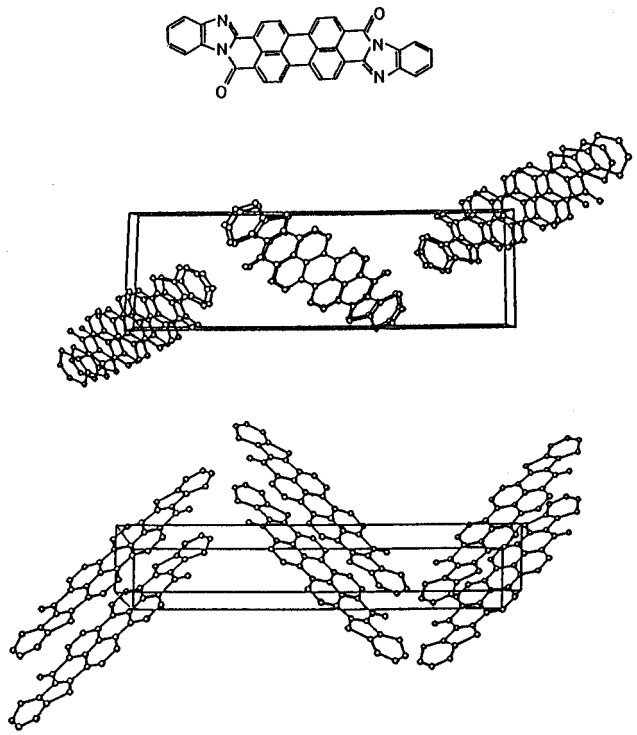

Figure 4-7. Perspective views of a PTCBI unit cell. Top: Molecular formula for PTCBI (from ref 135).

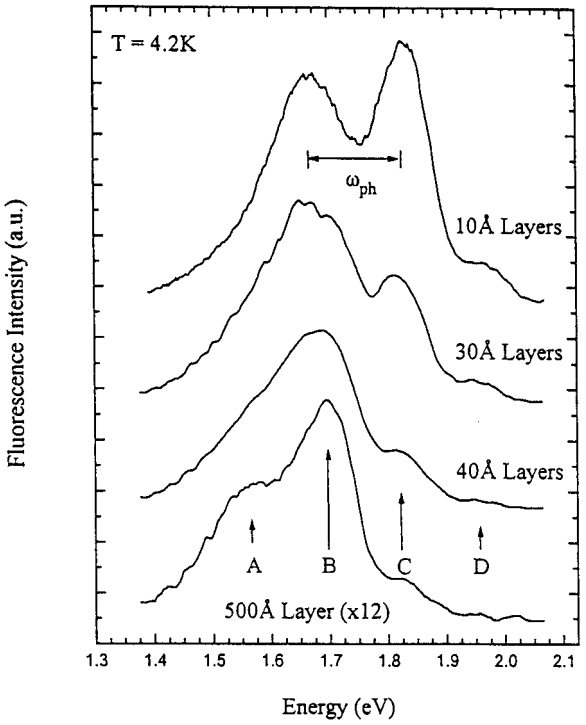

Figure 4-8. Low temperature (4.2 K) fluorescence spectra of PTCDA/NTCDA multilayer stacks for layer thicknesses of PTCDA ranging from 10 to 500 Å. The four peaks in the spectra are labeled A, B, C, and D, and the spectra are displaced vertically for clarity. These peaks correspond to the following $CT^{ST} \rightarrow S_0$ transitions shown in Figure 4-5: CT[ST-3], CT[ST-2], CT[ST-1], CT[ST-0], respectively (from ref 135).

finement phenomena were explored by measuring the spectral properties of PTCDA/NTCDA and PTCBI/NTCDA multilayer structures, where the film thicknesses were varied from 10 to 500 Å.[163] Here, PTCBI (or 3,4,9,10-perylenetetracarboxylic bisbenzimidazole) has a larger interplanar stacking distance of 3.45 Å as compared with 3.21 Å for PTCDA, although in many other respects these molecules are similar (see Figure 4-7 for the PTCBI unit cell structure). Hence, a combined study of these two compounds was used to develop a model with which to study the relationship of charge delocalization to quantum size effects.[135] Finally, the electroabsorption spectra of PTCDA and PTCBI thin films were measured to obtain a direct measurement of the exciton radius in order to quantitatively understand effects observed in the thinnest films.[135,176,177]

In a series of experiments described by Haskal and co-workers,[135,163] the low-temperature absorption and fluorescence spectra of alternating multilayer stacks of PTCDA and NTCDA, or PTCBI and NTCDA layers were measured, where the total thickness of all of the PTCDA or PTCBI layers was 500−600 Å. The thickness of the intermediate NTCDA layers matched the PTCDA or PTCBI layer thicknesses, except for the 50-period 10 ± 5 Å PTCDA structures. In that case, the NTCDA thickness was increased to 20 Å to ensure growth of a continuous layer. NTCDA was used as the intermediate layer since its lowest energy exciton state is ~1 eV higher than the excited state energies in PTCDA and PTCBI.[203] These multilayer structures are therefore similar to inorganic semiconductor multiple quantum well (MQW) structures, where the quantum well material is either PTCDA or PTCBI and the "larger bandgap", or barrier material, is NTCDA.

Fluorescence spectra, obtained by optically pumping the multilayer stacks of alternating layers of PTCDA and NTCDA at a wavelength of 488 nm from an Ar ion laser at $T = 4.2$ K, are shown in Figure 4-8. Four equally spaced peaks (A, B, C, and D) are due to vibronic transitions from the excited to the ground state. These peaks correspond well to the $CT^{ST} \rightarrow S_0$ transitions: CT[ST-3], CT[ST-2], CT[ST-1], and CT[ST-0], respectively. The energy spacings, ω_{ph}, of the vibronic peaks are observed to increase from 1065 cm^{-1} at 500 Å to 1226 cm^{-1} for the thinnest, 10 Å layers. These vibronic energies are similar to those observed in the fluorescence spectra of PTCDA solutions discussed in section 4.1.1, and listed in Table 7. Taking this, along with the direct measurement of the Raman spectrum of PTCDA, these dominant features are identified as the C−C bond stretch (measured[41] by Raman scattering at 1061 cm^{-1}).

The change in ω_{ph} (or $\Delta\omega_{ph}$) in PTCDA films as a function of layer thickness, as referenced to the 500 Å film, is shown by the solid squares in Figure 4-9. For each measurement, $\Delta\omega_{ph}$ is found by fitting the appropriate fluorescence spectrum to a series of four overlapping Gaussian curves using parameters similar to those used to fit the solution spectra of PTCDA (see section 4.1.1, Table 7)—a procedure which yields both the peak position and width. The increase in ω_{ph} with decreasing layer thickness was observed to be accompanied by an increase in the fluorescence intensity of the high-energy transitions at the expense of the low-energy transitions. The fluorescence intensity of the 10 Å film is approximately 12 times larger than for the 500 Å PTCDA film, indicating that interfaces assist in the radiative recombination of

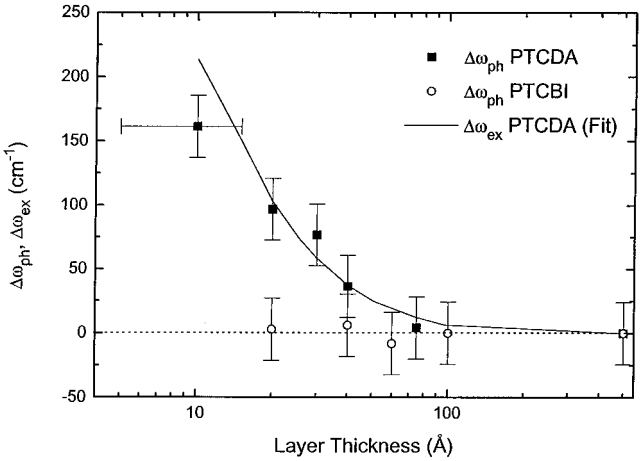

Figure 4-9. Measured change in the ground state vibrational frequency, $\Delta\omega_{ph}$, of both PTCDA (squares) and PTCBI (open circles) as a function of layer thickness, as referenced to their respective 500 Å films. The solid line is a fit to data of the observed exciton energy shift ($\Delta\omega_{ex}$) in PTCDA layers using the theory in ref 24 (from ref 135).

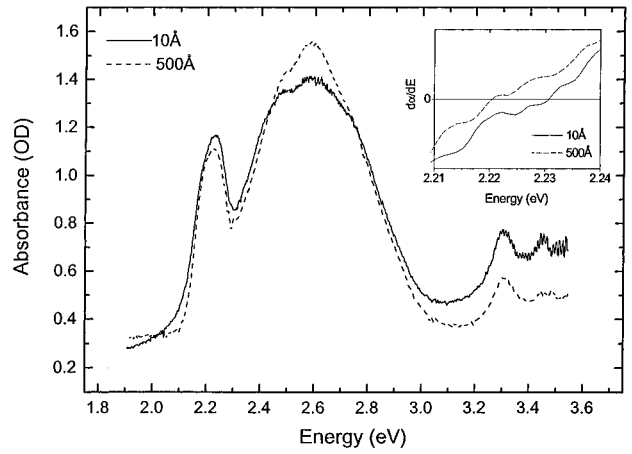

Figure 4-10. Low temperature (4.2 K) absorption spectra of a 500 Å PTCDA film and a 10 ± 5 Å PTCDA/20 Å NTCDA multilayer stack. Inset: Change in absorption coefficient as a function of wavelength, dα/dλ, for the samples in Figure 4-8 (from ref 135).

excitons in PTCDA layers, in the absence of a high density of interfacial defects, which would be expected to lead to fluorescence quenching. This increased radiative recombination is characteristic of exciton spatial confinement due to an increased overlap of the electron and hole wave functions (see section 4.2.3.2).

The low-temperature (4.2 K) absorption spectra of a single 500 Å thick PTCDA layer and a 50-period stack of 10 ± 5 Å PTCDA/20 Å NTCDA are shown in Figure 4-10. A graph of the derivative of the absorption with respect to photon energy, (dα/dE), in the energy range of the CT exciton peak is shown in the inset.[135] Note that the CT peak at 2.234 eV is shifted to higher energy (as shown clearly in the zero-crossing of each derivative curve) as the layer thickness is decreased. A similar blue shift in the CT peak in PTCDA/InPc-Cl multilayer structures has also been observed.[204] In that case, an energy increase of ~80 meV was obtained for a decrease in PTCDA thickness from ~250 to 3 Å, as shown in Figure 4-11. These shifts have been attributed to the change in the CT exciton binding energy as a result of quantum

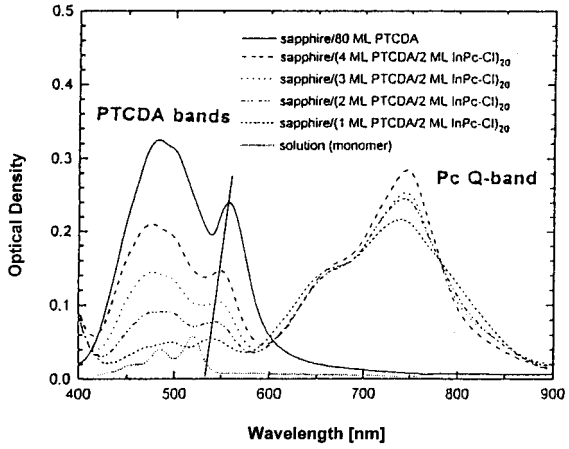

Figure 4-11. Absorption spectrum for PTCDA/InPc-Cl multilayers grown on sapphire showing the spectral shift in the low energy PTCDA (straight line). Also shown is the solution spectrum of PTCDA corresponding well with that in Figure 4-3 (from ref 204).

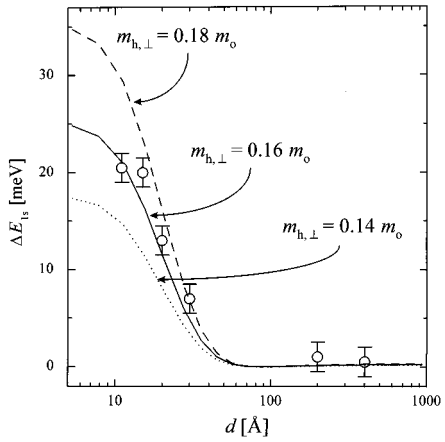

Figure 4-12. Energy shift of the PTCDA CT absorption peak, ΔE, as a function of PTCDA layer thickness d. The symbols correspond to the experimental data, and the solid curve is the fit using $m_{h,\perp} = 0.16\ m_o$. The fit is also compared with the dashed curve using $m_{h,\perp} = 0.18\ m_o$ and the dotted line using $m_{h,\perp} = 0.14\ m_o$ (from ref 176).

confinement in a finite potential well.[23,24] The potential well width corresponds to the PTCDA layer thickness, with the energy barriers provided by the HOMO offsets at the heterointerfaces with NTCDA layers (or possibly in the case of PTCDA/InPc-Cl, by the 2 ML thick phthalocyanine layer). Furthermore, no apparent shifts in the higher energy exciton lines are observed, possibly as a result of the Frenkel origin of these lines (see section 4.1.1).

Quantitative fits to the PTCDA/NTCDA data of So and Forrest,[24] and later by Shen and Forrest[176] found that the radius of the CT exciton in PTCDA is ~12 Å, or 3−4 molecules in the stacks of PTCDA normal to the substrate. This is consistent with spectroscopic assignments of this feature discussed in section 4.1.1, where the CT exciton is found to be an extended state existing only in macroscopic aggregates and thin films. The dependence of the CT exciton energy shift with well width is shown by the data points in Figure 4-12. The solid line is a fit to the data (see section 4.2.3.2) assuming that the shifts arise from CT exciton confinement in PTCDA layers whose dimensions are comparable to the exciton radius of 12 Å.

The low-temperature fluorescence spectra of multilayer stacks of PTCBI layers alternated with NTCDA layers, where PTCBI layer thicknesses were varied from 20 to 500 Å, were used for comparison to the PTCDA/NTCDA data.[135] In the case of PTCBI, only two fluorescence peaks were resolved at 1.478 eV and 1.427 eV. In contrast to the substantial spectral changes in the PTCDA spectrum shown in Figure 4-8, the only change observed in the PTCBI/NTCDA fluorescence spectrum as the PTCBI layer thickness was decreased to a 25-period stack of 20 Å PTCBI alternated with 20 Å NTCDA was a small redistribution of fluorescence intensity to higher energy, and a peak width broadening attributed to interface roughness in semiconductor (e.g., GaAs/AlGaAs) MQWs.[205] The change in spacing between the two peaks in the PTCBI fluorescence spectra as a function of layer thickness is shown by the open circles in Figure 4-9. If it is assumed that the peaks are due to the same intramolecular vibration, then these data suggest that the vibrational frequency in PTCBI does not change significantly as layer thickness is decreased ($\Delta\omega_{ph} \approx 0$).

The fluorescence efficiency of PTCBI was found to increase by only a factor of 3 from the widest (500 Å) to the narrowest (20 Å) layers, as compared with the 12-fold increase in PTCDA fluorescence efficiency as layer thickness was reduced over a similar range. This indicates that neither the presence of heterointerfaces nor quantum size effects in the PTCBI multilayer stacks are as active in enhancing radiative recombination as they are in the PTCDA multilayer stacks. Furthermore, no absorption peak shifts were observed in the PTCBI/NTCDA multilayer structures. This result is consistent with electroabsorption measurements for PTCBI,[135] where only small-radius ($a^* \leq 3$ Å), Frenkel excitons were identified, which are unlikely to exhibit confinement effects for the range of layer thicknesses used in these experiments.

To quantitatively understand the spectral dependence on layer thickness, Haskal et al. assumed that PTCDA could be approximated as an adiabatic system with a single, totally symmetric vibrational mode dominant in the ground state parabolic potential. This assumption provides a single value of ω_{ph} between the PTCDA vibronic transitions CT[ST-ν_n] in Figure 4-8. Figure 4-13 shows the modified molecular potential of Figure 4-5 of both a thin (Figure 4-13a) and a thick (Figure 4-13b) PTCDA layer, indicating the optical transitions between the excited and ground states in these films. The observed redistribution of intensity to higher energy vibronic transitions was attributed[135] to a change in the relative equilibrium configurational coordinate of the excited (q_m') and ground states (q_m^o), where $\Delta q_m = q_m' - q_m^o$ decreases with layer thickness (Figure 4-13). In the Condon approximation, the oscillator strengths of the transitions from the lowest vibrational level of the upper (excited) manifold to the nth excited vibrational level of the lower (ground) manifold can be described by a Poisson distribution.[206] The vibronic transitions in Figure 4-8 have been fit to such a distribution[135] to obtain Δq_m as a function of layer thickness, d shown in Figure 4-14a, assuming

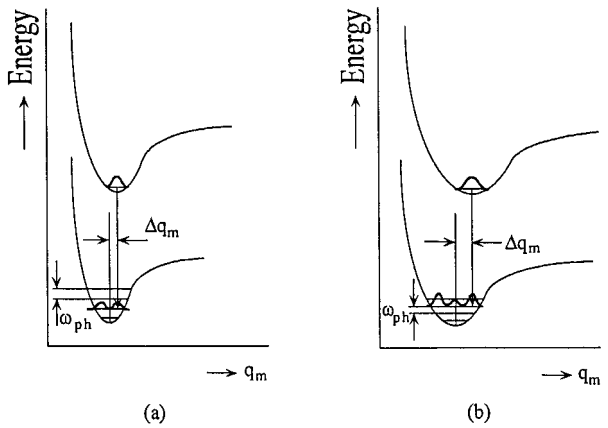

Figure 4-13. Configuration coordinate diagram showing the relative changes in the excited and ground state molecular potential energy wells of (a) thin and (b) thick PTCDA films (from ref 135).

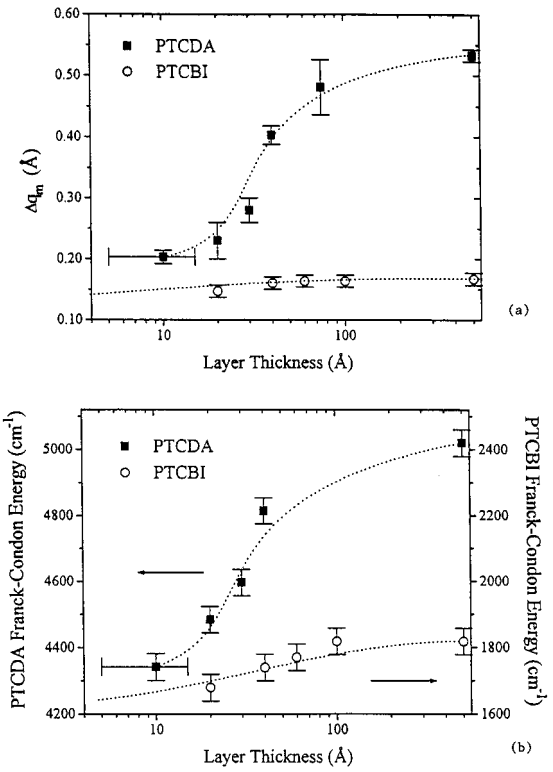

Figure 4-14. (a) Change in the relative equilibrium configurational coordinate (Δq_m) of the excited and ground states as a function of layer thickness for both PTCDA/NTCDA and PTCBI/NTCDA multilayer films. (b) Franck−Condon energy in PTCDA and PTCBI, measured as the difference from the CT[O-F] absorption peak to the first moment of the fluorescence spectrum. In both a and b, lines are drawn as a guide to the eye (from ref 135).

a vibrational reduced effective mass of $m_r = 6$ amu consistent with a C−C vibrational mode. Here, Δq_m is found to continuously *decrease* with PTCDA layer thickness over the range of 500−10 Å. The magnitude of Δq_m corresponds to a large molecular conformational change upon excitation which must take place in PTCDA, with its exceptionally large Franck−Condon energy, broad absorption spectrum, and lack of mirror symmetry between fluorescence and absorption (see Figure 4-2b).

Since Δq_m corresponds to the *total* molecular conformational change upon excitation, these results

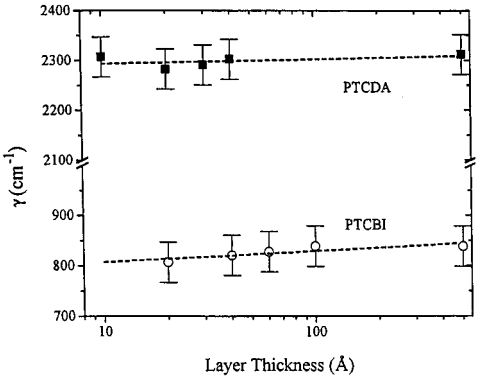

Figure 4-15. Exciton−phonon coupling frequency, γ, as a function of layer thickness for both PTCDA/NTCDA and PTCBI/NTCDA multilayer films. Data are obtained from Figure 4-14 using method described in text. The lack of variation in γ with thickness indicates that the structure of the layers is not a function of thickness, consistent with growth experiments discussed in section 3 (from ref 135).

suggest that the decrease in Δq_m with layer thickness is due to exciton confinement in ultrathin layers. That is, as the layer thickness is decreased, the exciton overlaps with fewer molecules, so that the total conformational change of the excited molecules is reduced. Similarly, a reduced exciton radius in the ultrathin layers results in a decreased dipole moment, which in turn decreases the observed conformational change. This is consistent with previous studies of the absorption spectra of organic/inorganic multilayer stacks, where it was also suggested that the intermolecular interaction decreases with layer thickness.[144]

The molecular potential diagrams shown in Figure 4-13 was also used to understand PTCBI/NTCDA multilayer stacks. The negligible change[135] in ω_{ph} suggests that the curvature of the potential is unaffected in MQW structures with even the thinnest (20 Å) layers. To account for the small redistribution of fluorescence intensity between the peaks in the fluorescence spectra, Δq_m for PTCBI was also calculated. With these assumptions, $\Delta q_m \approx 0.17$ Å, or roughly one-third that of PTCDA (Figure 4-14a), and shows only a minimal dependence on layer thickness.

Figure 4-14b shows the Franck−Condon energy (E_{FC}) in both PTCDA and PTCBI as a function of layer thickness. Here, E_{FC} is measured from the lowest energy absorption peak to the first moment[135] of the fluorescence spectrum. It has been shown that the exciton-phonon coupling is[27,206]

$$\gamma = (E_{FC}\omega_{ph}/\hbar)^{1/2} \qquad (4.1)$$

which is plotted for both PTCDA and PTCBI in Figure 4-15. Here, $\hbar$ is the Planck's constant divided by 2π. The exciton−phonon coupling is found to be independent of layer thickness. This result is expected for layers whose *structure* is independent of layer thickness, which is found to be the case for PTCDA and PTCBI layers grown by OMBD using the conditions described in section 3.3.2. Indeed, Fenter et al.[111] have conclusively shown that strain is *not* relieved, even for very thick layers (>70 ML) when molecular films are grown under nonequilibrium (i.e., QE) conditions, such as is the case in the experiments discussed here (see Figure 3-43a). Hence, strain relief is not the source of the observed spectral shifts. Finally, γ in PTCBI is ∼30% smaller than for PTCDA, consistent with the difference observed in Δq_m for these materials.

From results for PTCDA/NTCDA multilayers, the effects of confinement are significant due to the relatively large spatial extent of the exciton. That is, the extended exciton state (with a radius ∼12 Å, see section 4.2) overlaps a large number of PTCDA molecules in the crystal. As a result, the exciton binding energy, radius, and dipole moment are all changed in thin films whose dimensions approach the scale of the unbound, self-trapped CT state. The significant π-orbital overlap in this closely stacked molecular system has the additional affect of leading to strong coupling between molecules which results in an unusually large exciton−phonon coupling of $\gamma \sim 2300$ cm^{-1}. Such a large coupling implies that changes in exciton energy must result in changes in the intramolecular phonon energy, ω_{ph}, as observed. These findings for PTCDA are in contrast to PTCBI/NTCDA, where the PTCBI exciton is largely unaffected by the ultrathin layers, due to its small radius, Frenkel-like characteristics. Haskal has explained the differences between PTCDA and PTCBI as follows:[135] (i) Since the imidazole group in PTCBI acts as an electron donor, holes are easily trapped on the excited molecules, leading to the formation of Frenkel excitons. (ii) The random distribution of the *trans* and *cis* isomers present in the PTCBI crystal leads to a disruption of the π-orbital overlap between adjacent molecules in a stack, thereby limiting the spatial extent of the exciton. (iii) Calculation of the electronic overlap of the p orbitals of adjacent carbon atoms in two different molecules indicates that the overlap is over three times greater in the closely stacked PTCDA films as compared with that due to the 7% larger intermolecular separation in PTCBI. This implies that intermolecular carrier transfer is significantly reduced in PTCBI due to its relatively large interplanar stacking distance.

4.2. CT States in Nonpolar OMCs: Theory and Experimental Confirmation

Having eliminated extrinsic sources for the observed excitonic spectral shifts, we now consider the intrinsic physical origin of these phenomena. A comprehensive theoretical foundation has been developed to treat this apparent "exciton confinement", and has been used to quantitatively analyze both the electroabsorption (EA) spectra and CT state absorption blue shifts in PTCDA thin films. We will present highlights of this treatment in this section.

The delocalized Wannier−Mott exciton and the localized Frenkel exciton have been theoretically investigated over the past 50 years, and quantum mechanical models have been developed to describe these fundamental excitations. In the first case, the Wannier−Mott exciton is based on band structure in uncorrelated systems arising from significant overlap of crystalline periodic potentials. Assuming a single-electron model by applying the Hartree−Fock approximation, the Wannier−Mott exciton can be represented by an orthonormal complete set of spatially coherent, hydrogen-like wave functions.[207−209] In contrast, the Frenkel exciton is considered as an

intraatomic or intramolecular excitation characteristic of highly correlated systems, which can diffuse from site to site. Frenkel states have no internal degrees of freedom and, hence, no internal quantum numbers. As a result of polarization of the electronic subsystems of the surrounding lattice due to charges and excitons (i.e., many-body interactions), polaron-type quasi-particles are created. This renders the single-electron approximation inapplicable, and hence is typically replaced by a Hamiltonian[210,211] that describes the Frenkel state by the exciton band number and wave vector. However, the internal quantum number of the Wannier exciton may in fact correspond to the Frenkel exciton band number, while such Frenkel excitons can be regarded as a limiting case of the Wannier state, where the relative electron−hole (e−h) motion is confined to a small region of atomic or molecular scale.

The charge-transfer (CT) exciton state is usually considered as an unrelaxed polaron pair,[210] with both the positive and negative polarons of the charge pair localized on a set of discrete, identifiable, and nearly adjacent molecules.[212,213] The relaxed polaron state is called a charge pair (CP) state or self-trapped CT exciton,[172,197,209] which is at an energy lower than CT states due to strong exciton−phonon coupling (see Figure 4-5).

This localized picture is true only if each molecule is a point source of a δ-function-like potential. In that case, charges can only exist in a deep, narrow potential well at each nuclear or molecular site. In general, however, the charge is not static. And since the molecular ion has finite size, shape, and orientation, the potential cannot be accurately modeled by a δ function. In addition, for planar stacking molecules such as PTCDA and BTQBT[193,214] where there is significant overlap between the π systems of adjacent molecules in the stack, the electronic states can no longer be considered as highly localized at a single lattice site. As a result, the exciton wave function must be a somewhat uncorrelated, extended state with considerable spatial coherence, and whose shape and symmetry is dependent on the crystalline and molecular structures.[215]

As shown in the previous section, extended CT states and quantum exciton confinement in organic thin films have already been proposed and observed.[23,24,135,150,197] For multiple quantum wells consisting of ultrathin layers of PTCDA sandwiched between similar layers of NTCDA, the energies of the exciton absorption peak (Figure 4-12) and the vibrational frequencies in the PTCDA fluorescence spectrum (Figure 4-8) increase with decreasing layer thickness. Also, photoemission and inverse photoemission studies of PTCDA show that the electron−hole exchange energy, V_{exc}, which is the energy needed to remove an electron from one molecule and place it on another, is[215,216] $\sim$1 eV, or somewhat larger than the estimated molecular bandwidth of 0.1−0.4 eV.[171,197,217] This indicates weak correlation resulting from significant charge delocalization in PTCDA. All of these results suggest that extended CT excitons are best described using quantum (extended) rather than simple electrostatic (localized) models typically applied to organic molecular crystals.[195,210]

Starting from the real-space representation of chemical bonding, Mukamel and co-workers[28,218−220] proposed a second quantization approach to understand quantum size effects in ultrathin organic films. Their method is to map the electronic motions of the confined states onto a set of coupled harmonic oscillators. On the basis of the single electron, reduced density matrix, and then solving the time-dependent Hartree−Fock equation, the electronic charges and motion can be related to their optical response.[220] By using the tight-binding Hamiltonian for π electrons, a basis set of exciton states is chosen to correspond to the discrete e−h separations, where each state is perturbed by Coulomb interactions, electron−electron coupling, lattice polarization, aggregate response, chemical bond oscillations, and interactions which induce the intermolecular charge transfer. The relative magnitudes of these terms determine the characteristics[28,219,221] of the exciton (i.e., whether it follows Frenkel, CT, or Wannier behavior). By this means, it was found[218] that quantum confinement of the relative (correlated) e−h motion of the CT exciton plays an important role in determining the magnitude of the third-order nonlinear susceptibility, $\chi^{(3)}$, of conjugated polyenes.

At low exciton densities where exciton−exciton coupling can be neglected, the self-consistent field approximation is valid. In this case, the e−h motion can be described by a quasi-particle interacting with an average field of the remaining charges. Based on this quasi-particle picture, the main goal of the work of Shen and Forrest[176] was to find a simple approach (i.e., a one-electron Hamiltonian) to describe the relatively delocalized CT exciton in anisotropic, nonpolar organic crystals, to study the effect of crystalline anisotropy on CT exciton energies, and to understand the experimental phenomena such as "quantum confinement" in multilayer structures, the electroabsorption (EA) spectra,[177] as well as other quantum phenomena frequently observed in nonpolar organic molecular crystals. This treatment has been found to be quite general, and was also used to describe the EA spectra in inorganic semiconductors such as GaAs.[13]

4.2.1. Hamiltonian for CT Excitons

The following general form was chosen for the Hamiltonian describing the motion of electron−hole pairs in OMCs such as PTCDA:[176]

$$H_o = T + V_{e-h} + V_{pseudo} \qquad (4.2)$$

where T is the kinetic energy, V_{e-h} is the electron−hole binding energy (or Coulomb energy), and V_{pseudo} is the periodic crystalline pseudopotential. For semiconductors with a large overlap of atomic wave functions between ionic cores in the crystal, the periodic pseudopotential (which includes on-site correlation effects) applied on the valence electrons is weak enough to result in a modified free electron gas. In this limit, the motion of the electron can be described by the one-electron Schrödinger's equation, leading to a description of the energy levels in terms

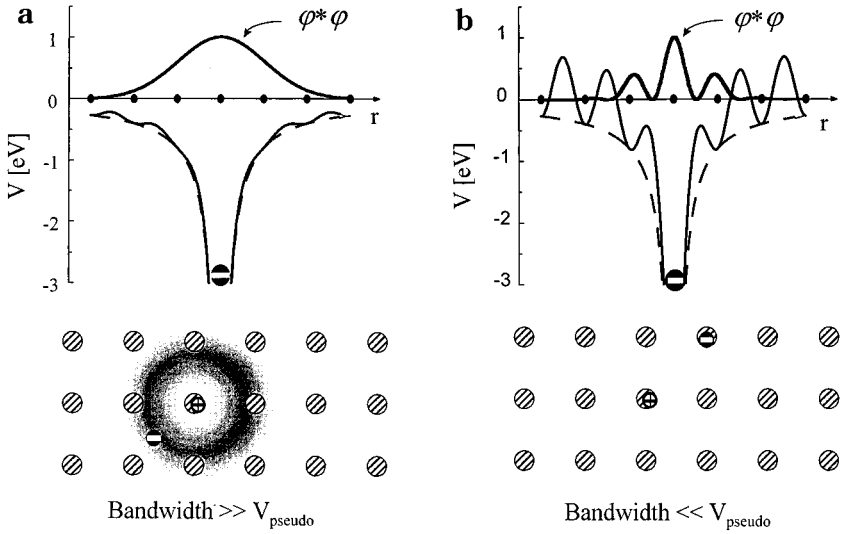

Figure 4-16. Schematic diagram showing V_{e-h} (dashed curve) with the periodic correction term (or pseudopotential, V_{pseudo}), which is a function of the molecular size, shape and separation. The sum of V_{e-h} and V_{pseudo} gives the total potential (solid curve) for an exciton as a function of e−h separation r. Also shown are plots of the wave function density, $\phi^*\phi$ vs r for (a) delocalized and (b) localized exciton states. The lower part of each figure provides a schematic representation of the localized and delocalized CT exciton states.

of a family of continuous functions, $E_n(\mathbf{k})$, each with the periodicity of the reciprocal lattice. This results in an incipient *band structure*, where n refers to the energy band, and $\mathbf{k}$ is the conserved crystal momentum. This small lattice periodic pseudopotential, V_{pseudo}, leads to relatively high carrier mobility (>0.01 $cm^2/(V\ s)$), and wide energy bands (greater than or on the order of the electron−hole exchange energy, V_{exc}). Figure 4-16a shows a schematic representation of V_{e-h}, and the total "delocalized" exciton potential $V_{deloc} = V_{e-h} + V_{pseudo}$, typical of ionic or covalently bonded semiconductors. Under such conditions, the exciton states are hydrogenic, where the lowest energy (s-like) electron wave function density is $(\phi^*\phi)_{deloc}$, with its characteristic monotonic decay and extended spatial coherence.

In contrast to inorganic semiconductors, organic molecular crystals are typically characterized by weak intermolecular vdW interactions. This leads to relatively small overlap of molecular orbitals and, hence, a strong localization of charge carriers. Under such conditions, both the one-electron approximation and the concept of extended energy bands are not appropriate. Additionally, elastic and inelastic interactions between the charge carrier and lattice are strongly coupled, such that the wave momentum $\mathbf{k}$ is not conserved (leading to poor spatial coherence), thus further increasing charge localization.[222,223] In this case, V_{pseudo} is large compared to V_{e-h}. Here, V_{pseudo} corresponds to the on-site correlation energy which approximately equals the difference between the exchange energy, V_{exc}, and the crystal polarization energy, $P_E(\mathbf{r})$. This is characteristic of many vdW solids, leading to a low charge carrier mobility ($<10^{-4}$ $cm^2/(V\ s)$) and narrow ($<kT$) energy bands. Figure 4-16 also shows the total potential, V_{loc}, and wave function density, $(\phi^*\phi)_{loc}$ for such "conventional", highly correlated OMCs where the e−h pair is localized on the molecular sites. Indeed, the calculated band structure for anthracene indicates that electronic polarization significantly reduces the effective bandwidth. The resulting electron mean free path is found to be smaller than the intermolecular spacing, demonstrating the inconsistency of the band model for anthracene-type crystals.[222,223]

However, the experimental fluorescence and absorption data for ultrathin PTCDA films suggest that for some molecular crystals where there is significant overlap between the π-systems of adjacent molecules, the energy bandwidth is comparable to or larger than[220] V_{pseudo} while the mean free path is at least as great as the intermolecular spacing, leading to significant charge delocalization. Since the electronic polarization time constant[210] is very short (10^{-16} to 10^{-15} s), the one-electron model might still apply in such cases.

Given the unusually small intermolecular distance in PTCDA which leads to a high hole mobility (∼1 $cm^2/V\text{-}s$) along the stacking direction,[172,224] spatially extended CT states,[23,24,135,177] with large oscillator strengths and a combined lowest unoccupied molecular orbital (LUMO) and highest occupied molecular orbital (HOMO) energy bandwidth of 0.1−0.4 eV,[171,197,215,217] is comparable to $V_{pseudo} \sim 0.5$ eV. Here, $V_{pseudo} = |V_{exc} - P_E|$, with $P_E = 1.5$ eV for PTCDA.[176] Using $V_{exc} \approx 1$ eV measured using photoelectron and inverse photoelectron spectroscopy,[215,216] we infer that for PTCDA and similarly "large bandwidth" vdW solids, V_{pseudo} is small and correlation effects do not dominate the electronic behavior of the material.

Using these arguments, the Hamiltonian for delocalized CT excitons in the center of mass coordinates has been written as[176]

$$H_o = T + V_{e-h} + V_{pseudo} \cong -\frac{\hbar^2}{2}\left(\frac{\nabla_{||}^2}{m_{||}} + \frac{\partial_\perp^2}{m_\perp}\right) - \frac{q^2}{r} + P_E(\boldsymbol{r}) \quad (4.3)$$

Here, $\mathbf{r} = \mathbf{r}_e - \mathbf{r}_h$ is the displacement vector of the e−h pair, $m_i = m_{e,i}m_{h,i}/(m_{e,i} + m_{h,i})$ is the reduced effective mass along direction $i = \perp$ or $||$, and m_e (m_h) is the effective electron (hole) mass. For PTCDA, $\perp$

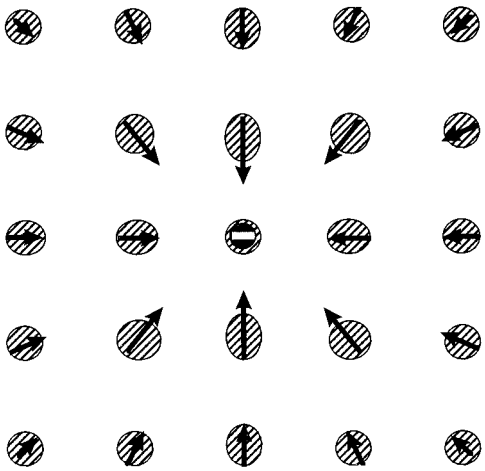

Figure 4-17. Schematic representation of lattice polarization in an OMC. The cross-hatched circles represent the molecular positions within the lattice, and an excess charge is placed at (−) in the center of the diagram.

is taken along the substrate normal,[73] z. Finally, the displacement-dependent polarization energy, $P_E(\mathbf{r})$, is a function of the crystal symmetry and molecular structure.

Polarization of the crystal due to the presence of an excess charge is illustrated schematically in Figure 4-17. These effects, which are typically on the order of 1−2 eV in OMCs, must be calculated to fully account for the binding energy between the electron and hole forming the exciton. Calculations of polarization energies using classical electrostatics were carried out by Silinsh using the self-consistent polarization field (SCPF) method[225] and by Bounds and Siebrand[226] in terms of Fourier-transformed lattice multipole sums. They found that, to first order, the e−h interaction potential (V_{e-h}) is essentially Coulombic, e.g., $V_{e-h} = -q^2/\epsilon_{avg}r$, for large charge pair separations, r (i.e., $r >$ one lattice constant), where ϵ_{avg} is the spatially averaged crystal dielectric constant. This result is, in some respects, similar to the case of conventional semiconductors where the crystal lattice consisting of electrons and nuclei can be regarded[227] quasi-macroscopically as polarizable media with a spatially averaged dielectric constant, ϵ_{avg}, as long as the e−h distance is large compared to the lattice constant. Fundamentally, an electron in the conduction band, or the lowest unoccupied molecular orbital (LUMO), as well as a hole in the valence band, or the highest occupied molecular orbital (HOMO), are always accompanied[228] by electronic polarization (via polarons) of the surrounding medium. This similarity suggests the feasibility of applying the Wannier exciton model to describe CT excitons with radii larger than one lattice constant.

Hence, the crystal polarization in the anisotropic OMC, PTCDA, as well as in NTCDA was calculated[176] using a method similar to that of Bounds et al.[226,229] From this analysis, $P_E(\mathbf{r})$ in the effective one-exciton Hamiltonian in eq 4.3 can be used to find energies and wave functions of CT excitons by solving Schrödinger's equation. To calculate $P_E(\mathbf{r})$, Shen and Forrest[176] considered a lattice with a basis whose unit cell volume is v, and a molecule at $\mathbf{r}(lk)$, where $l = \{l_x,l_y,l_z\}$ is the lattice index, and $k = \{1,2,3,...\}$ is the index of a particular basis molecule within the unit cell. The medium is polarized due to the electric field, $\mathbf{F}_o$, from excess charges in the crystal. The macroscopic field $\mathbf{F}_{mac}$ at site (lk) thus includes $\mathbf{F}_o$ and the induced dipole field, $\mathbf{F}_{ind}$ via

$$\mathbf{F}_{mac}(lk) = \mathbf{F}_o(lk) + \mathbf{F}_{ind}(lk) \tag{4.4}$$

where $\mathbf{F}_{ind}$ is the sum of the field due to the dipole at the same site (self-field, $\mathbf{F}_{self}$) and that due to the surrounding dipoles. Assuming a spherical dipole for homogenous and isotropic media, $\mathbf{F}_{self}$ is taken as[230] $-\boldsymbol{\mu}(lk)/3\nu\epsilon_o$, where ϵ_0 is the vacuum permittivity and $\boldsymbol{\mu}(lk)$ is the dipole moment tensor. Then

$$\boldsymbol{\mu}(lk) = \alpha(k)\cdot\mathbf{F}_{loc}(lk) \tag{4.5}$$

where $\alpha(k)$ is the effective polarizability of molecule k, and $\mathbf{F}_{loc}(lk)$ is the local (average) field at site (lk) excluding the induced field due to molecule (lk). Hence

$$\mathbf{F}_{loc}(lk) = \mathbf{F}_{mac}(lk) - \mathbf{F}_{self}(lk) \tag{4.6}$$

The total crystal polarization energy, P_E, is found by integrating over the individual molecular polarizations, $p_E(\mathbf{y})$ over the first Brillouin zone (1BZ)

$$P_E = -{}^1/_2\sum_k \tilde{\mathbf{F}}_o(lk)\cdot\boldsymbol{\mu}(lk) = -v/2\int_{1BZ} p_E(\mathbf{y})\, d\mathbf{y} \tag{4.7}$$

Thus, the e−h interaction energy is a sum of the unscreened Coulomb attraction and the crystal polarization energy, via

$$V_{e-h} = -\frac{q^2}{|\mathbf{r}(l_1k_1,l_2k_2)|} + P_E[\mathbf{r}(l_1k_1,l_2k_2)] \tag{4.8}$$

Equation 4.8 gives the potential energy of an e−h pair in a nonpolar organic crystal and includes the e−h attraction as well as the microscopic lattice response to the charge pair in terms of the polarization energy, as required in the Hamiltonian in eq 4.3.

Equation 4.8 has been used to calculate V_{e-h} in NTCDA and PTCDA, using known dielectric tensor elements.[175] The crystalline and dielectric anisotropies of NTCDA are much smaller than for PTCDA due to the herringbone stacking habit in NTCDA. This leads to a nearly isotropic index of refraction for NTCDA, resulting in a spatially averaged diagonal dielectric tensor whose elements along the principle axes are $\epsilon_{avg} = 2.6$.

The interaction energies, $V_{e-h}(r)$ for both NTCDA and PTCDA are shown in Figure 4-18. The results are compared with the "screened" Coulomb potential, $V_{scr} = -q^2/|\epsilon\cdot\mathbf{r}|$, where ϵ is the macroscopic dielectric tensor for the crystal. Since diagonal elements of the NTCDA dielectric tensor are approximately equal,[176] the e−h interaction energy in Figure 4-18a is compared with $V_{scr} = -q^2/\epsilon_{avg}r$, providing a good fit to the calculated values along all crystalline axes.

For the highly anisotropic PTCDA, V_{e-h} depends sensitively on the crystal direction for $r <$ 20 Å. The dashed curve in Figure 4-18b is a plot of $V_{scr} = -q^2/\epsilon_{avg}r$, where $\epsilon_{avg} = 3/(1/\epsilon_\perp + 2/\epsilon_{||}) = 3.2$. Using ϵ_{avg}

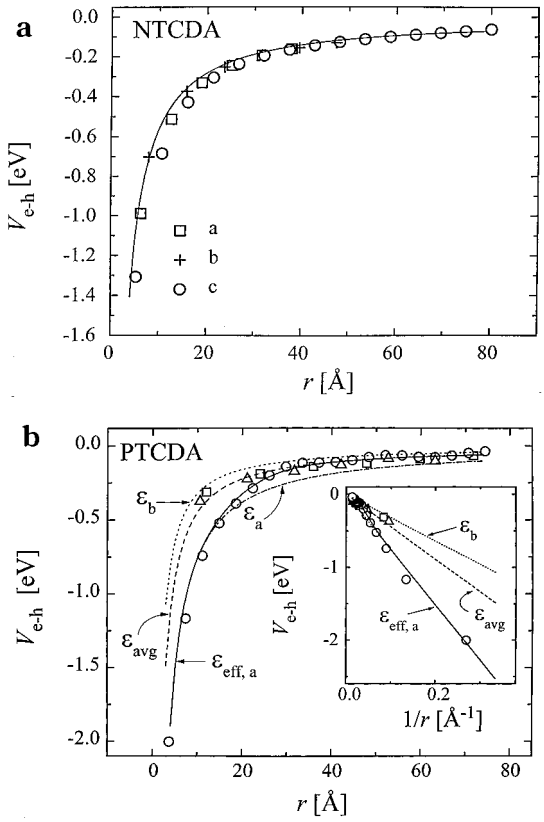

Figure 4-18. Electron-hole potential energy (V_{e-h}) calculated for (a) NTCDA and (b) PTCDA as a function of charge separation (r) along three crystalline axes (data points). Since NTCDA is isotropic, the calculation is compared with results obtained in the isotropic continuum approximation, where $\epsilon = 2.6$ (solid line). The calculation for the anisotropic PTCDA is carried out along three crystalline axes (*a* axis, circles; *b* axis, squares; *c* axis, triangles). The dashed−dotted curve is $V_{e-h} \approx V_{scr}$ using the dielectric constant along the *a* axis, $\epsilon_a = 21$, and the dotted curve uses value along the *b*, *c*, $\epsilon_b = 4.5$ (where $\epsilon_b \approx \epsilon_c$). The dashed curve uses the spatial averaged dielectric constant $\epsilon_{avg} = 3.2$. Note when $r > 25$ Å, ϵ_{avg} results in the best fit, and when $r < 15$ Å, ϵ_i, where i represents the crystalline axes, provides excellent approximations to the calculated values. The solid curve uses the effective dielectric constant, ϵ_{eff} described in text (from ref 176).

results in the best fit to V_{e-h} for large r (>25 Å), regardless of direction, suggesting that the potential becomes spatially averaged at distances of only a few molecular lattice constants from the origin, even for anisotropic systems such as PTCDA. However, for small r (<15 Å), V_{e-h} deviates significantly from the spatial average (clearly apparent in the inset of Figure 4-18b, where V_{e-h} is plotted as a function of $1/r$). For small r, the mean dielectric constant can be approximated using $V_{scr} = -q^2/\epsilon_i r$ (where i refers to crystalline directions), as shown by the corresponding curves in Figure 4-18b.

Once V_{e-h} was determined, a trial wave function was chosen to solve eq 4.3. Due to the relative isotropy of PTCDA in the || direction, cylindrical coordinates ($\mathbf{r} = (\rho,\phi,z)$ with ρ, ϕ in ||, and z in ⊥ directions) were used. In these reduced coordinates, the kinetic energy operator is isotropic, where the anisotropic mass and dielectric tensor elements are expressed in the parameter, $\beta_i = (m_i/m_o)^{1/2}\,\epsilon_{avg}/\epsilon_i$. Here m_o is the free electron mass and m_i is the reduced mass in the i direction. The trial wave function chosen for the lowest, 1s exciton state was[231]

$$\varphi_{1s} = \exp(-g)/\sqrt{\pi c_{||}^{\,2} c_{\perp}} \qquad (4.9a)$$

where

$$g = (\rho'^2/c_{||}^{\,2} + z'^2/c_{\perp}^{\,2})^{1/2} \qquad (4.9b)$$

Here, $c_{||}$ and $c_{\perp}$ are variational parameters used to minimize energy, $\rho' = \epsilon_i a_B \rho$, and $z' = \epsilon a_B z$, and $a_B = 0.529$ Å is the Bohr radius of the free electron. The lowest energy, $E_{1s}^{(0)}$, is found via

$$\bar{E}_{1s}^{(0)}(\bar{c}_{||},\bar{c}_{\perp}) = \min_{c_{||},c_{\perp}} \langle \varphi_{1s}|H_o|\varphi_{1s}\rangle$$

and the exciton radius along i is then

$$\bar{a}_i = a_B \bar{c}_i \epsilon_{avg} \sqrt{m_o/m_i}$$

4.2.2. Theoretical Fits to Electroabsorption and MQW Absorption Spectra

4.2.2.1. Electroabsorption Spectrum. The theory outlined above was used to fit the EA spectrum of PTCDA. Here, EA has been shown to be an extremely useful means for providing information about band structure and localized states in both organic and inorganic semiconductors.[13,177,212,232,233] Localized states in OMCs result in correspondingly smaller electric field effects than in inorganic semiconductors where the low exciton binding energy (~10 meV) can be strongly perturbed by even small external fields. In OMCs, the first- and second-order Stark effects are typically interpreted as due to a localized dipole moment interacting with the applied electric field.[212,234] For tightly bonded (~1 eV) Frenkel excitons, the change of absorption follows the first derivative of the absorption with respect to energy (i.e., the quadratic Stark effect), whereas for polar CT excitons with large transition dipoles and with binding energies ≤500 meV, the field-induced change of absorption is proportional to the second derivative of the absorption spectrum.[212,234] For example, electroreflectance studies of the $\pi-\pi^*$ excitations of the polydiacetylene single crystal poly-1,6-di-*N*-carbazolyl-2,4-hexadiynal (DCHD) provided evidence for an extended CT exciton state whose EA response is 10 times larger than for the localized Frenkel exciton lines in that same material.[212,233,235]

The room temperature excitonic EA spectrum due to excitons in crystalline thin films of PTCDA has been studied[177] at electric fields ranging from $F = |\mathbf{F}| = 100$ to 300 kV/cm . This field is sufficiently small to consider its effects to be a linear perturbation on the exciton binding energy. Given H_o, along with the basis wave functions, φ_n, provided in eq 4.13, the EA spectrum of PTCDA has therefore been fit using a perturbation Hamiltonian, H_1. Since an external field $\mathbf{F}_o$ will polarize the crystal, the local field $\mathbf{F}_{loc}$ at the exciton, and the macroscopic field $\mathbf{F}_{mac}$ in the crystal, may differ. Hence

$$H_1 = q\int_{r_e}^{r_h} \mathbf{F}_{loc}\, d\mathbf{r} = q\mathbf{F}_{mac}\cdot\mathbf{r} \qquad (4.10)$$

This treatment is valid only at low electric fields, where $qFa_{avg} = q|\mathbf{F}|a_{avg} < E^{(0)}_{1s} \cong 200$ meV, or $F < 2$ MV/cm, where

$$a_{avg} = \sqrt[3]{\bar{a}_{\perp}\bar{a}_{||}^{2}} \approx 11 \text{ Å}$$

Using the perturbed trial wave function[236]

$$\psi_{1s} = \varphi_{1s}\left\{1 - \frac{2H_1\epsilon_{avg}a_{avg}}{q^2}\left[1 + \frac{g_{1s}}{2}\right]\right\} \quad (4.11)$$

the energy shift in the CT absorption peak (ΔE) was found for a field oriented in the normal ($\perp$) and in-plane ($||$) film directions, as

$$\Delta E = E_{1s} - E^{(0)}_{1s} = \begin{cases} -\frac{9}{4}\epsilon_{avg}F_{\perp}^{2}\bar{a}_{\perp}^{2}a_{avg} \\ -\frac{9}{4}\epsilon_{avg}F_{||}^{2}\bar{a}_{||}^{2}a_{avg} \end{cases} \quad (4.12)$$

Also, the broadening of the state due to the external field is given by

$$\langle H_1^{2}\rangle = \langle (q\mathbf{F}_{mac}\cdot\mathbf{r})^2\rangle = \begin{cases} q^2\mathbf{F}_{\perp}^{2}\bar{a}_{\perp}^{2} \\ q^2\mathbf{F}_{||}^{2}\bar{a}_{||}^{2} \end{cases} \quad (4.13)$$

The ratio of the exciton line shift broadening is therefore *independent of crystal direction*:

$$\frac{\Delta E}{\langle H_1^{2}\rangle} = -\frac{9}{4}\frac{\epsilon_{avg}a_{avg}}{q^2} \quad (4.14)$$

In the limit of small fields, the change of the exciton absorption spectrum depends quadratically on the electric field, via

$$\Delta\alpha(\mathbf{F},E_{ph}) = \frac{\partial\alpha(E_{ph})}{\partial E_{ph}}\Delta E + \frac{\partial^2\alpha(E_{ph})}{\partial E_{ph}^{2}}\langle H_1^{2}\rangle + \ldots \quad (4.15)$$

where E_{ph} is the photon energy. The experimental quadratic dependence of $\Delta\alpha$ is shown in the inset of Figure 4-19 for PTCDA,[177] where the electric field was applied along $\perp$, and $\Delta\alpha$ was measured at the CT^{ST} and CT^{F} energies of $E_{ph} = 2.1$ and 2.2 eV, respectively (Table 7). The EA spectra obtained for the electric field oriented along $\perp$ and $||$ directions are plotted in Figure 4-20.

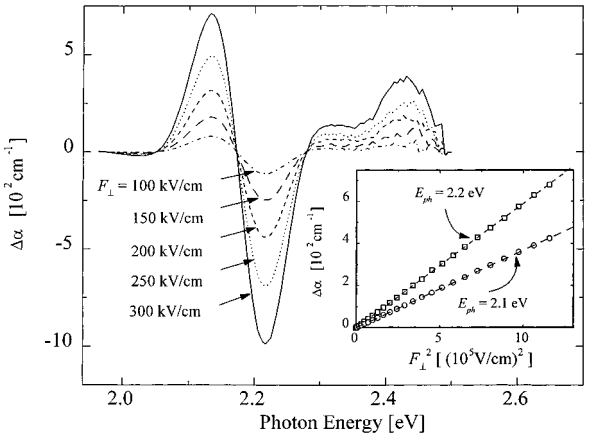

Figure 4-19. Room temperature PTCDA electroabsorption spectra at various electric fields oriented normal to the substrate, $F_{\perp}$. Inset: Electroabsorption magnitude as a function of $F_{\perp}^{2}$ at two different photon energies, $E_{ph} = 2.1$ and 2.2 eV (from ref 176).

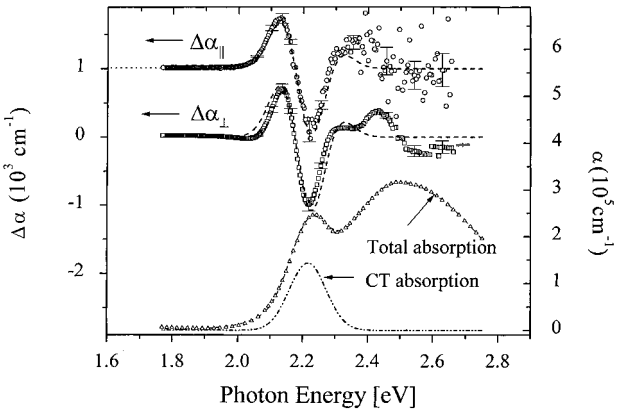

Figure 4-20. Absorption (α) and electroabsorption ($\Delta\alpha$) spectra of PTCDA. Top: Electroabsorption spectra and numerical fits (dashed lines) with fitting parameters listed in Table 8. For the field oriented parallel to the substrate, the electroabsorption (circles), $\Delta\alpha_{||}$, was obtained at $F_{||} = 0.16$ MV/cm, and for perpendicular fields (squares), $\Delta\alpha_{\perp}$, the field was $F_{\perp} = 0.15$ MV/cm. Bottom: Absorption spectrum (triangles) and the fit (lines). The fit of the total spectrum assumes a series of Gaussian line shapes corresponding to previously resolved (ref 197) exciton line shapes for PTCDA. The dashed−dotted line corresponds to the CT absorption component of the fit with a peak energy of 223 ± 0.03 eV and a width of 0.17 eV (from ref 176).

The lowest energy absorption peak at 2.23 ± 0.03 eV in the PTCDA spectrum was shown in section 4.1.1 to be a spatially extended CT state, whereas the higher energy absorption peaks correspond to Frenkel states.[197] Due to the localized nature of the Frenkel excitons, these later states are less sensitive to the applied electric field.[237] Furthermore, since Frenkel excitons respond to the electric field via the change in polarizability, the EA spectra of such states are proportional to the first derivative of absorption[212], $\partial\alpha/\partial E$. Hence, the high energy features (>2.3 eV in PTCDA) exhibit a smaller electric field dependence and different line shape as compared to the low energy CT states. The EA spectrum measured for PTCDA, shown in Figure 4-20, is therefore primarily due to line broadening of the lowest energy, extended CT state.

Hence, $\Delta\alpha$ was fit by Shen et al.[177] using two parameters ΔE and $\langle H_1^{2}\rangle$, while $\partial\alpha/\partial E$ and $\partial^2\alpha/\partial E^2$ were obtained from the lowest, inhomogeneously (phonon) broadened CT absorption line with a peak energy of 2.23 ± 0.03 eV and a width of 0.17 ± 0.02 eV (see Table 7). According to eq 4.14, broadening dominates the EA spectra due to the small exciton radius ($\Delta E/\langle H_1^{2}\rangle = -(0.14 \pm 0.02) \times 10^5$ V/cm^2/meV^2). Thus, the ratio $\Delta E/\langle H_1^{2}\rangle$ is used to estimate a_{avg}, while $\langle H_1^{2}\rangle_{\perp}/\langle H_1^{2}\rangle_{||}$ gives the ratio of the exciton radii along $\perp$ and $||$ directions. Figure 4-20 shows the EA data and fits (dashed lines) employing the theoretical treatment of section 4.2.1 for normal and in-plane fields,[176] obtained using $\bar{a}_{\perp} = 12.5 \pm 0.5$ Å and $\bar{a}_{||} = 10.2 \pm 0.4$ Å, indicating that the CT state does indeed extend over several molecular sites, consistent with the analysis of the solution fluorescence discussed in

Table 8. Summary of the Result for PTCDA (From Ref 176)

	symbol	unit	EA results	QC results
exciton binding energy	E_{1s}	meV	185 ± 20	177 ± 20
exciton radius along the normal direction	$a_\perp$	Å	12.5 ± 0.5	12.9 ± 1.0
exciton radius along the in-plane direction	$a_\parallel$	Å	10.2 ± 0.4	
effective reduced mass along the normal direction	$m_\perp$	m_o	0.17 ± 0.02	0.16 ± 0.02
effective reduced mass along the in-plane direction	$m_\parallel$	m_o	0.19 ± 0.02	

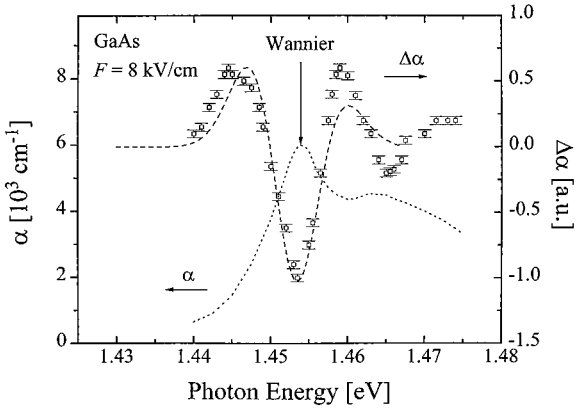

Figure 4-21. Top: Fit (dashed line) to the electroabsorption spectrum (squares) of GaAs at $F = 8$ kV/cm taken from ref 13 using the theory in text. Bottom: Band edge absorption spectrum of GaAs indicating the Wannier exciton state. Data also from ref 13 (from ref 176).

section 4.1.1. The small anisotropy found for the PTCDA exciton radii suggests a similarly small anisotropy in the effective reduced mass, which are calculated to be $m_\perp = (0.17 \pm 0.01)m_o$ and $m_\parallel = (0.19 \pm 0.01)m_o$. The exciton binding energy was $E_{1s} = 185 \pm 20$ meV. Results from the EA analysis for PTCDA are provided in Table 8.

While the apparent isotropies in the exciton mass and radii appear unexpected for such an anisotropic medium as PTCDA, EA provides the "Coulombic" effective mass of the nearly symmetric 1s state. On the other hand, hole mobility measurements indicate a large asymmetry (with[37] $\mu_{p,\perp} \cong 10^6\mu_{p,\parallel}$). Mobility, however, reflects the "transport" effective mass inferred from $\mu = q\tau/m$. Since $\mu \propto \tau$, where τ is the carrier scattering time, which can carry the anisotropy in μ due to enhanced scattering along a particular crystalline direction. For the case of PTCDA, the motion of a charge along $\parallel$ is easily scattered by the large intermolecular potential barriers (for example, V_{pseudo}, in Figure 4-16), leading to strong localization in that direction. Hence, we expect that $\tau_\parallel << \tau_\perp$, leading to the very anisotropic mobility observed, while the effective mass remains largely isotropic, since it is primarily due to the electronic distribution *within* a given molecule.

The analysis of the EA spectra has also been applied to study[176] Wannier excitons in GaAs. This is readily apparent by similarities between the EA spectra of PTCDA and GaAs[13] shown in Figure 4-21. The broadening observed in GaAs has been qualitatively attributed[13] to field ionization shortening of the exciton lifetime, optical-phonon collisions, etc. However, a simple, quantitative fit can be achieved by application of the wave function and potential employed to describe field-induced line broadening in CT excitons in organic films. The EA data in Figure 4-21 were fit (dashed line) assuming $a = 70$ Å, and $E_{1s} = 8$ meV, consistent with expected values for bulk GaAs.[238] This fit to the bulk GaAs EA line shape using eq 4.3 suggests that both Wannier and CT excitons have a common physical origin and can both be equally well approximated by hydrogenic wave functions broadened in an external electric field.

4.2.2.2. Quantum Confinement in Organic Multilayers. Evidence for quantum confinement of extended CT states in organic multilayer structures has previously been provided by So,[23,24] Haskal,[135,163] and Hong.[150] As discussed above, it was observed that the lowest energy absorption peak, the ground-state vibrational frequency of the exciton fluorescence spectra, and the exciton photoluminescence peak shift to higher energies as the layer thickness is decreased. Shen and Forrest[176] have applied the general Hamiltonian of eq 4.3 to quantitatively study these blue shifts in the CT absorption peak in PTCDA, and then compared the resulting exciton radius, effective mass and binding energy with those obtained from direct measurements obtained from the EA spectra presented in section 4.2.2.1.

The source of the confinement in the organic layers of thickness, d, are the energy discontinuities of the HOMO and LUMO bands at the heterointerfaces between the adjoining materials. The Hamiltonian of an e−h pair in the PTCDA/NTCDA multiple quantum well structure shown in Figure 4-22 has been expressed as[176]

$$H = T_\parallel + T_{e,\perp} + T_{h,\perp} + V_{e-h} + V_e(z_e) + V_h(z_h) \tag{4.16}$$

where $T_\parallel$ is the in-plane kinetic energy of the exciton center of mass, $m_{e-h,\parallel}$ is the reduced mass along $\parallel$, and $T_{e,\perp}$ and $T_{h,\perp}$ are the kinetic energies along the normal (i.e., molecular stacking) direction with corresponding masses $m_{e,\perp}$ and $m_{h,\perp}$. Also, z_e and z_h are the normal coordinates for the electron and hole, respectively, and V_e, V_h are the LUMO and HOMO levels in Figure 4-22. For multilayers consisting of PTCDA and NTCDA, energy barriers to carrier and energy transport are formed by the offsets of the LUMO and HOMO energy band minima. These energies were found[23] via analysis of the current−voltage characteristics of PTCDA/NTCDA heterojunctions, to be $\Delta E_{LUMO} = 980$ meV and $\Delta E_{HOMO} = 50$ meV (where NTCDA has the larger HOMO−LUMO energy gap). Since $\Delta E_{LUMO} \gg \Delta E_{HOMO}$, and $m_e \gg m_h$, the quantum well for electrons was approximated as having an infinite depth, with the electron confined in a single layer of "index" $N = 0$. In this analysis, only the lowest, nearly symmetric 1s CT state corresponding to the lowest energy absorption peak observed in the PTCDA spectrum was considered.

The trial wave function of the lowest exciton state for an electron in layer 0, and a hole in layer N can

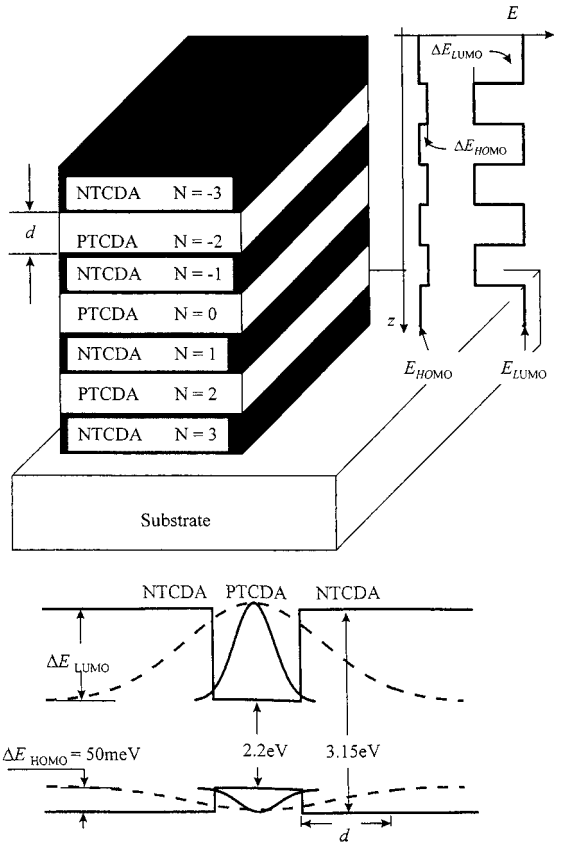

Figure 4-22. Top: Schematic diagram of a PTCDA/NTCDA MQW structure, where N is the layer index. The HOMO−LUMO energy diagram of this structure is shown to the right, and in greater detail at the Bottom. Also shown in the lower band diagram are schematic illustrations of confined wave functions (solid lines) and in the bulk (dashed lines).

be written as the product of the free exciton wave function ($\phi_{e-h}(\rho, z = z_e - z_h)$), and the electron ($\phi_e(z_e)$) and hole ($\phi_h(z_h)$) envelope functions. These latter functions are oscillatory in the wells and decaying in the barriers. The total wave function is

$$\psi = \phi_e(z_e)\phi_h(z_h)\phi_{e-h}(\rho, z = z_e - z_h) \quad (4.17a)$$

where

$$\varphi_e(z_z) = \begin{cases} \cos(\pi_0 z_e/d) & |z_e| \le d/2 \\ 0 & |z_e| > d/2 \end{cases} \quad (4.17b)$$

$$\varphi_h(z_h) = \begin{cases} \cos[k(z_h - Nd)] & N \in \text{even} \\ \dfrac{\cos(kd/2)\cosh[\kappa(z_h - Nd)]}{\cosh(kd/2)} & N \in \text{odd} \end{cases} \quad (4.17c)$$

and

$$\varphi_{e-h}(\rho, z = z_h - z_e) = \begin{cases} A(N)\exp(-g) & N \in \text{even} \\ A(N)\exp\left(-\dfrac{m_{h,b,\perp} g}{m_{h,w,\perp}}\right) & N \in \text{odd} \end{cases} \quad (4.17d)$$

with N = even (odd) corresponding to the layer index for wells (barriers), and $A(N)$ is a constant depending on both g and the effective masses in the $\perp$ direction. Thus, k and κ are obtained from solutions of the time independent Schrodinger equation. Minimizing E_{1s} the CT[O-F] absorption peak shift data obtained by So[24] and Haskal[135] in multilayer structures, where d was varied from 10 to 500 Å, have been fit[176] to obtain the exciton radius and reduced masses in the $\perp$ direction.

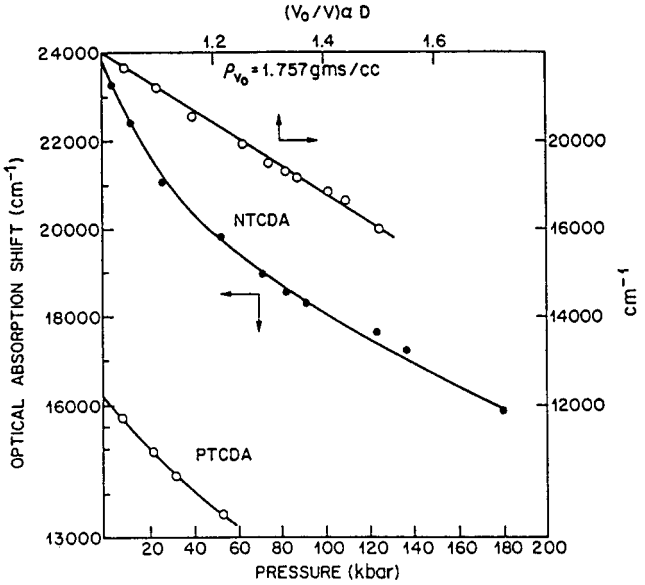

Figure 4-23. The low-energy absorption tail shift as a function of pressure for NTCDA and PTCDA films. Upper straight line is the same plot for NTCDA vs relative density (from ref 240).

The results obtained from this fit for different hole masses are shown in Figure 4-12, where the dashed curve corresponds to $m_{h,\perp} = 0.18m_o$ and the dotted line corresponds to $m_{h,\perp} = 0.14m_o$. The best fit (solid line) is obtained for $m_{h,\perp} = (0.16 \pm 0.01)m_o$. The blue shift of the exciton energy vs d tapers off for $d < 10$ Å due to the onset of tunneling between wells, in which case the holes are no longer further confined as $d \rightarrow 0$. This condition corresponds to that observed for organic bilayers reported by Hong et al.[150]

The effective mass, radius ($a_\perp = 12.9 \pm 1.0$ Å) along the normal direction, and exciton binding energy measured using the absorption blue shift data for PTCDA/NTCDA MQWs are consistent with the results obtained independently from fitting the EA data for homogeneous PTCDA thin films (see Table 8). These data provide the first *conclusive* evidence that Wannier-like CT excitons exist in molecular compounds characterized by closely spaced planar molecules, resulting in a large molecular wave function overlap between adjacent molecules with extended, Bloch-like, spatially coherent electronic states.

This situation is analogous to the directly observed transition from Frenkel to Wannier excitons in pressurized fluid xenon.[239] Furthermore, the narrowing of the optical bandgap of PTCDA under hydrostatic pressure,[240] shown in Figure 4-23, supports the delocalized picture for the CT exciton in this material. That is, the $\pi-\pi^*$ transition energy is found to significantly decrease with pressure due to the broadening of the energy bands on close approach of the adjacent molecules in the stacks.

To further test the effects of quantum confinement, room temperature, time-resolved fluorescence measurements of the CT[ST-2] transition peak at $E =$

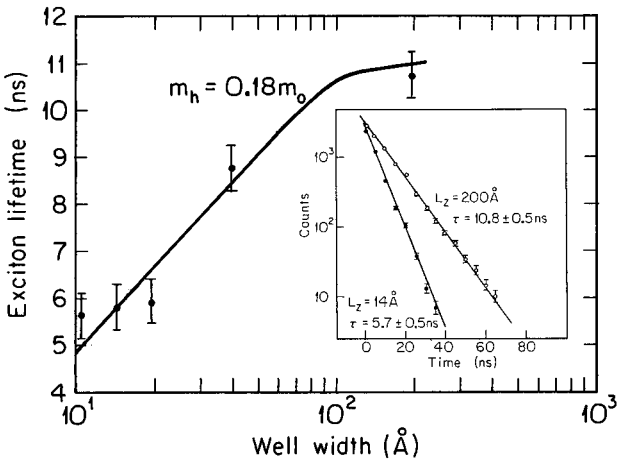

Figure 4-24. Exciton lifetime as a function of PTCDA layer width in symmetric PTCDA/NTCDA multilayer structures. The solid line is a fit to the data based on the theory of So (ref 24) and Shen (ref 176). Inset: Photoluminescence time decay transients for two MQW samples. The transient for the $d = 200$ Å sample has been shifted upward by 0.1 decade in this plot for clarity (from ref 24).

1.70 eV were carried out by optically pumping the MQWs with a 4 ns pulsed Ar ion laser.[24] At this energy, excitons were generated only in the PTCDA layers since NTCDA is transparent at this wavelength. The fluorescence decay transients for two MQW samples obtained at 20 K are shown in the inset of Figure 4-24. Here, the exponential decay over several decades in intensity of the transient is apparent. In addition, the dependence of the exciton lifetime (τ_{ex}) on well width (d) is shown by data points in Figure 4-24, with τ_{ex} decreasing from 10.8 ± 0.5 ns for $d = 200$ Å, to 5.7 ± 0.5 ns for $d = 10$ Å. Now, the total recombination rate is $\tau^{-1} = \tau_{ex}{}^{-1} + \tau_{nr}{}^{-1}$, where τ_{nr} is the time constant for nonradiative decay, such as due to trapping at the PTCDA/NTCDA interfaces. If the nonradiative recombination rate is such that $\tau_{ex}{}^{-1} < \tau_{nr}{}^{-1}$, the lifetime should decrease due to traps, thereby decreasing the intensity of the radiative emission. The time-integrated room temperature fluorescence intensity, however, was found to be independent of layer thickness,[24] indicating that nonradiative recombination is not significant. On the contrary, Haskal[135] found that the integrated fluorescence intensity significantly *increased* with decreasing d (Figure 4-8). A similar inference can be made from experiments[34] which indicate that carrier collection after photogeneration is enhanced in PTCDA/vanadyl-oxide Pc (VOPc) multilayer structures. In that case, nonradiative centers at the multiple interfaces would tend to decrease the carrier collection efficiency, in stark contrast to observation. Finally, if the exciton lifetime is dominated by traps, it should decrease with increasing temperature.[241] However, time-resolved measurements have shown that the radiative decay time of OMBD-grown PTCDA/NTCDA MQWs is independent of temperature from 20 to 295 K.

The decrease of τ_{ex} with decreasing d, therefore, results from an increase in the overlap of the electron and hole wave functions in the PTCDA potential wells. A similar explanation of the dependence of the exciton lifetime on well width has been used to analyze radiative decay in GaAs/GaAlAs quantum wells.[242] For the hydrogenic 1s state, $\tau_{ex}{}^{-1}$ is proportional to the exciton volume.[243] Using the quantum mechanical treatment of the CT state, the exciton volume ($\sim\int|\psi|^2\, d^3\mathbf{r}$) in a MQW decreases with well width, thus accounting for the decrease in exciton lifetime. On the basis of the above analysis, the dependence of exciton volume, and hence τ_{ex} on d, is shown by the solid line in Figure 4-24 using the exciton radius and effective mass provided in Table 8. These results are in good agreement with the lifetime data, indicating the exciton quantum-confinement model can quantitatively account for the observed changes in both the exciton binding energy and lifetime.

4.2.3. Correspondence between MQW Absorption and Fluorescence Spectra

The analyses of the EA and the fluorescence spectral dependencies on layer thickness have shown that spatially extended CT excitons exist in PTCDA, while Frenkel excitons dominate the spectral features in the similar compound, PTCBI. In addition, analysis of the fluorescence spectra has shown that the amount of molecular conformational change upon excitation decreases with layer thickness in ultrathin layers of PTCDA (Figure 4-14a). The large change in dipole moment which accompanies the creation of an excited state[244] indicates strong CT exciton−phonon coupling. To quantitatively investigate the exciton−phonon interactions in strongly coupled OMCs such as PTCDA, and in particular to understand why the absorption blue shift ($\Delta\omega_{ex}$) and change in phonon frequency ($\Delta\omega_{ph}$) with layer thickness are similar in magnitude (Figure 4-9), Haskal et al.[135] analyzed the interaction of excitons and phonons in external radiation fields. The Hamiltonian used to calculate linear exciton−phonon interactions was[27]

$$H = \hbar(\omega_{ex} - \omega)a^+a + \sum_\beta \hbar\omega_{ph,\beta} b_\beta{}^+ b_\beta - \sum_\beta \hbar\gamma a^+a(b_\beta + b_\beta{}^+) - \mu a^+F - \mu aF^* \quad (4.18)$$

where $\hbar\omega_{ex}$ is the exciton binding energy, ω is the photon frequency, $\hbar\omega_{ph,\beta}$ is the energy of the phonon mode β, and μ is the electric dipole moment of the exciton. Further, $a^+(a)$ and $b_\beta{}^+(b_\beta)$ are the exciton and phonon creation (annihilation) operators, respectively.

The exciton population (a^+a) and phonon amplitude ($b_\beta{}^+ + b_\beta$) are calculated in steady state assuming the external field F is small, and only a single dominant phonon mode is present, in which case

$$a^+a \cong \frac{\Omega^2}{\eta^2 + \delta^2} \quad (4.19a)$$

and

$$b + b^+ = \frac{2\gamma a^+a}{\omega_{ph}} \quad (4.19b)$$

In eq 4.19a, $\Omega = \mu F/2\hbar$ is the Rabi frequency, δ is the exciton dephasing rate, and $\eta = (\omega_{ex} - \omega)$ is the

detuning parameter. In general, $\delta \ll \omega_{ex}$. From eq 4.19, the exciton−phonon interaction energy is[135]

$$E_{int} = -2E_{FC}[\Omega/\eta]^4 \qquad (4.20)$$

Assuming that E_{int} is independent of changes in E_{FC} or E_{ex} which accompany a reduction in layer thickness, and using $\Delta\eta = \Delta\omega_{ex}$, then

$$\frac{\Delta E_{FC}}{E_{FC}} = 4\frac{\Delta E_{ex}}{E_{ex}} = -\frac{\Delta\omega_{ph}}{\omega_{ph}} \qquad (4.21)$$

Thus, *the change in the exciton binding energy* ($\Delta E_{ex} = \hbar\Delta\omega_{ex}$) *is directly proportional to the change in the phonon frequency* ($\Delta\omega_{ph}$) with layer thickness. Here, E_{int} corresponds to the polaron energy[195,245] which from the fluorescence spectra of PTCDA MQWs, is found to decrease with layer thickness. This indicates that the exciton in the ultrathin layer induces a smaller lattice distortion in the thinnest films. However, Haskal[135] found that $\Delta\omega_{ph}$ (and thus ΔE_{FC}) for PTCDA is ~25% of the value predicted by eq 4.21 (the measurement is shown by the solid line, Figure 4-9). Since $E_{int} \approx \mu^4$ (c.f., eq 4.20), this unexpectedly small value of E_{int} suggests that the dipole moment decreases by ~10% as the layer thickness is decreased from 500 to 10 Å. Since μ is proportional to the exciton radius, this implies that a is also decreased by a similar amount as $a \rightarrow 0$. This reduction in radius is a consequence of confinement of extended exciton states in the thinnest layers.[231]

4.3. Optical and Electronic Properties of Other Organic Multilayer Systems

Since the first demonstration of the growth of an organic MQW structure using ultrahigh vacuum deposition,[23] there have been numerous studies on the growth[24,50,135,138,139,141−143,146,148−151,163,176,183,184,204,246] and theory[25−29,176,218,220,221,247−251] of multilayer structures aimed at understanding and exploiting their unique optoelectronic properties. A considerable interest in hybrid organic/inorganic heterostructures and MQWs has also developed for similar reasons.[144,145,159,160,189,190] In this section, we summarize results of studies which have been directed at understanding the physics of fundamental excitations in organic nanostructures other than the very well characterized perylene and naphthalene-based systems discussed in sections 4.1 and 4.2.

Quantum confinement has also been used[150,246] to explain blue shifts with decreasing layer thickness in the optical absorption and fluorescence spectra of self-assembled ultrathin alternating bilayers of the conjugated copolymer, poly(1,4-phenylenevinylene-*co*-*A*,*B*-naphthylenevinylene), or co(*A*,*B*-NV) and the nonconjugated insulating polymer, poly(styrene-4-sulfonate), or SPS. In that work, both $A,B = 1,4$ and $A,B = 2,6$ copolymers with differing concentrations of naphthalene were employed. The copolymer units facially stack when deposited by self-assembly from solution onto ultra-smooth, float glass substrates in a layer-by-layer fashion. The facial stacking results in significant π system overlap, and hence carrier delocalization, in the substrate-normal direction (i.e., perpendicular to the polymer chain axis). By varying

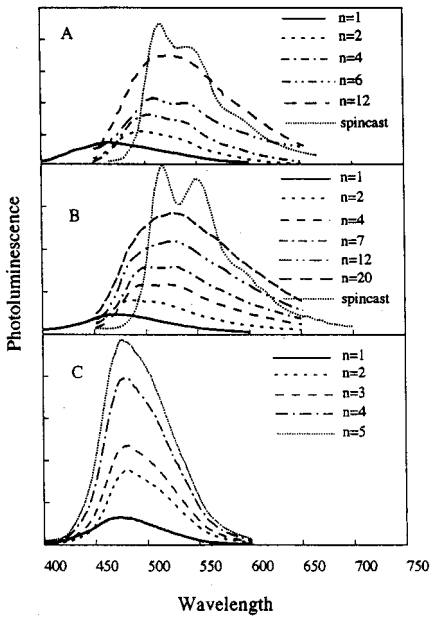

Figure 4-25. Photoluminescence spectra of self-assembled multilayers as a function of the number of bilayers, *n*. (a) 20% *co*-(2,6-NV)/SPS, (b) 20% *co*-(1,4-NV)/SPS, and (c) 20% *co*-(2,6-NV)/(SPS+0.4M $CaCl_2$). For comparison, the spectra of 1000 Å thick spincast films is also shown in a and b. Note the blue shift as *n* is decreased for these latter films. Also, note that by addition of $CaCl_2$ (curve c), the PL spectra are independent of assembly thickness (from ref 150).

the naphthalene concentration in the copolymer, and the number of bilayers in the assembly, an ultrathin layer bounded by air and glass on the opposing surfaces forms the resulting potential well of "infinite" depth to the trapped excitons. Typically, the thickness of each co(*A*,*B*-NV)/SPS bilayer was between 12 and 16 Å, again dependent of the naphthalene concentration in the co(*A*,*B*-NV). Since the well consists of a collection of bilayers, it was assumed that the insulating SPS was sufficiently thin such that it did not present a significant tunneling barrier to the charge carriers (holes) with allowed states in the copolymer layers.

Systematic blue shifts with decreasing layer thickness in both the photoluminescence and absorption spectra of co(*A*,*B*-NV)/SPS bilayer assemblies were observed. The photoluminescence peak shift is clearly apparent in the series of spectra shown in Figure 4-25 for samples of different compositions and number of bilayers (*n*). In Figure 4-26, the peak shift (ΔE) is plotted as a function of $1/d^2$, where d is the total assembly thickness between air and the glass substrate. The binding energy of excitons confined in an energy well of infinite depth is increased by: $\Delta E = h^2/8d^2m^*$, where h is Planck's constant, and the reduced effective mass, m^* is $1/m^* = 1/m_e + 1/m_h$. In PPV-like polymers such as co(*A*,*B*-NV), $m_e \gg m_h$. Hence, straight line fits to the data in Figure 4-26 yields the hole effective mass, which is found to range from $0.06m_o$ to $0.09m_o$ for naphthalene in co(*A*,*B*-NV), with the naphthalene concentration ranging from 1% to 20%, respectively. Given that the fits to the data using this simple confinement model are quite good for bilayer assemblies of thickness $d > 40$ Å using values of effective hole mass which are consistent with those found for PPV-like materials, it was

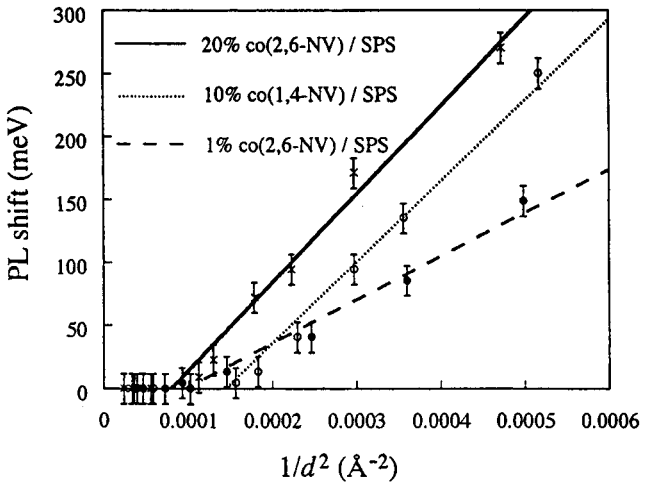

Figure 4-26. Photoluminescence peak shift vs $1/d^2$ for various *co*-(2,6-NV)/SPS and *co*-(1,4-NV)/SPS assemblies. The shift is measured with respect to the peak position for thick assemblies. Here *d* is the assembly thickness measured using X-ray reflectivity data (from ref 150).

concluded[150,246,252] that the observed spectral shifts result from changes in the exciton binding energy due to the presence of energy barriers surrounding the polymer layers, similar to the case of PTCDA/NTCDA multilayer assemblies.

As a test of this hypothesis, the thickness of the insulating spacer layers between the conducting layers was varied. When the spacer layer thickness exceeded ~40 Å, the spectral shifts in the absorption spectrum were not observed. This suggests that with sufficiently thick layers, there is poor delocalization of the excitons along the stacking direction, thereby eliminating the expected thickness dependence in the absorption and emission spectra. That is, when the spacer layers are thin (~20 Å or less), confinement is determined by the entire stack, and not solely by the thickness or even the flatness of a particular layer in the stack.[252] Furthermore, by comparing spectra from both bilayers and multiple bilayer copolymer assemblies, molecular conformational effects were eliminated, suggesting that the blue shifts observed are indeed the result of exciton delocalization along the bilayer assembly stacking direction (i.e., normal to the substrate plane).

More recently, confinement along the chain axis has also been claimed[253] for the conjugated block copolymer, TBA-4 (consisting of poly(2,5 benzoxazole)-*block*-poly(*p*-phenylene benzobisthiazole)-*block*-poly(2,5 benzoxazole)). In this case, confinement is induced by the HOMO−LUMO gap differences (estimated as 0.7eV) between the blocks along the chain. While this represents a different geometry to that offered by planar stacking molecules, in both cases charge is localized along one spatial dimension, and hence the confinement mechanisms (due to potential barriers interposed between wells) are fundamentally the same.

The absorption spectra attributed to excitons in the organic thin-film component of organic/inorganic multilayer structures consisting PTCDI and MgF_2 have also been observed to shift to higher energies with decreasing organic thin-film thickness.[145] These OMBD grown structures were found to have consid-

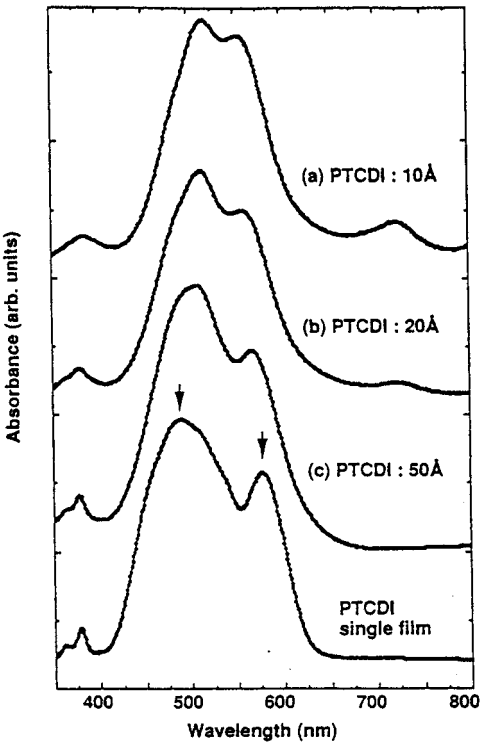

Figure 4-27. Optical absorption spectra of PTCDI/MgF_2 multilayer structures with varying PTCDI thicknesses. Also shown is the spectrum from a single, 1000 Å thick PTCDI film. Arrows indicate the prominent excitonic peaks in the spectrum which shift and change oscillator strength with PTCDI thickness (from ref 145).

erable interface flatness (as determined by grazing incidence X-ray diffraction, see section 3.4.2), for PTCDI layer thicknesses ranging from 5 Å (or slightly more than 1ML) to 50 Å. Blue shifts in the lowest energy peak in the PTCDI optical absorption spectrum are clearly observed, as indicated in Figure 4-27. Following earlier analyses of PTCDA/NTCDA quantum wells,[23] Tokito et al.[145] also attribute this phenomenon to quantum size effects in the PTCDI exciton. However, these authors note that the spectrum of PTCDI-doped MgF_2 films also exhibits changes when the PTCDI concentration is very high (>20%). This observation does not contradict the conclusion that quantum size effects are responsible for the spectral shifts, since aggregate formation at such high PTCDI concentrations is anticipated. Such aggregates would form a distribution whose mean radius would depend on concentration. Hence, size effects are also expected in such composite systems, although the spectral changes for the mixtures might differ somewhat from the more structurally homogenous, alternating layer structures, as has been observed.[145]

In a second series of experiments, Tokito and coworkers[145] studied CuPc/MgF_2 multilayer structures (section 3.4.2). While a redistribution of energy between spectral peaks in the CuPc *Q* bands was found on varying the layer thickness from 13 to 50 Å, there were no clear spectral shifts that could be attributed to quantum size effects. This finding is similar to that obtained for PTCBI/NTCDA multilayer stacks[135] (see section 4.1.2). In both cases, the spectra are due to small-radius, Frenkel excitations. In the case of CuPc/MgF_2, it was speculated[145] that

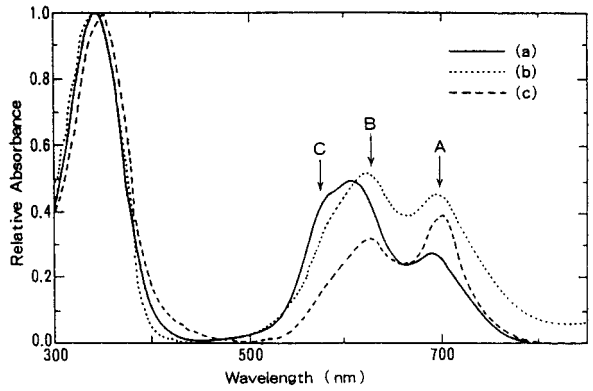

Figure 4-28. Absorption spectra for (a) simple summation of the spectra for 50 Å thick CuPc and NTCDA films; and for multilayer films with (b) 50 Å per layer and (c), 10 Å per layer. The prominent spectra features are indicated by A, B, and C (from ref 142).

the energy redistribution is due to the presence of two different solid phases of CuPc (known as the α and β forms[21]) coexisting in the thinnest layers (~13−26 Å), with both phases contributing their characteristic absorption to the total multilayer spectrum. To our knowledge, no spatially extended CT states have been identified in PTCBI, and hence no quantum size effects are anticipated, consistent with observations for both of these multilayer systems.

Multiple quantum well structures consisting of alternating layers of CuPc and NTCDA, where the layer thicknesses were varied from 10 to 50 Å were also studied.[142] A shoulder near the low-energy peak of the CuPc at a wavelength of 700 nm was clearly observed in the samples with the thinnest layers and was less pronounced in the 50 Å thick layers (Figure 4-28). Confinement within the organic nanostructure tends to increase the oscillator strength of this particular feature, which may result from a change in the energetics provided by the barriers formed by the adjacent NTCDA layers. Note that feature C, which is due to a CT exciton within the CuPc stack,[254,255] is suppressed in the thinnest layers.

Quantum size effects have also been suggested to be the source of shifts in the spectra of ultrathin layers of Alq_3, a material of considerable recent interest[31,32,256] due to its high electroluminescence efficiency when used in organic light-emitting devices (OLEDs). Ohmori[146] observed significant (70 meV) blue shifts in the Alq_3 photoluminescence peak as the layer thickness was decreased from 300 to 20 Å. In these experiments, Alq_3 was grown in multilayer stacks along with equally thick layers of the wider HOMO−LUMO gap "barrier" material, [*N*,*N*′-diphenyl-*N*,*N*′-bis(3-methylphenyl)-1,1′-biphenyl-4,4′-diamine], or TPD. Energy barrier arguments[146,147] were employed to interpret this spectral shift as resulting from confinement of electrons of mass $1.5m_o$ in 0.9 eV deep, Alq_3 energy wells. A qualitatively similar explanation[159] was given for shifts observed in both the photoluminescence and absorption spectra consisting of alternating organic/inorganic Alq_3/MgF_2 structures whose individual layer thicknesses were comparable to those used in the Alq_3/TPD studies.

While quantum size effects cannot be ruled out for Alq_3-based structures, they are not likely to exist due to the Frenkel-like nature of excitons in this material.[257,258] Furthermore, unlike the perylene- and phthalocyanine-based crystalline MQW structures, Alq_3 thin films are amorphous. Hence, we expect there to be very little spatial coherence of these molecular excited states, further reducing the possibility that "macroscopic" layer structures exceeding a few Ångstroms in thickness can significantly modify the exciton binding energy.

An alternative explanation for the spectral shifts is that the Frenkel states bind to the Alq_3 surface at the interface with the adjacent layer. The energy shift in this case arises from the discontinuity in polarizabilities of the two materials.[25,247−249] Since exciton energy, to first order, is proportional to $1/\epsilon^2$, we expect that the exciton energy can be either red- or blue-shifted from its bulk value, depending on the relative dielectric constants of the well and barrier materials. As discussed in section 4.2, such differences in material polarizability have been taken into account in describing the energy shifts in systems where extended excitonic states have been clearly identified.[176] Indeed, to first order, the polarization energy difference simply modifies the well depth by a factor of $1/\epsilon$, and hence these two effects can not be independently determined. Thus, to clearly identify a spectral shift as due to quantum size effects, the spatial dimensions of the exciton of a given material must first be determined using independent measurement methods such as solution or gas phase spectroscopy,[197] electroabsorption or electroreflectance,[177,212,213,255,259] etc.

The observations discussed above indicate that quantum confinement has been observed in systems where spatially extended states arise from close intermolecular stacking within a unit cell. While this phenomenon is therefore limited to a class of nearly planar organic molecules which can be grown into highly ordered structures, ultrathin layers, nevertheless, generally have different optical and electronic properties from those found in the bulk material. These differences can have several sources, ranging from material intermixing,[144] binding of excited states to the numerous heterointerfaces,[25,249] dipole−dipole interactions,[26,29,183,189,251] chemistry between contacting molecular layers, etc. Hence, the realization of organic/organic and organic/inorganic nanostructures is expected to lead to new physical phenomena which can deepen our understanding of molecular organic materials, and should also lead to applications which were not anticipated prior to the ability to fabricate this new class of structures. For example, several recent theoretical studies of organic/organic and hybrid organic/inorganic nanostructures suggest that these materials will have unique nonlinear optical properties.[26−28,218,220,221] In addition, organic multilayers have been found to induce rectification of injected charge[260] and have been shown to result in output light polarization when incorporated into OLEDs.[148,261]

One interesting application of organic heterostructures is in the enhancement of the collection efficiency of photogenerated carriers due to dissociation at the numerous, closely spaced heterointerfaces.[34] A shortcoming of solar cells based on organic materi-

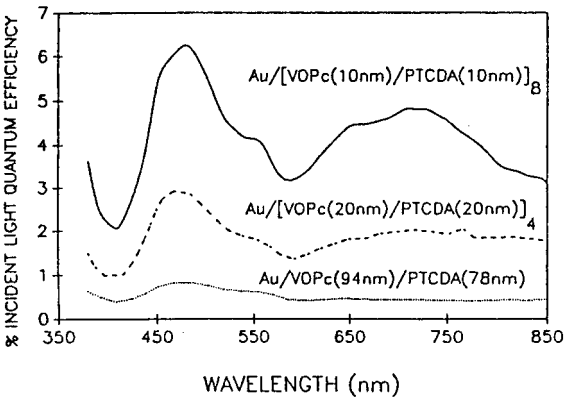

Figure 4-29. Photocurrent yield for various VOPc/PTCDA multilayer assemblies. The subscript after the layer description indicates the number of bilayers in the particular assembly. A significant enhancement in photocurrent yield is observed as the layer thickness is increased (from ref 34).

als (see section 5.2) is that the exciton diffusion length is often significantly less than the optical absorption length, leading to low (<1%) power conversion efficiencies.[20,190,262] Hence, excitons generated far from contacts in organic thin film solar cells often recombine prior to dissociation, and subsequent carrier collection at the device contacts. While it has been shown[172,263] that ordered, OMBD-grown organic films can support excitons with very long diffusion lengths (>200 nm) due to the low density of crystalline defects which act as recombination sites, the photocarrier collection efficiency is nevertheless low (~1%).

Arbour et al.[34] found that organic photoconductors consisting of alternating multilayer stacks of VOPc and PTCDA, whose individual layer thicknesses ranged from 100 to 940 Å, could be used to significantly enhance the photogenerated carrier collection efficiency over that obtained using a single layer structure. Collection efficiencies of three such structures as a function of wavelength are shown in Figure 4-29. It was observed that the collection efficiency in these samples increased linearly with the number of VOPc/PTCDA interfaces: an effect attributed to the proximity of interfaces at distances comparable to the exciton diffusion length. As noted above, the heterojunctions in the multilayer photoconductor serve as sites for exciton dissociation into electron−hole pairs which are subsequently separated by the built-in electric fields and collected at the contacts. The enhancement in collection efficiency is quite pronounced, with an increase in quantum efficiency from ~0.5% for the thickest layers, to 6% for an 8 period, 100 Å VOPc/100 Å PTCDA structure. It was also found[34] that simply codepositing the two molecular constituents, VOPc and PTCDA, leads to *reduced* photoactivity from that obtained from pristine, single-layer structures. From this, it was concluded that the interaction at the heterojunctions of individual molecules is not responsible for the observed enhancement. Rather, it is the presence of a structure consisting of highly pure, ordered molecular layers separated by molecularly flat, nearly defect-free boundaries which ultimately improves the carrier generation and collection efficiencies in this demanding application. The increased fluorescence efficiency observed in organic multilayer stacks is also a strong indication of the lack of dissipative recombination sites at the heterointerfaces.[24,34,135,163] To our knowledge, the level of material and structural purity required to obtain such a pronounced improvement in photoconductor efficiency has only been obtained using organic multilayer nanostructures grown by OMBD.

Photoconductivity enhancements have also been observed[190,191] in the hybrid organic/inorganic multilayer system, CuPc/TiO_x. It was suggested that the larger electron affinity of TiO_x (4.2 eV) as compared with CuPc (3.1 eV) acts to collect and conduct charges in the TiO_x layers which were originally photogenerated in the adjacent CuPc layer. In these experiments, multilayers consisting of 50−400 Å thick CuPc layers were grown between TiO_x layers of comparable thickness. The growth temperature was maintained at 200 °C in order to obtain α-CuPc without significant interface roughening. Takada et al.[191] observed that the photoconductivity of the multilayers at high incident optical flux (~100 mW/cm^2) was 40 times larger than that obtained for CuPc single layer samples, with the 400 Å thick CuPc samples exhibiting the largest photoconductivities. This increase was attributed to a two-step process, beginning with exciton generation in the CuPc upon absorption of the incident light. Next, the excitons either dissociate at O_2^- trap centers induced on growth of the TiO_x films (which occurs in the presence of an oxygen plasma), or they diffuse to a nearby CuPc/TiO_x heterointerface where dissociation can also be promoted. Once the free electrons are produced, they drift into the high electron affinity, relatively high mobility TiO_x and then to the contacts at the device periphery. The decrease in carrier collection efficiency at lower incident optical fluxes is possibly due to the presence of interface defects which act as recombination centers for both excitons and free charges.

4.4. Implications and Applications of Exciton Confinement in OMCs

We have shown that accurate methods to analytically treat CT excitons in tightly packed neutral molecular crystals have been developed to describe several different spectroscopic features of vacuum-deposited organic nanostructures. It was found that closely packed organic crystals are characterized by a large overlap between the orbitals in adjacent molecules, resulting in delocalization of the CT charge pair. In this case, the crystalline pseudopotential (or the on-site correlation energy) becomes comparable to or even larger than the energy bandwidth, with the consequence that the CT exciton can be represented by a hydrogen-like wave function.

Using a Hamiltonian modified to account for the calculated molecular polarization and suitable hydrogenic trial wave functions, the electroabsorption data for homogeneous PTCDA thin films, as well as the absorption spectral shifts observed in PTCDA-based multiple quantum wells was accurately fit, further testing the picture of an extended CT state in certain OMCs. The analyses of such experiments give independent and consistent estimations of the

exciton radii for PTCDA along different crystal axes. This treatment was extended to other exciton systems found in a wide range of interesting neutral organic molecular and inorganic semiconductors (such as GaAs), suggesting that Wannier and CT excitons have a common physical origin which can be approximated by a hydrogenic wave function. This provides conclusive evidence that PTCDA and similarly close packed molecular compounds such as[192,193] BTQBT and possibly even C_{60} and its analogs[259] form an important "transitional" class of materials that share many properties with both conventional semiconductors and insulator-like organic molecular crystals.

While these results can be easily generalized to explain a variety of observations of the optical properties relating to the layer thickness or aggregate size of both organic and inorganic nanostructures, they also provide a new viewpoint with which to consider vdW-bonded solids represented by the archetype compound: PTCDA. The broad and rich range of physics developed for understanding quantum confinement in inorganic semiconductors which has ultimately led to the precise control and manipulation of their densities of states to attain desired optoelectronic properties, appears to be equally applicable to organic nanostructures provided there is sufficient charge delocalization resulting from details of the crystal structure. In that sense, "transitional" materials such as PTCDA and related compounds have bridged the gap between highly delocalized semiconducting systems and insulators.

Indeed, it has already been found that multilayer structures exhibit new properties beyond those exhibited in conventional, homogeneous thin films. Multiple phases and mixtures of compounds have been identified for both organic/organic and organic/inorganic multilayers with interesting optical properties. In two cases,[34,191] an increase in photoconductivity of the multilayers as compared with single film structures has been found, suggesting that these types of engineered materials may eventually find application in solar energy conversion. The observation of quantum confinement in MQWs consisting of closely packed OMCs[24] also suggests that these structures can be used to tailor the electronic densities of states of the constituent materials. Following the example of inorganic semiconductor structures, the density of states in the reduced dimensionality of MQWs is useful for, among other applications, decreasing laser threshold current.[12] Hence, one potential application of organic MQWs may be in the realization of organic solid-state current injection lasers with reduced threshold currents (and thus reduced power dissipation and longer operational lifetime).

These represent only a few of the interesting physical and technological possibilities opened up by the recent achievement of both organic and organic/inorganic (hybrid) multilayer nanostructures in several laboratories worldwide. In the following section, we will briefly discuss a few practical optoelectronic devices which have recently been demonstrated based on high-purity, vacuum-deposited organic thin films.

5.0. Applications of Thin-Film Structures Grown in Vacuum

A primary motivation for the extensive research over the last several years concentrating on the growth and physics of vacuum-deposited organic thin films is their very real potential for use in applications which are not accessible to more conventional, inorganic semiconductors. Indeed, the recent demonstration of efficient electroluminescence from organic thin-film devices[31,32,264] promises to transform the flat panel display industry, with the potential of replacing liquid crystal displays with an entirely new generation of efficient, emissive, full-color flat panels based on light-emitting organic devices. In more recent developments, organic thin films are showing promise for use as thin-film transistors[265−270] which might eventually replace amorphous or polysilicon TFTs currently used in the back planes of active-matrix liquid crystal displays (AMLCD). These new developments must also be placed in the context of long efforts and progress which has been directed at employing organic thin films for solar energy conversion[20,271] and in sensors of various kinds. Finally, vacuum-deposited OMCs have also been proposed as materials with large second- or third-order optical nonlinearities,[18,26−28,160,218,220,221,272−279] or large $\chi^{(3)}$. There are, in addition, many, somewhat less conventional uses of organic thin films deposited in vacuum, including waveguides and optical couplers,[22,102,280,281] organic/inorganic photodetectors,[38,282] lasers, etc.

The primary attraction of OMCs is their potential low cost and the extreme flexibility which the device engineer has in choosing a material whose properties have been specifically tailored to meet the needs of a particular application. The materials are easily integrated with conventional semiconductor devices, thereby providing additional functionality to existing photonic circuits and components. This potential, however, must be balanced against the problems which have traditionally impeded the acceptance of OMCs for use in active electronic or optoelectronic device applications. These problems include unstable device characteristics, sensitivity to adverse environments (e.g., temperature, humidity, oxygen, etc.), nonideal metal/organic contacts, and lack of reproducibility of material composition, purity, and fabrication conditions. From the foregoing discussion on OMBD of molecular organic thin films, it is clear that the ultrahigh-vacuum environment characteristic of this deposition process can provide the necessary material purity and structural and chemical reproducibility necessary in modern, high-performance optoelectronic device applications. While the costs and complexities associated with UHV deposition processes may offset the attractive (but possibly misleading) "simplicity" often attributed to organic-based devices, it is clear that the advantages in performance of such structures outweigh these apparent disadvantages. Furthermore, while purity and structural precision are key to the ultimate success of all optoelectronic device technologies, it is not clear how sophisticated the OMBD system must be to achieve acceptable device performance. At this point, OMBD serves as our most powerful tool for investigating the detailed growth and physical char-

acteristics of OMCs, and hence will ultimately be able to address questions regarding the need for UHV in the production of practical display, transistor, NLO, or other molecular organic thin-film device applications.

In this section, we briefly review several potentially important applications where OMCs have been used to improve upon or expand the functionality of the device beyond that which can be achieved using conventional, inorganic semiconductors. Indeed, rather than focusing on all the many areas where OMCs have proven to have properties amenable to practical application, we concentrate here on those applications where the use of OMCs may *transform* current device technology by providing a significant advantage over present methods. This section will therefore describe the use of OMCs in organic/inorganic (OI) semiconductor heterojunction devices, solar cells, organic light-emitting devices (OLEDs) and lasers, and thin-film transistors (TFTs). The discussion is by no means intended to be encyclopedic, but rather should provide a useful introduction to the state-of-the-art of some of the most important current and future devices based on vacuum-deposited organic molecular thin-film materials.

5.1. Integrated Organic-on-Inorganic Heterojunction Devices

The first demonstration[38] of an organic/inorganic semiconductor device employing a vacuum deposited thin film consisted of a 1000−2000 Å thick PTCDA film on (100) p-Si (see inset, Figure 3-52). The contact between the organic and inorganic layers forms a rectifying heterojunction (or organic−inorganic heterojunction, OI-HJ). Given the p-type nature of PTCDA, when deposited on a p-type semiconductor substrate an isotype heterojunction is formed, whereas an anisotype heterojunction is formed on an n-type substrate. These OI-HJ devices have been shown to be useful in the nondestructive mapping of the free-carrier concentrations in the inorganic substrates. Indeed, rectifying OI-HJ contacts have been successfully demonstrated for this purpose on a wide range of group II−VI, III−V, and IV semiconductors[283−286] using a variety of organic thin-film materials.[37,38,170,283,287,288] They have a very high reverse breakdown voltage and low dark currents determined by the properties of the inorganic substrate rather than the organic thin film itself. This allows for depletion of the free carrier distribution deep into the substrate by application of large reverse voltages. Employing conventional capacitance−voltage profiling of the free carrier concentration in the substrate, this parameter is obtained as a function of depth into the semiconductor.[63,285,289,290] Once the free carrier concentration is obtained, the organic thin film and contacts are nondestructively removed from the semiconductor surface (e.g., by dissolving PTCDA in a high pH solution), allowing for further use and processing of the characterized material. Furthermore, the nondestructive deposition of the organic film onto inorganic substrates has been shown to be a means for quantitatively determining the electronic surface state density distribution of the substrate.[170,291−293] Surface states are known to govern the properties of many semiconductor devices

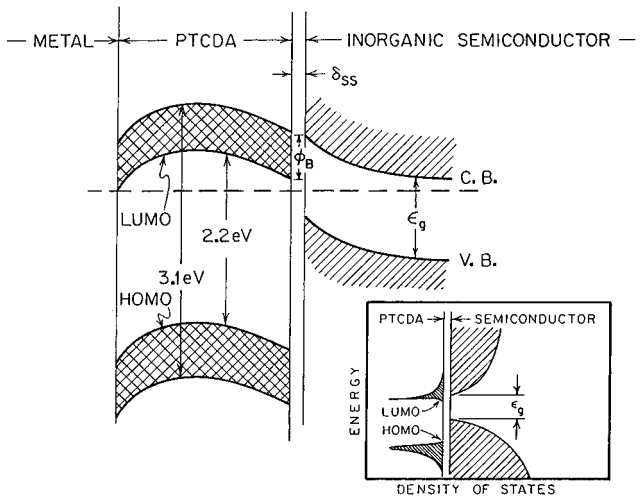

Figure 5-1. Proposed energy band diagram of an OI-HJ consisting of PTCDA on an inorganic semiconductor substrate. In this diagram, ϵ_g is the semiconductor energy gap, ϕ_B is the heterojunction LUMO/conduction band barrier potential, and δ_{ss} is the thickness of a layer at the semiconductor surface. Inset: Proposed densities of states at the OI-HJ interface (from ref 63, p 199).

such as metal−insulator−semiconductor (MIS) devices and surface-passivated rectifiers and transistors. Hence, obtaining detailed characteristics of the semiconductor surface is a crucial first step in the process of fabricating high-performance devices. The noninvasive organic/inorganic HJ contact has therefore proven to be an extremely useful new tool in obtaining the characteristics of electrically active defects at semiconductor surfaces, which have otherwise not been possible to obtain using conventional analysis techniques which tend to be more destructive of the fragile, as grown surface properties.

The OI-HJ can be understood in terms of the energy band diagram[63] in Figure 5-1. In this case, PTCDA is in contact with an n-type semiconductor substrate. This diagram illustrates an "optical bandgap" between the HOMO and LUMO levels of 2.2 eV, along with the relatively smaller bandwidth characteristic of the organic material. The heterojunction energy offset, ϕ_B, controls the injection of charge from the metal/organic contact (which is found to be nearly ohmic for many metal/organic systems such as In/PTCDA) into the semiconductor substrate. Also shown is an interface region of thickness δ_{ss} which is due to the thin native oxide that typically exists at the semiconductor surface. This interface region is a source of charge of density D_{ss} due to dangling bonds at the semiconductor surface (see Figure 3-50). These surface states can exist at the as-grown (or intrinsic) semiconductor surface, as well as at surfaces exposed to atmosphere, as is typically the case for OI-HJ devices. The presence of the energy barrier, ϕ_B, results in the rectification of current by the OI-HJ. In reverse bias (i.e., where the substrate is at a positive potential relative to the metal contact), the carriers must overcome the barrier potential. Under forward bias, the carriers are injected from the substrate into the organic thin film, which ultimately limits the current due to the small mobilities ($\mu < 1$ cm^2/V-s) typical of ordered molecular materials such as PTCDA. The current−voltage characteristics of the OI-HJ are described by eq

Table 9. Barrier Energies for PTCDA-on-Inorganic Semiconductor Diodes (From Ref 171)

inorganic substrate	majority carrier type	$q\phi_B$ (eV)	ΔE_v (eV)[a]
Si	n	0.39 ± 0.01	
	p	0.56 ± 0.02	0.50 ± 0.02
Ge	p	0.30 ± 0.03	0.25 ± 0.04
GaSb	p	0.37	0.29 ± 0.04
	n	ohmic	
GaAs	n	0.39	
	p	0.52	0.43 ± 0.05
InP	n	0.30	

[a] ΔE_v for p-type substrates only. For these calculations $m^* = m_o$ for PTCDA. The value for p-Si is measured, whereas for other materials, ΔE_v is calculated using ϕ_{B_p} obtained from ref 284 and reproduced here. Doping of p-Si and p-GaSb: 5×10^{15} cm^{-3}; p-Ge: 5×10^{14} cm^{-3}; and p-GaAs: 2×10^{16} cm^{-3}.

(3.14), where the saturation current, J_{so} is determined by the barrier height[171] viz.

$$J_{so} = [qN_{cs}\langle v_c\rangle/(1 + \langle v_c\rangle/v_d)] \exp(-q\phi_B/kT) \qquad (5.1)$$

Here, N_{cs} is the semiconductor effective conduction band density of states, $\langle v_c\rangle$ is the mean carrier velocity in the organic semiconductor (~500−1000 cm/s for PTCDA), and v_d is the diffusion velocity in the inorganic substrate. The barrier height can be inferred from the current−voltage characteristics of the OI-HJ device, or can be measured directly using internal photoemission.[217] Barrier heights (ϕ_B) have been obtained for PTCDA on various p-type group IV and III−V semiconductor substrates[171] and are listed in Table 9. From ϕ_{Bp}, we can derive the energy offset (ΔE_v) between the HOMO and the valence band of the semiconductor using $\Delta E_v = q\phi_{Bp} + \Delta_s - \Delta_o$, where Δ_s and Δ_o are the energy differences between the equilibrium Fermi levels in the bulk of the inorganic semiconductor and the organic thin film, respectively. Values of ΔE_v for several PTCDA/p-type inorganic semiconductor systems are also listed in Table 9.

It has been found that the characteristics of OI-HJ diodes follow the ideal expression in eq 3.14, exhibiting a nearly exponential increase in current with voltage in the forward biased direction (Figure 5-2) until the mobility-limited internal organic film resistance results in a decrease in current at high voltages.[171] In contrast, the reverse-biased characteristics (Figure 5-3) are limited by dark current generation in the inorganic semiconductor, until the electric field at the OI-HJ becomes sufficiently large to induce avalanche breakdown in the substrate.[37] Other, less ideal sources of dark current and high voltage breakdown can also be observed, depending on the characteristics and quality of the substrate material. However, when the applied electric field is sufficiently high to induce avalanche, such as is the case for the PTCDA/p-Si device in Figure 5-3, large photocurrent multiplication can be observed. In the device shown, photogenerated electron multiplication in the p-Si substrate exceeds 100.

These results indicate that OI-HJ devices can be used as photodetectors which are both simple to fabricate and have performance characteristics comparable to or better than that obtained using conventional inorganic semiconductor devices. An interesting example of this application is an PTCDA/p-Si photodetector where the metal top contact was replaced by a sputter-deposited, transparent indium-tin-oxide (ITO) hole injecting contact.[282] This device could be reverse biased into avalanche breakdown, exhibiting uniform gain characteristics in the presence of very low primary dark currents (6 μA/cm^2) even at high reverse voltages (>50 V). The bandwidth of the device was ultimately limited by the hole

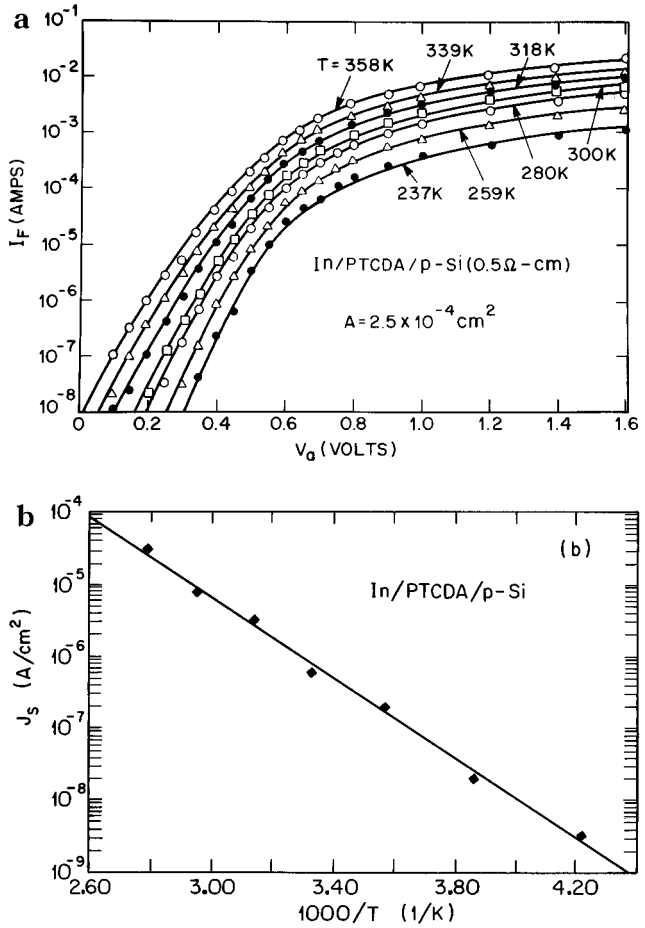

Figure 5-2. (a) Forward current-voltage characteristics of an In/2000 Å PTCDA/p-Si OI-HJ device measured at several different temperatures (from ref 65). (b) Saturation current density vs $1/T$ for the diode in a. The solid line represents a best fit to the data, giving a barrier diffusion potential of $\phi_{Bp} = 0.56$ V (from ref 171).

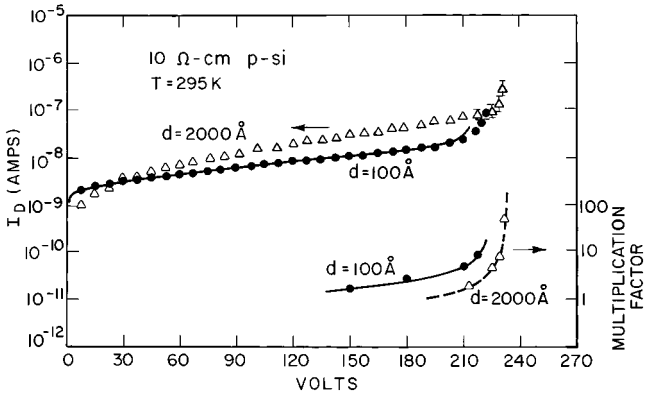

Figure 5-3. Reverse current vs voltage characteristics of In/PTCDA/p-Si devices obtained at room temperature. PTCDA thicknesses of $d = 100$ and 2000 Å were deposited on 10 Ω cm p-Si substrates. Also shown is the photocurrent multiplication factor for the devices (from ref 37).

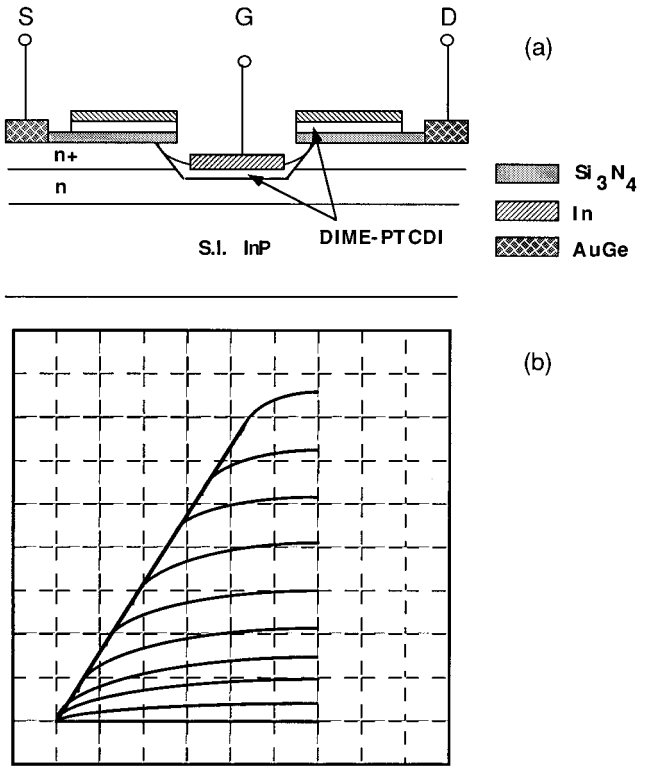

Figure 5-4. (a) Cross-sectional diagram of a self-aligned organic-on-inorganic semiconductor transistor (OISTR) employing a 500 Å thick layer of DM-PTCDI to form a contact barrier to the ion implanted, InP substrate. (b) Drain current characteristics of the OISTR (horizontal scale, 1 V/div; vertical scale, 5 mA/div; gate voltage step, 0.5 V) (from ref 297).

transit time across the PTCDA layer. By making this layer very thin (~100 Å), bandwidths exceeding 500 MHz are possible using such structures.

To be practical, it is essential that OI-HJ diodes be stable over long periods when exposed to adverse environmental conditions such as elevated temperatures and high humidity. Prabhakar et al.[294] demonstrated both photolithographic patterning and environmental passivation of an OI-HJ diode using a relatively low temperature (125 °C) pyrolytic process to deposit a SiO_2 encapsulating layer onto the organic surface. The dark current characteristics under reverse bias of the resulting diodes were measured as a function of time and temperature. The devices were found to be stable up to temperatures as high as 100 °C over extended periods (>3000 h). These results suggest that molecular organic materials can be patterned and passivated using photolithographic techniques adapted for this purpose and that many organic materials have physical characteristics which are compatible with applications where elevated temperatures are required.[295]

Indeed, devices with very small patterns such as optical modulators[296] and narrow gate (~2 μm) OI-HJ transistors based on OMC/InP contacts[297] have been demonstrated using patterning techniques developed specifically for their compatibility with the chemistry and physical properties of molecular organic materials. A cross section of the transistor structure and its drain current characteristics are shown in Figure 5-4. The problem of micropatterning of the 1.5 μm gate contact was solved by creating an undercut pattern in the substrate, which provides for a "self-aligned" structure. The fabrication proceeded as follows:[297] After ion implantation of the semiinsulating (100) InP substrate to form the channel and contact regions, a Si_3N_4 mask was deposited by plasma-enhanced chemical vapor deposition (PECVD). This mask was photolithographically patterned to open areas for the gate, source and drain contacts. After standard metal deposition of the source and drain, an etchant was used which selectively exposes the (111) planes of InP tilted at 54° to the substrate normal while undercutting this pattern beneath the Si_3N_4 mask. This undercut etched groove provides the pattern for the organic thin film deposition. In this case, *N*,*N*′-dimethyl-3,4,9,10-perylenetetracarboxylic diimide (DM-PTCDI) was deposited at an angle such that it covered regions underneath the overhang. Finally, the gate metal (In) was deposited with the wafer positioned perpendicular to the metal beam flux to ensure the metal did not short to the substrate. These narrow gate transistors had excellent output characteristics as shown in Figure 5-4b. For example, the transconductance was $g_m = 80$ mS/mm, comparable to that obtained with conventional InP FETs. The bandwidth of such OI-HJ devices is ultimately limited by the carrier transit time across the thin organic layer. In practice, this can exceed 1 GHz for 100 Å thick, ordered films.[282] More significantly, the devices showed no indication of drain−current instability (or "drift") commonly observed in InP metal−insulator−semiconductor devices.[298] The organic heterojunction also enhanced the gate barrier height (0.54 eV) over most metal−semiconductor contacts (where the barrier height of most metals to INP is only ~0.4 eV), thereby greatly reducing gate leakage. In effect, the use of OI-HJ gates significantly improved the device performance over that which could be obtained using conventional, all-inorganic materials systems.

It was noted above that one of the attractive aspects of molecular organic thin films is their ability to be nondestructively integrated with inorganic semiconductor devices. One example device, discussed in section 3.3.2.4, is a recently demonstrated molecular organic waveguide coupled to an $In_{0.53}Ga_{0.47}As$ photodiode for use in optical communications systems,[22] and shown schematically in Figure 5-5. In this device, a PTCDA waveguide is grown on a previously vacuum-deposited and patterned amorphous Teflon ridge on the (100) surface of an InP substrate held at $T_{sub} = -100$ °C during growth. Amorphous Teflon was employed as the waveguide buffer since its index of refraction ($n = 1.15-1.30$) is lower than the PTCDA index either perpendicular ($n_\perp = 1.36$) or parallel ($n_\parallel = 2.12$) to the substrate,[175] allowing for propagation of light independent of polarization direction. The waveguide width was varied between 4 and 20 μm. A second, vacuum-deposited Teflon buffer layer was deposited onto the PTCDA surface, thus completing the waveguide. The waveguide was butt-coupled into the $In_{0.53}Ga_{0.47}As$ optical absorption region in a reverse-based, planar p−i−n photodiode with sensitivity extending to a wavelength of $\lambda = 1.65$ μm. Waveguide losses between 2.7 and 4.6 dB/cm were measured,

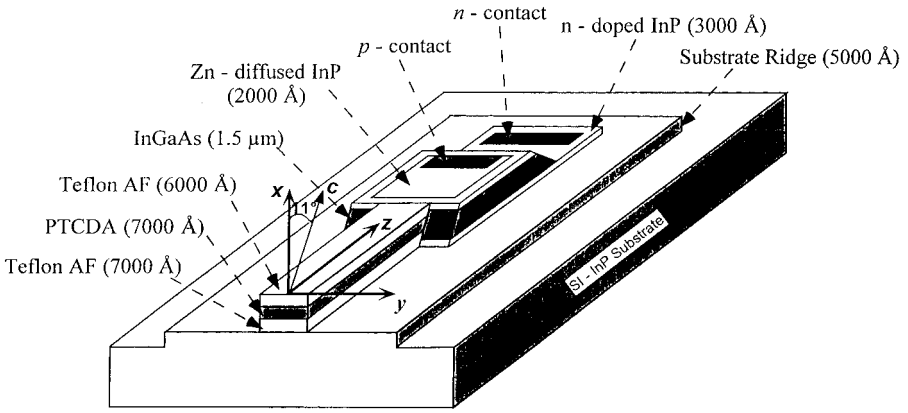

Figure 5-5. Schematic view of an integrated organic waveguide/photodetector with axes indicating the relationship of the PTCDA optic *c* axis relative to the waveguide (from ref 22).

with the higher losses corresponding to the narrowest guides due to optical out-coupling at the rough waveguide edges.

The most interesting feature of these guides is that they were polarization preserving.[22,115] That is, if polarized light is launched at the waveguide input, the output polarization after propagation along a 0.5 cm long guide remains in the same direction as at the input. Since the optic axis (indicated as the "*c*" axis in Figure 5-5) of the OMC has a unique orientation with respect to the PTCDA unit cell, this lack of polarization rotation indicates that the *c* axis lies in the waveguide $x-z$ plane. This, coupled to the relatively low loss of the waveguides, suggests that the growth and fabrication conditions used in producing these integrated devices result in molecular alignment and smooth surface morphologies over extended (~1 cm) distances for QE-grown films. This unique aspect of OMCs grown by OMBD can lead to novel applications such as the edge-coupled integrated waveguide/photodetector shown in Figure 5-5.

5.2. Organic Solar Cells

It has long been recognized that thin-film OMCs have promise for solar energy conversion due to the potential for very low cost manufacture of solar cells employing such materials.[20] In particular, crystalline organic semiconductors such as the Pc's, perylenes and other relatively low molecular weight polyacenes have been identified as having the greatest potential for this purpose due to their ability to be controllably deposited via OMBD and other more conventional vacuum techniques, their relatively high purity, environmental robustness, and high mobilities (hence relatively low series resistance).[19,271,299−310] More recently, solar cells employing these materials in combination with C_{60} have also been explored[311,312] for many of the same reasons. In spite of considerable research in both bilayer organic p−n junction and Schottky barrier crystalline organic photovoltaic (PV) cells over the past 20 years, however, there has yet to be a demonstration of a cell whose characteristics are adequate for even the most undemanding of solar conversion applications.[20] Their poor performance can be ascribed principally to the following causes: (i) Due to the intrinsic nature of photoconductivity in crystalline organic materials where free electron−hole pairs are generated in a *second-order* process following absorption and exciton generation, the efficiencies realized to date are low (typically <1% for AM0 to AM2 illumination). (ii) Due to the limited π-orbital overlap between adjacent molecules in an organic crystalline stack and due to the numerous defects in the crystalline order in the deposited materials, the free carrier mobilities in many organics are low (typically $<10^{-3}$ cm^2/(V s)). This leads to high film resistance, and hence low power conversion efficiency. (iii) The exciton diffusion length (L_D) is typically considerably shorter than the optical absorption length, $1/\alpha$, where α is the absorption coefficient (see section 4.3). Hence, the exciton is often photogenerated far from an interface where dissociation into free carriers can occur, leading to recombination and a concomitant loss in quantum yield. (iv) A final consideration is one of environmental stability of the organic thin-film materials, and in particular the stability of the intramolecular bonds to prolonged exposure to ultraviolet radiation.

While these problems currently prevent the realization of fully organic, low-cost PV cells, significant advances in OMBD growth and processing of molecular organic thin-film devices made by researchers worldwide suggest that such materials may eventually find practical application for low-cost solar energy conversion. As discussed in section 4.3, MQW structures can significantly increase the quantum yield and carrier diffusion lengths in organic materials. Indeed, extending the photoactive region width by inserting multiple junctions, each of thickness $\sim 1/\alpha$, represents a recent, promising approach made practical due to the uniformity control inherent in OMBD growth.[34] Furthermore, the same films grown with a high degree of stacking order (e.g., those based on perylenes and Pc's), typically also have enhanced π-orbital overlap, thereby increasing carrier mobility with its concomitant decrease in bulk layer resistance.

There are two basic solar cell structures: the metal/organic Schottky-type cell, and the fully organic bilayer cell which employs two ohmic metal contacts. The Schottky cell consists of a light-absorbing organic film sandwiched between two metal contacts: one rectifying and the other ohmic. For a p-conducting organic material, the Schottky contact consists of a low work function metal such as Al, Mg, or In, whereas for n-conductivity films, a high work function metal such as Au is preferred. Charge separation is induced by exciton dissociation in the space−

charge region due to the built-in electric field at the rectifying contact, which therefore requires that optical absorption occur in this "photoactive" region as well. A photoactive region width of ~200−400 Å is typical.

In the bilayer cell, charge separation occurs at the organic heterojunction whose built-in potential is determined by the size of the HOMO−LUMO gap energy difference[300] between the contacting materials. The HOMO offset is equal to the difference of ionization potentials (IP) of the two contacting materials, and the LUMO offset is equal to the HOMO offset plus the difference in HOMO−LUMO gap energies (E_{H-L}) of the two materials. To avoid creating barriers at the organic heterojunction which impede carrier transport, it is necessary for the material with the larger hole mobility to also have a larger IP and IP − E_{H-L} (i.e., the electron affinity) than the high electron mobility material. Absorption can occur in either of the two organic films, thereby doubling the photoactive region width where optical absorption can result in efficient charge separation by the built-in field. Note that it is not important whether a "p−n"-like junction or a simple isotype (i.e., p-P or n-N) heterojunction is employed, since it is only the diffusion potential created at the heterojunction due to the HOMO−LUMO gap offsets that is effective in carrier drift.

Whether or not an organic material shows p-type or n-type character depends *only* on the background free carrier concentration of the material, which is primarily a function of unintentional doping by defects or impurities.[268,300,313] These impurities then determine the position of the Fermi energy within the HOMO−LUMO gap. A much more significant feature of an organic semiconductor (which is independent of Fermi energy depth in the gap) is whether electrons or holes have a higher mobility. Unlike the free carrier concentration, this is an *intrinsic* feature of the organic material, determined by the crystal symmetry and periodicity which provide a higher overlap of HOMO (LUMO) levels in adjacent molecules, giving rise to a higher hole (electron) mobility.[80] Indeed, sometimes the chemical character of the molecule itself is not the most important consideration in determining this overlap. For example, the anhydride groups in PTCDA have a strongly electron donor character. However, molecular orbital calculations of the molecule show that the frontier orbitals for this model compound are on the perylene core, while the anhydride orbitals are located deep in the LUMO band, thereby contributing little to the electronic conduction properties of the crystalline PTCDA film.[43,58] Current conduction experiments indicate that the hole mobility of PTCDA exceeds that of the electron mobility by several orders of magnitude, suggesting the importance of band structure in ultimately determining the carrier conduction properties of a material.[172,173,224] This distinction between majority carrier type and mobility is very often misunderstood by the organic thin-film device community. Hence, the assignment in the literature of a material as "n" or "p" type to explain solar cell behavior must be viewed with caution. It has been shown that isotype heterojunctions formed between materials of the *same* conductivity type can equally well lead to excellent diode properties, and can be used to fully quantitatively explain the forward and reverse biased characteristics of such rectifying junctions.[300,314,315] Hence, the most reliable data available concern materials where mobility and conductivity measurements have been independently measured using such techniques as the analysis of metal−organic Schottky barrier conduction, and time of flight measurements.[37]

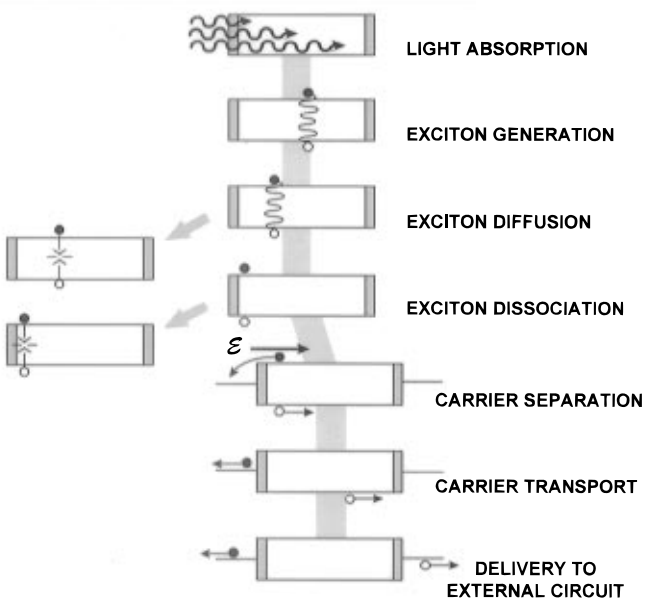

Figure 5-6. Schematic diagram of the photoconductivity process in organic thin film solar cells.

Low quantum yield (η) in organic PV cells is attributed to the intrinsic nature of the photoconductivity process, illustrated in Figure 5-6. The absorbed solar energy first results in the efficient generation of excitons in the film bulk[316] (described by the process $S_o + h\nu \Rightarrow S_o^*$, where S_o and S_o^* denote the molecular ground and excited states, respectively). Subsequently, the exciton drifts to a contact, impurity, interface or other inhomogenity within the structure (denoted M), at which point it dissociates into a free carrier pair (via $S_o^* + M \Rightarrow e^- + h^+$), or alternatively, suffers recombination. The recombination process accounts for a loss of roughly 95% to 99% of the excitons. Although exciton ionization is not fully understood,[226] it is often attributed to dissociation in the presence of the built-in electric field surrounding the crystal defect. If this dissociation occurs in an otherwise neutral region of the film, the photogenerated free electron−hole pair may remain localized within the vicinity of the defect where they recombine without being collected in the external circuit. Hence, to significantly increase η, two conditions must be met: (i) The film must be relatively free of defects which generate local electric fields, and (ii) the exciton and free carrier diffusion lengths must be sufficiently long such that these particles can migrate to regions of the film where the built-in electric field from an adjacent junction is high enough to separate the free electron−hole pairs prior to recombination.

If dissociation occurs at a contact or organic heterojunction, the built-in potential at that junction leads to charge separation, followed by carrier transport to the contacts and delivery of power to an external load. This two-step mechanism (exciton

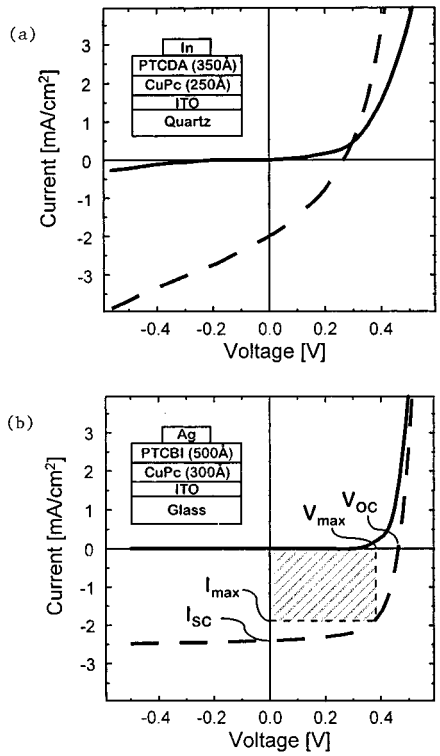

Figure 5-7. Two representative current vs voltage characteristics for the highest efficiency cells reported to date. (a) PTCDA/CuPc bilayer heterojunction cell with a power conversion efficiency of 1.8% at an optical power of 10 mW/cm^2 (from ref 174). (b) PTCBI/CuPc cell with an efficiency of 0.95% at 75 mW/cm^2 (from ref 271). Both light-on (dashed lines) and light-off (solid lines) characteristics are shown. Also, various terms used to describe solar cell performance are indicated in b: V_{oc} = open circuit voltage, I_{sc} = short circuit current. The maximum power rectangle shown by the cross-hatched region has an area equal to $I_{max}V_{max}$. The cell fill factor is defined by ff = $I_{max}V_{max}/I_{sc}V_{oc}$ < 1.

generation followed by carrier generation) is typically a very low efficiency process which is not expected to lead to power conversion efficiencies exceeding ~5%. To date, the highest power conversion efficiency (1.8%) has been reported for a PTCDA/CuPc bilayer cell[174] under an illumination intensity of 10 mW/cm^2. Here, the power conversion efficiency is defined as

$$\eta_P = \mathrm{ff} V_{oc} I_{sc} / P_{inc} \qquad (5.2)$$

where ff is the forward-biased "fill factor",[19] V_{oc} is the open circuit voltage, I_{sc} is the short circuit current, and P_{inc} is the incident optical power. These variables are defined in Figure 5-7. At the higher incident power of 75 mW/cm^2 (equivalent to AM2 illumination), a maximum power conversion efficiency of η_P = 0.95% was reported for a CuPc/PTCBI bilayer cell.[271] One problem with organic-based photovoltaic cells is their high contact and series resistances which lead to space-charge build-up with increasing incident power. It has been shown[307] that there is a roughly 2-fold decrease in efficiency resulting from space charge effects as the power density increases from 10 to 75 mW/cm^2, suggesting that the results for the CuPc/PTCBI and PTCDA/CuPc cells are nominally equal. The $I-V$ characteristics of these p-P heterojunction cells,[300] as well as schematic cross sections of both the PTCDA/CuPc and CuPc/PTCBI cells are shown in Figure 5-7, parts a and b, respectively. Of particular note is the low series resistance of the latter structure, as indicated by the abrupt increase in current at $V > V_{oc}$. This leads to the high fill factor observed, although the authors found that the ff characteristics degrade after prolonged exposure of the cell to air.[271]

A summary of recent results for organic PV cells using both Schottky and bilayer geometries is provided in Table 10. The best results obtained after those in Figure 5-7 were reported for a H_2Pc/DM-PTCDI bilayer cell with a built-in potential enhanced by H_2 doping, due to a lowering of the Fermi level within the DM-PTCDI.[303] Increasing the built-in potential (and hence increasing V_{oc}) has been attempted using several different approaches, the most notable being insertion of additional organic layers[304] or even fabricating series−connected "tandem" PV cells in a single stack.[302] These methods have proven successful in increasing V_{oc} which extends the effective width of the photoactive region, although they generally also result in an increase in series resistance (with its concomitant decrease in ff), thereby limiting the overall power efficiency of the devices to values somewhat less than those reported for the best, single junction cells.

It has been suggested that increased order within the film also results in an increased exciton and carrier diffusion length, which ultimately should produce a higher carrier mobility along the molecular stacks. These effects have been extensively studied[172,305] in the model compound, PTCDA, which is well-known to have extremely close $\pi-\pi$ stacking and long-range stacking order. Assuming that all exciton dissociation (and subsequent free carrier generation) occurs at contacts in a metal/organic/metal cell, Ghosh and Feng[262] have shown that the photocurrent density (J) is governed by exciton diffusion, $J = -D_{ex}\, dn(x)/dx$, where D_{ex} is the exciton diffusion constant, and $n(x)$ is the exciton density as a function of distance with respect to the contact on which the light is incident (i.e., the "near" contact), or the counter electrode (the "far" contact) depending on where the exciton dissociation occurs. Now, $n(x)$ is simply proportional to the optical flux ($\phi(x)$) at x, given by $\phi(x) = \phi_o \exp[-\alpha x]$, where ϕ_o is the flux at the near contact. From this analysis, it can be shown that the quantum yield due to exciton generation primarily at the near and far interfaces follows a straight line when $1/\eta_{NEAR}$ or $1/[\eta_{FAR} \exp(\alpha d)]$ are plotted as a function of $1/\alpha$, respectively. Here, d is the film thickness. Results of this analysis for three different wavelength regions for PTCDA films grown by OMBD[172] are shown in Figure 5-8. At short wavelengths where Frenkel excitons are generated (c.f. Figure 4-2b), the diffusion length is $L_D = 88 \pm 6$ nm, consistent with independent studies of Karl et al.[305] However, the diffusion length of the CT exciton at low energies (~2.0 eV) is $L_D = 225 \pm 15$ nm which, to our knowledge is the longest diffusion length

Table 10. Representative Molecular Organic-Based PV Cell Results

cell composition	V_{oc} (mV)	I_{sc} (mA/cm^2)	P_{inc} (mW/cm^2)	*ff*	η_P (%)	comments	ref(s)
Ag/PTCBI/CuPc/ITO	450	2.3	75	0.65	0.95		271
In/PTCDA/CuPc/ITO	260	2.0	10	0.35	1.8	low P_{inc}	300
Au/H_2Pc/DM-PTCDI/ITO	550	2.6	100	0.30	0.77	H_2 doped	303
	580	2.0		0.23	0.49	NH_3 doped	
	660	1.6		0.22	0.41	undoped	
Au/H_2Pc/DM-PTCDI/PTCBI/ITO	370	0.5	25	0.27	0.20		304
Au/H_2Pc/PTCBI/ITO	370	0.18	25	0.32	0.08		304
Al/merocyanine/Ag	1200	0.18	78	0.25	0.62	Schottky cell, best at $d = 150$ Å	262
Al/ZnPc/Au	590	5.6×10^{-4}	0.1	0.1	3×10^{-4}	Schottky cell	306
Au/ZnPc/DM-PTCDI/ITO[a]	450	0.036	0.1	0.25	0.014	comparison with Schottky cell	306
In/PPEI/PVP(TPD)/ITO[b]	530	0.038	8	0.3	0.075	$\lambda = 500$ nm	301
Au/CuPc/DM-PTCDI/ITO	415	1.9	100	0.41	0.33		307
Au/ZnPc/DM-PTCDI/ITO	276	0.78	100	0.26	0.07	solvent washed	307
	380	2.11		0.36	0.29	twice sublimed	
	405	3.53		0.30	0.43	$d_{DIME}/d_{ZnPc} = 25/50$ nm	
	385	2.17		0.30	0.25	$d_{DIME}/d_{ZnPc} = 100/100$ nm	
Au/H_2Pc/PTCBI/ITO	580	0.75	100	0.24	0.10		307
Au/TPP/DM-PTCDI/ITO[c]	490	0.21	100	0.18	0.019		310
Au/TBP/DM-PTCDI/ITO	103	2.57		0.27	0.07		
Au/H_2Hc/DM-PTCDI/ITO	280	0.21		0.37	0.023		
Au/H_2Pc/DM-PTCDI/ITO	400	2.7	78	0.56	0.76		302
(Au/H_2Pc/DM-PTCDI)$_2$/ITO	800	0.75		0.21	0.16	tandem with Au[d]	
Au/(H_2Pc/DM-PTCDI)$_2$/ITO	300	0.55		0.35	0.08	tandem without Au	
Al/C_{60}/TiOPc/ITO	420	4×10^{-4}	10^{-2}	0.20	0.35	illumination through Al	312
Al/C_{60}/VOPc/ITO	530	5.4×10^{-5}		0.16	0.099	low P_{inc} at $\lambda = 720$ nm	
Al/ C_{60}/PPV/ITO[e]	800	3.8×10^{-3}	0.25	0.48	0.58	PPV spun on	311

[a] Contacts inferred from text, not explicitly stated. [b] PPEO: 3,4,9,10-perylenetetracarboxyl-*N*,*N*′-bis(phenylethylimide). PVP(TPD): 55 wt % *N*,*N*′-diphenyl-*N*,*N*′-ditolylbenzidine in poly(vinylpyridine) spin coated onto ITO surface prior to PPEI deposition. [c] TPP: 5,10,15,20-21*H*,31*H*-tetraphenylporphyrin. TBP: tetrabenzoporphyrin (29*H*,31*H*-tetrabenzo[2,3-*b*:2′,3′-*g*:2″,3″-l:2‴,3‴-*q*]porphyrazine). H_2Nc: metal-free naphthalocyanine (29*H*,31*H*-tetranaphtho[2,3-*b*:2′,3′-*g*:2″,3″-l:2‴,3‴-*q*]porphyrazine). [d] Comparison of single layer cell with tandem cells with and without interstitial 2 nm thick Au layer separating organic bilayers. [e] PPV: poly(phenylene vinylene).

measured for an exciton in an organic thin film. The voltage dependence of the quantum yield apparent in the figure arises from improved carrier collection efficiency at either the near or far contact (depending on the sign and magnitude of the voltage) due to increased fields within the film bulk. The long diffusion lengths observed for OMBD grown samples clearly suggests the need for extended stacking order to achieve long diffusion lengths with its concomitant increase in quantum yield.

Finally, a detailed study of the effects on performance due to material purity and deposition conditions on bilayer DM-PTCDI cells employing phthaocyanine, perylene and porphyrinic compounds as the second organic material, have also been recently reported.[307] For example, the source materials for ZnPc/DM-PTCDI cells were purified prior to deposition using three different methods: solvent extraction, reprecipitation of ZnPc from concentrated sulfuric acid, and multiple step sublimation in vacuum as discussed in section 2. The primary figure of merit was η_P, which was highest for sublimed materials (with $\eta_P = 0.29\%$) and lowest (by a factor of 3) for material which underwent solvent extraction ($\eta_P = 0.07\%$). From these results, it was inferred that material purity is a key parameter in achieving high efficiency solar energy conversion. Impurities acting as ionic trapping centers, or which disrupt the stacking order of the films, ultimately increase series resistance, charging (and hence space−charge build-up), and decreases the mobility of the charge carriers and excitons in the films. Furthermore, trapped charge can shift the Fermi-energy positions within the films, thereby decreasing (or increasing) V_{bi}, ultimately determining the width of the photoactive region.

The study was extended to examine the effects of deposition rate, which was varied between 0.1 and 15 Å/s. For these materials, no systematic surface morphology dependence was observed over this range of rates, suggesting that the film order was also unaffected. This was also consistent with the finding that η_P and other device performance parameters were not dependent on deposition rate.

An additional parameter which has been systematically varied in the growth of DM-PTCDI/ZnPc PV cells is substrate temperature,[307] varied from 25 to 200 °C. Due to roughening of the surface at the highest temperatures (>100 °C), short circuits developed and the PV cells ceased to function. Below this temperature, there is a systematic decrease in η_P from 0.33% at $T_{sub} = 25$ °C to 0.28% at $T_{sub} = 100$ °C. This reduction in η_P was attributed to elimination of shorts (which reduce V_{oc}) as the growth

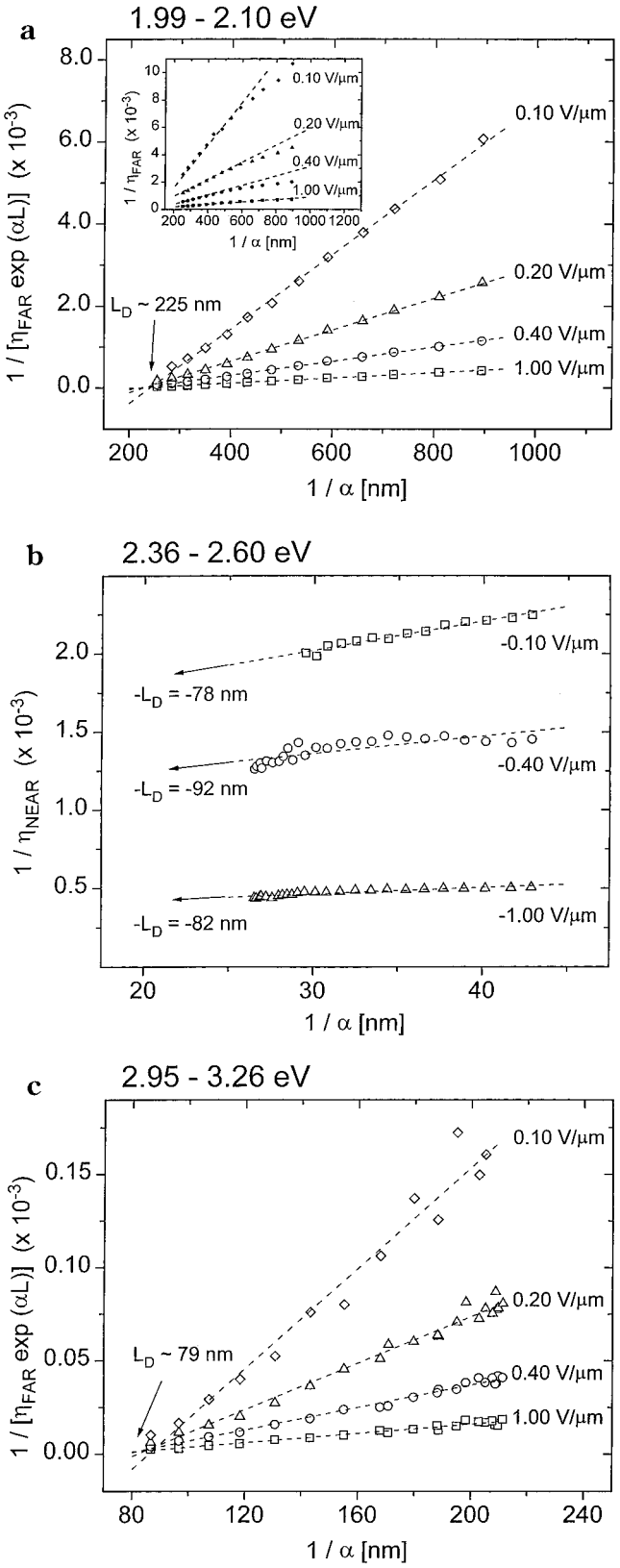

Figure 5-8. Inverse quantum yield ($1/\eta$) at different applied fields vs inverse absorption coefficient ($1/\alpha$). (a) A diffusion length of $L_D = 225 \pm 15$ nm is found for $E = 2.10$ to 1.99 eV region. Inset: The data replotted vs $1/\eta$. At other wavelengths, diffusion lengths observed are (b) $L_D = 88 \pm 6$ nm for absorption between $E = 2.60$ and 2.36 eV and (c) $L_D = 79 \pm 7$ nm for the $E = 3.2$ eV absorption peak were determined from linear least squares fits to the data (from ref 172).

temperature was lowered. That is, as observed for the OMBD growth of PTCDA[111] (see section 3.3.3), the film surface becomes quite smooth as T_{sub} is lowered into the quasi-epitaxial (i.e., kinetically controlled) growth regime.

The implication of the these results is that continued improvements in η_P can be obtained for PV cells grown by OMBD at $T_{sub} < 300$ K under UHV conditions where an extremely high degree of crystalline order and material purity can be assured. However, it is equally apparent that the resulting materials grown in this manner are unlikely to perform at levels which will make them attractive for use in practical solar energy conversion applications. For this purpose, novel multiple quantum well structures such as those discussed in sections 4.2 and 4.3 which optimize the overlap between the optical, excitonic and carrier distributions provide the most likely means for achieving the long sought-after goal of low cost power generation via the use of efficient thin film molecular organic PV cells.[34]

A promising, alternative use of organic thin films in PVs is as fluorescent down converters layered on the surface of conventional solar cells. It is well known that the efficiency of conventional Si photodiodes and solar cells decreases rapidly in the near-UV range, while numerous organic thin films exhibit strong UV absorption followed by radiation at lower energies (known as "down conversion"). The down converted light can be more readily detected by the Si solar cell than the original UV radiation, thus a down-converting organic thin film deposited on the surface of a conventional solar cell effectively increases the solar cell efficiency in the UV range. The down conversion is due to the Frank−Condon red shift from absorption to luminescence characteristic of organic molecules. If the film coating thickness is appropriately adjusted, this same film can also be employed as an antireflection coating for light in the visible spectral region.[317]

Experimental and theoretical studies of organic fluorescent down converters for Si solar cells have been pursued for almost 20 years.[318,319] In the initial studies, thick (2−5 μm) layers of laser dye molecules in sol-gel or in plastic matrices were used, and wavelength down conversion (from 400 to 510 nm) with efficiencies exceeding 90% was demonstrated.[320] Later, deposition of "monocompositional" solid films of coronene[318] and metachrome[321] on CCD sensor surfaces resulted in the commercial production of UV sensitivity-enhanced cameras. Further studies of successful utilization of such wavelength down converters combined with Si photodiodes have been limited to tris(8-hydroxyquinoline)aluminum (Alq_3) films.[317] Alq_3 has a strong absorption at $\lambda < 370$ nm ($\alpha > 10^5$ cm^{-1}), with a photoluminescence peak at $\lambda = 530$ nm (where the Si PV cell efficiency is high) and has a thin-film photoluminescence efficiency exceeding 30%.[322] An Alq_3 film deposited directly on top of a conventional Si solar cell has, therefore, been observed to increase the UV collection efficiency of the cell by an order of magnitude.[317] A similar organic coating with a 100% conversion efficiency would increase the solar cell efficiency by as much as 11% under AM0 illumination. Hence, it is probable that new organic thin film materials will lead to the realization of UV-enhanced Si photodiodes and

solar energy converters with efficiencies sufficiently high to suit many commercial applications.

5.3. Molecular Organic Light-Emitting Devices

Efficient electroluminescence (EL) from an organic solid was first demonstrated in large (50 μm to 1 mm thick) single crystals of anthracene.[323,324] Although these devices showed a high EL quantum efficiency of up to 8%, they were impractical due to the large applied voltage (>1000 V) required to inject electrons and holes into the crystal. More recently, practical organic light-emitting devices (OLEDs) consisting of sequentially vacuum-deposited layers of hole- and electron-transporting molecular materials[31] have been demonstrated with active device thicknesses of only a few hundred Ångstroms. In contrast to electronic devices where crystalline order results in a high carrier mobility, and hence a good device performance (e.g., in organic TFTs or OI-HJ devices), vacuum-deposited OLEDs typically consist of amorphous thin films. The amorphous structure leads to a high radiative recombination efficiency of Frenkel excitons due to a reduction in quenching from internal conversion processes linked to highly coupled, crystalline organic systems. These heterojunction devices have resulted in a decrease in operating voltage to <10 V with a brightness of several hundred candela per meter squared which is adequate for most video display applications.

A schematic cross section of a conventional, molecular OLED with three organic layers (a double heterostructure) is shown in Figure 5-9. The top, ohmic, electron-injecting electrode consists of a low work function metal alloy, typically Mg-Ag or Li-Al, deposited by vacuum evaporation. The bottom, hole-injecting, electrode is typically a thin film of the transparent semiconductor indium tin oxide (ITO), deposited onto the substrate by sputtering or electron beam evaporation. Light is emitted through this electrode when the device is operated in "forward bias", i.e., with the ITO biased positive with respect to the top electrode. The next layer deposited is a hole transporting layer (HTL) of a material such as *N*,*N*′-diphenyl-*N*,*N*′-bis(3-methylphenyl)-1,1′-biphenyl-4,4′-diamine (TPD), shown with other widely used molecules in Figure 5-10. This is followed by the light emitting (EL) layer consisting of, for example, Alq'_2OPh for blue light emission, or Alq_3 for green light. An electron transporting layer (ETL), consisting of a material such as TAZ (Figure 5-10) completes the double heterostructure. Doping a small amount (~1 mol %) of a fluorescent dye into the EL layer can significantly improve the device efficiency, and >5 lm/W in the green is now routinely obtained.[325] Typical deposition rates of all organic molecular layers is from 1 to 5 Å/s. Examples of molecules used for red (R), green (G), and blue (B) light emission are also shown in Figure 5-10, along with four examples of charge-transporting molecules. In many cases (Alq_3, for example) the functions of electron transporter and light emitter may be combined in a single layer, resulting in "single heterostructure" devices.

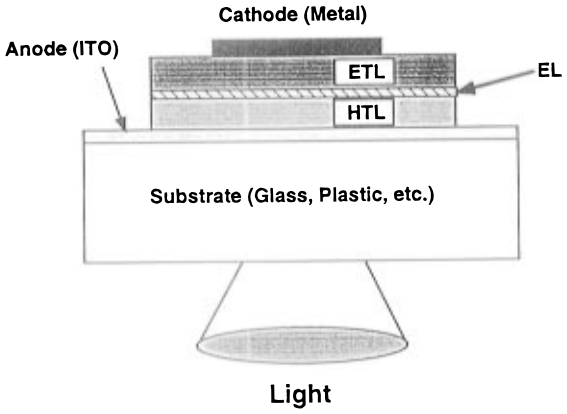

Figure 5-9. Conventional organic light emitting device (OLED) double heterostructure showing the contacts, the electron transport layer (ETL), light-emitting layer (EL), and hole transport layer (HTL). The total organic thin film thickness is typically ~1000 Å.

There are many variations on the single and double heterostructures, including hybrid materials combinations such as Alq_3 deposited on the polymer hole injecting and luminescent material, poly(*p*-phenylene vinylene), or PPV.[326] In addition, organic/inorganic OLEDs based on the layered perovskite semiconductor, $(C_6H_5C_2H_4NH_3)_2PbI_4$, or PAPI, used as the hole injection layer in combination with the electron injecting oxadiazole derivative, OXD7, were shown[327] to exhibit very narrow spectral emission centered at $\lambda = 520$ nm.

While OLEDs based on vacuum-deposited molecular materials[31,32,264,325,328−330] or on polymers[331−333] have both been investigated,[330] the discussion in sections 2 and 3 clearly shows that vacuum deposition offers the advantages of better control over layer thickness and uniformity, and access to reproducible, higher purity starting materials—all critical parameters for displays. In addition, since all of the device layers are vacuum deposited at room temperature, OLED fabrication is compatible with conventional semiconductor processes. Failure mechanisms of such devices are primarily related to dark spot formation at the contact/organic thin film interfaces. These effects have been extensively studied,[334−337] and recently continuous operating lifetimes of vacuum-deposited green OLEDs at video brightness have been shown to exceed 20 000 h,[338,339] making them sufficiently long-lived for commercial flat panel display applications.

The devices have also been found to be vulnerable to structural instabilities as the temperature is increased beyond the glass transition temperature (T_g) of one of the layers composing the OLED heterostructure.[340−342] The OLED structure under temperature stress was thoroughly studied using glancing incidence X-ray,[341] employing the same techniques and tools discussed in section 3.3.2.3 as well as via energy dispersive X-ray diffraction,[342] with both investigations resulting in essentially similar results. Here, we discuss briefly the results of Fenter et al.,[341] since they illustrate some of the advantages to using vacuum-deposited materials in achieving precise structural control, and also provide information as to the degradation under thermal stress of OLED heterostructures.

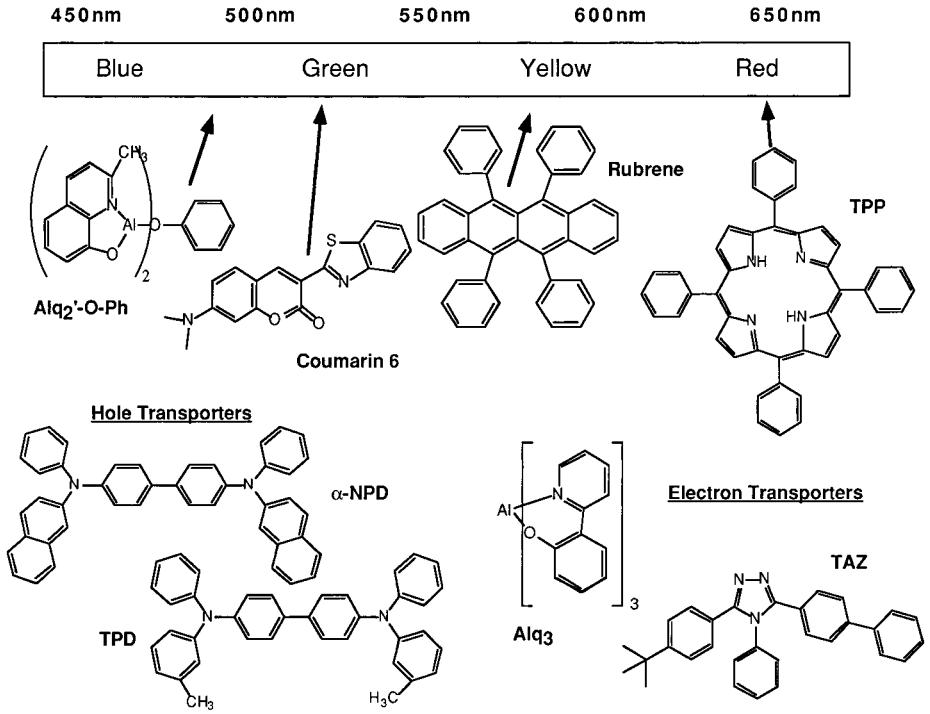

Figure 5-10. Structural formulae for several compounds typically used in OLEDs.

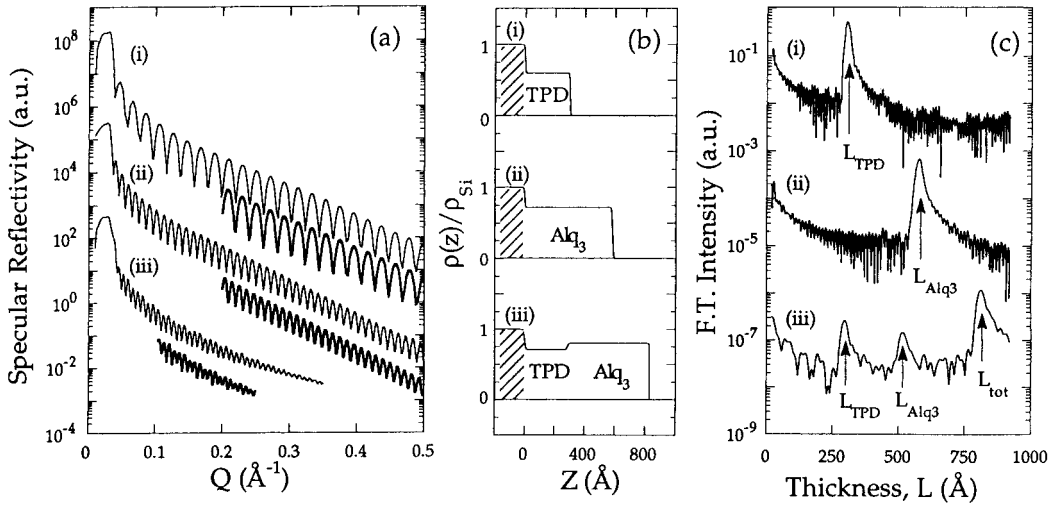

Figure 5-11. (a) X-ray specular reflectivity (thin lines) of (i) Alq_3, (ii) TPD and (iii) Alq_3/TPD films grown on Si substrates. Corresponding fits to the data are shown by the bold lines, with data and fits offset for clarity. (b) Electron density profiles derived for each film structure. (c) Fourier transform (FT) of the data shown in a (from ref 341).

In Figure 5-11a, the X-ray specular reflectivity of a series of thin film structures (thin and bold lines are experimental data and theoretical fits, respectively), is shown. These structures are (i) TPD on a Si substrate, (ii) Alq_3 on Si, and (iii) Alq_3/TPD on Si. The reflectivity is dominated by the Fresnel reflectivity of a highly flat interface, whose intensity asymptotically follows $1/Q^4$, where Q is the X-ray momentum transfer. A least-squares fit to the data (bold lines, Figure 5-11a) using standard Fourier analysis techniques,[343] provides the electron density profiles of the layers (Figure 5-11b). These fits suggest that the mean-square interface roughness in all three structures is <4.5 Å. This roughness is comparable to the dimensions of a single molecule and is only ~1% of the total film thickness, providing evidence that vacuum deposition of organic films can result in extraordinarily flat (on the molecular scale) films and interfaces necessary to realize many, high performance optoelectronic devices.

Fourier transforms (FT) of the reflectivity oscillations provide extremely clean data (Figure 5-11c) as a result of the flatness of all interfaces. The layer thicknesses obtained from these transforms for both the single-layer structures and the compound structure are clearly indicated by the peaks in the figure and correspond very well to the thicknesses measured during growth using a quartz crystal microbalance. Using such precision data, Fenter et al.[341] were able to accurately measure such film properties as thermal expansion coefficients and degradation of OLED structures under thermal stress. An example of the changes which occur to a TPD film as its temperature is elevated above $T_g \approx 60$ °C is shown in Figure 5-12. The reflectivity spectra in Figure 5-12a for a TPD/Si film clearly indicate an attenua-

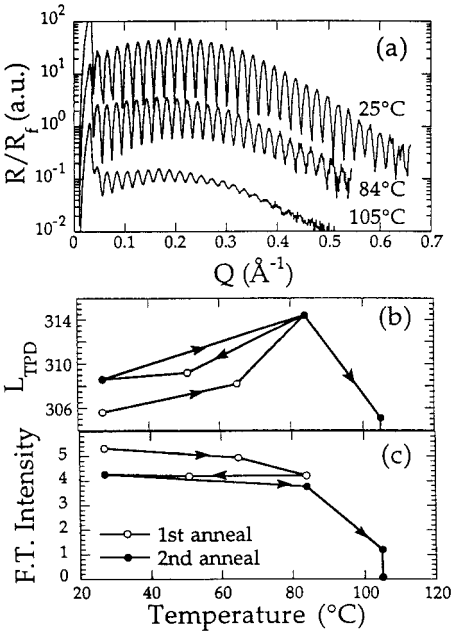

Figure 5-12. (a) Normalized X-ray specular reflectivity for TPD/Si vs temperature. (b) Film thickness and (c) calculated FT intensity vs temperature. The arrows in b and c indicate the thermal history of the sample (from ref 341).

tion of the signal as temperature is increased, with irreversible changes occurring at $T > 85$ °C. By taking the FT of these data, the film thickness can be directly tracked as the film is thermally cycled. This is indicated in Figure 5-12, parts b and c, where the film is first heated to 85 °C, then cooled, and then reheated to 105 °C. It is observed that in the first cycle, the film expands by 9 Å, from which a thermal expansion coefficient of $\alpha = 1.2 \times 10^{-4}$/K is inferred. Upon cooling, it is found that the film thickness actually increases slightly, along with a slight decrease in FT peak intensity. During the second cycling above the melting point of TPD, the FT intensity decreases by a factor of 10^2, although the film thickness decreases only slightly. The FT intensity decrease rules out the possibility that the film has simply densified due to the thermal cycle, suggesting instead that laterally inhomogeneous desorption occurs, leaving small TPD islands whose thickness is nearly unchanged from that of the original film. Indeed, the X-ray data do not support the presence of any recrystallization,[340] but rather only that morphological changes are occurring.

Further X-ray studies of the compound Alq_3/TPD/Si structure along these same lines were used to develop a complete picture of OLED structural failure during thermal stress.[341] It was concluded that the primary driving force for the degradation of Alq_3/TPD heterostructures, and which is undoubtedly similarly active in many other organic heterojunction systems, is the large thermal expansion of one of the components (TPD) associated with its glass transition, creating catastrophic strain release at the heterointerface between the materials. This conclusion is supported by the observation that Alq_3/TPD structures grown at elevated temperatures ($T_{sub} = 73$ °C) exhibited better morphology and greater thermal stability than those grown at room temperature.[334]

Thermally induced failure of OLEDs is reduced under normal device operating conditions by increasing the T_g of all materials incorporated into the structure. For this reason, TPD has now largely been replaced by α-NPD ($T_g \approx 110$ °C) in vacuum deposited OLEDs (see Figure 5-10). Tokito et al.[344] have shown that a tetramer of triphenylamine (TPTE) with $T_g = 130$ °C can also be used as an efficient hole-transporting material. Such TPTE/Alq_3-based devices were demonstrated to have stable operation at $T \leq T_g$. Indeed, storage at $T = 150$ °C was not found to result in significant degradation of the device characteristics when operated after returning to room temperature. Many other aromatic amines have also been investigated for their suitability as high stability, high melting temperature hole transport materials for OLED applications.[295] Finally, we note that in addition to thermal instabilities and dark spot formation, photochemical instabilities[334,345] of the organic materials can also influence the lifetime of these interesting devices.

In the remainder of this section, we discuss the fundamental processes leading to current conduction and electroluminescence in vacuum-deposited OLEDs. Discussion of these processes leads to a more complete understanding of the relationship between film structure and device properties. This is followed by a discussion of some of the interesting OLED architectures which are apparently unique to this new generation of organic devices.

5.3.1. Current Transport and Electroluminescence Mechanisms in OLEDs

It has recently been shown[32,258,346] that the electrical and optical characteristics of vacuum-deposited molecular OLEDs can be modeled by assuming that the fundamental mechanism controlling both current conduction and EL yield is space charge effects in the presence of an intrinsic trap distribution. The depth and distribution of the traps is consistent with their being formed by molecular relaxation on ionization by injected charge carriers. That is, once a charge carrier (e.g., an electron) localizes on a molecule (i.e., it is trapped), a charge of opposite polarity (a hole) injected from the counter electrode becomes similarly localized on that same molecule. This electron−hole pair, whose energy is less than the ionized molecular energy by their Coulomb binding energy, eventually recombines, emitting either light or heat. Most of the recombination occurs within only a few hundred Ångstroms of the HTL/ETL interface determined by the diffusion length of carriers in the emitting material. This region is known as the "recombination zone".

It has been found[32,347] that exciton diffusion lengths in such amorphous thin films as Alq_3 are approximately 100−300 Å. Hence, in optimal devices, the Alq_3 layer thickness must be only slightly larger than this thickness (see below), suggesting that significant control over film deposition as well as on substrate flatness afforded by vacuum deposition of molecular organics is necessary.

A very clear demonstration of the extent of the recombination zone was provided by Adachi et al.[348] using a single heterostructure OLED shown sche-

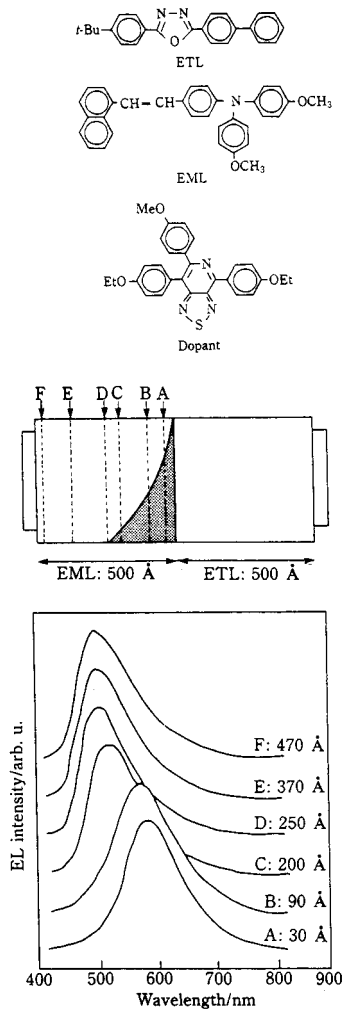

Figure 5-13. Top: Chemical structural formulae for the organic molecules used to determine the width of the recombination region. Center: Schematic of the doped single−heterostructure OLED. Bottom: Electroluminescence spectra of six doped single heterostructure OLEDs, with the positions (A−F) of the dopant layers indicated in the diagram of the OLED (from ref 348).

matically in Figure 5-13. For this device, the 500 Å thick hole transport and light-emitting layer consisted naphthostyrylamine (NSD), and the 500 Å thick ETL consisted of an oxidiazole derivative. Structural formulae for molecules used in this study are also shown in Figure 5-13. To determine the extent of the recombination zone, a highly emissive dopant chromophore, a thiadiazole derivative, was grown in very thin (10 Å) slabs located at different distances from the HTL/ETL interface in different devices. The emission spectrum of each of these devices was then measured, with the results shown in the figure. For dopant slabs located within ~100 Å of the heterointerface, the emission peaks at 590 nm (spectra labeled A and B), characteristic of the spectrum from the thiadiazole derivative. However, when the dopant is moved farther from the interface (spectra C−F), the emission peak shifts to 500 nm due to recombination in the undoped NSD. This result clearly indicates that virtually all radiative recombination occurs in the HTL, within 100 Å of the HTL/ETL interface for this heterostructure. These conclusions about the width and position of the recombination zone has been confirmed by measure-

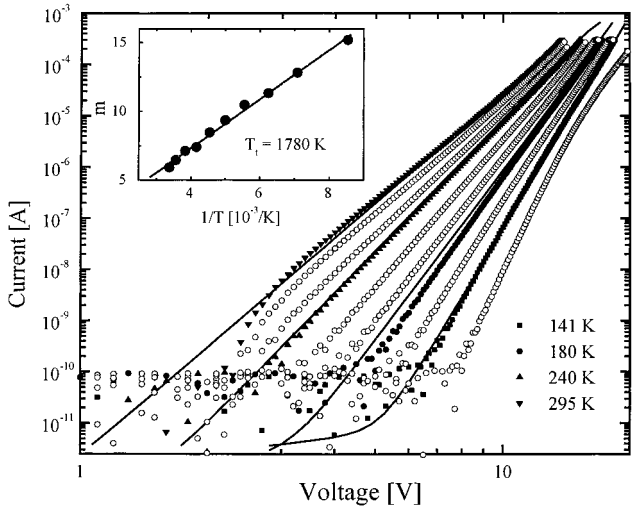

Figure 5-14. Current as a function of applied voltage in a 270 Å thick TPD, and 550 Å thick Alq_3 OLED at various temperatures (open symbols). The solid lines show a fit to the space-charge limited model discussed in the text, using $N_t = 3.1 \times 1018$ cm^{-3}, and $\mu N_{LUMO} = 4.8 \times 1014$ (cm V s^{-1}). Inset: Temperature dependence of the power law parameter, m, ($I \approx Vm + 1$) giving $T_t = 1780 \pm 50$ K (from ref 258).

ments of exciton dynamics in Alq_3 and at Alq_3/TPD interfaces.[349,350] Undoubtedly, these conclusions can be generalized to understand almost all small molecular weight, vacuum-deposited OLEDs.

Typically, the power-law dependence of current-on-voltage observed for OLEDs and expected from the trapped charge model fits experimental data over many decades of current and over a wide range of temperature. However, effects due to low efficiency of charge injection from the electrodes, particularly the low work function cathode, can complicate the process by adding extra resistance which results in a voltage offset.[351]

In the trapped−charge model, we assume that the current density is bipolar, in that it consists primarily of holes injected from the ITO contact into the HTL (e.g., TPD), with electrons injected from the low work function cathode (e.g., Mg-Ag) into the ETL (e.g., Alq_3). Of the two carriers, electrons have the lower mobility and hence limit the current conduction process. Radiative recombination occurs when holes are injected from the TPD into the Alq_3, where, within a short distance (a few hundred Ångstroms) of the TPD/Alq_3 heterojunction, they bind to an electron on an Alq_3 molecule forming a short lifetime, Frenkel exciton. Radiative recombination competes with nonradiative (dissipative) recombination occurring at the TPD/Alq_3 interface as well as at the contacts.

The power-law dependence of current-on-voltage (Figure 5-14), commonly observed in both molecular organic[32,258,326,346,351,352] and polymer-based[353−355] OLEDs, is interpreted in terms of the injection of space charge into a trap-filled insulator (Alq_3). At very low applied voltage, ohmic conductivity dominates, where the current density, J, is described by $J = q\mu_n n_o V/d$. Here, n_o is the background density of free electrons in Alq_3, μ_n is the electron mobility, and d is the layer thickness. Previous observations of ohmic conduction at extremely low injection currents[32] (<0.1 μA/cm^2) sets an upper limit to $n_o\mu_n$ in this expression of 10^7

$(V\ cm\ s)^{-1}$. At higher injection currents, the filling of traps below the electron quasi-Fermi level results in the current being governed by the density and energy distribution of the traps. An analytical expression relating current to voltage in this trap charge limited (TCL) regime is obtained by assuming, for simplicity, a continuous exponential energy distribution of traps below the LUMO following[356]

$$N_t(E) = (N_t/kT_t)\exp[(E - E_{LUMO})/kT_t] \quad (5.2)$$

Here, N_t is the total trap density, E_{LUMO} is the Alq_3 LUMO energy, and $T_t = E_t/k$, where E_t is the characteristic trap energy. The current density is then given by

$$J_{TCL} = N_{LUMO}\mu_n q^{(1-m)}\left[\frac{\epsilon m}{N_t(m+1)}\right]^m \times \left(\frac{2m+1}{m+1}\right)^{(m+1)} \frac{V^{(m+1)}}{d^{(2m+1)}} \quad (5.3)$$

where ϵ is the permittivity and N_{LUMO} is the LUMO density of states. It is clear from eq 5.3 that $m = T_t/T$ determines the temperature dependence of the $I-V$ characteristics. A weaker effect is the temperature dependence of the mobility, which in organic materials empirically follows $\mu_n(T) \approx T^{-n}$, where n varies from 0 to 3. Conduction and scattering by phonons in narrow bands characteristic of organic molecular solids has been shown to yield a temperature dependence[357] of $\mu_n \approx T^{-2}$. However, small changes in the exponent or functional form or even the small expected dependence on electric field, chosen for $\mu(T)$ do not significantly affect the fit, which is primarily governed by the strong power-law dependence of eq 5.3. Finally, the temperature dependence of N_{LUMO} has also been shown to be negligible.[258]

The forward-biased $I-V$ characteristics of TPD/Alq_3 OLEDs at temperatures ranging from 120 to 300 K at 20 K intervals have been fit to the model described above,[258,346] as shown by the solid lines in Figure 5-14. For these fits, it was assumed that the OLED current is limited by the 550 Å thick Alq_3 layer, and hence the contacts play a less significant role in limiting current transport in optimum devices with thin organic layers. With N_t and $\mu_n N_{LUMO}$ as parameters, eq 5.3 fits the data over six decades of current, with m varying from 6 ± 1 at 300 K to 15 ± 1 at 120 K. The inset to Figure 5-14 shows the variation of m with $1/T$, which is fit by a straight line corresponding to $E_t = 0.15 \pm 0.02$ eV. A further test of the validity of the trap-limited model is the prediction from eq 5.3 that V is approximately proportional to d^2 at constant current, which has also been confirmed for TPD/Alq_3 devices.[258,346]

Using the measured value of T_t, the density of traps can be determined by fitting the temperature dependent data to eq 5.3. From this, it was found that[258,346] $N_t = 3.1 \times 10^{18}\ cm^{-3}$, and $\mu_n N_{LUMO} = 4.8 \times 10^{14}\ (cm\ V\ s)^{-1}$. Using time-of-flight measurements, Hoskawa et al.[358] determined that $\mu_n(300\ K) = (5 \pm 2) \times 10^{-5}\ cm^2/(V\ s)$, from which we infer $N_{LUMO} = (1.0 \pm 0.5) \times 10^{19}\ cm^{-3}$. Finally, this model yields $n_o < 10^{11}\ cm^{-3}$, consistent with the insulating nature of Alq_3.

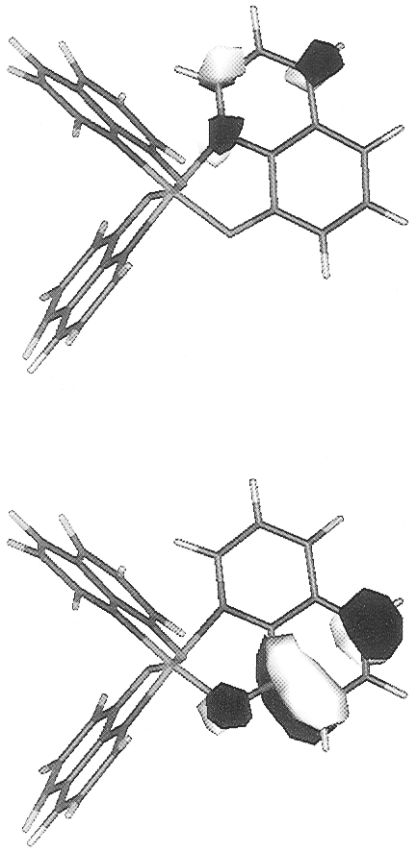

Figure 5-15. (Bottom) The location of the filled orbitals (HOMO states) in a molecule of Alq_3 and (top) the location of the empty orbitals (LUMO states) (from ref 258).

The fact that N_{LUMO} and N_t are roughly equal (and within 2 orders of magnitude of the density of molecular sites) suggests that each conduction electron is *self-trapped* on an Alq_3 molecule[32,258,346] due to the resulting generation of a polaron, i.e., each molecular site serves both as an available electron state and a trapping site. This is consistent with molecular orbital calculations[258] which indicate that the Alq_3 anion LUMO is ~0.2 eV lower in energy than the neutral state—a value approximately equal to the neutral polaron energy, E_t. Hence, an electron and hole which localize on the same *quinolate ligand* of an Alq_3 molecule (which are the sites of the calculated HOMO and LUMO as shown in Figure 5-15), are lowered in energy from their conduction states by the Coulomb binding energy of the resulting Frenkel exciton. The exponential distribution of energies, as suggested by the above analysis, is due to the presence of a high density of intramolecular phonons at room temperature leading to a distribution of nondegenerate molecular conformations. Evidence for the effects of phonons is also apparent from the broad EL and PL emission spectra[32,347] which are at significantly lower energies from the absorption spectrum of Alq_3 due to the large Franck–Condon shift. In section 5.3.2, we show that this substantial red shift in luminescence is useful in transparent OLEDs which have a wide range of device applications.[256]

These relaxation processes can be put in the context of the HOMO–LUMO energy diagram for an OLED shown in Figure 5-16. Here, electrons are injected from the cathode into the Alq_3, and holes are

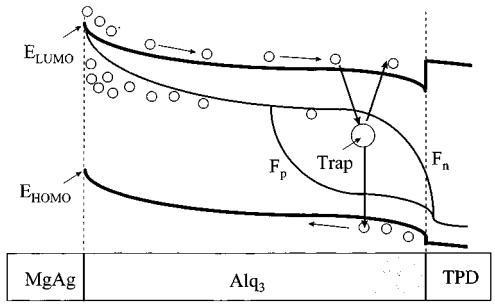

Figure 5-16. Schematic energy level diagram showing the process of charge transport and subsequent relaxation of trapped electrons in Alq_3 with a minority hole, to form a distribution of Frenkel excitons in the Alq_3 bandgap. These self-trapped excitons subsequently recombine to generate electroluminescence. Electrons are indicated by shaded circles in the LUMO band, and holes by open circles in the HOMO band. F_p and F_n indicate the quasi-Fermi levels for holes and electrons, respectively (from ref 258).

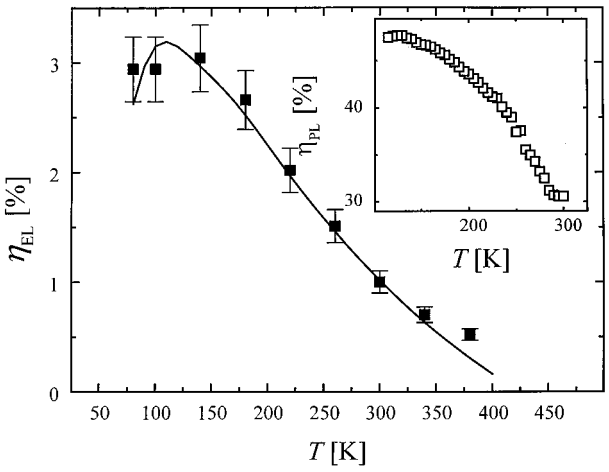

Figure 5-17. Dependence of electroluminescence efficiency on temperature of a 270 Å thick TPD and 550 Å thick Alq_3 OLED (closed squares), and fit to a model assuming that trapped charge gives rise to EL (line). Inset: Dependence of photoluminescence efficiency on temperature of a 1000 Å thick Alq_3 film vacuum evaporated on a UV-transparent quartz substrate (from ref 258).

injected from the TPD from the opposite electrode. These carriers hop from molecule to molecule, with the electrons arriving in the vicinity of the ETL/HTL interface before localizing on an Alq_3 molecule. This localization is a "self-trapping", or polaron generation process which lowers the energy of the molecule in its anionic form to well below E_{LUMO}. Subsequently, a carrier of opposite sign (in this example, a hole) localizes on the anion, further decreasing the now-excited molecular state by the Coulomb pair binding energy. At some time later equal to the exciton lifetime, the pair recombines (either radiatively, generating light, or nonradiatively, generating heat) and the molecule is free to accept the next injected carrier.

The role of self-trapping has in fact been extended to quantitatively explain the mechanisms for EL.[258,346] In Figure 5-17, the EL quantum efficiency at a constant current of 50 μA (solid symbols) is plotted as a function of temperature. Now, the EL flux (Φ_{EL}) is proportional to the rate at which electrons in the filled trap states recombine with holes in the Alq_3 HOMO (at energy E_{HOMO}) via an intermediate, relaxed Frenkel exciton state. Since holes (of density $p(x)$) are minority carriers in Alq_3, the recombination rate per volume as a function of the distance from the electron injecting Mg:Ag electrode at x is

$$r(x) = p(x)/\tau_p(x) \tag{5.4}$$

where $\tau_p(x)$ is the hole lifetime in the Alq_3 layer, which can be determined from steady state recombination statistics.[359] Also, $p(x)$ is found using

$$\frac{p(x)}{\tau_p(x)} = D_p\frac{d^2p(x)}{dx^2} - \mu_p\frac{d}{dx}[p(x)F(x)] \tag{5.5}$$

where $D_p = \mu_p kT/q$ is the hole diffusion constant, μ_p is the hole mobility and $F(x)$ is the electric field. The total recombination rate is $R \cong p(d)\mu_p F(d)$. Since the ratio of radiative to total recombination is proportional to the photoluminescence (PL) efficiency, η_{PL}, in Alq_3, the temperature dependent EL flux is

$$\Phi_{EL}(T) = \alpha\eta_{PL}(T)R = \alpha\eta_{PL}(T)p(d)\mu_p F(d) \tag{5.6}$$

The factor, α, includes all losses that do not exhibit a significant temperature dependence (e.g., due to spin statistics, small-energy nonradiative transitions, etc.). Here, $\eta_{PL}(T)$ is shown in the inset in Figure 5-17. The forward-scattered external PL quantum efficiency, which can be directly compared to the EL in an OLED, was measured to be 7%.

Assuming $\mu_p = 0.01\mu_n$, $E_p - E_{HOMO} = 20 \pm 1$ meV at $x = d$, $\alpha = 0.25$ and $N_{HOMO} = 0.07N_{LUMO}$, the EL data of Figure 5-17 have been fit (solid line) to eq 5.6. The EL intensity increases with decreasing temperature due to a decrease in the hole lifetime−diffusion length product. The increase saturates at the lowest temperatures due to the reduced hole injection into the Alq_3 as a result of a decrease in $p(d)$. The calculated room temperature external EL quantum efficiency ($\eta = q\Phi_{EL}/J$) obtained from this fit is ~1%, consistent with the measured value of 0.5−1%.

This study clearly suggests a link between the filled traps that give rise to the $I-V$ characteristics and the EL intensity, providing detailed insight into the physical origin of EL in OLEDs. One consequence drawn of this analysis is that only ~1% of the Alq_3 molecules are optically active under even the highest drive currents. This is not surprising in that very high currents should lead to a large electron space charge in the film which would serve to halt (via Coulombic interactions) further current injection. This analysis is essentially a "one-electron" picture which does not account for electron−electron interactions. Nevertheless, the model suggests that optimal performance can be achieved by lightly doping a conducting host molecular film with ~1% of a different, highly luminescent guest molecule to achieve maximum EL efficiency. This effect was observed[264] for several different molecular dopants in Alq_3, including[360,361] the red-emitting tetraphenylporphine (TPP). It was found that, as predicted, maximum red luminescence efficiency (with a peak wavelength of $\lambda = 655$ nm, Figure 5-18) is achieved for TPP dopings of ~1% (by mol wt), with the device red-emission efficiency decreasing at both higher and lower con-

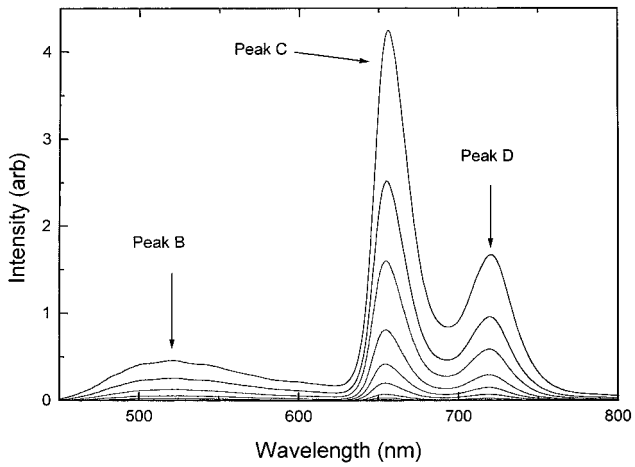

Figure 5-18. Output from a Mg-Ag/Alq_3:TPP/TPD/ITO organic light-emitting device as a function of drive current. For this device, the TPP concentration in Alq_3 is very small (~0.5% by wt) to show effects of energy transfer saturation. The drive currents for the 0.8 mm^2 device are (starting from the highest intensity curve) 3 mA, with the drive current for each successive curve reduced by approximately a factor of 2 from the adjacent, higher intensity spectrum. Peaks C and D are characteristic of TPP, whereas peak B is characteristic of Alq_3. It is observed that the intensity of peak B scales with pump intensity, indicating a saturation of luminescence from the limited concentration of TPP molecules. Furthermore, the ratio of intensities of peak C to B also decreases as drive current is increased above 500 μA providing further evidence for saturation of energy transfer. For TPP concentrations exceeding 1%, energy transfer is ~100%, completely eliminating emission from Alq_3 at all practical OLED output powers (from ref 362).

centrations of TPP in Alq_3. The energy transfer from Alq_3 into TPP is complete at this level of doping, as shown by the lack of measurable Alq_3 emission (typically observed with a peak wavelength at ~530 nm), falling off as the TPP concentration is further reduced. In Figure 5-18 is shown the OLED spectrum for very lightly doped TPP (<0.5%) in Alq_3, where incomplete energy transfer is evident from the emergence of Alq_3 emission (peak B) at high injection levels.[362] For concentrations >1%, only the two TPP emission features (peaks C and D) are evident at all injection levels.[360]

Other models have also been suggested to explain the current conduction in OLEDs. For example, the $I-V$ characteristics in OLEDs have been fit over two to three decades of current by a Schottky-type thermionic emission model,[363,364] although a large discrepancy (2−6 orders of magnitude) between the measured and predicted values of the saturation current was observed. A model which assumes that current is limited by tunneling from the contacts into the organic layer[258,365] can also be made to fit the observed data for polymeric OLEDs over one to two decades of current in the high-field regime.

The efficiency of OLEDs may be strongly influenced by subtle changes in the organic film structure. For example, Joswick et al. systematically investigated the effect of film crystallinity on EL device performance.[366] Their results indicate that increasing the polycrystallinity of the EL layer made from conjugated oligomers dramatically decreases both carrier mobility and EL quantum efficiency. Such effects are almost certainly also present in molecular organic films. Amorphous, glassy films, or alternatively highly crystalline films such as those grown by OMBD, are therefore desirable for achieving efficient, low-voltage OLEDs.

Finally, the trap-filled conduction model is clearly valid only when the cathode and anode contacts are ohmic, with a sufficiently low resistance such that the current is limited primarily by transport through the thin films.[258] This condition is met in optimal OLEDs where the Alq_3 layer thickness is ~500−700 Å, and is approximately double that of the HTL thickness.[367] Furthermore, the formation of dark spot defects at the low work function metal/ETL interface ultimately determines the operational lifetime of the devices.[336,337,345] Consequently, understanding the fundamental properties of the organic/metal interface[368] and other organic thin film systems[369,370] is of the greatest importance in OLEDs, TFTs, and virtually all electrically active organic devices, and hence has been of considerable recent interest. While it is generally thought that low work function metals are required to obtain a low electron injecting barrier at the ETL/cathode interface, it is apparent that mechanisms resulting in ohmic contact behavior are quite subtle, involving significant metal/organic interdiffusion,[371] and chemical reactions between the species.[372] These processes can generate a high density of interface defect states which dominate the injection properties of the contact into the organic film. In photoelectron spectrographic studies of metal/PTCDA contacts, Hirose et al.[369] have found that these defect states may be responsible for the low resistance contacts observed, as opposed to simple work function and energy band alignment arguments.

The optimization of contacts in current injection devices such as OLEDs, organic lasers, and transistors is possibly one of the most important considerations in making practical organic-based electronic devices, and hence continued studies of the metal/organic interface are of the utmost importance.

5.3.2. Organic Light-Emitting Device Structures and Applications

One of the principal reasons that OLED technology has attracted such interest in recent years has been the prospect for using these devices in full color, red-green-blue (RGB) emissive displays which might eventually replace active matrix liquid crystal displays. Several techniques have been proposed for generating RGB displays,[373] as shown in Figure 5-19. Simple, side-by-side photolithographic patterning combined with shadow masking allowed Wu et al.[374] to fabricate red, green, and blue polymer OLEDs on the same substrate, although at very low resolution. This approach, shown in Figure 5-19a, while architecturally obvious, can result in a high-cost process where growth and fabrication of the three color segments must be alternated without damage to the predeposited and prefabricated subpixels. Alternatively, optical filtering of white OLEDs can produce acceptable red, green, and blue emission (Figure 5-19b), but at a great cost to device efficiency due to the large amount of light absorbed in the filters. Several demonstrations of bright, white-light emit-

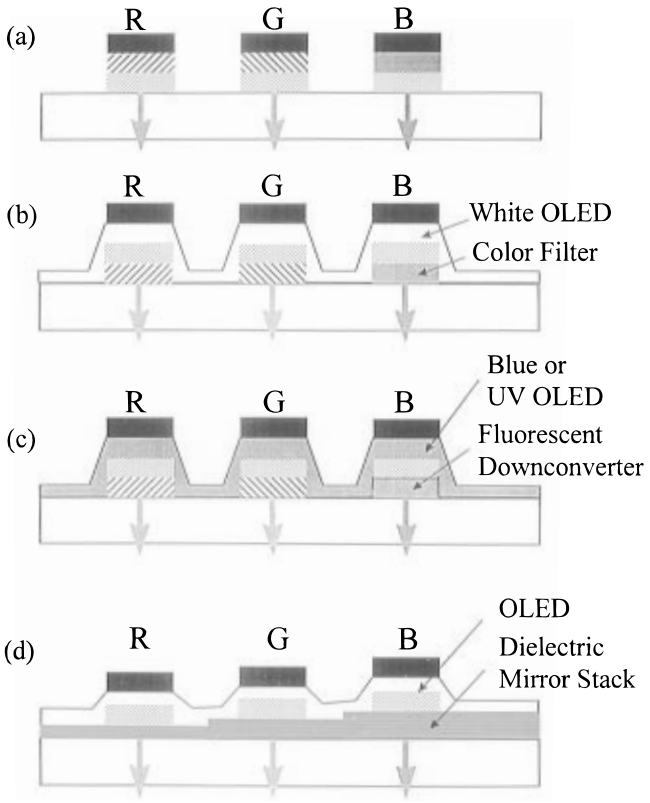

Figure 5-19. Schemes for creating full color displays based on organic light-emitting devices placed in a side-by-side configuration. The methods are (a) closely positioned, separate red, green, and blue emissive pixels; (b) a single white OLED positioned above red, green, and blue color filters; (c) a single blue or UV OLED positioned above red, green, and blue fluorescent down converting layers. In the case of the red pixel, it may be necessary to first generate green through fluorescent down conversion, followed by a second step to red; (d) a single, very broad spectral emission OLED positioned above dielectric mirror stacks to provide microcavities tuned with their optical band pass in the red, green, and blue spectral regions. (Figure courtesy of Y. Sato.)

ting OLEDs[375,376] utilized multiple EL layers where the molecular composition was varied to give the spectral content necessary for white emission. Attempts at using rare-earth complexes to build OLEDs which emit "white" light concentrated into the red, green, and blue spectral bands, however, greatly reduced the efficiency of the OLED itself.[377]

Less efficiency is wasted by using a single blue OLED[378] to pump organic wavelength "down converters" (Figure 5-19c). Each down converter consists of a prepatterned film of fluorescent material which efficiently absorbs blue light and reemits the energy as either green or red light, depending on the compound used.[379,380] Luminescent organic systems can have a conversion quantum efficiency approaching 100%, although the power efficiency is reduced since the energy of the emitted photon is less than that of the absorbed photon. This is particularly important in the generation of red light by a blue pump, which results in a maximum down-conversion power efficiency of ~50%, assuming the down-conversion quantum efficiency is 100%. Nevertheless, a low-resolution display using down converters has recently been reported.[381]

Use of OLEDs which are intrinsically color tunable obviates the need for separate RGB elements, resulting in a 3-fold improvement in resolution and display fill-factor as compared to the various side-by-side architectures. Only one OLED structure is grown over the entire area of the display, although this simplicity is somewhat offset by additional complexity required in the drive circuit, which must simultaneously control color, brightness, and gray scale. For example, polarity-dependent, two-color operation has been obtained from OLEDs doped in different regions of the heterostructure with molecular species which emit at different wavelengths.[382] In this case, the color is tuned by varying the polarity and the magnitude of the applied voltage; higher voltage results in more emission from the blue emitting component, while also resulting in higher overall brightness due to increased current injection into the device. To reduce this problem, emission intensity can be controlled by using a pulsed current source at reduced duty cycles. In a color display, therefore, high drive voltages at very low duty cycles may be necessary for blue pixels, which is likely to enhance degradation. Note that molecular organic color-blend structures have not yet been demonstrated which can continuously access all regions of the color spectrum. In a high-resolution display, color tuning the pixels while independently controlling brightness and grey scale appears to be problematic.

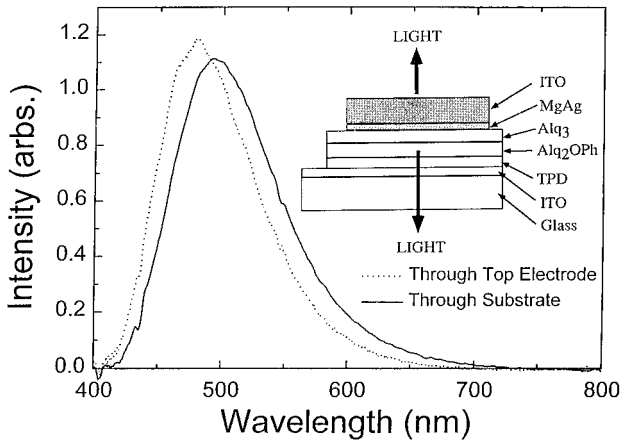

Figure 5-20. Spectral emission from a blue, transparent organic light emitting device (TOLED) from the top and substrate surfaces. Inset: Structure of the double heterostructure TOLED (from ref 384).

Organic thin films, however, allow for the realization of completely new display concepts which, among other advantages, may also lead to the practical realization of low cost RGB displays. For example, Gu et al.[256,383] demonstrated transparent OLEDs (or TOLEDs), useful for transparent head-up, or very high contrast displays (inset: Figure 5-20). These devices employ the large Franck−Condon shift characteristic of many organic molecules[196,197,347] which result in significant red shifts of the emission relative to the absorption spectrum. Hence, these films are transparent to their own emitted light. In Figure 5-20, we show the spectral output from a blue double heterostructure TOLED[373,384] consisting of a 500 Å thick TPD layer used as the HTL, followed by a 200 Å thick Alq_2OPh as the emission layer, a 500 Å thick Alq_3 ETL, and a cathode contact consisting of 100 Å Mg-Ag followed by a sputter-coated ITO contact. The light emission from the top surface of the TOLED

(with a total efficiency of 3.65%) is somewhat blue shifted with respect to the substrate emission due to absorption in the Mg-Ag contact.

In addition to being a transparent light emitter, the top ITO surface of the TOLED can serve as the hole injecting electrode for a second TOLED built on top of the first device. Each device in the stack is then independently addressable and can be tailored to emit its own color through the adjacent transparent organic layers, the transparent contacts and the glass substrate. This allows the entire area of the vertically stacked pixel to emit any mixture of the two primary TOLED colors. Recently, both two- and three-color SOLEDs have been demonstrated,[361,385] with the three-color device shown schematically in Figure 5-21a. Since each color element in the stack is independently addressable, a stacked OLED (SOLED) display can be built with independent control of brightness, color, and gray scale. In the SOLED in Figure 5-21a, the blue double heterostructure (with a structure similar to that shown in Figure 5-20 except with the TPD replaced with the improved stability, α-NPD) was grown at the bottom, and is separated by the second (green) subpixel by a common, semitransparent Mg-Ag electrode. The conventional green emitter was then grown with its Alq_3 ETL and emission layer sharing this same cathode, followed by a α-NPD HTL. Since this structure requires the somewhat destructive sputter deposition of ITO on top of the HTL to form the anode contact, a thin layer of PTCDA is first deposited onto the α-NPD prior to ITO deposition. PTCDA serves two purposes: (i) Since it is an extremely robust molecule, it prevents sputter damage to the underlying α-NPD, and (ii) its high hole mobility[37,172] improves carrier injection into the green emitter. Note that the contact properties for organics deposited onto the surface of the Mg-Ag are considerably different than from those where the Mg-Ag is deposited onto the organic thin film. Indeed, in the later case, the contact appears to have significantly lower resistance than in the former, presumably due to chemistry which occurs during the condensation of highly energetic atoms onto the surface of the organic material.[367]

To complete the three-color device, a third α-NPD layer was deposited onto the sputtered ITO contact, followed by a 3% TPP:Alq_3 ETL and light emitting layer. The final cathode was a conventional, nontransparent Mg-Ag layer.

The electroluminescence spectrum from the several different emitters in the stack is shown in Figure 5-21b. The quantum efficiencies for the red, green, and blue subpixel elements were 0.3%, 0.55%, and 1.6%, with output luminances of 35, 70, and >200 cd/m^2, respectively, adequate for many display applications. Note that these spectra are significantly different than those obtained for three discrete OLEDs using the same emitting molecules.[385] This is due to the existence of optical cavities formed by the several different organic dielectric layers and the reflective, semitransparent metal contacts comprising the stack. These so-called "microcavity effects" have been extensively studied[386−393] and have been found to not only affect the spectral content of the emitted

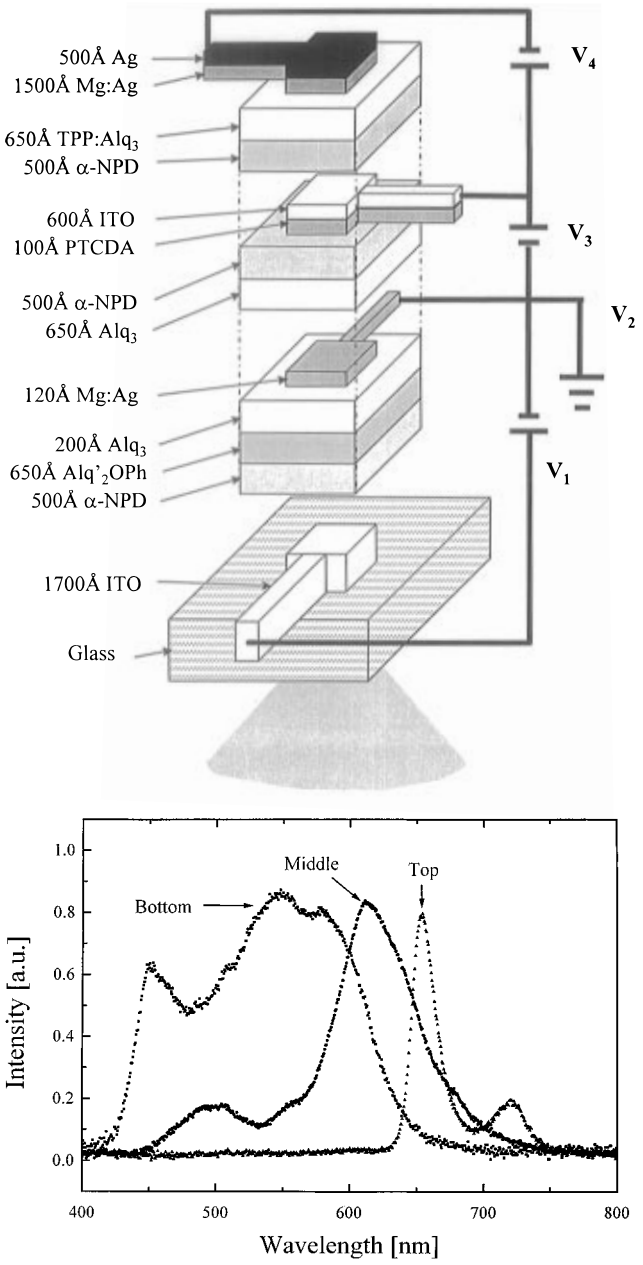

Figure 5-21. (a) Exploded schematic view of a three-color stacked organic light emitting device (SOLED) showing the various material layers and the biasing scheme. The total thickness of the contacts and organic layers is ~0.8 μm. (b) The output spectra from the three separate subpixels in the SOLED. Under operation, the total spectrum is a linear superposition of the separate spectra of the individual subpixels (from ref 385).

light, but also its angular distribution. While such effects are often undesirable, it has recently been proposed[388] that multicolor displays consisting of OLEDs tuned by external dielectric reflecting layers can be one approach to achieving full color, as shown in Figure 5-19d.

As discussed extensively in this review, organic thin films have high mechanical flexibility, and do not require lattice matching with the substrate. This property creates new possibilities for the device engineer, such as the 12-layer SOLED shown in Figure 5-21, which is a unique combination of amorphous and crystalline organic films, inorganic conductive oxides and metal films all comprising a single, integrated and efficient structure. Currently,

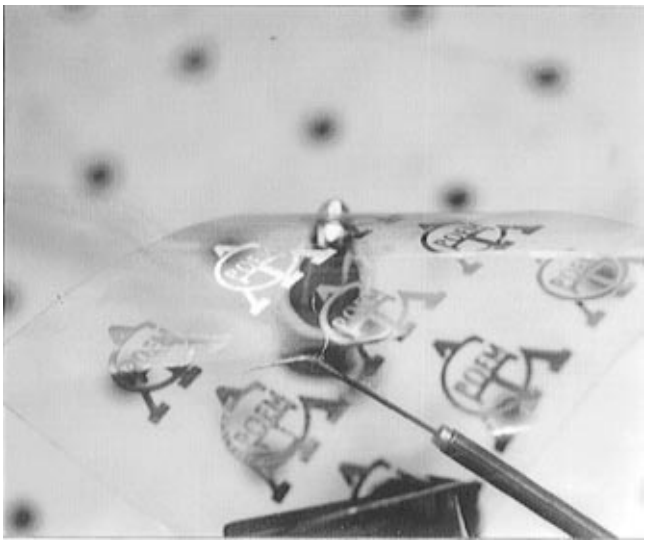

Figure 5-22. Photograph of an array of nine, unpackaged 1 cm^2 vacuum-deposited, nonpolymeric flexible OLEDs. One device (near top of photo) contacted with the probe arm (shown as the diagonal cylinder at the lower right) is operating in air in a well-illuminated room at normal video display brightness (~100 cd/m^2) (from ref 396).

it is not possible to fabricate such heterogeneous layered structures based on inorganic semiconductor material systems.

In other applications of organic-based light emitters, polarized EL, with potential applications for optical memories, has been obtained by either orienting the organic molecules on the substrate surface[394,395] or confining the EL layer in a multilayer structure.[148,261] In addition, flexible, molecular OLEDs as shown in Figure 5-22, have been demonstrated on ITO-coated polyester substrates,[256,396] which complement earlier demonstrations of flexible polymeric OLEDs,[331,397] creating the potential for roll-up or conformable displays on curved surfaces. Vacuum deposition on plastic sheets also allows mass-production of large-area OLEDs via roll-to-roll processing. The successful development of such a process could result in extremely low cost manufacture.

We conclude this section by noting that work published by over 80 laboratories worldwide[398−400] in the last few years has shown that arrays of vacuum-deposited, green OLEDs are sufficiently bright and long-lived to be a realistic alternative to conventional technologies such as back-lit liquid crystal displays, and indeed are currently being adopted for early entry into commercial markets.[30,401] OLEDs based on vacuum-deposited organic thin films exhibit unique properties of transparency, flexibility, and simplicity of manufacture which are unobtainable using conventional, inorganic semiconductors. These properties enable new display applications. The intense worldwide effort to exploit OLED technology appears poised to succeed in producing an entirely new generation of low-cost flat panel displays with novel properties inaccessible with existing display concepts.

5.4. Thin-Film Transistors

One area where remarkable progress has been made during the last two years[265−270,402−404] has been in the understanding and fabrication of organic thin film transistors (TFTs). Interest in these devices stems from their potential use in very low cost display back plane active transistor matrices, and in low-cost (albeit low performance) electronics applications such as in credit card ID encoding, etc.[405] Organic TFTs have the potential for roll-to-roll production due to their compatibility with low-temperature fabrication processes. Indeed, if work in this area is successful, organic TFTs may one day replace such devices currently based on amorphous Si which require elevated temperature deposition (typically ~200−500 °C), making them incompatible with integration on ultralow cost polymer substrates.

Charge carrier mobility, the characteristic of greatest importance to TFT performance, is determined by the degree of π-orbital overlap between adjacent molecules forming the conducting channel from transistor source to drain. In addition, to minimize the dark conductivity of the transistor channel, the background free carrier concentration must be minimized, placing stringent requirements on material purity (where defects and impurities give rise to shallow donor or acceptor states). For these reasons, it has been suggested[268] that the most promising approach to achieving the required high mobility and low impurity concentration is via vacuum deposition of highly pure planar aromatic compounds such as pentacene,[269] the oligothiophenes (e.g., α-hexathienylene, $\alpha-6T$),[266,270] perylene and naphthalene-based compounds,[224,406] and the Pc's.[407]

The structure of a typical organic TFT is shown schematically in Figure 5-23a. Here, an organic thin film which serves as the transistor channel is deposited to a thickness of 1000−2000 Å onto an oxidized, conductive Si surface between ohmic metal (e.g., Au) or polymer (e.g., polyaniline) contact fingers. The contact fingers serve as the source and drain electrodes of width W, and separation (i.e., channel length) L. The Si substrate provides the gate contact. Conduction occurs at the organic/SiO_2 interface when a bias, V_{GS}, whose polarity depends on the n or p-type character of the organic thin film, is placed between the gate and grounded source contact. For p-channel accumulation mode TFTs, for example, application of a sufficiently high V_{GS} lowers the surface Fermi-energy of the film below the HOMO, thus creating a conducting pathway between source and drain, with the total current determined by the drain voltage, $-V_{DS}$. Inversion mode and n-channel devices work in much the same fashion, although the sign of the gate and drain potentials are reversed.

While the best device performance to date[269] has been achieved using the structure in Figure 5-23a, we note that all of the gate contacts in a multitransistor integrated circuit using such a device geometry will be shorted. For practical application, the substrate must be an insulator such as a polymer sheet or glass. In this case, a conducting gate electrode is first deposited and patterned, followed by deposition of the gate insulator, which can be either a polymer, a vacuum-deposited organic film, or an inorganic material such as SiO_2 or SiN_x. After the gate insulator is deposited, further processing follows the

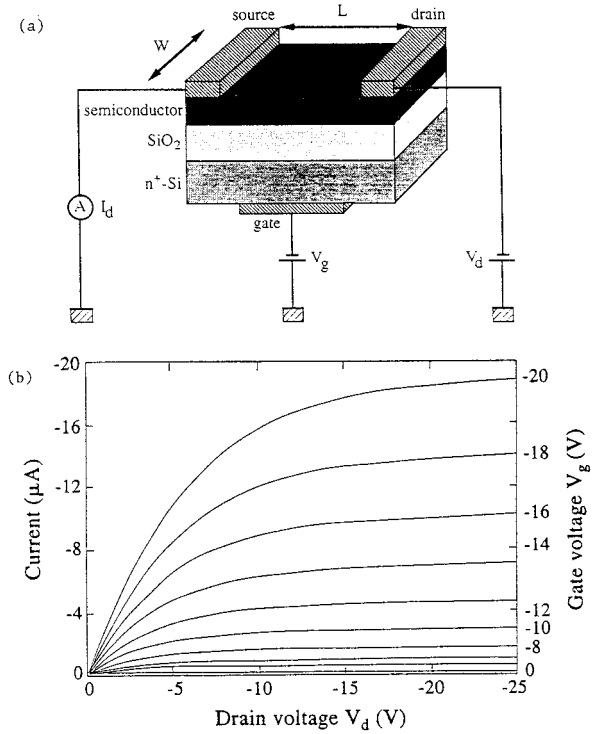

Figure 5-23. (a) Schematic view of an organic thin film transistor fabricated on a Si substrate. W and L is the channel width and length, respectively, V_g and V_d is the gate and drain voltages, and I_d is the drain current. (b) TFT drain current characteristics. The TFT structure consists of a α-6T organic channel layer deposited between Au source and drain electrodes on a glass substrate. The insulating gate layer is polymethacrylate with a capacitance, $C_i = 10$ nF. Device dimensions are $W = 5$ mm, $L = 50$ μm (from ref 268).

same route as discussed for TFTs on Si substrates.

Transistor characteristics, such as those reported for α-6T-based channels (see Figure 5-23b) are broken into two operating regions: the linear regime at low V_{DS}, and the saturation regime at higher V_{DS}. Highest transistor gain is achieved in the saturation regime. The drain current for an ideal transistor is thus[313]

$$I_{DS} = (W/Ld)\epsilon_i\mu_{eff}[(V_{GS} - V_T)^2 - V_{DS}^2/2] \qquad V_{DS} < V_{GS} - V_T \quad (5.7a)$$

$$I_{DSS} = (W/2Ld)\epsilon_i\mu_{eff}(V_{GS} - V_T)^2 \qquad V_{DS} > V_{GS} - V_T \quad (5.7b)$$

Here, ϵ_i is the permittivity of the gate insulator, d is its thickness, V_T is the threshold voltage, μ_{eff}, is the "effective" carrier mobility, and I_{DSS} is the drain saturation current. The voltage gain in a common source circuit configuration, where R_L is the load resistance at the TFT drain, is $A_v \approx g_m R_L$, where g_m is the transconductance (i.e., $g_m = [dI_{DS}/dV_{GS}]$). Since g_m is largest in saturation, we obtain

$$g_m = (W/Ld)\epsilon_i\mu_{eff}(V_{GS} - V_T) \quad (5.8)$$

Now the gain of the amplifier is also limited by the output conductance of the TFT, g_o, which is simply the slope of the drain current characteristics in saturation, viz.: $g_o = [dI_{DS}/dV_{DS}]$. The maximum

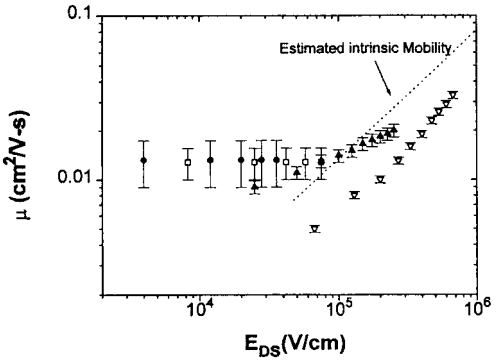

Figure 5-24. Mobility as a function of electric field (E_{DS}) in the channel. Gate dimensions are $L = 25$ μm (full dots), $L = 12$ μm (open squares), $L = 4$ μm (full triangles), and $L = 1.5$ μm (open triangles). The bars indicate the error in the measurement of the mobility which have a slight dependence on V_{GS} (from ref 403).

gain is therefore $A_v < g_m/g_o$, suggesting that practical transistors require a minimum output conductance and a maximum transconductance. Furthermore, a low g_o assures that the channel leakage current in the "off" state (I_{DO}) will be small. Coupled with a large mobility which ensures a large I_{DSS}, the switching ratio (I_{DSS}/I_{DO}) is large. Indeed, $I_{DSS}/I_{DO} > 10^6$ is necessary for most high contrast AMLCD applications. Finally, the frequency response of the transistor is determined by the cut-off frequency:

$$f_T = g_m/2\pi C_{GS} = (\mu_{eff}/2\pi L^2)(V_{GS} - V_T) \quad (5.9)$$

where C_{GS} is the gate-source capacitance. From the forgoing discussion, it is apparent that the critical performance parameters of a TFT, i.e., its maximum current, I_{DSS}, transconductance, g_m, and operational bandwidth, $\sim f_T$, all depend on the figure of merit, μ_{eff}/L, which must be maximized, along with minimizing g_o to ensure high-gain operation. In addition, it is important that V_T be small (approaching 0 V) to allow for low-voltage operation. Since L is a function of device geometry, it is important to engineer structures where $L \approx 2-5$ μm can be routinely achieved. Both g_o and μ_{eff} are determined by thin-film properties, with the optimal values achieved using highly ordered and high purity organic thin films such as those grown by OMBD. Since μ_{eff} is primarily due to interface properties between the channel layer and gate insulator,[267] g_o can be reduced by maintaining a highly flat, but thin channel film in order to decrease current shunts through the film bulk. Film flatness is routinely achieved by OMBD growth, which is probably essential for routine fabrication of high performance TFTs competitive with existing hydrogenated amorphous Si (a-Si:H) transistors.

As inferred from these considerations, the channel mobility (μ_{eff}) is not generally the same as its bulk, or intrinsic, value (μ_o). Thus, μ_{eff} is determined primarily by defects at the interface, which may generate deep trapping levels. Alternatively, such defects can arise in the film itself due to boundaries between crystalline domains in the channel.[267,268,402,403] In any case, μ_{eff}, which is inferred from the drain current characteristics of the TFT (see eq 5.7), is often 1−3 orders of magnitude less than μ_o. This is clearly indicated from the data in Figure 5-24, where μ_{eff} is

plotted vs electric field for α-6T TFTs with different channel lengths. It is found that $\mu_{eff} < 0.03$ cm^2/(V s) for the shortest gates (and hence those gates whose dimensions are comparable to the crystalline grain size), a value considerably smaller than expected for bulk material (indicated by the dashed line). For these reasons, devices employing gate insulators have characteristics significantly inferior (i.e., lower gains, higher operating voltages, larger dark channel conductivities) to those based on thermally grown SiO_2 on Si substrates.

Attempts to increase μ_{eff} by doping, as has been demonstrated for In and Sb incorporation into C_{60} channels,[408] unfortunately also increases g_o to unacceptably high levels due to the resulting increase in channel conductivity by nearly 6 orders of magnitude.

The device whose characteristics are shown in Figure 5-23b was fabricated on a poly(parabanic acid) resin substrate which allowed for flexing of the completed devices. The metal (Ag or Au) gate electrode was sputter deposited onto the substrate, followed by the casting of a polymeric gate insulator (cyanoethylpullulan). Vacuum deposition of 500 Å of α-6T formed the channel, followed by evaporation of Au source and drain electrodes. The completed device had $L = 50$ μm, $W = 2.5$ mm. Device performance characteristics include $g_m = 3 \times 10^{-7}$ S, $\mu_{eff} = 0.46$ cm^2/(V s), $V_{TH} = -1.3$ V, $g_o = 10^{-8}$ S at $V_{DS} = -20$ V and $V_{GS} = -8$ V, and $f_T = 30$ kHz. The highest μ_{eff} reported[269,404,409] is from 0.7 to 1.5 cm^2/(V s) obtained for vacuum-deposited pentacene films on thermally grown SiO_2 using the TFT configuration shown in Figure 5-23a. Similar structures have also been demonstrated[267] with $I_{DSS}/I_{DO} > 10^6$. These values are similar to those obtained[313] with a-Si:H used in AMLCDs. While a weak increase in mobility of many organic films has been observed with increasing electric field[61,267,381,410] (and therefore V_{GS}), there is little prospect for exceeding $\mu_{eff} \approx 1-5$ cm^2/(V s) at room temperature using even perfectly ordered planar stacking molecules since the μ_o is ultimately limited to these values by thermally induced molecular librations. For pentacene TFTs, $\mu_{eff} \approx \mu_o$.

Given $\mu_{eff} = 1$ cm^2/(V s), $L = 5$ μm, and $V_{GS} - V_T = 10$ V, we obtain a maximum bandwidth of $f_T = 8$ MHz which is suitable for many display and low-cost electronic circuit applications.

The role of mesoscopic organization has been investigated for 6T-based TFTs, where the substrate temperature was varied during vacuum deposition.[411] For this molecular structure, charge propagates along the stacking axis which therefore must be oriented parallel to the substrate plane to ensure high-channel mobility using the geometry in Figure 5-23a. Devices fabricated by deposition at room temperature or below tend to nucleate with their stacking axis perpendicular to the plane,[412] thus leading to a low mobility (2×10^{-3} cm^2/(V s)). The mobility is further reduced for growth at the lowest temperatures (77 K) due to impurity adsorption onto the cold substrates. As noted in section 2, deposition onto cooled substrates necessitates growth under UHV conditions if impurity incorporation into the film is to be minimized. The room temperature deposition resulted in polycrystallites with ~50 nm diameters. However, at higher temperatures (≥190 °C) the preferred molecular orientation with stacking parallel to the substrate plane is achieved. Large polycrystallites (30×200 nm^2) with this orientation are observed, leading to mobilities as high as 2.5×10^{-2} cm^2/(V s) along with a low film dark conductivity. At the highest temperatures of growth (260 °C), rough surface morphology develops, typical of most of the materials discussed in section 3. While these films do not have a mobility as high as pentacene, they nevertheless have a very low dark conductance ($\sim 10^{-7}$ S cm^{-1}) required for high transistor gain and switching ratio. Attempts to anneal the as-grown layers of lutetium and thulium bisphthalocyanines (Pc_2Lu and Pc_2Tm, respectively), as well as for α-6T, at 150 °C has also led to an increased domain size, and hence an increased mobility.[267,407] As discussed in section 3, this high-temperature process can result in some film rearrangement which may increase the polycrystallite diameter in the channel. Systematic studies of rapid thermal annealing of α-6T TFTs have shown[413] that heating the film near to its melting point significantly increases grain size, which leads to a concomitant increase in the device on/off (I_{DSS}/I_{DO}) ratio and a decrease in V_T to near 0 V. Indeed, heating above the film melting point appears to completely eliminate deep grain boundaries between adjacent α-6T islands.

Since most TFTs are generally operated in the accumulation mode, this places constraints on the types of circuits that can be realized. The most ubiquitously employed integrated circuit technology used today is based on Si complementary metal−oxide semiconductor (CMOS) field effect transistor (FET) electronics. The ability to fabricate both p- and n-channel FETs in a single integrated circuit platform allows for the realization of very low power dissipation circuits which only draw current when a transistor is switched. However, in circuits where only a single layer organic film is used for the channel of all transistors, complementary logic is not possible. Dodabalapur et al.[266,414] addressed this issue by demonstrating a novel device in which a 100−200 Å thick p-channel layer (α-6T) and a 200−400 Å thick n-channel layer (C_{60}) were sequentially deposited on an SiO_2 gate ($L = 4$ μm) insulator. By using either positive or negative V_{GS}, the transistor was able to conduct either electrons or holes in the accumulation mode. The operation of this device can be understood in terms of the band diagram in Figure 5-25a, which shows the results of ionization potential measurements of the relative positions of the HOMO and LUMO levels of α-6T and C_{60} obtained in vacuo from photoelectron spectroscopy data.[415,416] When $V_{GS} > 0$, the HOMO of the α-6T rises above the Fermi energy (left diagram, Figure 5-25a), opening conductivity in the p channel which is in the accumulation mode. However, when $V_{GS} < 0$, the energy "well" formed at the α-6T/C_{60} heterointerface (right diagram, Figure 5-24a) provides an n-type accumulation channel. The resulting "bipolar" I_{DS} vs V_{DS} characteristics in both n and p accumulation modes are

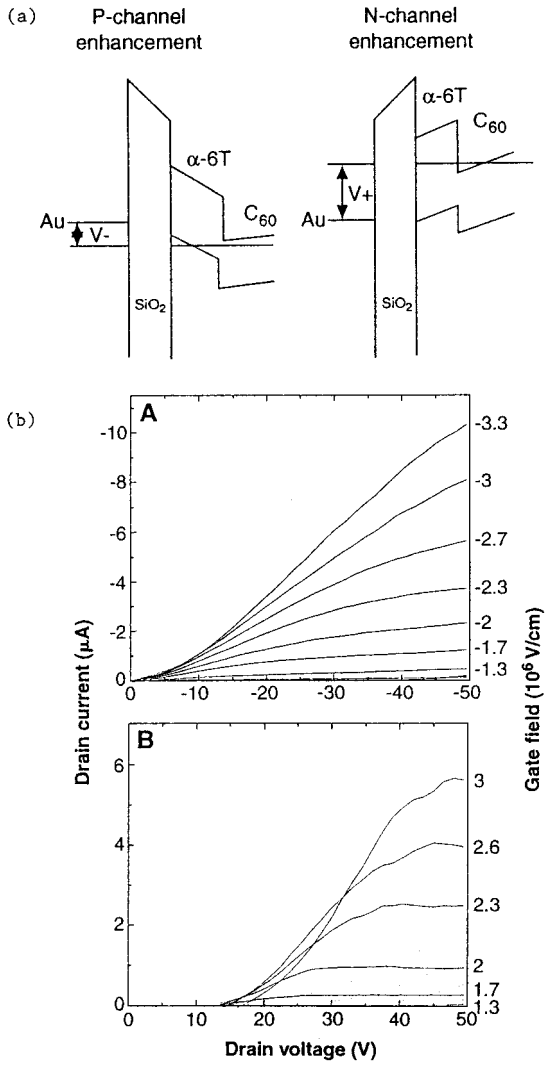

Figure 5-25. (a) Proposed energy band diagrams of the heterojunction transistor in the p-channel and n-channel modes of operation. In the p-channel mode, an accumulation layer of holes is formed at the α-6T/SiO_2 interface, while in the n-channel mode, the accumulation layer of electrons is formed in the C_{60} at the C_{60}/α-6T interface. (b) Drain current characteristics for the heterostructure TFT in p-channel mode (A) and n-channel mode (B) of operation. The device gate length is $L = 4$ μm (from ref 266).

shown in Figure 5-25b, with a clear shift in polarity of I_{DS} and V_{DS} for these two cases. Analysis of these characteristics in both modes yields an effective channel mobility of $\mu_{eff} = 4 \times 10^{-3}$ cm^2/(V s) (with $V_T \approx 0$ V) for p-channel operation, and $\mu_{eff} = 5 \times 10^{-3}$ cm^2/(V s) (with $V_T \approx 40$ V) for n-channel operation. While both the mobility and threshold voltages of this TFT were not as good as discrete p- and n-channel TFTs, it nevertheless is an important demonstration of the potential for using organics for complementary logic circuit applications. Indeed, these device characteristics critically depend on the film thicknesses used, as well as on their crystalline quality,[266] suggesting that there remains considerable room for improvement as these parameters are brought under control. A further outcome of this work is that it demonstrates that semiconductor-like band pictures can be used to understand some of the more complex behavior of narrow bandwidth molecular organic compounds employed in electronic device structures.

6.0. The Future of Ordered Organic Thin Films Grown in the Vapor Phase

6.1. Limitations of OMBD

In this review, we have shown that vacuum growth of small molecular weight organic molecular crystals can lead to unprecedented control over the structure and purity of the resulting thin films. This is particularly true when using the ultrahigh-vacuum process of organic molecular beam deposition employing highly purified organic source materials. OMBD has been demonstrated to result in long range crystalline order of the as-grown films. If the appropriate thermodynamic conditions are chosen during growth, unique crystalline thin-film structures can be realized whose characteristics depend on the detailed balance between growth kinetics, substrate−film interactions, and the degrees of freedom available to the organic crystal itself. Long-range order and strain incorporated during growth do not always result in defects. On the contrary, "templating" by the substrate has led to the growth of crystalline isomorphs which differ significantly in both structure and properties from the bulk. Overall, lattice matching of organic films to the substrate structure does not appear to be influential in generating low defect density films, as is the case in inorganic semiconductor epitaxial film growth.

By manipulating the film structure and achieving ultrathin, ordered OMCs, OMBD has made the growth of multilayer structures such as organic multiple quantum wells a reality. These organic MQWs have been instrumental in revealing important physical properties of OMCs which were, prior to this point, inaccessible. For example, organic MQW structures have been grown which clearly demonstrate excitonic quantum size effects, providing, for the first time, direct measurements of exciton radius of extended charge-transfer states which have long been viewed as an essential element in organic semiconductor photoconductivity and other optoelectronic phenomena. The film perfection achieved in OMBD growth has led to increased carrier diffusion lengths which has already been used to increase organic solar cell efficiency, as well as to increase the effective channel mobility in organic thin-film transistors. In particular, initial results obtained for MQWs consisting of organic heterojunctions as well as hybrid organic/inorganic multilayers have suggested that these structures may provide significant performance improvements in photovoltaic and photoconductive devices. Perhaps the most complex device demonstrated to date employing OMBD-grown films, and one that most clearly demonstrates their promise, is the three-color, stacked light emitting diode discussed in section 5.3 (see Figure 5-21). That device, consisting of 12 different layers composed of amorphous and crystalline organic thin films, metals and conducting oxides, to our knowledge can only be achieved using vacuum-deposited organic semiconductor materials. The successful demonstration of such a complex structure was made possible by steady scientific and engineering progress made in understanding organic molecular compounds by numerous laboratories worldwide over the previous 10−15 years.

In spite of this remarkable progress, vacuum growth of highly ordered organic films is only just now being exploited to the extent that practical applications may be achieved for active optoelectronic organic thin-film devices such as those discussed in section 5. There still remain both significant opportunities and problems in OMBD growth of organic thin films and the devices which employ these materials. For example, many of the same capabilities provided by MBE of inorganic compounds may also apply to the growth of organic thin films. We showed in section 3.4 that molecular layer deposition (which is analogous to atomic layer epitaxy) can be used to obtain saturated monolayer growth control over organic superlattices.[50] This was implemented by precise substrate temperature control which allowed for selective adsorption of alternating monolayers of functionalized organic molecules. Extending this control to two dimensions via such techniques as laser-assisted growth[417] may eventually allow for in situ patterning of films across a substrate surface.

Electric fields applied either parallel or perpendicular to the substrate surface during growth in UHV has also been demonstrated to be useful in manipulation of structure. These techniques have been applied to both small molecular weight polar[418] and nonpolar[419] OMCs, and polymers[420−424] as a means to orient dipolar molecules with large nonlinear optical coefficients. The applied fields are a means for in situ molecular poling, similar to methods used to align electrooptic chromophores in polymers heated above their glass transition temperature.[14] For this purpose, orienting the field in-plane using closely spaced electrodes pre-patterned on the substrate prior to growth[419−421,423,424] can be more effective in generating high fields which are sufficient($>10^5$ V/cm) to induce molecular ordering, than using fields oriented perpendicular to the substrate using external field apparatus such as grids,[418,422] where comparatively small fields ($\sim 10^4$ V/cm) are possible.

The use of electric fields in orienting molecules during growth was clearly demonstrated in two experiments performed on strongly polar,[425] vinylidene flouride (VDF)-based thin films. In the first series of investigations,[422] 3000 Å thick VDF/trifluorethylene (TrFE) copolymer films with 73% VDF were deposited in vacuum at a pressure of 3×10^{-6} Torr at a rate of 2.5 Å/s and with $T_{sub} = 25$ °C. In this case, electric fields as high as 62 kV/cm were oriented normal to the substrate which consisted of a metal (Cu or Al) contact predeposited onto an optically flat SiO_2 slide. The orientational dependence of the resulting films on electric field are shown by the energy dispersive X-ray diffraction pattern shown in Figure 6-1a. Here, the peak identified as the (110) or (200) Bragg reflection is seen to increase in strength as the field is increased. This feature is due to the molecular axes of form I VDF/TrFE crystals oriented parallel to the substrate as field is increased. This is equivalent to the molecular dipole moment, shown schematically in Figure 6-1b also lying parallel to the electric field direction. As anticipated, the degree of alignment was reduced as the substrate was heated, resulting in nearly complete disorder as the temperature was increased above 100 °C.

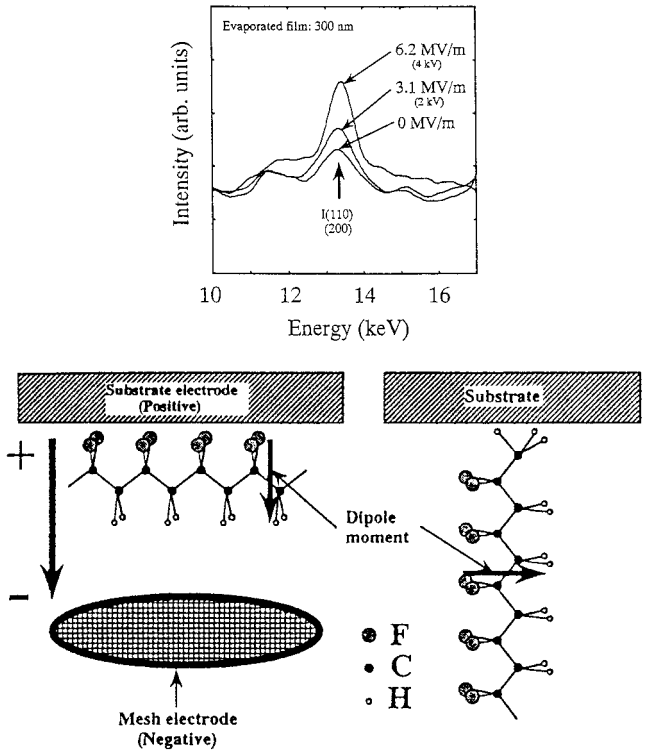

Figure 6-1. (a) Total reflection dispersive X-ray diffraction patterns of evaporated films of VDF/TrFE showing the dependence of the (110) and (200) reflections for various applied electric fields. (b) Schematic representation of the proposed molecular orientation to the substrate when the sample is evaporated with (left) and without (right) the application of an electric field (from ref 422).

As a final test of the usefulness of the application of the electric field during the growth process, the structure of films grown under high electric field were compared with those grown in the absence of such fields. It was found that only a very small (110),(200) peak intensity was observed for the latter films as compared with that observed for films deposited under high electric fields (42 kV/cm). In addition, it was not possible to recover the peak intensity by postpoling the precrystallized films; that is even after an electric field was applied in vacuuo at $T_{sub} = 140$ °C for 1 h immediately following deposition, no additional film alignment was induced.

In a second series of experiments on a similar compound, the effectiveness of in-plane fields was explored as a means for molecular "poling" during growth.[423] In this case, deposition of poly-VDF (PVDF) was done on glass substrates in the 50 μm gap between Al electrodes across which fields of up to 160 kV/cm were applied. Conditions for these experiments included deposition at 7.5×10^{-6} Torr at a rate from 0.18 to 0.31 Å/s for substrate temperatures maintained between −130 and 100 °C. As has been widely observed for thin film growth by OMBD (see section 3), rough surfaces were observed at the highest (~100 °C) temperatures, and thus only results for $T_{sub} < 80$ °C were reported. Second-harmonic intensity (SHG) of the as-deposited films was used as the means to investigate the order of

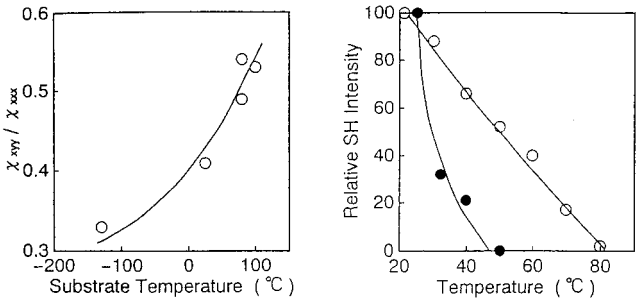

Figure 6-2. (a) Ratio of second-order nonlinear susceptibility tensor elements, $R = \chi_{xyy}/\chi_{xxx}$ for PVDF films as a function of substrate temperature during growth. As R decreases, the dipole orientation in the direction of the applied electric field (i.e., in the substrate plane) increases. (b) Relative second-harmonic generation intensity as a function of annealing temperature for films deposited in the presence of an electric field (open circles), and for films deposited in the absence of field and poled after deposition. The SH intensities are normalized to their room temperature values (from ref 423).

the product. In this case, a decreasing ratio of the nonlinear susceptibility tensor elements, $R = \chi_{xyy}/\chi_{xxx}$ is interpreted as an increase of dipole orientation in the direction of the applied electric field (i.e., in the substrate plane defined as the x,y plane in this work). Two observations were made, as is apparent in Figure 6-2: (i) Dipole alignment increases as substrate temperature decreases, as is apparent from a decrease in R by a factor of two as T_{sub} is lowered from 100 to −130 °C. (ii) The SHG efficiency of films deposited in the absence of an electric field, and then post-poled in situ at $T_{sub} = 25$ °C in an electric field of 160 kV/cm was negligibly small compared to films deposited in the presence of such a field (Figure 6-2b). This latter result is similar to that found by Yoshida and co-workers[422] in applying fields normal to the substrate. This suggests that the dipoles in post-poled films could not be efficiently reordered since the energy stored in the large crystalline domains which are produced during growth (particularly when T_{sub} is small) is very large. In contrast, during growth, the molecules themselves along with small clusters of molecules nucleating on the surface, are easily reoriented by the application of the modest electric fields employed in these experiments.

These experiments are very promising in that they open new avenues for manipulating the structure of polar molecular crystals, thereby enhancing a desired property of the materials. Many other methods, such as application of magnetic fields, local substrate temperature control, or irradiation with strong optical fields may also prove useful for in situ tailoring the structure of OMCs deposited by OMBD in the near future.

One significant shortcoming of OMBD is that it is inherently limited to growth of compounds which are UHV compatible. While this property is essential if environmentally stable, single-component systems are desirable, which is overwhelmingly the case for use in any practical application, there are numerous compounds consisting of two or more organic molecular species whose structures might *individually* be volatile (and hence incompatible with UHV deposition processes), although the compound itself might

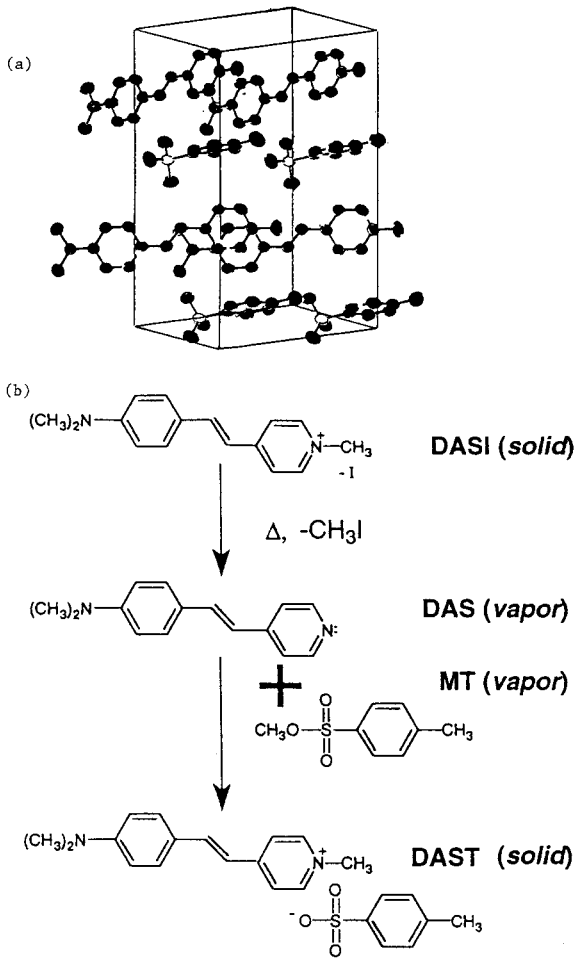

Figure 6-3. (a) Perspective of a unit cell of DAST and (b) proposed scheme for the synthesis of DAST molecules by organic vapor phase deposition (from ref 430).

be highly stable. An example compound with these properties is the organic salt, 4′-(dimethylamino)-*N*-methyl-4-stilbazolium tosylate (DAST) shown in Figure 6-3a, which has been shown to have a second-order susceptibility value of $\chi^{(2)} \sim 10^3$ times greater than that of urea due to dipole alignment of its cation and anion constituents.[426] Although in situ reactions of multicomponent organic molecules to synthesize polymer films previously have been demonstrated using such vacuum techniques as physical vapor deposition or vapor deposition polymerization,[427] attempts in our laboratory at double-source coevaporation of the DAST neutral precursors 4′-(dimethylamino)-4-stilbazole (DAS) and methyl *p*-toluenesulfonate (methyl tosylate, MT) to form DAST have been unsuccessful due to the radically different vapor pressures of DAS and MT, which leads to highly nonstoichiometric growth. To solve problems of incongruent growth employing high-vapor pressure molecular precursors incompatible with the UHV environment, vapor-phase epitaxy has been developed to grow epitaxial thin films of many III−V compound semiconductors, such as InP and GaAs.[428] Here, a high vapor pressure compound (typically a metal halide or a metallorganic) of each respective metal is carried independently, via a carrier gas, into a high-temperature reaction zone. In that zone, the compounds are deposited onto a heated substrate where they thermally decompose and react to yield

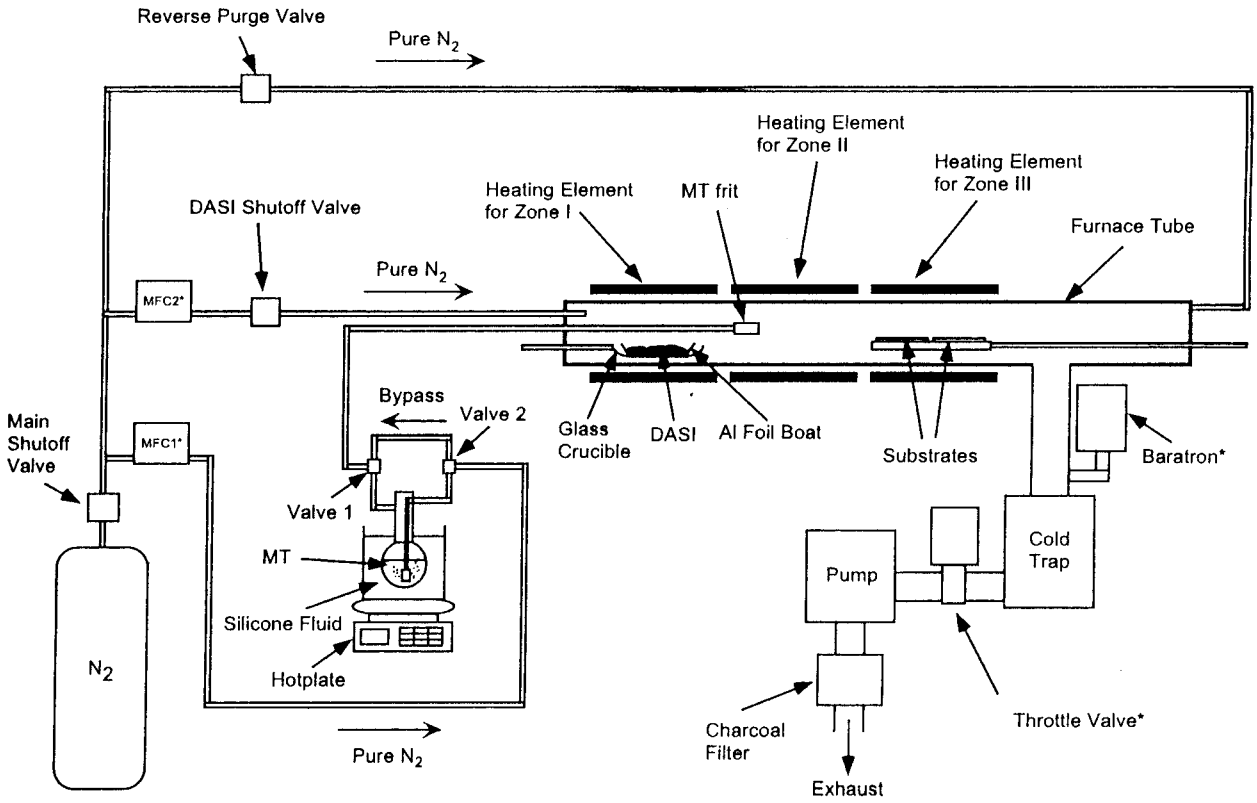

Figure 6-4. Schematic layout of a low-pressure, organic vapor-phase deposition system currently used in the author's laboratory.

the desired III−V compound. The excess reactants and reaction products are then exhausted from the system via a scrubber.

An analogous technique was recently developed to grow DAST by the reaction of two volatile organic materials in a hot-wall, atmospheric pressure reactor.[429,430] Nuclear magnetic resonance (NMR) analysis was used to determine that the stoichiometry of polycrystalline DAST films grown by this novel technique was >95% pure (limited by instrumental sensitivity). By using X-ray and e-beam diffraction and other analytical methods, a significant dependence of film quality, such as ordering and crystallite size, on the substrate composition and other deposition conditions used for growth was found. This suggests that it may be possible to generate optical quality thin films of DAST and similar organic salts and compounds by OVPD using suitable substrates.

The reaction scheme for the preparation of DAST by OVPD is shown in Figure 6-3b. In step 1, thermal demethylation of 4′-(dimethylamino)-*N*-methyl-4-stilbazolium iodide (DASI) gives neutral DAS with the elimination of volatile CH_3I. In step 2, the DAS reacts with MT, resulting in methylation of the pyridine ring at the nitrogen atom. The resulting stilbazolium and tosylate ions form DAST crystals.

The OVPD reactor designed to grow DAST by the proposed scheme is shown schematically in Figure 6-4. The reaction tube is a hot-walled glass cylinder in which an alumina crucible filled with a small amount of DASI is placed in a hot zone of the furnace while a stream of pure N_2 gas provides a slight pressure gradient, causing the DAS vapor to flow along the reactor tube. The very high vapor pressure MT is loaded into a glass bubbler whose temperature is maintained by a silicone oil bath. Again, N_2 gas passes through a flow meter and bubbles through the MT, thereby carrying its vapor through a heated transfer tube (to prevent recondensation prior to introduction into the hot zone) into the furnace tube. The DAS vapor mixes with the MT vapor in the reaction zone, along which a temperature gradient is maintained. There it reacts to form DAST on substrates supported along the length of the tube. Excess, unreacted MT vapor, and any volatile side-reaction products, are exhausted from the cold end of the reactor. To avoid diffusive flow conditions which tend to result in highly nonuniform film morphology, growth is carried out at reduced pressure (typically 5 Torr).

Optimal growth of the reddish-brown DAST films results, thus far, in somewhat textured film surfaces as shown in the micrograph in Figure 6-5, where a surface roughness of ∼200 Å is observed for the 2 μm thick film shown. Such films are obtained at substrate temperatures between 140 and 150 °C in the ∼200 °C reaction zone. The DASI crucible temperature is 253 ± 2 °C, and the MT bubbler is 55 ± 2 °C,[430] resulting in growth rates of ∼1−10 Å/s, depending on the gas flow rates and the diameter of the reactor tube. The films, grown on amorphous Au substrates, are polycrystalline,[429] suggesting that substrates with appropriate structure and symmetry are needed to initiate more ordered growth. Nevertheless, the structural and chemical purity of the films give rise to intense second harmonic generation at $\lambda = 0.95$ μm, approaching that of pure, oriented DAST crystals.[429]

While the OVPD method has shown promise of growing multicomponent films consisting of organic

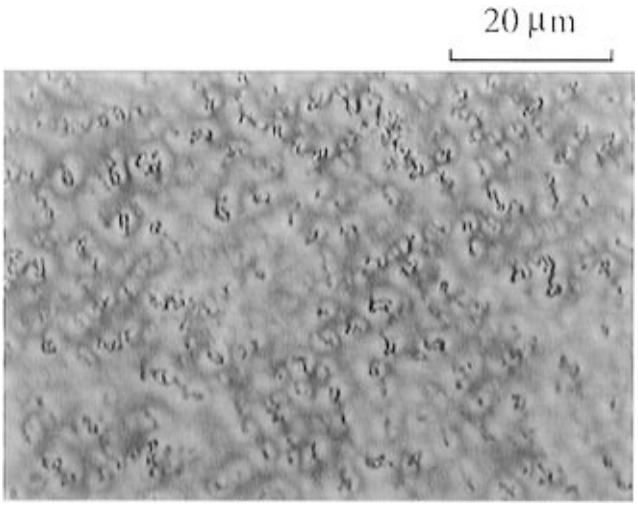

Figure 6-5. Optical micrograph of a 2 μm thick film of DAST grown by organic vapor phase deposition. A slight surface texture is apparent from this micrograph. The second-harmonic generation intensity of such films is approximately equal to that obtained for bulk DAST grown from solution (ref 429).

molecular constituents with widely different vapor pressures, as in the case of most such techniques, it is difficult to maintain precise control over both substrate and reactor temperature. This suggests that adapting the method to growth in UHV conditions has the potential of yielding very ordered films (similar to those discussed in section 3) while at the same time assuring the purity of the product. Such a technique would be similar to "chemical beam epitaxy", or CBE, employed in the growth of III−V and II−VI compound semiconductor materials.[158,431,432] By analogy to CBE, the high volatility molecular constituents can be introduced into a UHV, organic chemical beam deposition (or OCBD) chamber similar to that shown in Figure 2-1 via a bubbler and appropriate gas injector. The low vapor pressure adducts can be evaporated from standard effusion cells, similar to those used in conventional OMBD. By heating the precursor molecules to sufficiently high temperatures, they can be reduced to their ionic states (i.e., "cracked"), thereby allowing for the growth of the desired, two-component compound. This straightforward hybrid combination of OMBD and OVPD may eventually allow for the growth of a considerably expanded range of organic materials, including organic salts (such as nonlinear optical compounds exemplified by DAST, superconducting materials such as the Bechgaard salts, or charge-transfer complexes), and doped compounds such as those required for high luminance organic light emitting devices (e.g., TPP in Alq_3).

Note that in the example of guest−host systems, controlling the doping of one molecular species at low concentrations (~1%) in a high concentration organic matrix, is extremely difficult using conventional vacuum evaporation techniques. The reason for this difficulty is easily understood when we consider that the evaporation rate follows an exponential dependence: $R \approx \exp(-L_{s-g}/kT)$, where L_{s-g} is the latent heat of sublimation of a material. To introduce a small concentration of a guest chromophore into a host matrix, the temperature of the Knudsen cell must therefore be very carefully adjusted to avoid rapid, uncontrolled evaporation. However, using the process of OVPD (or OCBD), the dilution of the guest is primarily determined by the carrier gas mass flow rate rather than the bubbler or boat temperature, which is far easier to control to the required accuracy. Hence, OVPD, or its high-vacuum analog, OCBD, potentially offers many advantages in the deposition of organic thin-film materials consisting of more than a single molecular organic component.

Finally, we note that the ability to initiate ordered growth on all substrates requires the existence of a substrate potential which is spatially varying with a symmetry similar to that of the adsorbed film. While we have seen that such substrate "templating" may exist on glass substrates,[65] polymers,[102,433,434] step edges,[115] rubbed substrates,[179] and even crystals,[70,73,98,111] the requirements which must be satisfied to provide a substrate leading to a high degree of order in the resulting film are not straightforward to achieve. One very promising approach which has only just begun to be followed is that of substrate "templating", or derivatization, using self-assembled monolayers of functional organic molecules predeposited (generally from solution) onto the inorganic substrate surface.[4,435,436] A surface molecule which chemically reacts with the vacuum deposited species can anchor the deposited molecule in an ordered monolayer as it arrives at the substrate. To be successful, the functionalized molecules must be deposited (perhaps by Langmuir−Blodgett or other wet chemical process) in such a way that a saturated monolayer completely fills the substrate surface area prior to the vacuum deposition of the desired thin film molecular species. These self-assembly techniques provide a unique ability to achieve ordering of the resulting layers. Properties that this templating layer must possess are compatibility with the substrate temperatures, ultrahigh-vacuum environment, and chemistry of the material to be deposited in the OMBD chamber.

In addition to our need to extend the capabilities of the growth technology as discussed above, there remain numerous open questions regarding the physics and chemistry of OMCs. Given the structural and material purity afforded by this precision growth technology, we now have, for the first time, a clear opportunity to construct structures which probe the fundamental physics of this fascinating class of materials. A primary goal of past work on UHV growth of organic thin films was to understand, in detail, the conditions which lead to organized mesoscopic and macroscopic molecular order. While initial work was focused on understanding equilibrium structure, almost nothing has been done to explore the thermodynamic conditions leading to near-perfect thin-film growth. Acquiring such an understanding should have the immediate consequence of providing insight into the class of materials and the growth conditions needed to achieve long-range crystalline order. The nature of extended exciton states appears to be accessible using OMBD-grown organic nanostructures. Correlation effects, the dependence on orbital overlap both in-plane and normal to the stacking axis, charge transport across organic and organic/inorganic interfaces, and many

other fundamental phenomena still require considerable study using such structures before this class of materials can be fully understood and exploited for a particular device application. We note that many organic systems such as planar stacking molecules, typified by PTCDA, support one-dimensional transport. By growing ultrathin films of such materials, a 0D environment is created. Hence, OMBD of nearly perfect nanostructures appears to be an excellent means to probe transitions from 3D to 2D to 1D to 0D phenomena.

Finally, fundamental questions persist on the role that defects play in determining the optoelectronic properties of OMCs. We still need to explore how dislocations, molecular fractions, and other impurities affect carrier transport and the optical properties of this important and enormous class of materials. Once this is fully understood from both a theoretical as well as empirical viewpoint, we will be able to appreciate the importance of UHV growth techniques such as OMBD in achieving and tailoring the materials properties desired.

6.2. Applications on the Horizon

It is becoming increasingly apparent that the control over thin-film structure (with the ability to monitor the evolution of structure in *real* time), and ultrahigh materials purity uniquely afforded by growth in UHV are important for producing high performance devices with manufacturing yields and long operational lifetimes sufficient to generate a cost-effective device technology. The properties of almost all optical and electronic devices are sensitive to control of vertical device dimensions (i.e., layer thicknesses) and material doping. For example, a practical display technology must be based on pixels with highly uniform operating characteristics (e.g., operating voltage and current), and extremely high device yields across the full display area which may consist of $>10^6$ individual light-emitting elements extending over $>10^3$ cm^2. As we have shown in section 5.3, these properties are strongly determined by the ability to deposit very thin films ($\sim$200−500 Å thick) with extremely high thickness uniformity across these large areas. To our knowledge, only vacuum deposition currently provides this level of control, and only UHV processes such as OMBD can ensure the requisite control over material purity.

A key performance factor of any practical technology is cost. Indeed, the potential for producing an entirely new class of extremely low cost devices is one of the principal reasons that organic thin films are of interest. Hence, it is reasonable to question whether UHV techniques can lead to low production costs. Experience in III−V-based devices has certainly indicated that MBE growth can produce large volumes of ultralow-cost components, the most notable example being the fact that in 1995, $\sim$50% of the worldwide production of compact disc lasers[437] (with a wholesale price of $\sim$\$1) was accomplished via MBE. Hence, while the infrastructural costs of UHV growth are high, this does not necessarily present a barrier to the low-cost manufacture of optoelectronic components. The purity and uniformity afforded by OMBD appear to be essential for the understanding of organic materials, and in particular the growth of solar cells, OLEDs, TFTs, and numerous other devices. Whether or not these conditions can be relaxed in an effort to further reduce cost will largely depend on the requirements of the specific application.

Numerous device opportunities which can be addressed using vacuum deposited organic thin films remain to exploited. One area of particular interest is in electrically pumped, organic thin-film lasers.[390,438−443] Such devices have potential application for very low cost optical memory reading and recording, printing, laser scanners, etc. Some unique features of electrically pumped organic lasers would include ease of integration with electronic interconnection ribbons and other such "platforms", accessibility to a wide range of emission wavelengths via molecular compositional tuning, and insensitivity of the output power and wavelength to wide variations in operating temperature.

Stimulated emission by optical pumping of solid-state organic materials is well known, with the first demonstration of lasing in dye-doped gels and molecular crystals in the late 1960s.[444−447] Demonstration of similar effects in conducting organic thin films can therefore lead to an entirely new class of electrically pumped laser diodes based on organic semiconductor thin films, provided that sufficiently low optical pump threshold energies can be obtained.

Lasing (in contrast to amplified spontaneous emission, superluminescence or related phenomena) can be unambiguously identified from five phenomena: (i) a clear indication of a threshold in output energy as a function of input (or pump) energy, with a high lasing efficiency above threshold, (ii) strong output beam polarization, (iii) spatial coherence (as indicated by a diffraction-limited output beam or speckle), (iv) significant spectral line narrowing, and (v) the existence of laser cavity resonances, or modes. While several recent reports on polymer-based optically pumped thin films have discussed structures exhibiting one or two of the above phenomena,[439−441,448] to our knowledge, the only report to date where lasing is clearly identified in conducting organic films is in Alq_3 doped with DCM[443] (see Figure 6-4). In that work, a very low lasing threshold at a pump energy density of 1 μJ/cm^2 with a 500 ps excitation pulse, was reported.

Alq_3 doped with DCM provides an excellent laser material[443] since the red stimulated emission of DCM at a wavelength of λ = 645 nm is far from the ultraviolet absorption edge of the Alq_3 host (at λ = 450 nm),[347] while the absorbance of the DCM is centered near the emission maximum of Alq_3 (at λ = 530 nm), thereby providing for efficient Förster energy transfer[196] from UV-excited Alq_3. Doping also allows for reduction of the density of the optically active DCM molecules (thereby reducing the effective density of states), which lowers the threshold and increases the efficiency of a laser.[449] In fact, efficient orange electroluminescence for DCM doped Alq_3 films has been demonstrated.[264]

Lasers shown in Figure 6-6 were grown on InP substrates precoated with a 2 μm thick layer of SiO_2, deposited by plasma-enhanced chemical vapor deposition. The organic films were deposited by high-

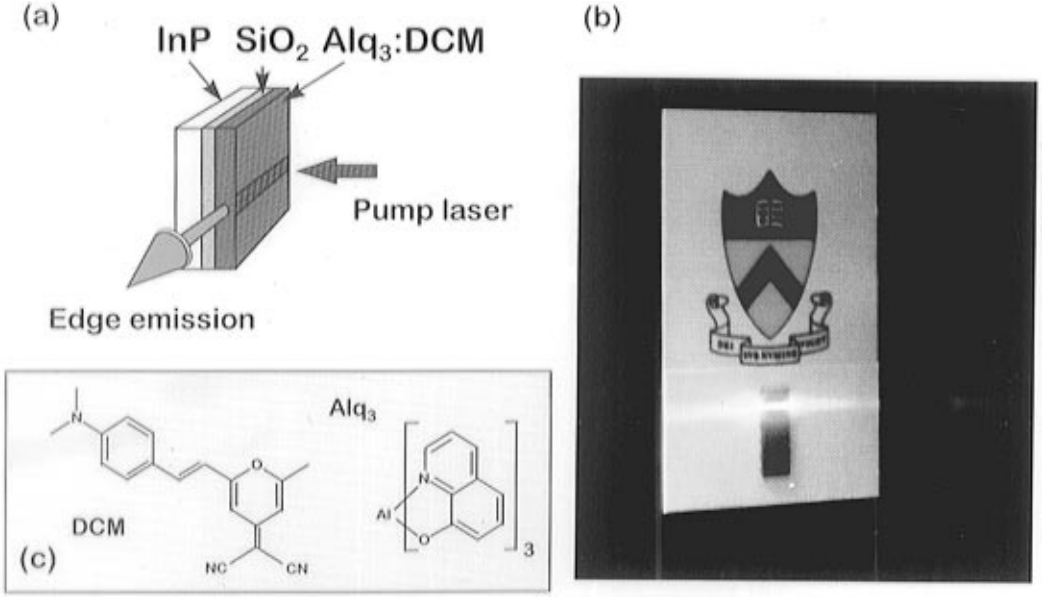

Figure 6-6. (a) Schematic of the laser structure and experimental setup, (b) photograph of the Alq_3/DCM slab waveguide laser showing the red output beam diverging with distance from the laser facets indicated by the intense radiation of the black InP substrate (photo courtesy of A. Forrest using the Princeton shield for contrast), and (c) chemical structural formulae of DCM and Alq_3 (from ref 443).

vacuum coevaporation of 40:1 (mass ratio) Alq_3 and DCM. A 3000 Å thick film of Alq_3/DCM (with optical index of refraction $n = 1.7$) forms a slab optical waveguide, with SiO_2 ($n = 1.4$) as a cladding layer on one side, and air ($n = 1$) on the other. Prior to organic film deposition, the (100) InP substrate was cleaved, ultimately defining the laser length while forming parallel edges. The vacuum-deposited organic film conforms to the shape of the underlying substrate, resulting in optically smooth, parallel facets with reflectivities ~7%.

The pump provided lateral confinement using the focused beam from a pulsed nitrogen laser ($\lambda = 337$ nm, pulse width = 500 ps at a 50 Hz repetition rate), as shown in Figure 6-6. A photograph of an operating slab laser device also shown in Figure 6-6 indicates a well-defined beam of bright red laser emission in a direction orthogonal to the facets. Figure 6-7a shows a high-resolution spectrum for a short cavity, 500 μm long slab laser, revealing numerous peaks (inset) evenly spaced at 2 Å and each with a <1 Å FWHM, corresponding to the free spectral range of the cavity, clearly indicating resonant cavity modes. The laser output power was highly stable—i.e., no significant degradation in the laser performance was observed after operating ~24 h at a very high peak power of ~50 W in a nitrogen atmosphere (~4×10^6 pulses). Such stability is essential for the eventual practical application of electrical injection lasers based on these compounds. Finally, the dependence of output energy on the pump energy for the devices, shown in Figure 6-7b, clearly indicates a threshold. To reduce mirror losses, long (~1 mm) laser cavities were used to obtain the differential quantum efficiency (η) above threshold. It was found that $\eta = 30\%$ for the slab device.

Several advantages to using vacuum deposited organic films are readily apparent from these early experiments. For example, facet formation is easily

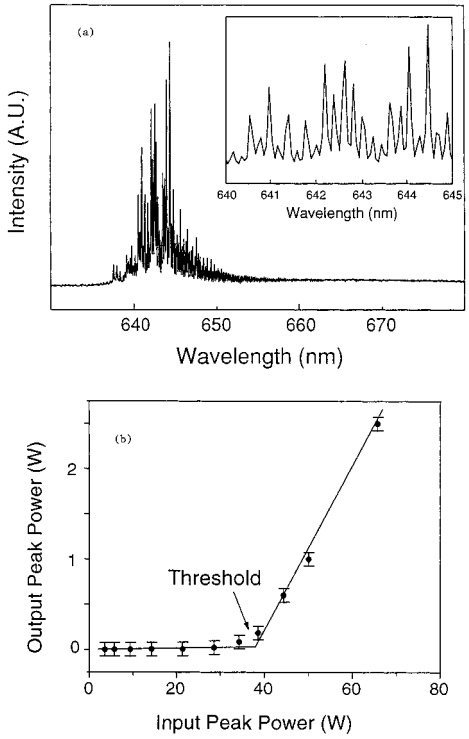

Figure 6-7. (a) High-resolution edge emission spectrum of a 500 μm long slab laser at a pump energy density of 1.7 μJ/cm^2. Inset: A portion of the same spectrum under higher resolution, showing evenly spaced resonant cavity modes and indicating a modal FWHM < 1 Å. (b) Dependence of output energy near threshold for a 1 mm long slab device. Solid lines are fits to the data yield an external efficiency above theshold of ~30% (from ref 443).

accomplished simply by depositing the films on a substrate with sharp, parallel edges. Alternatively, the facets can be formed by cleaving of the substrate after film deposition. In either case, no external feedback, or etched facets which tend to reduce performance are required, as may be the case in polymer structures. Furthermore, the films are

extremely flat and smooth, resulting in very low scattering losses along the cavity, along with the ability to form very abrupt interfaces between ultrathin organic layers which may be necessary in the fabrication of double heterostructure injection lasers. Compatibility between two different vacuum-deposited layers is also rarely an issue in choosing materials and structures best suited for a particular device application. Given that a laser typically consists of several layers with different optical and electronic functions, this materials compatibility is an extremely advantageous feature as compared to the situation in polymers and inorganic semiconductors.

Many issues must still be addressed before a practical, *electrically pumped* device can be realized. Contact degradation presents the largest limitation to OLED lifetime. This problem is considerably more difficult to resolve in lasers where the current densities are increased by a factor of 10^5 or more over that used in OLEDs. Indeed, if we assume that the intrinsic lifetime of the organic materials is $\sim 10^5$ h at an intensity of 100 cd/m^2 (which corresponds to a drive current of ~ 1 mA/cm^2 for most OLEDs of moderate efficiency), then the intrinsic CW solid state organic laser lifetime will only be in the range of 1−10 h. This is clearly inadequate for most practical applications and must be increased by increasing the luminance efficiency (or optical gain) of the organic materials, by employing pulsed operation (which can increase the lifetime by at least the inverse of the laser duty cycle), and by choosing organic molecules which are extremely robust in the presence of the large current densities and optical field intensities found in laser cavities.

Other devices which have the potential for transforming various device industries include very high efficiency organic photovoltaics as discussed in section 5.2. Use of multilayer stacks to improve efficiency has shown early promise, although to date the best power efficiencies lie between 1% and 2%. The need for structural order and precision afforded by the OMBD process will be required to make further progress in this important application area. Whether or not success will ultimately be achieved will depend critically on increasing the current research effort concentrated in this field.

There appear to be numerous opportunities for organic thin-film devices in nonlinear optic applications as well. However, most OMCs deposited in vacuum possess a center of symmetry, eliminating their usefulness in $\chi^{(2)}$ applications such as electrooptic modulators, etc. Once again, OMBD-grown MQW structures may have some limited application here. By the appropriate choice of molecular species characterized by a very high degree of orbital overlap between adjacent molecules, such processes as the quantum confined Stark effect may be employed to increase the second-order nonlinear effects in OMCs. A more promising approach, however, is to use crystals with large built-in dipole moments such as the organic salts. As discussed in section 6.1, successful growth of these multicomponent materials will require OVPD or modified OMBD such as organic chemical beam deposition. Furthermore, the modest vacuum combined with the horizontal glass reactor geometry characteristic of OVPD and associated techniques can be adapted to bulk materials growth using roll-to-roll deposition processes. This approach has considerable potential for drastically reducing the cost of growth of molecular organic films deposited on polymeric or other lightweight, flexible substrates.

Finally, we note that significant challenges remain in developing microfabrication processes for OMC-based devices. That is, a major impediment to the practical application of these materials is their fragility when exposed to water, solvents, elevated temperatures, and other conditions commonly encountered in standard semiconductor fabrication.[294] Hence, to fabricate high-resolution displays, TFTs, or optical waveguide devices requires redesign of many of these processing methods. One approach is to employ all dry patterning using reactive ion etching and multiple level photoresist and/or insulator (or metal) layers to prevent exposure to the wet chemistry used in photolithographic processes.[296] While early demonstrations of such modified fabrication methods have achieved modest success, it remains to be determined whether or not employment of these processes on a large scale will result in the high device yields and low costs required for practical implementation of small molecular weight organic thin-film devices.

In conclusion, whether or not a new generation of optoelectronic devices based on vacuum-deposited OMCs will gain a foothold in the spectrum of applications currently being fulfilled by more conventional semiconductor materials depends on three factors: (i) The ability of OMCs to provide a low-cost solution with higher performance than can otherwise be achieved, (ii) the successful development of high yield, simple to implement, very low cost device fabrication technologies, and (iii) the long-term operational and environmental stability of the materials used in the devices. Enormous strides have been made in resolving all of these issues, and OMBD of organic molecular thin films has played a major role in improving the reproducibility, stability, performance and uniformity of organic nanostructures to levels which only a few years were not thought to be achievable. Hence, it is very likely that this technology will soon lead to the realization of a large class of new optoelectronic systems based primarily on OMC thin films grown by high-vacuum deposition. Most probably, the first such demonstrations will be organic electroluminescent displays which may become commercially available in the very near future.

7.0. Conclusions

In this review, we have described in detail the progress and current state-of-the-art in the high-vacuum growth technology of molecular organic thin films. We have shown that OMC thin films can be grown into highly ordered structures independent of lattice matching with the underlying substrate, provided that the substrate bond energy is sufficiently small. The resulting film structure is unique to van der Waals bonded solids in that significant strain can be maintained even for very thick films grown under nonequilibrium (i.e., quasi-epitaxial)

conditions. Furthermore, the resulting thin-film nanostructures have been used as "laboratories" useful in the investigation of fundamental optical and electronic properties of the materials. These investigations have led to a deeper understanding of the physics of this enormous class of materials, while at the same time have shown that precision growth of the thin films afforded by the UHV process of OMBD can lead to significant modification of the materials properties which can be exploited in numerous device applications. We have discussed several archetype devices, and have shown that integrated organic/inorganic devices such as waveguides and photodiodes, solar cells, organic light-emitting devices, and thin-film transistors based on OMBD-grown thin films are just now reaching performance and cost levels which make them extremely attractive for use in a large range of optoelectronic systems applications.

Given the relative youth of this technology, and the exciting and rapid advances made using organic molecular thin films, high-vacuum growth is poised to make a significant contribution to our understanding and exploitation of these exciting materials well into the next century.

8.0. Acknowledgments

The author is indebted to numerous friends, collaborators, and students who have contributed data to this review as well as to the author's understanding of growth, phenomena, and applications of molecular organic thin films. Foremost among these collaborators are Dr. M. L. Kaplan, Mr. P. H. Schmidt, and Dr. P. E. Burrows who have always freely shared their ideas, talents, and enthusiasm of this subject, and who have contributed enormously to the understanding and manipulation of organic molecular crystals by the process of OMBD. I am also deeply grateful for the contributions of many students. Among these, Dr. Franky So, Mr. Vladimir Bulovic, and Dr. Zilan Shen have made major advances in the development of OMBD science and technology. I also thank Professor Mark Thompson for his many insights, as well as for synthesizing numerous materials used in our OLED structures. Many other collaborators deserve acknowledgment, including Professor P. Eisenberger, Dr. P. Fenter, Mr. G. Gu, Dr. E. I. Haskal, Dr. Y. Hirose, Professor A. Kahn, and Dr. C. Kendrick. Numerous helpful discussions with Professors S. Mukamel and Z. Soos are also acknowledged. The author thanks the Air Force Office of Scientific Research for their vision in supporting the effort in my laboratory long before there was the slightest reason to believe that it would generate any practical outcome, as well as DARPA, the National Science Foundation, and Universal Display Corporation. Finally, I express my deepest thanks to my wife Rosamund and my children for their nearly infinite patience and support of my work.

Figures that are cited with a reference number in the figure caption have been reprinted with the permission of the publisher of the publication cited in the corresponding reference.

9.0. References

(1) Forrest, S. R.; Burrows, P. E.; Haskal, E. I.; So, F. F. *Phys. Rev. B* **1994**, *49*, 11309.
(2) Hara, M.; Sasabe, H.; Yamada, A.; Garito, A. F. *Jpn. J. Appl. Phys.* **1989**, *28*, L306.
(3) Koma, A. *Prog. Cryst. Growth Charact.* **1995**, *30*, 129−152.
(4) Tredgold, R. H. *Order in Thin Organic Films*; Cambridge University Press: Cambridge, 1994.
(5) Hong, H.; Tarabia, M.; Chayet, H.; Davidov, D.; Faraggi, E. Z.; Avny, V.; Neumann, R.; Kirstein, S. *J. Appl. Phys.* **1996**, *79*, 3082.
(6) Herman, M. A.; Sitter, H. *Molecular Beam Epitaxy*, 1st ed.; Springer-Verlag: Berlin, 1988.
(7) *Optoelectronic Integration: Physics, Technology and Applications*; Wada, O., Ed.; Kluwer Academic Publishers: Boston, 1994.
(8) Fetterman, M.; Chao, C.-P.; Forrest, S. R. *IEEE Photonics Technol. Lett.* **1995**, *8*, 69.
(9) Chao, C.-P.; Shiau, G.-J.; Forrest, S. R. *IEEE Photonics Technol. Lett.* **1994**, *6*, 1406.
(10) Sasaki, T.; Yamaguchi, M.; Kitamura, M. *J. Cryst. Growth* **1994**, *145*, 846.
(11) Shiau, G.-J.; Chao, C.-P.; Burrows, P. E.; Forrest, S. R. *Appl. Phys. Lett.* **1994**, *65*, 892.
(12) Coldren, L. A.; Corzine, S. W. *Diode Lasers and Photonic Integrated Circuits*; John Wiley: New York, 1995.
(13) Miller, D. A. B.; Chemla, D. S.; Damen, T. C.; Gossard, A. C.; Wiegmann, W.; Wood, T. H.; Burrus, C. A. *Phys. Rev. B* **1985**, *32*, 1043.
(14) Chemla, D. S.; Zyss, J. *Nonlinear Optical Properties of Organic Molecules and Crystals*; Academic Press: Orlando, 1987.
(15) Mukamel, S. *Principles of Nonlinear Optical Spectroscopy*; Oxford University Press: New York, 1995.
(16) *Organic Materials for Nonlinear Optics II*; Hann, R. A., Bloor, D., Eds.; The Royal Soc. of Chemistry: Cambridge, 1991.
(17) Seto, J.; Asai, N.; Fujiwara, I.; Ishibashi, T.; Kamei, T.; Tamura, S. *Thin Solid Films* **1996**, *273*, 97.
(18) Maruyama, Y.; Hoshi, H.; Fang, S. L.; Kohama, K. *Synth. Met.* **1995**, *71*, 1653.
(19) Simon, J.; Andre, J.-J. *Molecular Semiconductors: Photoelectrical Properties and Solar Cells*; Springer-Verlag: Berlin, 1985.
(20) Wohrle, D.; Meissner, D. *Adv. Mater.* **1991**, *3*, 129.
(21) *Phthalocyanines: Properties and Applications*; Leznoff, C. C., Lever, A. B. P., Eds.; VCH Publishers: New York, 1989.
(22) Taylor, R. B.; Burrows, P. E.; Forrest, S. R. *IEEE Photonics Technol. Lett.* **1997**, *9*, 365.
(23) So, F. F.; Forrest, S. R.; Shi, Y. Q.; Steier, W. H. *Appl. Phys. Lett.* **1990**, *56*, 674−676.
(24) So, F. F.; Forrest, S. R. *Phys. Rev. Lett.* **1991**, *66*, 2649−2652.
(25) Agranovich, V. M. *Phys. Scr.* **1993**, *149*, 699.
(26) Agranovich, V. M.; LaRocca, G. C.; Bassani, F. *Chem. Phys. Lett.* **1995**, *247*, 355.
(27) Lam, J. F.; Forrest, S. R.; Tangonan, G. L. *Phys. Rev. Lett.* **1991**, *66*, 1614.
(28) Wang, N.; Jenkins, J. K.; Chernyak, V.; Mukamel, S. *Phys. Rev. B* **1994**, *49*, 17079.
(29) Zakhidov, A. A.; Yoshino, K. *Synth. Met.* **1994**, *64*, 155.
(30) Nakada, H.; Tohma, T. 8th Int. Workshop on Electroluminescence, Berlin, 1996; p 385.
(31) Tang, C. W.; VanSlyke, S. A. *Appl. Phys. Lett.* **1987**, *51*, 913.
(32) Burrows, P. E.; Forrest, S. R. *Appl. Phys. Lett.* **1994**, *64*, 2285.
(33) Fang, S.; Kohama, K.; Hoshi, H.; Maruyama, Y. *Synth. Met.* **1994**, *64*, 167−170.
(34) Arbour, C.; Armstrong, N. R.; Brina, R.; Collins, G.; Danziger, J.; Dodelet, J.-P.; Lee, P.; Nebesny, K. W.; Pankow, J.; Waite, S. *Mol. Cryst. Liq. Cryst.* **1990**, *183*, 307.
(35) Forrest, S. R.; Kaplan, M. L.; Schmidt, P. H.; Venkatesan, T.; Lovinger, A. J. *Appl. Phys. Lett.* **1982**, *41*, 708.
(36) Lovinger, A. J.; Forrest, S. R.; Kaplan, M. L.; Schmidt, P. H.; Venkatesan, T. *J. Appl. Phys.* **1984**, *55*, 476.
(37) Forrest, S. R.; Kaplan, M. L.; Schmidt, P. H. *J. Appl. Phys.* **1984**, *55*, 1492.
(38) Forrest, S. R.; Kaplan, M. L.; Schmidt, P. H.; Feldmann, W. L.; Yanowski, E. *Appl. Phys. Lett.* **1982**, *41*, 90.
(39) Danziger, J.; Dodelet, J.-P.; Lee, P.; Nebesny, K. W.; Armstrong, N. R. *Chem. Mater.* **1991**, *3*, 821.
(40) Zimmermann, U.; Schnitzler, G.; Karl, N.; Umbach, E. *Thin Solid Films* **1989**, *175*, 85.
(41) Akers, K.; Aroca, R.; Hor, A.-M.; Loutfy, R. O. *J. Phys. Chem.* **1987**, *91*, 2954.
(42) Ludwig, C.; Gompf, J.; Glatz, W.; Petersen, J.; Eisenmenger, W.; Mobus, M.; Karl, N. *Z. Phys. B* **1992**, *86*, 397.
(43) Hoshino, A.; Isoda, S.; Kurata, H.; Kobayashi, T. *J. Appl. Phys.* **1994**, *76*, 4113.
(44) Vincett, P. S.; Popovic, Z. D.; McIntyre, L. *Thin Solid Films* **1981**, *82*, 357.
(45) Debe, M. K.; Kam, K. K.; Liu, J. C.; Poirier, R. J. *J. Vac. Sci. Technol. A* **1988**, *6*, 1907.
(46) Mobus, M.; Karl, N.; Kobayashi, T. *J. Cryst. Growth* **1992**, *116*, 495−504.

(47) So, F. F.; Forrest, S. R.; Shi, Y. Q.; Steier, W. H. Mat. Res. Soc. Ann. Mtg., 1990; p 71.
(48) So, F. F.; Leu, L. Y.; Forrest, S. R. SPIE Symp. on Growth of Semiconductor Structures and High T_c Thin Films on Semiconductors, San Diego, 1990; p 95.
(49) Tanigaki, K.; Kuroshima, S.; Ebbesen, T. W.; Ichihashi, T. *J. Cryst. Growth* **1991**, *114*, 3.
(50) Yoshimura, T.; Tatsuura, S.; Sotoyama, W. *Appl. Phys. Lett.* **1991**, *59*, 482.
(51) Tsang, W. T. In *Lightwave Communications Technology*; Tsang, W. T., Ed.; Academic Press: Orlando, 1985; Vol. 22A.
(52) Haskal, E. I.; So, F. F.; Burrows, P. E.; Forrest, S. R. *Appl. Phys. Lett.* **1992**, *60*, 3223−3225.
(53) Tada, H.; Kawaguchi, T.; Koma, A. *Appl. Phys. Lett.* **1992**, *61*, 2021−2023.
(54) Hirose, Y.; Chen, W.; Haskal, E. I.; Forrest, S. R.; Kahn, A. *J. Vac. Sci. Technol. B* **1994**, *12*, 2616.
(55) Hirose, Y.; Forrest, S. R.; Kahn, A. *Appl. Phys. Lett.* **1995**, *66*, 944−946.
(56) Zimmermann, U.; Karl, N. *Surf. Sci.* **1992**, *268*, 196.
(57) Ludwig, C.; Gomph, B.; Petersen, J.; Strohmaier, R.; Eisenmenger, W. *Z. Phys. B* **1994**, *93*, 365−373.
(58) Kendrick, C.; Kahn, A.; Forrest, S. R. *Appl. Surf. Sci.* **1996**, *104/105*, 586.
(59) Gutmann, F.; Lyon, L. E. Rob't. E. Krieger Publishing: Malabar, FL, 1981.
(60) Karl, N. *Mol. Cryst. Liq. Cryst.* **1989**, *171*, 157.
(61) Warta, W.; Stehle, R.; Karl, N. *Appl. Phys. A* **1985**, *36*, 163.
(62) Karl, N.; Marktanner, J.; Stehle, R.; Warta, W. *Synth. Met.* **1991**, *41−43*, 2473.
(63) Forrest, S. R.; Kaplan, M. L.; Schmidt, P. H. In *Annu. Rev. Mater. Sci.*; Huggins, R. A., Ed.; Annual Reviews: Palo Alto, CA, 1987; Vol. 17.
(64) Weston, G. F. Butterworths: London, 1985.
(65) Forrest, S. R.; Kaplan, M. L.; Schmidt, P. H. *J. Appl. Phys.* **1984**, *56*, 543.
(66) Tanigaki, K.; Kuroshima, S.; Ebbesen, T.; Ichihashi, T. *Mol. Cryst. Liq. Cryst. Sci. Technol., Nonlinear Optics* **1992**, *B2*, 179−192.
(67) Matthews, J. W.; Blakeslee, A. E. *J. Cryst. Growth* **1974**, *27*, 118.
(68) Kim, D. S.; Forrest, S. R.; Lange, M. J.; Olsen, G. H.; Cohen, M. J. *IEEE Photonics Technol. Lett.* **1994**, *6*, 235−237.
(69) Koma, A. *Surf. Sci.* **1992**, *267*, 29−33.
(70) Burrows, P. E.; Zhang, Y.; Haskal, E. I.; Forrest, S. R. *Appl. Phys. Lett.* **1992**, *61*, 2417.
(71) Venables, J. A.; Spiller, G. D. T.; Hanbucken, M. *Rep. Prog. Phys.* **1984**, *47*, 399−459.
(72) Zhang, Y.; Forrest, S. R. *Phys. Rev. Lett.* **1993**, *71*, 2765−2768.
(73) Fenter, P.; Burrows, P. E.; Eisenberger, P.; Forrest, S. R. *J. Cryst. Growth* **1995**, *152*, 65−72.
(74) Fenter, P.; Eisenberger, P.; Burrows, P.; Forrest, S. R.; Liang, K. S. *Physica B* **1996**, *221*, 145−151.
(75) Novaco, A. D.; McTague, J. P. *Phys. Rev. Lett.* **1977**, *38*, 1286−1289.
(76) Jerome, B. *Rep. Prog. Phys.* **1991**, *54*, 391−451.
(77) Shi, Y.; Cull, B.; Kumar, S. *Phys. Rev. Lett.* **1993**, *71*, 2773−2776.
(78) Forrest, S. R.; Burrows, P. E. *Supramol. Sci.* **1997**, *4*, 127.
(79) Kitaigorodsky, A. I. *Molecular Crystals and Molecules*; Academic Press: New York, 1973.
(80) Ashcroft, N. W.; Mermin, N. D. *Solid State Physics*; Saunders College: Philadelphia, 1976.
(81) Yamamoto, H.; Tada, H.; Kawaguchi, T.; Koma, A. *Appl. Phys. Lett.* **1994**, *64*, 2099−2101.
(82) Tada, H.; Morioka, T.; Koma, A. *J. Phys.: Condens. Matter* **1994**, *6*, 1881−1892.
(83) Tada, H.; Saiki, K.; Koma, A. *Surf. Sci.* **1992**, *268*, 387.
(84) Hoshi, H.; Maruyama, Y. *J. Appl. Phys.* **1991**, *69*, 3046−3052.
(85) Hoshi, H.; Fang, S.; Maruyama, Y. *J. Appl. Phys.* **1993**, *73*, 3111.
(86) Dann, A. J.; Hoshi, H.; Maruyama, Y. *J. Appl. Phys.* **1990**, *67*, 1371.
(87) Hoshi, H.; Maruyama, Y.; Masuda, H.; Inabe, T. *J. Appl. Phys.* **1990**, *68*, 1396.
(88) Hoshi, H.; Dann, A. J.; Maruyama, Y. *J. Appl. Phys.* **1990**, *67*, 1845.
(89) Hoshi, H.; Dann, A. J.; Maruyama, Y. *J. Appl. Phys.* **1990**, *67*, 6871.
(90) Buchholz, J. C.; Somorjai, G. A. *J. Chem. Phys.* **1977**, *66*, 573.
(91) Kawaguchi, T.; Tada, H.; Koma, A. *J. Appl. Phys.* **1994**, *75*, 1486−1492.
(92) Schmicker, D.; Schmidt, S.; Skofronick, J. G.; Toennies, J. P.; Vollmer, R. *Phys. Rev. B* **1991**, *44*, 10995−10997.
(93) Krakow, W.; Rivera, N. M.; Roy, R. A.; Ruoff, R. S.; Cuomo, J. J. *J. Mater. Res.* **1992**, *7*, 784.
(94) Li, Y. Z.; Patrin, J. C.; Chander, M.; Weaver, J. H.; Chibante, L. P. F.; Smalley, R. E. *Science* **1991**, *252*, 547.
(95) Seidel, C.; Awater, C.; Liu, X. D.; Ellerbrake, R.; Fuchs, H. *Surf. Sci.* **1997**, *371*, 123.
(96) Hoshino, A.; Isoda, S.; Kurata, H.; Kobayashi, T. *J. Cryst. Growth* **1995**, *146*, 636.
(97) Tada, H.; Saiki, K.; Koma, A. *Jpn. J. Appl. Phys.* **1991**, *30*, L306.
(98) Dietrich, T.; Schlesser, R.; Erler, B.; Kundig, A.; Sitar, Z.; Gunter, P. *J. Cryst. Growth* **1997**, *172*, 473.
(99) Forrest, S. R.; Zhang, Y. *Phys. Rev. B* **1994**, *49*, 11297−11308.
(100) Burrows, P. E.; Forrest, S. R. *Appl. Phys. Lett.* **1993**, *62*, 3102−3104.
(101) Hirose, Y.; Forrest, S. R.; Kahn, A. *Phys. Rev. B* **1995**, *52*, 14040.
(102) Zang, D. Y.; Shi, Y. Q.; So, F. F.; Forrest, S. R.; Steier, W. H. *Appl. Phys. Lett.* **1991**, *58*, 562−564.
(103) Komiyama, M.; Sakakibara, Y.; Hirai, H. *Thin Solid Films* **1987**, *151*, L109.
(104) Hoshino, A.; Isoda, S.; Kurata, H.; Kobaysahi, T.; Yamashita, Y. *Jpn. J. Appl. Phys.* **1995**, *34*, 3858.
(105) Sakurai, M.; Tada, H.; Saiki, K.; Koma, A.; Funasaka, H.; Kishimoto, Y. *Chem. Phys. Lett.* **1993**, *208*, 425−430.
(106) Fartash, A. *Appl. Phys. Lett.* **1995**, *67*, 3901−3903.
(107) Merwe, J. H. v. d. *Philos. Mag. A* **1982**, *45*, 127.
(108) Reiss, H. *J. Appl. Phys.* **1968**, *39*, 5045.
(109) Hashimoto, S.; Ogawa, T.; Asaka, N.; Isoda, S.; Kobayashi, T. *J. Cryst. Growth* **1995**, *146*, 649.
(110) Itoh, C.; Miyazaki, T.; Aizawa, K.; Aoki, H.; Okazaki, M. *J. Phys. C, Solid State Phys.* **1988**, *21*, 4527−4544.
(111) Fenter, P.; Schreiber, F.; Zhou, L.; Eisenberger, P. E.; Forrest, S. R. *Phys. Rev. B* **1997**, *56*, 3046.
(112) Abe, A.; Jernigan, R. L.; Flory, P. J. *J. Am. Chem. Soc.* **1966**, *88*, 631.
(113) Scott, R. A.; A. Scheraga, H. *J. Chem. Phys.* **1965**, *42*, 2209.
(114) Cox, J. D.; Pilcher, G. *Thermochemistry of Organic and Organometallic Compounds*; Academic Press: New York, 1970.
(115) Taylor, R. B.; Shen, Z.; Forrest, S. R. *Top. Mtg. on Organic Thin Films for Photonics Applications Tech. Dig.*, 1995; p 38, Paper MB5.
(116) McTague, J. P.; Novaco, A. D. *Phys. Rev. B* **1979**, *19*, 5299−5306.
(117) Liu, D.-J.; Selinger, R. L. B.; Weeks, J. D. *J. Chem. Phys.* **1996**, *105*, 4751.
(118) Dogo, S.; Germain, J.-P.; Maleysson, C.; Pauly, A. *Thin Solid Films* **1992**, *219*, 244.
(119) Shimada, T.; Suzuki, A.; Sakurada, T.; Koma, A. *Appl. Phys. Lett.* **1996**, *68*, 2502.
(120) Hiller, A. C.; Ward, M. D. *Phys. Rev. B* **1996**, *54*, 14037.
(121) Fecht, H. J. *Philos. Mag. Lett.* **1989**, *60*, 81.
(122) Strohmaier, R.; Ludwig, C.; Petersen, J.; Gompf, B.; Eisenmenger, W. *Surf. Sci.* **1996**, *351*, 292.
(123) Kendrick, C. E. Princeton University, 1997.
(124) Mobus, M.; Schreck, M.; Karl, N. *Thin Solid Films* **1989**, *175*, 89.
(125) Seo, D. K.; Ren, J.; Wangbo, M. H. *Surf. Sci.* **1997**, *370*, 252.
(126) Kotzian, M.; Rosch, N.; Schroeder, H.; Zerner, M. C. *J. Am. Chem. Soc.* **1989**, *111*, 7687.
(127) Anderson, W. P.; Edwards, W. D.; Zerner, M. C. *Inorg. Chem.* **1986**, *25*, 2728.
(128) Anderson, W. P.; Cundari, T. R.; Drago, R. S.; Zerner, M. C. *Inorg. Chem.* **1990**, *29*, 1.
(129) Ohuchi, F. S.; Shimada, T.; Parkinson, B. A.; Ueno, K.; Koma, A. *J. Cryst. Growth* **1991**, *111*, 1033−1037.
(130) Sakurai, M.; Tada, H.; Saiki, K.; Koma, A. *Jpn. J. Appl. Phys.* **1991**, *30*, L1892-L1894.
(131) Ueno, K.; Sakurai, M.; Koma, A. *J. Cryst. Growth* **1995**, *150*, 1180−1185.
(132) Tanigaki, K.; Kuroshima, S.; Fujita, J.-I.; Ebbesen, T. W. *Appl. Phys. Lett.* **1993**, *63*, 2351.
(133) Nebesny, K. W.; Collins, G. E.; Lee, P. A.; Chau, L.-K.; Danziger, J.; Osburn, E.; Armstrong, N. R. *Chem. Mater.* **1991**, *3*, 829.
(134) Fritz, T.; Miskowiec, P. *Mol. Cryst. Liq. Cryst.* **1996**, *283*, 151.
(135) Haskal, E. I.; Shen, Z.; Burrows, P. E.; Forrest, S. R. *Phys. Rev. B* **1995**, *51*, 4449.
(136) Dobson, P. J.; Joyce, B. A.; Neave, J. H.; Zhang, J. *J. Cryst. Growth* **1987**, *81*, 1.
(137) Cho, A. Y. *J. Appl. Phys.* **1971**, *42*, 2074.
(138) Nonaka, T.; Mori, Y.; Nagai, N.; Nakagawa, Y.; Saeda, M.; Takahagi, T.; Ishitani, A. *Thin Solid Films* **1994**, *239*, 214.
(139) Nonaka, T.; Mori, Y.; Nagai, N.; Matsunobe, T.; Nakagawa, Y.; Saeda, M.; Takahagi, T.; Ishitani, A. *J. Appl. Phys.* **1993**, *73*, 2826.
(140) Fuchigami, H.; Tanimura, S.; Uehara, Y.; Kurata, T.; Tsunoda, S. *Jpn. J. Appl. Phys.* **1995**, *34*, 3852.
(141) Collins, G. E.; Williams, V. S.; Chau, L.-K.; Nebesny, K. W.; England, C.; Lee, P. A.; Lowe, T.; Fernando, Q.; Armstrong, N. R. *Synth. Met.* **1993**, *54*, 351.
(142) Imanishi, Y.; Hattori, S.; Kakuta, A.; Numata, S. *Phys. Rev. Lett.* **1993**, *71*, 2098.
(143) Nonaka, T.; Date, T.; Tomita, S.; Nagai, N.; Nishimura, M.; Murata, Y.; Ishitani, A. *Thin Solid Films* **1994**, *237*, 87.
(144) Takada, J.; Awaji, H.; Koshioka, M.; Nevin, W. A. *J. Appl. Phys.* **1994**, *75*, 4055.
(145) Tokito, S.; Sakata, J.; Taga, Y. *J. Appl. Phys.* **1995**, *77*, 1985−1989.

(146) Ohmori, Y.; Fujii, A.; Uchida, M.; Morishima, C.; Yoshino, K. *Appl. Phys. Lett.* **1993**, *62*, 3250.
(147) Ohmori, Y.; Fujii, A.; Uchida, M.; Morishima, C.; Yoshino, K. *Appl. Phys. Lett.* **1993**, *63*, 1871.
(148) Fujii, A.; Yoshida, M.; Ohmori, Y.; Yoshino, K. *Jpn. J. Appl. Phys.* **1995**, *34*, L621.
(149) Fujii, A.; Yoshida, M.; Ohmori, Y.; Yoshino, K. *Jpn. J. Appl. Phys.* **1995**, *34*, L499.
(150) Hong, H.; Tarabia, M.; Chayet, H.; Davidov, D.; Faraggi, E. Z.; Avny, V.; Neumann, R.; Kirstein, S. *J. Appl. Phys.* **1996**, *79*, 3082.
(151) Armstrong, N. R.; Nebesny, K. W.; Collins, G. E.; Chau, L.-K.; Lee, P. A.; England, C.; Diehl, D.; Douskey, M.; Parkinson, B. A. *Thin Solid Films* **1992**, *216*, 90.
(152) Nanai, N.; Yudasaka, M.; Ohki, Y.; Yoshimura, S. *Thin Solid Films* **1995**, *265*, 1.
(153) Born, L.; Heywang, G. *Z. Kristallogr.* **1990**, *190*, 153.
(154) Burrows, P. E.; Hara, M.; Sasabe, H. *Mol. Cryst. Liq. Cryst. Sci. Technol. B, Nonlinear Opt.* **1992**, *2*, 193.
(155) Ludwig, C.; Strohmaier, R.; Petersen, J.; Gompf, B.; Eisenmenger, W. *J. Vac. Sci. Technol. B* **1994**, *12*, 1963.
(156) Nagao, S.; Takashima, M.; Inoue, Y.; Katoh, M.; Gotoh, H. *J. Cryst. Growth* **1991**, *111*, 521.
(157) Lyons, M. H. *J. Cryst. Growth* **1989**, *96*, 339.
(158) Shiau, G.-J.; Chao, C.-P.; Burrows, P. E.; Forrest, S. R. *J. Appl. Phys.* **1995**, *77*, 201.
(159) Tokito, S.; Sakata, J.; Taga, Y. *Appl. Phys. Lett.* **1994**, *64*, 1353.
(160) Yudson, V. I.; Reineker, P.; Agranovich, V. M. *Phys. Rev. B* **1995**, *52*, R5543.
(161) Vlieg, E.; Gon, A. W. D. v. d.; Veen, J. F. v. d.; Macdonald, J. E.; Norris, C. *Phys. Rev. Lett.* **1988**, *61*, 2241.
(162) Mobus, M.; Karl, N. *Thin Solid Films* **1992**, *215*, 213−217.
(163) Haskal, E. I.; Zhang, Y.; Burrows, P. E.; Forrest, S. R. *Chem. Phys. Lett.* **1994**, *219*, 325.
(164) Li, D.; Nakamura, Y.; Otsuka, N.; Qiu, J.; Kobayashi, M.; Gunshor, R. L. *J. Vac. Sci. Technol. B* **1991**, *9*, 2167.
(165) Li, D.; Pashley, M. D. *Phys. Rev. B* **1994**, *49*, 13643.
(166) Pashley, M. D.; Li, D. *J. Vac. Sci. Technol. A* **1994**, *12*, 1848.
(167) Hirose, Y.; Chen, W.; Haskal, E. I.; Forrest, S. R.; Kahn, A. *Appl. Phys. Lett.* **1994**, *64*, 3482.
(168) Chadi, D. J. *J. Vac. Sci. Technol. A* **1987**, *5*, 834.
(169) Larsen, P. K.; Veen, J. F. v. d.; Mazur, A.; Pollmann, J.; Neave, J. H.; Joyce, B. A. *Phys. Rev. B* **1982**, *26*, 3222.
(170) So, F. F.; Forrest, S. R. *J. Appl. Phys.* **1988**, *63*, 442.
(171) Forrest, S. R.; So, F. F. *J. Appl. Phys.* **1988**, *64*, 399.
(172) Bulovic, V.; Forrest, S. R. *Chem. Phys.* **1996**, *210*, 13.
(173) Bulovic, V.; Forrest, S. R. *Chem. Phys. Lett.* **1995**, *238*, 88.
(174) Forrest, S. R.; Yoon, W. Y.; Leu, L. Y.; So, F. F. *J. Appl. Phys.* **1989**, *66*, 5908.
(175) Zang, D. Y.; So, F. F.; Forrest, S. R. *Appl. Phys. Lett.* **1991**, *59*, 823−825.
(176) Shen, Z.; Forrest, S. R. *Phys. Rev. B* **1997**, *55*, 10578.
(177) Shen, Z.; Burrows, P. E.; Forrest, S. R.; Ziari, M.; Steier, W. H. *Chem. Phys. Lett.* **1995**, *236*, 129.
(178) Sakurai, M.; Koma, A. *Trans. Mater. Res. Soc. Jpn.* **1994**, *14B*, 1145−1148.
(179) Nagayama, K.; Mitsumoto, R.; Araki, T.; Ouchi, Y.; Seki, K. *Physica B* **1995**, *208*−209, 419.
(180) Gimzewski, J. K.; Modesti, S.; Gerber, C.; Schlittler, R. R. *Chem. Phys. Lett.* **1993**, *213*, 401−406.
(181) Altman, E. I.; Colton, R. J. *Surf. Sci.* **1992**, *279*, 49−67.
(182) Viswanathan, R.; Zasadzinski, J. A.; Schwartz, D. K. *Science* **1993**, *261*, 449−452.
(183) Akimichi, H.; Inoshita, T.; Hotta, S.; Noge, H.; Sakaki, H. *Appl. Phys. Lett.* **1993**, *63*, 3158.
(184) Yoshimura, T.; Tatsuura, S.; Sotoyama, W. *Thin Solid Films* **1992**, *207*, 9.
(185) Ahonen, M.; Pessa, M.; Suntola, T. *Thin Solid Films* **1980**, *65*, 301.
(186) Bedair, S. M.; Tischler, M. A.; Katsuyama, T.; El-Masry, N. A. *Appl. Phys. Lett.* **1985**, *47*, 51.
(187) Ide, Y.; McDermott, B. T.; Hashemi, M.; Bedair, S. M.; Goodhue, W. D. *Appl. Phys. Lett.* **1988**, *53*, 2314.
(188) Isshiki, H.; Aoyagi, Y.; Sugano, T.; Iwai, S.; Meguro, T. *Appl. Phys. Lett.* **1993**, *63*, 1528.
(189) An, N. B. *Phys. Lett. A* **1996**, *214*, 99.
(190) Takada, J. *Jpn. J. Appl. Phys.* **1995**, *34*, 3864.
(191) Takada, J.; Awaji, H.; Koshioka, M.; Nakajima, A.; Nevin, W. A. *Appl. Phys. Lett.* **1992**, *61*, 2184.
(192) Hasegawa, S.; Mori, T.; Imaeda, K.; Tanaka, S.; Yamashita, Y.; Inokuchi, H.; Fujimoto, H.; Seki, K.; Ueno, N. *J. Chem. Phys.* **1994**, *100*, 6969.
(193) Inokuchi, H.; Imaeda, K. *Acta Phys. Pol. A* **1995**, *88*, 1161.
(194) Imeada, K.; Yamashita, Y.; Li, Y.; Mori, T.; Inokuchi, H.; Sano, M. *J. Mater. Chem.* **1992**, *2*, 115.
(195) Silinsh, E. A. *Organic Molecular Crystals: Their Electronic States*; Springer-Verlag: Berlin, 1980.
(196) Pope, M.; Swenberg, C. E. *Electronic Processes in Organic Crystals*; Clarendon Press: Oxford, 1982.
(197) Bulovic, V.; Burrows, P. E.; Forrest, S. R.; Cronin, J. A.; Thompson, M. E. *Chem. Phys.* **1996**, *210*, 1.
(198) Kelly, M. K.; Etchegoin, P.; Fuchs, D.; Kratschmer, W.; Fostiropoulos, K. *Phys. Rev. B* **1992**, *46*, 4963.
(199) Sebastian, L.; Weiser, G.; Bässler, H. *Chem. Phys.* **1981**, *61*, 125.
(200) Tanaka, J. *Bull. Chem. Soc. Jpn.* **1963**, *36*, 1237.
(201) Schreiber, M.; Toyozawa, Y. *J. Phys. Soc. Jpn.* **1982**, *51*, 1544.
(202) Mataga, N.; Torihashi, Y.; Ota, Y. *Chem. Phys. Lett.* **1967**, *1*, 385.
(203) So, F. F.; Forrest, S. R. *Mol. Cryst. Liq. Cryst. Sci. Technol. B: Nonlinear Optics* **1992**, *2*, 205−222.
(204) Anderson, M. L.; Williams, V. S.; Schuerlein, T. J.; Collins, G. E.; England, C. D.; Chau, L.-K.; Lee, P. A.; Nebesny, K. W.; Armstrong, N. R. *Surf. Sci.* **1994**, *307*−*309*, 551.
(205) Weisbuch, C.; Dingle, R.; Gossard, A. C.; Wiegmann, W. *Solid State Commun.* **1981**, *38*, 709.
(206) Broude, V. L.; Rashba, E. I.; Sheka, E. F. *Spectroscopy of Molecular Excitons*; Springer-Verlag: Berlin, 1985.
(207) Sugano, S.; Tanabe, Y.; Kamimura, H. *Multiplets of Transition Metal Ions in Crystals*; Academic: New York, 1970.
(208) Pikus, G. E.; Bir, G. L. *Symmetry and Deformation Effects in Semiconductors*; Nauka: Moscow, 1972 (English Translation, Wiley: New York, 1974).
(209) Cho, K. *Excitons*; Springer-Verlag: Berlin, 1979.
(210) Silinsh, E. A.; Capek, V. *Organic Molecular Crystals*; American Institute of Physics: New York, 1994.
(211) Ueta, M.; Kanazaki, H.; Kobayashi, K.; Toyozawa, Y. *Excitonic Processes in Solids*; Springer-Verlag: New York, 1986.
(212) Sebastian, L.; Weiser, G.; Bassler, H. *Chem. Phys.* **1981**, *61*, 125.
(213) Bounds, P. J.; Petelenz, P.; Siebrand, W. *Chem. Phys.* **1981**, *63*, 303.
(214) Hasegawa, S.; Tanaka, S.; Yamashita, Y.; Inokuchi, H.; Fujimoto, H.; Kamiya, K.; Seki, K.; Ueno, N. *Phys. Rev. B* **1993**, *48*, 2596.
(215) Wu, C. I.; Hirose, Y.; Sirringhaus, H.; Kahn, A. *Chem. Phys. Lett.* **1997**.
(216) Hirose, Y.; Aristov, V.; Soukiassian, P.; Bulovic, V.; Forrest, S. R.; Kahn, A. *Phys. Rev. B* **1996**, *54*, 13748.
(217) So, F. F.; Forrest, S. R. *Appl. Phys. Lett.* **1988**, *52*, 1341.
(218) Dubovsky, O.; Mukamel, S. *J. Chem. Phys.* **1992**, *15*, 417.
(219) Huang, H. X.; Mukamel, S. *Chem. Phys. Lett.* **1992**, *192*, 417.
(220) Mukamel, S.; Takahashi, A.; Huang, H. X.; Chen, G. *Science* **1994**, *266*, 250.
(221) Wang, N.; Mukamel, S. *Chem. Phys. Lett.* **1994**, *231*, 373.
(222) Silbey, R.; Jortner, J.; Rice, S. A.; Vala, M. T. *J. Chem. Phys.* **1965**, *43*, 2925.
(223) Silbey, R.; Jortner, J.; Rice, S. A.; Vala, M. T. *J. Chem. Phys.* **1965**, *42*, 733.
(224) Ostrick, J. R.; Dodabalapur, A.; Torsi, L.; Lovinger, A. J.; Kwock, E. W.; Miller, T. M.; Galvin, M.; Berggren, M.; Katz, H. E. *J. Appl. Phys.* **1997**, *81*, 6804.
(225) Jurgis, A.; Silinsh, E. A. *Phys. Status Solidi B* **1972**, *53*, 735.
(226) Bounds, P. J.; Siebrand, W. *Chem. Phys. Lett.* **1980**, *75*, 414.
(227) Mott, N. F.; Gurney, R. W. *Electronic Processes in Ionic Crystals*; Clarendon: Oxford, 1940.
(228) Toyozawa, Y. *Prog. Theor. Phys.* **1954**, *12*, 421.
(229) Bounds, P. J.; Munn, R. W. *Chem. Phys.* **1979**, *44*, 103.
(230) Jackson, J. D. *Classical Electrodynamics*, 2nd ed.; Wiley: New York, 1975.
(231) Shinozuka, Y.; Matsuura, M. *Phys. Rev. B* **1983**, *28*, 4878.
(232) Ruff, M.; Streb, D.; Dankowski, S. U.; Tautz, S.; Kiesel, P.; Knupfer, B.; Kneissl, M.; Linder, N.; Dohler, G. H.; Keil, U. D. *Appl. Phys. Lett.* **1996**, *68*, 2968.
(233) Sebastian, L.; Weiser, G. *Chem. Phys.* **1981**, *62*, 447.
(234) Meyling, J. H.; Wiersma, D. A. *Chem. Phys. Lett.* **1973**, *20*, 383.
(235) Sebastian, L.; Weiser, G. *Chem. Phys.* **1981**, *62*, 447.
(236) Schiff, L. I. *Quantum Mechanics*; McGraw-Hill: New York, 1968.
(237) Sebastian, L.; Weiser, G. *Phys. Rev. Lett.* **1981**, *46*, 1156.
(238) Boer, K. W. *Survey of Semiconductor Physics: Electrons and Other Particles in Bulk Semiconductors*; Van Nostrand Reinhold: New York, 1990.
(239) Laporte, P.; Subtil, J. L. *Phys. Rev. Lett.* **1980**, *45*, 2138.
(240) Jayaraman, A.; Kaplan, M. L.; Schmidt, P. H. *J. Chem. Phys.* **1985**, *82*, 1682.
(241) Matsui, A.; Mizuno, K. *Chem. Phys.* **1987**, *113*, 111.
(242) Goebel, E. O.; Jung, H.; Kuhl, J.; Ploog, K. *Phys. Rev. Lett.* **1983**, *51*, 1588.
(243) Bebb, H. B.; Williams, E. W. In *Semiconductors and Semimetals*; Willardson, R. K., Beer, A. C., Eds.; Academic Press: New York, 1978; Vol. 8.
(244) Haarer, D. *Chem. Phys. Lett.* **1974**, *27*, 91.
(245) Munn, R. W.; Siebrand, W. *J. Chem. Phys.* **1970**, *52*, 47.
(246) Hong, H.; Davidov, D.; Avny, Y.; Chayet, H.; Faraggi, E. Z.; Neumann, R. *Adv. Mater.* **1995**, *7*, 846.
(247) Munn, R. W. *J. Chem. Phys.* **1994**, *99*, 1404.
(248) Agranovich, V. M.; Atanasov, R. D.; Bassani, G. F. *Chem. Phys. Lett.* **1992**, *199*, 621.
(249) An, N. B.; Hanamura, E. *J. Phys.: Condens. Matter* **1996**, *8*, 2273.
(250) Shen, Z.; Forrest, S. R. *Phys. Rev. B* **1993**, *48*, 17584.

(251) Yudson, V. I.; Neidlinger, T.; Reineker, P. *Phys. Lett. A* **1995**, *204*, 313.
(252) Hong, H.; Davidov, D.; Chayet, H.; Faraggi, E. Z.; Tarabia, M.; Avny, Y.; Neumann, R.; Kirstein, S. *Supramol. Sci.* **1997**, *4*, 67.
(253) Chen, X. L.; Jenekhe, S. A. *Appl. Phys. Lett.* **1997**, *70*, 487.
(254) Tokura, Y.; Koda, T.; Iyechika, Y.; Kuroda, H. *Chem. Phys. Lett.* **1983**, *102*, 174.
(255) Yoshida, H.; Tokura, Y.; Koda, T. *Chem. Phys.* **1986**, *109*, 375.
(256) Gu, G.; Bulovic, V.; Burrows, P. E.; Forrest, S. R.; Thompson, M. E. *Appl. Phys. Lett.* **1996**, *68*, 2606−2608.
(257) Burrows, P. E.; Sapochak, L. S.; McCarty, D. M.; Forrest, S. R.; Thompson, M. E. *Appl. Phys. Lett.* **1994**, *64*, 2718.
(258) Burrows, P. E.; Shen, Z.; Bulovic, V.; McCarty, D. M.; Forrest, S. R.; Cronin, J. A.; Thompson, M. E. *J. Appl. Phys.* **1996**, *79*, 7991.
(259) Petelenz, P.; Slawik, M.; Pac, B. *Synth. Met.* **1994**, *64*, 335.
(260) Fischer, C. M.; Burghard, M.; Roth, S. *Synth. Met.* **1995**, *71*, 1975.
(261) Fujii, A.; Yoshida, M.; Ohmori, Y.; Yoshino, K. *Thin Solid Films* **1996**, *273*, 199.
(262) Ghosh, A. K.; Feng, T. *J. Appl. Phys.* **1978**, *49*, 5982.
(263) Karl, N.; Baurer, A.; Holzapfel, J.; Marktanner, J.; Mobus, M.; Stolzle, F. *Mol. Cryst. Liquid Cryst.* **1994**, *252*, 243.
(264) Tang, C. W.; VanSlyke, S. A.; Chen, C. H. *J. Appl. Phys.* **1989**, *65*, 3610.
(265) Torsi, L.; Dodabalapur, A.; Rothberg, L. J.; Fung, A. W. P.; Katz, H. E. *Science* **1996**, *272*, 1462.
(266) Dodabalapur, A.; Katz, H. E.; Torsi, L.; Haddon, R. C. *Science* **1995**, *269*, 1560.
(267) Dodabalapur, A.; Torsi, L.; Katz, H. E. *Science* **1995**, *268*, 270.
(268) Garnier, F.; Horowitz, G.; Fichou, D.; Yassar, A. *Supramol. Sci.* **1997**, *4*, 155.
(269) Lin, Y.-Y.; Gundlach, D. J.; Jackson, T. N. Mat. Res. Soc. Spring Mtg., San Francisco, CA, 1997; p 143.
(270) Garnier, F.; Horowitz, G.; Peng, X.; Fichou, D. *Adv. Mater.* **1990**, *2*, 1990.
(271) Tang, C. W. *Appl. Phys. Lett.* **1986**, *48*, 183.
(272) Fang, S.; Hoshi, H.; Kohama, K.; Maruyama, Y. *J. Phys. Chem.* **1996**, *100*, 4104.
(273) Fang, S.; Kohama, K.; Hoshi, H.; Maruyama, Y. *Chem. Phys. Lett.* **1995**, *234*, 343.
(274) Fang, S.; Kohama, K.; Hoshi, H.; Maruyama, Y. *Jpn. J. Appl. Phys.* **1993**, *32*, L1418.
(275) Hoshi, H.; Kohama, K.; Fang, S.; Maruyama, Y. *Appl. Phys. Lett.* **1993**, *62*, 3080.
(276) Leegwater, J. A.; Mukamel, S. *Phys. Rev. A* **1992**, *46*, 452.
(277) Dubovsky, O.; Mukamel, S. *J. Chem. Phys.* **1991**, *95*, 7828.
(278) Samoc, M.; Prasad, P. N. *J. Chem. Phys.* **1989**, *91*, 6643.
(279) Yamamoto, H.; Katogi, S.; Watanabe, T.; Sato, H.; Miyata, S.; Hosomi, T. *Appl. Phys. Lett.* **1992**, *60*, 935.
(280) Zang, D. Y.; Forrest, S. R. *Appl. Phys. Lett.* **1992**, *60*, 189−191.
(281) Zang, D. Y.; Forrest, S. R. *IEEE Photonics Technol. Lett.* **1992**, *4*, 365.
(282) So, F. F.; Forrest, S. R. *IEEE Trans. Electron. Dev.* **1989**, *36*, 66.
(283) Forrest, S. R.; Kaplan, M. L.; Schmidt, P. H.; J. M. Parsey, J. *J. Appl. Phys.* **1985**, *58*, 867.
(284) Schmidt, P. H.; Forrest, S. R.; Kaplan, M. L. *J. Electrochem. Soc.* **1986**, *133*, 769.
(285) Forrest, S. R.; Schmidt, P. H.; Wilson, R. B.; Kaplan, M. L. *J. Vac. Sci. Technol. B* **1986**, *4*, 37.
(286) Chang, S. J.; Leu, L. Y.; Forrest, S. R.; Jones, C. E. *Appl. Phys. Lett.* **1989**, *54*, 1040.
(287) Al-Mohamad, A.; Smith, C. W.; Al-Saffar, I. S.; Salfin, M. A. *Thin Solid Films* **1990**, *175*, 181.
(288) Al-Mohamad, A.; Soukieh, M. *Thin Solid Films* **1995**, *271*, 132.
(289) Forrest, S. R.; Schmidt, P. H.; Wilson, R. B.; Kaplan, M. L. *Appl. Phys. Lett.* **1984**, *45*, 1199.
(290) Forrest, S. R.; Kaplan, M. L.; Schmidt, P.; Gates, J. V. *J. Appl. Phys.* **1985**, *57*, 2982.
(291) Forrest, S. R.; Schmidt, P. H. *J. Appl. Phys.* **1986**, *59*, 513.
(292) Forrest, S. R.; Kaplan, M. L.; Schmidt, P. H. *J. Appl. Phys.* **1986**, *60*, 2406.
(293) Antohe, S.; Tomozeiu, N.; Gogonea, S. *Phys. Status Solidi* **1991**, *125*, 397.
(294) Prabhakar, V.; Forrest, S. R.; Lorenzo, J. P.; Vaccaro, K. *IEEE Photonics Technol. Lett.* **1990**, *2*, 724.
(295) Adachi, C.; Nagai, K.; Tamoto, N. *Appl. Phys. Lett.* **1995**, *66*, 2679.
(296) Yap, D.; Burrows, P. E.; Forrest, S. R. *Top. Mtg. Organic Thin Films for Photonics Applications Tech. Dig.* **1995**, Paper WB2, p 302.
(297) Cheng, C.-L.; Forrest, S. R.; Kaplan, M. L.; Schmidt, P. H.; Tell, B. *Appl. Phys. Lett.* **1985**, *47*, 1217.
(298) Johnson, J. G.; Forrest, S. R.; Zeisse, C. R.; Nguyen, R. *Appl. Phys. Lett.* **1988**, *52*, 495.
(299) Chamberlain, G. A.; Clooney, P. J. *Chem. Phys. Lett.* **1979**, *66*, 88.
(300) Forrest, S. R.; Yoon, W. Y.; Leu, L. Y.; So, F. F. *J. Appl. Phys.* **1989**, *66*, 5908.
(301) Gregg, B. A. *Appl. Phys. Lett.* **1995**, *67*, 1271.
(302) Hiramoto, M.; Suezaki, M.; Yokoyama, M. *Chem. Lett.* **1990**, 327.
(303) Hiramoto, M.; Kishigami, Y.; Yokoyama, M. *Chem. Lett.* **1990**, 119.
(304) Hiramoto, M.; Fukusumi, H.; Yokoyama, M. *Appl. Phys. Lett.* **1992**, *61*, 2580.
(305) Karl, N.; Bauer, A.; Holzapfel, J.; Marktanner, J.; Mobus, M.; Stozle, F. *Mol. Cryst. Liq. Cryst.* **1994**, *252*, 243.
(306) Siebentritt, S.; Gunster, S.; Meissner, D. *Synth. Met.* **1991**, *41*−*43*, 1173.
(307) Wohrle, D.; Kreienhoop, L.; Schnurpfeil, G.; Elbe, J.; Tennigkeit, B.; Hiller, S.; Schlettwein, D. *J. Mater. Chem.* **1995**, *5*, 1819.
(308) Yamashita, K.; Harima, Y.; Matsubayashi, T. *J. Phys. Chem.* **1989**, *93*, 5311.
(309) Panayotatos, P.; Bird, G.; Sauers, R.; Piechowski, A.; Husain, S. *Sol. Cells* **1987**, *21*, 301.
(310) Gunster, S.; Siebentritt, S.; Elbe, J.; Kreienhoop, L.; Tennigkeit, B.; Wohrle, D.; Memming, R.; Meissner, D. *Mol. Cryst. Liq. Cryst.* **1992**, *218*, 117.
(311) Halls, J. J. M.; Pichler, K.; Friend, R. H.; Moratti, S. C.; Holmes, A. B. *Appl. Phys. Lett.* **1996**, *68*, 3120.
(312) Yonehara, H.; Pac, C. *Thin Solid Films* **1996**, *278*, 108.
(313) Sze, S. M. *Physics of Semiconductor Devices*, 2 ed.; John Wiley: New York, 1981.
(314) *Heterojunction Band Discontinuities: Physics and Device Applications*; Capasso, F., Margaritondo, G., Eds.; North-Holland: Amsterdam, 1987.
(315) Kao, K. C.; Hwang, W. *Electrical Transport in Solids*; Pergamon: Oxford, 1981.
(316) Chaiken, R. F.; Kearns, D. R. *J. Chem. Phys.* **1966**, *45*, 3966.
(317) Garbuzov, D. Z.; Forrest, S. R.; Tsekoun, A. G.; Burrows, P. E.; Bulovic, V.; Thompson, M. E. *J. Appl. Phys.* **1996**, *80*, 4644.
(318) Blouke, M. M.; Cowens, M. W.; Hall, J. E.; Westphal, J. A.; Christensen, A. B. *Appl. Opt.* **1980**, *19*, 3318.
(319) Goetzberger, A.; Greubel, W. *Appl. Phys.* **1977**, *14*, 123.
(320) Viehmann, W. Conf. Meas. Opt. Rad. 1979; p 90.
(321) Sims, G.; Griffin, F.; Lesser, M. Opt. Sensors and Electron. Photog. 1989; p 31.
(322) Garbuzov, D. Z.; Bulovic, V.; Burrows, P. E.; Forrest, S. R. *Chem. Phys. Lett.* **1996**, *249*, 433.
(323) Dresner, J. *RCA Rev.* **1969**, *30*, 322.
(324) Helfrich, W.; Schneider, W. G. *Phys. Rev. Lett.* **1965**, *14*, 229.
(325) Tang, C. W. *Inf. Dis.* **1996**, 16.
(326) Wu, C. C.; Chun, J. K. M.; Burrows, P. E.; Sturm, J. C.; Thompson, M. E.; Forrest, S. R.; Register, R. A. *Appl. Phys. Lett.* **1995**, *66*, 653.
(327) Era, M.; Morimoto, S.; Tsutsui, T.; Saito, S. *Appl. Phys. Lett.* **1994**, *65*, 676.
(328) Forrest, S. R.; Burrows, P. E.; Thompson, M. E. *Laser Focus World* **1995**, 99.
(329) Sheats, J. R.; Antoniadis, H.; Hueschen, M. R.; Leonard, W.; Miller, J. N.; Moon, R. L. *Science* **1996**, *273*, 884.
(330) Rothberg, L. J.; Lovinger, A. J. *J. Mater. Res.* **1996**, *11*, 3174.
(331) Greenham, N. C.; Friend, R. H. *Solid State Phys.* **1995**, *49*, 1.
(332) Brown, A. R.; Bradley, D. D. C.; Burroughes, J. H.; Friend, R. H.; Greenham, N. C.; Burns, P. L.; Holmes, A. B.; Kraft, A. *Appl. Phys. Lett.* **1992**, *61*, 2793.
(333) Burroughes, J. H.; Bradley, D. D. C.; Brown, A. R.; Marks, R. N.; Mackay, K.; Friend, R. H.; Burns, P. L.; Holmes, A. B. *Nature* **1990**, *347*, 539.
(334) Sato, Y.; Kanai, H. *Mol. Cryst. Liq. Cryst.* **1994**, *253*, 143.
(335) Do, L. M.; Han, E. M.; Niidome, Y.; Fujihira, M.; Kanno, T.; Yoshida, S.; Maeda, A.; Iksushima, A. J. *J. Appl. Phys.* **1994**, *76*, 5118.
(336) McElvain, J.; Antoniadis, H.; Hueschen, M. R.; Miller, J. N.; Roitman, D. M.; Sheats, J. R.; Moon, R. L. *J. Appl. Phys.* **1996**, *80*, 6002.
(337) Burrows, P. E.; Bulovic, V.; Forrest, S. R.; Sapochak, L. S.; McCarty, D. M.; Thompson, M. E. *Appl. Phys. Lett.* **1994**, *65*, 2922.
(338) VanSlyke, S. A.; Chen, C. H.; Tang, C. W. *Appl. Phys. Lett.* **1996**, *69*, 2160.
(339) Shi, J.; Tang, C. W. *Appl. Phys. Lett.* **1997**, *70*, 1665.
(340) Han, E.-M.; Do, L.-M.; Nidome, Y.; Fujihira, M. *Chem. Lett.* **1994**, 969.
(341) Fenter, P.; Schreiber, F.; Bulovic, V.; Forrest, S. R. *Chem. Phys. Lett.* **1997**, in press.
(342) Orita, K.; Morimura, T.; Horiuchi, T.; Matsushige, K. Int. Conf. on Electrolum. of Molec. Mat. and Related Phenom., Kitakyushu, Japan, 1997; p 106.
(343) Tidswell, I. M.; Ocko, B. M.; Pershan, P. S.; Wasserman, S. R.; Whitesides, G. M.; Axe, J. D. *Phys. Rev. B* **1990**, *41*, 1111.
(344) Tokito, S.; Tanaka, H.; Okada, A.; Taga, Y. *Appl. Phys. Lett.* **1996**, *69*, 878.
(345) Papadimitrakopoulos, F.; Zhang, X.-M.; Thomsen, D. L., III; Higginson, K. A. *Chem. Mater.* **1996**, *8*, 1363.
(346) Shen, Z.; Burrows, P. E.; Bulovic, V.; McCarty, D. M.; Thompson, M. E.; Forrest, S. R. *Jpn. J. Appl. Phys. Lett.* **1996**, *35*, L401.
(347) Garbuzov, D. Z.; Bulovic, V.; Burrows, P. E.; Forrest, S. R. *Chem. Phys. Lett.* **1996**, *249*, 433.

(348) Adachi, C.; Tsutsui, T.; Saito, S. *Optoelectron.—Dev. Technol.* **1991**, *6*, 25.
(349) Kalinowski, J.; Giro, G.; Marco, P. D.; Camaioni, N.; Fattori, V. *Chem. Phys. Lett.* **1997**, *265*, 607.
(350) Lin, L.-B.; Jenekhe, S. A.; Young, R. H.; Borsenberger, P. M. *Appl. Phys. Lett.* **1997**, *70*, 2052.
(351) Hung, L. S.; Tang, C. W.; Mason, M. G. *Appl. Phys. Lett.* **1997**, *70*, 152.
(352) Wu, C.-C.; Chun, J.; Burrows, P.; Forrest, S. R.; Register, R. A.; Sturm, J. C.; Thompson, M. E. *Polym. Prepr.* **1994**, *35*, 101.
(353) Suzuki, H.; Hoshino, S. *J. Appl. Phys.* **1996**, *79*, 858.
(354) Suzuki, H.; Hoshino, S. *J. Appl. Phys.* **1996**, *79*, 8816.
(355) Blom, P. W. M.; deJong, M. J. M.; Vleggar, J. J. M. *Appl. Phys. Lett.* **1996**, *68*, 3308.
(356) Lampert, M. A.; Mark, P. *Current Injection In Solids*; Academic: New York, 1970.
(357) Friedman, L. *Phys. Rev. A* **1965**, *140*, 1649.
(358) Hosokawa, C.; Tokailin, H.; Higashi, H.; Kusumoto, T. *Appl. Phys. Lett.* **1992**, *60*, 1220.
(359) Shockley, W.; Read, W. T. *Phys. Rev.* **1952**, *87*, 835.
(360) Forrest, S. R.; Shen, Z.; Burrows, P. E.; Bulovic, V.; Thompson, M. E. Inorganic and Organic Electroluminescence/EL '96, Berlin, 1996; p 83.
(361) Burrows, P. E.; Forrest, S. R.; Sibley, S. P.; Thompson, M. E. *Appl. Phys. Lett.* **1996**, *69*, 2959.
(362) Burrows, P. E.; Forrest, S. R.; Sibley, S. M.; Thompson, M. E. Mat. Res. Soc. Ann. Mtg., Boston, 1996; p D3.10.
(363) Matsumura, M.; Akai, T.; Saito, M.; Kimura, T. *J. Appl. Phys.* **1996**, *79*, 264.
(364) Matsumura, M.; Jinde, Y.; Akai, T.; Kimura, T. *Jpn. J. Appl. Phys.* **1996**, *35*, 5735.
(365) Parker, I. D. *J. Appl. Phys.* **1994**, *75*, 1656.
(366) Joswick, M. D.; Campbell, I. H.; Barashkov, N. N.; Ferraris, J. P. *J. Appl. Phys.* **1996**, *80*, 2883.
(367) Bulovic, V.; Tian, P.; Burrows, P. E.; Gokhale, M. R.; Forrest, S. R.; Thompson, M. E. *Appl. Phys. Lett.* **1997**, *70*, 294.
(368) Sugiyama, K.; Yoshimura, D.; Ito, E.; Miyazaki, T.; Hamatani, Y.; Kawamoto, I.; Ouchi, Y.; Seki, K.; Ishii, H. *Mol. Cryst. Liq. Cryst.* **1996**, *285—286*, 239.
(369) Hirose, Y.; Kahn, A.; Aristov, V.; Soukiassian, P.; Bulovic, V.; Forrest, S. R. *Phys. Rev. B* **1996**, *54*, 13748.
(370) Narioka, S.; Ishii, H.; Yoshimura, D.; Sei, M.; Ouchi, Y.; Seki, K.; Hasegawa, S.; Miyazaki, T.; Harima, Y.; Yamashita, K. *Appl. Phys. Lett.* **1995**, *67*, 1899.
(371) Probst, M.; Haight, R. *Appl. Phys. Lett.* **1997**, *70*, 1420.
(372) Mori, Y. In *Organic Electroluminscent Materials and Devices*; Miyata, S., Nalwa, H. S., Eds.; Gordon & Breach: Amsterdam, 1997.
(373) Burrows, P. E.; Gu, G.; Bulovic, V.; Forrest, S. R.; Thompson, M. E. *IEEE Trans. Electron. Dev. Lett.* **1997**, *44*.
(374) Wu, C. C.; Sturm, J. C.; Register, R. A.; Thompson, M. E. *Appl. Phys. Lett.* **1996**, *69*, 3117.
(375) Strukelj, M.; Jordan, R. H.; Dodabalapur, A. *J. Am. Chem. Soc.* **1996**, *118*, 1213.
(376) Kido, J.; Kimura, M.; Nagai, K. *Science* **1995**, *267*, 1332.
(377) Kido, J.; Ikeda, W.; Kimura, M.; Nagai, K. *Jpn. J. Appl. Phys.* **1996**, *35*, L394.
(378) Hamada, Y.; Adachi, C.; Tsutsui, T.; Saito, S. *Jpn. J. Appl. Phys.* **1992**, *31*, 1812.
(379) Matsura, M.; Tokailin, H.; Eida, M.; Hosokawa, C.; Hironaka, Y.; Kusumoto, T. Proc. Asia Display, '95, 1995; p 269.
(380) Tasch, S.; Brandstatter, C.; Meghdadi, F.; Liesing, G.; Froyer, G.; Athouel, L. *Adv. Mater.* **1997**, *9*, 33.
(381) Nakamura, H.; Hosokawa, C.; Kusumoto, T. Inorganic and Organic Electroluminescence/EL 96, Berlin, 1996; p 95.
(382) Yoshida, M.; Fujii, A.; Ohmori, Y.; Yoshino, K. *Jpn. J. Appl. Phys.* **1996**, *35*, L397.
(383) Bulovic, V.; Gu, G.; Burrows, P. E.; Thompson, M. E.; Forrest, S. R. *Nature* **1996**, *380*, 29.
(384) Burrows, P. E.; Gu, G.; Bulovic, V.; Forrest, S. R.; Thompson, M. E. Device Research Conference, Santa Barbara, 1996.
(385) Shen, Z.; Burrows, P. E.; Bulovic, V.; Forrest, S. R.; Thompson, M. E. *Science* **1997**, *276*, 2009.
(386) Takada, N.; Tsutsui, T.; Saito, S. *Appl. Phys. Lett.* **1993**, *63*, 2032.
(387) Takada, N.; Tsutsui, T.; Saito, S. *Jpn. J. Appl. Phys.* **1994**, *33*, L863.
(388) Dodabalapur, A.; Rothberg, L. J.; Miller, T. M. *Appl. Phys. Lett.* **1994**, *65*, 2308.
(389) Dodabalapur, A.; Rothberg, L. J.; Miller, T. M.; Kwock, E. W. *Appl. Phys. Lett.* **1994**, *64*, 2486.
(390) Lidzey, D. G.; Pate, M. A.; Wittaker, D. M.; Bradley, D. D. C.; Weaver, M. S.; Fisher, T. A.; Skolnick, M. S. *Chem. Phys. Lett.* **1996**, *263*, 655.
(391) Cimrova, V.; Neher, D. *J. Appl. Phys.* **1996**, *79*, 3299.
(392) Jordan, R. H.; Rothberg, L. J.; Dodabalapur, A.; Slusher, R. E. *Appl. Phys. Lett.* **1996**, *69*, 1997.
(393) Dodabalapur, A.; Rothberg, L. J.; Jordan, R. H.; Miller, T. M.; Slusher, R. E.; Phillips, J. M. *J. Appl. Phys.* **1996**, *80*, 6954.
(394) Marks, R. N.; Biscarini, F.; Zamboni, R.; Taliani, C. *Europhys. Lett.* **1995**, *32*, 523.
(395) Era, M.; Tsutsui, T.; Saito, S. *Appl. Phys. Lett.* **1995**, *67*, 2436.
(396) Gu, G.; Shen, Z.; Burrows, P. E.; Forrest, S. R. *Adv. Mater.* **1997**, *9*, 725.
(397) Gustaffson, G.; Treacy, G. M.; Cao, Y.; Klavertter, F.; Colaneri, N.; Heeger, A. J. *Synth. Met.* **1993**, *57*, 4123.
(398) Gymer, R. W. *Endeavor* **1996**, *20*, 115.
(399) Tsutsui, T. *Mater. Res. Soc. Bull.* **1997**, *22*, 39.
(400) Burrows, P. E.; Forrest, S. R.; Thompson, M. E. *Curr. Opinion Sol. State Mater. Sci.* **1997**, *2*, 236.
(401) Wakimoto, T.; Murayama, R.; Nagayama, K.; Okuda, Y.; Nakada, H.; Tohma, T. *Soc. Inf. Disp. Dig.* **1996**, 849.
(402) Lovinger, A. J.; Davis, D. D.; Ruel, R.; Torsi, L.; Dodabalapur, A.; Katz, H. E. *J. Mater. Res.* **1995**, *10*, 2958.
(403) Torsi, L.; Dodabalapur, A.; Katz, H. E. *J. Appl. Phys.* **1995**, *78*, 1088.
(404) Gundlach, D. J.; Lin, Y. Y.; Jackson, T. N. *IEEE Electron. Dev. Lett.* **1997**, *18*, 87.
(405) deLeeuw, D. M.; Brown, A. R.; Matters, M.; Chmil, K.; Hart, C. M. Mat. Res. Soc. Spring Mtg., San Francisco, 1997; p Paper H3.5, 144.
(406) Dodabalapur, A.; Laquindanum, J.; Katz, H. E.; Bao, Z. *Appl. Phys. Lett.* **1996**, *69*, 4227.
(407) Guillaud, G.; Sadoun, M. A.; Maitrot, M.; Simon, J.; Bouvet, M. *Chem. Phys. Lett.* **1990**, *167*, 503.
(408) Hoshimono, K.; Fujimori, S.; Fujita, S.; Fujita, S. *Jpn. J. Appl. Phys. Part 2* **1993**, *32*, L1070.
(409) Lin, Y. Y.; Gundlach, D. J.; Nelson, S. F.; Jackson, T. N. 55th Ann. Dev. Res. Conf., Ft. Collins, CO, 1997; p 60.
(410) Blom, P. W. M.; Jong, M. J. M. d.; vanMunster, M. G. *Phys. Rev. B* **1997**, *55*, R656.
(411) Severt, B.; Horowitz, G.; Ries, S.; Lagorse, O.; Alnot, P.; Yassar, A.; Deloffre, F.; Srivastava, P.; Hajlaoui, R.; Lang, P.; Garnier, F. *Chem. Mater.* **1994**, *6*, 1809.
(412) Narioka, S.; Ishii, H.; Edamatsu, K.; Kamiya, K.; Hasegawa, S.; Ohta, T.; Ueno, N.; Seki, K. *Phys. Rev. B* **1995**, *52*, 217.
(413) Torsi, L.; Dodabalapur, A.; Lovinger, A. J.; Katz, H. E.; Ruel, R.; Davis, D. D.; Baldwin, K. W. *Chem. Mater.* **1995**, *7*, 2247.
(414) Dodabalapur, A.; Katz, H. E.; Torsi, L.; Haddon, R. C. *Appl. Phys. Lett.* **1996**, *68*, 1108.
(415) Ohno, T. R.; Chen, Y.; Harvey, S. E.; Kroll, G. H.; Weaver, J. H.; Haufler, R. E.; Smalley, R. E. *Phys. Rev. B* **1991**, *44*, 13747.
(416) Hosokawa, C. *Appl. Phys. Lett.* **1993**, *62*, 3238.
(417) Sugiura, H.; Iga, R.; Yamada, T. *J. Cryst. Growth* **1992**, *120*, 389.
(418) Forrest, S. R.; Burrows, P. E.; Haskal, E. I.; Zhang, Y. Mat. Res. Soc. Ann. Mtg., Boston, MA, 1994; p 37.
(419) Hayashi, K.; Kawato, S.; Fujii, Y.; Horiuchi, T.; Matsushige, K. *Appl. Phys. Lett.* **1997**, *70*, 1384.
(420) Tatsuura, S.; Sotoyama, W.; Motoyoshi, K.; Matsuura, A.; Hayano, T.; Yoshimura, T. *Appl. Phys. Lett.* **1993**, *62*, 2182.
(421) Tatsuura, S.; Sotoyama, W.; Yoshimura, T. *Appl. Phys. Lett.* **1992**, *60*, 1661.
(422) Yoshida, Y.; Horiuchi, T.; Matsushige, K. *Jpn. J. Appl. Phys.* **1993**, *32*, 1248.
(423) Kubono, A.; Kitoh, T.; Kajikawa, K.; Umemoto, S.; Takezoe, H.; Fukuda, A.; Okui, N. *Jpn. J. Appl. Phys.* **1992**, *31*, L1195.
(424) Takeno, A.; Okui, N.; Kitoh, T.; Muraoka, M.; Umemoto, S.; Sakai, T. *Thin Solid Films* **1991**, *202*, 213.
(425) Takeno, A.; Okui, N.; Kitoh, T.; Muraoka, M.; Umemoto, S.; Sakai, T. *Thin Solid Films* **1991**, *202*, 205.
(426) Perry, J. W.; Marder, S. R.; Perry, K. J.; Sleva, E. T. *Proc. SPIE* **1991**, *1560*, 302.
(427) Kubono, A.; Higuchi, H.; Umemoto, S.; Okui., N. *Thin Solid Films* **1993**, *232*, 256.
(428) *GaInAsP Alloy Semiconductors*; Pearsall, T. P., Ed.; John Wiley: New York, 1982.
(429) Forrest, S. R.; Burrows, P. E.; Stroustrup, A.; Strickland, D.; Ban, V. S. *Appl. Phys. Lett.* **1996**, *68*, 1326—1328.
(430) Burrows, P. E.; Forrest, S. R.; Sapochak, L. S.; Schwartz, J.; Buma, T.; Ban, V. S.; Forrest, J. L. *J. Cryst. Growth* **1995**, *156*, 91.
(431) Tsang, W. T. *J. Cryst. Growth* **1990**, *105*, 1.
(432) Tsang, W. T. *J. Cryst. Growth* **1992**, *120*, 1.
(433) Feller, M. B.; Chen, W.; Shen, Y. R. *Phys. Rev. A* **1991**, *43*, 6778.
(434) Zhuang, X.; Marrucci, L.; Shen, Y. R. *Phys. Rev. Lett.* **1994**, *73*, 1513.
(435) Tillman, N.; Ulman, A.; Penner, T. L. *Langmuir* **1989**, *5*, 101.
(436) Wu, S. *Polymer Interface and Adhesion*; Marcel Dekker: New York, 1982.
(437) Forrest, S. R. *Optoelectronics in Japan and the United States*; Loyola College: Baltimore, 1996.
(438) Kuwata-Gonokami, M.; Jordan, R. H.; Dodabalapur, A.; Katz, H. E.; Schilling, M. L.; Slusher, R. E. *Opt. Lett.* **1995**, *20*, 2093.
(439) Tessler, N.; Denton, D. J.; Friend, R. H. *Nature* **1996**, *382*, 695.
(440) Hide, F.; Schwartz, B. J.; Diaz-Garcia, M. A.; Heeger, A. J. *Chem. Phys. Lett.* **1996**, *256*, 424.
(441) Hide, F.; Diaz-Garcia, M. A.; Schwartz, B. J.; Andersson, M. R.; Pei, Q.; Heeger, A. J. *Science* **1996**, *273*, 1833.

(442) Schwartz, B. J.; Hide, F.; Andersson, M. R.; Heeger, A. J. *Chem. Phys. Lett.* **1997**, *265*, 327.
(443) Kozlov, V. G.; Burrows, P. E.; Forrest, S. R. Conf. on Lasers and Electrooptics (CLEO '97), Baltimore, MD, 1997; p CPD-18. Kozlov, V. G.; Buloviç, V.; Burrows, P. E.; Forrest, S. R. *Nature*, in press.
(444) Soffer, B. H.; McFarland, B. B. *Appl. Phys. Lett.* **1967**, *10*, 266.
(445) Kogelnik, H.; Shank, C. V. *Appl. Phys. Lett.* **1971**, *18*, 152.
(446) Karl, N. *Phys. Status Solidi* **1972**, *13*, 651.
(447) Hermes, R. E.; Allik, T. H.; Chandra, S.; Hutchinson, J. A. *Appl. Phys. Lett.* **1993**, *63*, 877.
(448) Diaz-Garcia, M. A.; Hide, F.; Schwartz, B. J.; McGehee, M. D.; Andersson, M. R.; Heeger, A. J. *Appl. Phys. Lett.* **1997**, *70*, 3191.
(449) Schafer, F. P. *Dye Lasers*; Springer-Verlag: Berlin, 1977.
(450) Haskal, E. I. University of Southern California, 1994.

CR941014O